Massive star-forming regions across the Galaxy

Initial stages of massive star formation in infrared high extinction clouds
and
Trigonometric parallaxes to 6.7 GHz methanol masers

Dissertation

zur

Erlangung des Doktorgrades (Dr. rer. nat)

der

Mathematisch-Naturwissenschaftlichen Fakultät

der

Rheinischen Friedrich-Wilhelms-Universität Bonn

vorgelegt von

Kazi Lucie Jessica Rygl

aus

Amsterdam, die Niederlande

Bonn (April 2010)

Angefertigt mit Genehmigung der Mathematisch-Naturwissenschaftlichen Fakultät
der Rheinischen Friedrich-Wilhelms-Universität Bonn

1. Gutachter **Prof. Dr. Karl M. Menten**

2. Gutachter **Prof. Dr. Pavel Kroupa**

Tag der Promotion: June 14, 2010

Erscheinungsjahr: 2010

Contents

Abbreviations

APEX:	Atacama Pathfinder Experiment
ATLASGAL:	APEX Telescope Large Area Survey of the Galaxy
CH_3CN:	Methyl cyanide
CH_3OH:	Methanol
CO:	Carbon monooxide
EVN:	European VLBI Network
FFTS:	Fast Fourier Transform Spectrometer
FSRQ:	Flat-Spectrum Radio Quasar
FWHM/P:	Full Width at Half Maximum/Power
GLIMPSE:	Galactic Legacy Infrared Mid-Plane Survey Extraordinaire
H_2CO:	Formaldehyde
H_2O	Water
HCO^+:	Hydroxymethylidyne
HEC	High Extinction Cloud
Hipparcos:	High Precision Parallax Collecting Satellite
HMPO:	High-mass Proto Stellar Object
IF:	Intermediate Frequency
IR:	Infrared
IRAC:	Infrared Array Cameras

IRAM:	Institut de Radioastronomie Millimétrique
IRDC:	Infrared Dark Cloud
ISM:	Interstellar Medium
JIVE:	Joint Institute for VLBI in Europe
LSR:	Local Standard of Rest
MAMBO:	Max-Planck Bolometer Array
MIPS:	Mid Infrared Photometer
MSX	Midcourse Space Expriment
NH_3:	Ammonia
N_2H^+:	Diazenylium
SFR:	Star Formation Region
SO:	Sulfur oxide
UCHII region	Ultra Compact HII region
UT:	Universal Time
UV:	Ultra Violet
VLA:	Very Large Array
VLBI:	Very Long Baseline Interferometry

Constants, quantities and units

Speed of light c	$2.997 \times 10^{10}\,\mathrm{cm\,s^{-1}}$
Gravitational constant G	$6.67 \times 10^{-8}\,\mathrm{cm^3\,g^{-1}\,s^{-2}}$
Constant of Planck h	$6.63 \times 10^{-27}\,\mathrm{erg\,s}$
Constant of Boltzmann k	$1.38 \times 10^{-16}\,\mathrm{erg\ K^{-1}}$
mass of hydrogen atom m_H	$1.67 \times 10^{-24}\,\mathrm{g}$
Jansky (Jy)	$1 \times 10^{-26}\,\mathrm{W\,m^{-2}\,Hz^{-1}}$
Solar mass ($\mathrm{M}_\odot$)	$1.989 \times 10^{33}\,\mathrm{g}$
parsec (pc)	$3.08 \times 10^{18}\,\mathrm{cm}$
Astronomical unit (AU)	$1.496 \times 10^{11}\,\mathrm{cm}$
α	right ascension or R.A. (h:m:s)
δ	declination or dec. ($^\circ$:$'$:$''$)
η	depletion
θ	elevation ($^\circ$)
Θ	Galactic rotation speed (km $\mathrm{s^{-1}}$)
κ	dust opacity per unit mass column density ($\mathrm{cm^2\,g^{-1}}$)
λ	wavelength (mm)
μ_α	proper motion in right ascencion (mas $\mathrm{yr^{-1}}$)
μ_δ	proper motion in declination (mas $\mathrm{yr^{-1}}$)
μ_D	molecular dipole moment (D)

μ=2.33	mean molecular weight
ν	frequency (GHz)
π	parallax (mas=milli arc second)
ρ	mass density (g cm^{-3})
τ	opacity, optical depth
χ	abundance
$A_{\rm V}$	visual extinction (mag)
$B_{\rm eff}$	main beam efficiency of a single dish radio antenna
d	distance (kpc)
$E(X-Y)$	color excess between wavelengths X and Y (mag)
E_u	energy of upper level of a two level system (K)
F^i	integrated flux (Jy)
F^p	peak flux (Jy beam^{-1})
$F_{\rm eff}$	forward efficiency of a single dish radio antenna
g	degeneracy
J	angular momentum quantum number
K	angular momentum along the symmetry axis of the molecule
l	Galactic latitude (degree)
b	Galactic longitude (degree)
M	mass (M$_\odot$)
n	(volume) density (cm^{-3})
N	column density (cm^{-2})
R	radius (pc)
T	temperature (K)
R_0	distance between the Sun and the Galactic center (kpc)
U	velocity vector toward the Galactic center (km s^{-1})
V	velocity vector toward the direction of Galactic rotation (km s^{-1})
W	velocity vector toward the North Galacic Pole (km s^{-1})
v	velocity (km s^{-1})
Δv	line width (km s^{-1})
δv	skewness parameter (km s^{-1})

CHAPTER 1

Introduction

Massive stars play a fundamental role in the evolution of galaxies through their strong UV radiation, stellar winds and supernovae explosions, which contribute to the chemical enrichment of the interstellar medium. Observations of other spiral galaxies show that the spiral arms are dominated by massive stars, recognizable by the blue light they emit and by the dust lanes that harbor the still embedded young massive stars in HII regions (see Fig. 1.1). Star formation, and evidently *massive* star formation, takes place in the spiral arms. Also the Milky Way, our Galaxy, is a spiral galaxy. Since we are located in the Galactic disk we are not able to see the structure of the spiral arms directly, but evidence of it is found in velocity-longitude diagrams of the observed HI and CO gas. From our position, most young massive stars are located in the Galactic plane, but the majority of them is hidden from us in the optical light due to the extinction of dust.

Massive star formation

Theoretically there is a problem in understanding the formation of massive stars ($M_\star > 8\,\mathrm{M}_\odot$), because they start their hydrogen fusion and become stars, while still accreting matter. The radiation released by the fusion results in a huge radiation pressure directed outwards, which should make further accretion difficult if not impossible. A possible solution to continue the accretion was found in non-spherical accretion via, for example, an accretion disc (Krumholz et al. 2009) or competitive accretion (Bonnell et al. 2001; Clark et al. 2008). This debate is still ongoing since it is very difficult to observe the early stages of massive star formation.

Massive stars are rare and form in clusters at large distances, so it is impossible to resolve any single massive star during formation. Additionally, young protostars are still deeply embedded in the natal cloud, which makes them invisible in many frequencies. However, it also causes their natal clouds to extinct the background light emitted by the numerous stars in the Galactic plane at infrared wavelengths. This inspired the first search of infrared dark clouds (IRDCs) in the infrared survey by the Midcourse Space Experiment (MSX) (Perault et al. 1996; Egan et al. 1998). IRDCs are currently thought to be the earliest observable stages of massive star formation.

As a consequence of the relatively low number of massive stars, large scale unbiased surveys are necessary to find them in an early stage when they are still forming. The Galactic Legacy Infrared Mid-Plane Survey Extraordinaire (GLIMPSE) survey was performed using the Spitzer Space Telescope and observed the complete inner part of the Galactic plane in four infrared wavelength bands (Infrared Array Cameras (IRAC), Fazio et al. 2004) with unprecedented sensitivity. This enabled

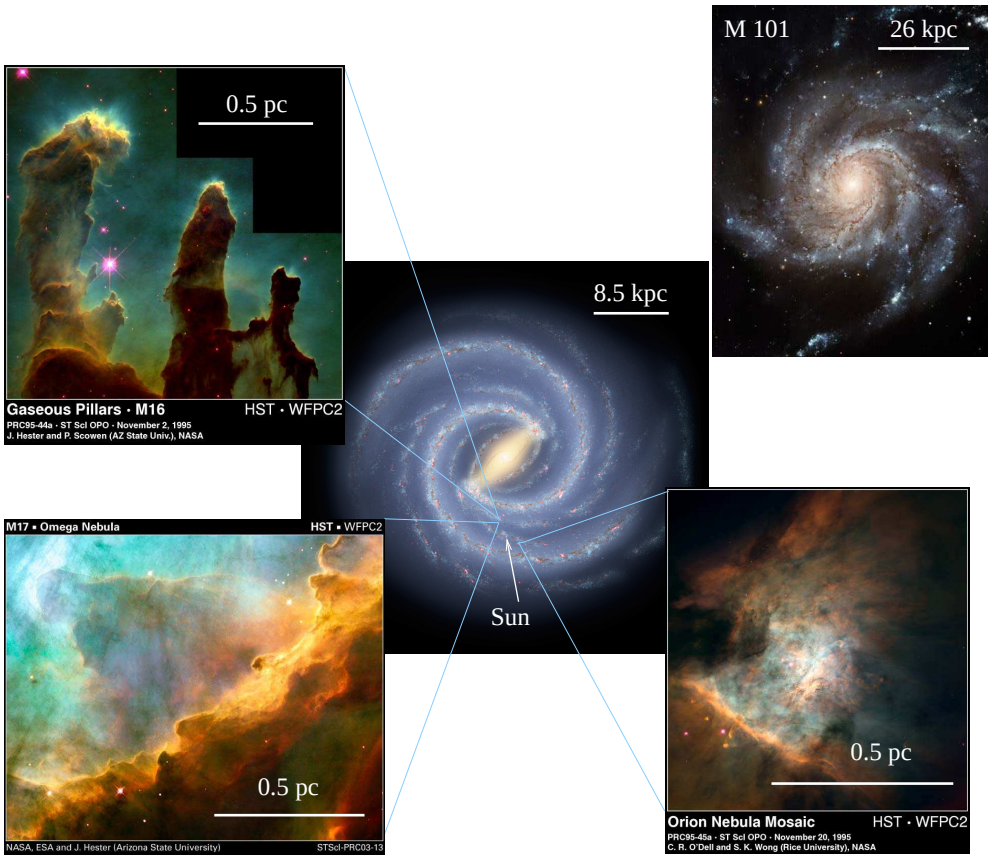

Figure 1.1: In the middle is shown an artist impression of the Milky way (image credit: R.Hurt/NASA/JPL-Caltech/SSC) where the arms are delineated by star formation. One can compare the spiral structure of our Galaxy to a typical spiral galaxy, M101, in the top right plot (image credit: HST/NASA/ESA/STScI, K. Kuntz (JHU), F. Bresolin (University of Hawaii), J. Trauger (JPL), J. Mould (NOAO), Y.-H. Chen (University of Illinois), CFHT: J.-C. Cuillandre/Coelum, NOAO: G. Jacoby, B. Bohannan,M. Hanna (NOAO/AURA/NSF)). Several Hubble Space Telescope (HST) images of star-forming regions are shown in the top left, bottom left and bottom right pop-ups. The top left image shows the "Pillars of Creation" in M16 (image credit: NASA/ESA/STScI, J. Hester and P. Scowen (Arizona State University)). In the bottom left, there is M17 (image credit: NASA/ESA, J.Hester (ASU)), and in the bottom right is the most nearby massive star-forming region in Orion (image credit: NASA, C.R. O'Dell and S.K. Wong (Rice University)).

us to start a new search for the earliest stages of massive star formation: using the color excess between the two shortest wavelength bands of GLIMPSE, we made extinction maps covering the same Galactic extent. Extinction is a direct measure of column density, and therefore also of mass. Our extinction maps allow to locate all massive regions in the inner part of the Galaxy up to a certain distance ($\sim 5\,\mathrm{kpc}$). Infrared extinction maps are a more powerful tool for finding high column densities than extinction maps in shorter wavelengths, such as the near infrared or optical, because extinction decreases with increasing wavelength allowing to reach higher visual extinctions at longer wavelengths. We selected and cataloged only compact regions of high column density for to avoid any confusion with the large scale density structure of the Galaxy itself.

High extinction clouds are defined by their selection criteria to have column densities, $N_{\mathrm{H_2}}$, $> 10^{22}\,\mathrm{cm}^{-2}$. Since gas and dust trace dense regions in the inter stellar medium, they are the main tools to study these clouds. Dust emission is optically thin at millimeter or submillimeter wavelengths, and therefore the dust emission reveals the mass distribution of a cloud. Furthermore, this wavelength regime contains a wealth of transitions of molecules in the gas phase. For a sample of the high extinction clouds, extensive observations of dust emission and molecular lines were carried out to find the physical parameters such as kinematic distances, masses, kinetic temperatures, column densities, and their morphology. Based on the morphology we divided the sample into three cloud classes to understand the evolution of the clouds and the clumps within. The clumps found in the high extinction clouds can become star clusters of which the more massive ones can host massive stars. By searching for signs of gravitational collapse of the clump (infall), outflows, depletion, and star formation tracers, such as masers and hot core molecules, we tried to understand the stage of star formation in the clumps. For one cloud, G017.19+00.81, we expanded the study of its kinematics by spectral line imaging.

Distance measurements

For the understanding of star formation regions (SFRs), accurate distances play a very important role, because they determine important physical parameters such as the size scales, masses, luminosities and ages. But, also to study the large scale structure of the Milky Way, which is still poorly understood, accurate distances on Galactic scales, of 1 to more than 10 kpc, are needed. Currently, not only the Galactic rotation curve, but also the number of spiral arms and the presence of a Galactic bar are debatable.

The most common (Galactic) distance methods are:

- Kinematic distances; these rely on the knowledge of the Galactic rotation curve and are ambiguous towards the inner part of the Galaxy.
- Photometric distances; these rely on the knowledge of the Galactic extinction.
- Luminosity distances; these rely on the knowledge of the stellar spectral type and are affected by Galactic extinction.

Since neither the Galactic extinction nor the rotation curve of our Galaxy are very accurately known, these methods have large uncertainties.

Of all the methods available for distance measurements the trigonometric parallax is the most reliable one. It is the only method that does not depend on physical assumptions, since it is merely a geometric effect of the projected motion of the Earth's motion around the Sun on close by (Galactic) objects with respect to distant sources (extra galactic radio quasars). However, its measurement requires a very high astrometric accuracy of milli to micro arcseconds and therefore other methods are more common.

To study the kinematics of the Galaxy, it is also necessary to measure the velocities of the stars, HII regions and other constituents of the Galaxy. Spectral lines yield the radial velocity component, but for the tangential components the distance and the proper motion are required. The proper motion of an object is the (angular) motion in right ascension (R.A.) and declination measured in milli arcseconds per year. In a parallax experiment the position of the source (relative to a well-known reference position) is observed several times during at least one year. The results

contain two superimposed signatures: the parallax sinusoid and a linear trend; the proper motion. Combining the proper motions and the distance with the radial velocity allows to calculate the three-dimensional space velocity. With this space velocity one can study the total motion of the object in the Galactic plane, and understand if the object is rotating on a circular orbit or if it exhibits significant peculiar motion.

Molecular maser emission

To measure the trigonometric parallax with Very-Large-Baseline Interferometry (VLBI) one requires very strong and compact sources that emit in the radio regime. Molecular masers are the ideal targets:

- Masers occur in obscured and dusty regions such in star forming regions and asymptotic giant branch stars.
- Masers are very bright and compact objects.
- The host regions of masers, e.g. SFRs, are important research topics; so knowledge of their distance is important.

At radio frequencies we find several strong maser species, such as the 22 GHz $6_{16} \rightarrow 5_{23}$ transition of water, the 43 GHz $J = 1 \rightarrow 0$ $v = 1$ and 2 vibrationally excited states of SiO, and the 6.7 GHz $5_1 \rightarrow 6_0$ A^+ and 12.2 GHz $2_0 \rightarrow 3_{-1}$ E transitions of methanol. H_2O masers are commonly used for astrometry, because they are the strongest masers – they can have fluxes of the order of kJy. They are usually associated with protostellar outflows (Menten 1996), since they have such a large velocity spread and proper motions of 20–200 km s^{-1} (Hachisuka et al. 2006). This makes it difficult to measure the true proper motion of the object to which the maser belongs; one would need to correctly subtract the outflow motion. Another difficulty with H_2O masers is their variability; maser spots can vanish on timescales shorter than a year, and new ones can arise elsewhere. Parallax measurements require the same maser spot to be followed over a period of *minimally* one year.

The 6.7 GHz methanol maser transition was first observed by Menten (1991). Observations find 6.7 GHz masers to be exclusively associated with the early stages of massive star formation before or during the formation of an ultra compact HII (UCHII) region (Menten 1991; Walsh et al. 1998; Ellingsen 2006; Pestalozzi et al. 2007). The kinematics suggest that the methanol masers are not formed in outflows, since their velocity spread and proper motions are both small. This, combined with the strength and ubiquity of the transition make them ideal for astrometric purposes. In 2006, when this project started, the European VLBI Array (EVN) together with the Australian Large Baseline Array were the only VLBI arrays equipped with 6 GHz receivers. Ours was the first parallax experiment performed with the EVN to explore the possibility of using the 6.7 GHz methanol masers for trigonometric parallax measurements.

1.1 Aim and structure of this thesis

The main questions posed and answered in this thesis are:

- Do the infrared extinction maps follow the millimeter dust continuum emission, e.g. are the extinction maps able to trace high column density? And what are the limits of this method?
- What are the characteristics of the high extinction clouds - are they similar to IRDCs?
- Can the morphology of the clouds be used to trace their evolution?
- Do the conditions in the clumps of high extinction clouds allow massive star formation?
- What is the distribution between the various stages of starless, prestellar and ongoing star formation clumps?

- Is cloud G017.19+00.81 a case of triggered star formation and in which evolutionary stages are the clumps of this cloud?
- Can one use 6.7 GHz methanol masers for measuring trigonometric parallexes? What are the advantages and disadvantages of astrometric observations at this frequency?
- How do the obtained distances for the SFRs compare with other parallax measurements?
- What are the 3-dimensional velocities for the studied SFRs and how do they compare with Galactic rotation?

The high extinction cloud section begins in the next chapter, with a presentation of the extinction maps and the physical parameters of the clouds and the clumps therein, such as kinematic distances, sizes, masses, temperatures and densities. In Chapter 3, we continue with a molecular line survey of the high extinction clouds and discuss infall, outflow, temperatures and column densities, presence of young stellar objects and depletion in the clumps. We end the high extinction clouds by presenting in Chapter 4 a case study of cloud G017.19+00.81, which was mapped by single dish and interferometer. The VLBI measurements of methanol masers are described in Chapter 5. Also the parallax results and their discussion are presented there. Each chapter ends with a summary. A final thesis-wide summary is given in Chapter 6.

CHAPTER 2

Physical properties of clumps in high extinction clouds

Accepted for publication in A&A, as Rygl, Wyrowski, Schuller, & Menten (2010b)

2.1 Introduction

Massive stars play a fundamental role in the evolution of galaxies through their strong UV radiation, stellar winds and supernovae explosions, which contribute to the chemical enrichment of the interstellar medium. Massive stars are rare, hence usually found at large distances. They form very rapidly while still deeply embedded in their natal molecular clouds. These characteristics impose several observational obstacles, like the necessity of high resolution and sensitivity in an un-absorbed frequency range, to study their formation.

Currently, the earliest stage of massive star formation is thought to take place in the very dense clumps found in Infrared Dark Clouds (IRDCs). The properties of IRDCs are shown by Carey et al. (1998) to be dense ($n_{\rm gas} > 10^5\,{\rm cm}^{-3}$) and cool ($T < 20\,{\rm K}$) aggregations of gas and dust in the Galaxy. They contain clumps with typical masses of $\geq 100\,{\rm M}_\odot$ (Rathborne et al. 2006; Pillai et al. 2006; Simon et al. 2006b). From IRDC clumps to the next stage, the high-mass protostellar objects (HMPOs, Beuther et al. 2002a; Sridharan et al. 2002), the temperatures increase ($30\,{\rm K} < {\rm T} < 60\,{\rm K}$), the line widths increase, densities and masses rise (Motte et al. 2007). HMPOs are usually found prior to the formation of ultra compact HII (UCHII) regions, before the newly formed star begins to ionize its surrounding medium.

Motte et al. (2007) demonstrated the difficulty of finding massive objects in an early evolutionary phase: in their survey of 3 deg^2 in Cygnus X, they found little evidence for dense clumps without any trace of star formation, however dense clumps with already ongoing star formation were found to be abundantly present. Based on these results, the statistical life time of the high-mass protostars and prestellar cores was estimated $\leq 3\times10^4\,{\rm yr}$ (Motte et al. 2007), which is much shorter than what is found in nearby low-mass star-forming regions: $\sim3\times10^5\,{\rm yr}$ (Kirk et al. 2005). It is these very early stages, which provide important clues to construct a theoretical model of massive star formation, since the initial fragmentation of the gas and dust in a clump will be different in the case of monolithical collapse (Krumholz et al. 2009) compared to the competitive accretion model (Bonnell et al. 2001; Clark et al. 2008).

Massive stars generally form in clusters (Lada & Lada 2003), of which the precursors are massive clumps or the so-called precluster forming clumps, hereafter just clumps, of a $\sim$1 pc size. For many

massive star-forming regions, we do not yet have the capacity to resolve the clumps into prestellar cores and study the fragmentation (Beuther et al. 2007; Rathborne et al. 2007, 2008; Zhang et al. 2009; Swift 2009). In this chapter, we report on the physical parameters of the clumps, such as their morphology, density and temperature. Based on this, we hypothesize on an evolutionary sequence of cluster formation.

Our understanding of the clumps increased considerably with the discovery of IRDCs. IRDCs are detected by a local absence of infrared (IR) emission against the diffuse mid IR emission of the Galactic plane (Perault et al. 1996; Egan et al. 1998) and are observed numerously throughout the Milky Way (Simon et al. 2006b). At the typical low temperatures of IRDCs ($\sim 20\,\mathrm{K}$), the dust emission peaks in the far-infrared and is optically thin at mm/submm wavelengths. For a majority of IRDCs the mm dust emission coincides with the morphology of the IR absorption (Rathborne et al. 2006; Pillai et al. 2006). Many clumps in IRDCs show signs of star formation via infrared emission at $24\,\mu$m, or SiO emission from shocks driven by outflows (Motte et al. 2007; Beuther & Sridharan 2007; Chambers et al. 2009). Observations tell that clumps in IRDCs span a very wide range of masses, indicating that not all will form clusters with massive stars (Rathborne et al. 2006; Pillai et al. 2006).

The detection method of IRDCs is very sensitive to the local properties of the background emission. Also, not all massive dust condensations will be infrared dark if there is enough foreground emission. Hence, to find the high mass end of molecular clouds in an unbiased fashion, new, complementary approaches are needed. We have developed such a new method, well known from studies of low mass star-forming regions, to target more efficiently the most massive clouds: Lada et al. (1994) pioneered the method of measuring high amounts of extinction through stellar color excess in the infrared. Applied to the $2\,\mu$m data of the 2MASS survey, they covered the range up to 40 magnitudes in visual extinction, A_V. However, this is not sufficient to probe the dense birthplaces of massive stars. Here the results of the Spitzer Space Telescope GLIMPSE survey (Benjamin et al. 2003) came to help: by applying the extinction curve of Indebetouw et al. (2005) we have extended the color excess method to reach up to peaks in A_V of $\sim$100 magnitudes (or column densities $N_{\mathrm{H_2}}$ of $9 \times 10^{22}\,\mathrm{cm^{-2}}$), thus entering the realm where massive star formation becomes possible. The extinction method, however, is limited by the number of available background stars, and will therefore detect mainly nearby clouds (discussed in Sect. 2.2.1). In the meanwhile, complementary, unbiased dust continuum surveys were carried out: the ATLASGAL survey of the complete inner Galactic plane at $870\,\mu$m by Schuller et al. (2009) and the 1.1 mm BOLOCAM survey (Rosolowsky et al. 2009) of the Galactic plane accessible from the northern hemisphere.

We selected the more compact and high extinction (mean $A_{\mathrm{V}} > 20\,\mathrm{mag}$ or $N_{\mathrm{H_2}} > 2\times10^{22}\,\mathrm{cm^{-2}}$) sources from large scale extinction maps of the inner Galactic plane ($-60^\circ < l < 60^\circ$, $0.9^\circ < b < -0.9^\circ$). These *high extinction clouds* (HECs) were studied in the millimeter dust continuum and the rotational transitions of ammonia (NH_3). NH_3 has proven to be a reliable tracer of dense gas in dark clouds: not only does the NH_3 emission match the submillimeter dust emission peaks (Pillai et al. 2006), but also do observations show that, unlike other molecules, NH_3 does not deplete from the gas phase for the typical IRDC densities of $< 10^5\,\mathrm{cm^{-3}}$ – Pagani et al. (2005) observed that NH_3 depletes at densities of $10^6\,\mathrm{cm^{-3}}$ in agreement with the prediction of Bergin & Langer (1997). Moreover, throughout the evolutionary stages of massive star formation, NH_3 shows an increasing trend in averaged line widths and temperatures from less to more evolved sources (Pillai et al. 2006), which indicates that the NH_3 molecule is also a tracer of evolutionary phase.

This study, published as Rygl et al. (2010b), presents an overview from the high extinction complexes on Galactic size-scales, covering several tens of parsecs, to the clumps found in the 1.2 mm continuum of 0.1–0.7 pc in size. The connection between the largest and smallest scale is important for a comprehensive view of cluster formation in giant molecular clouds. In Sect. 2.2 , we present the method of extinction mapping. Observations and data reduction are described in Sect. 2.3, and the results follow in Sect. 2.4. The analysis and discussion of the physical parameters are given in Sect. 2.5, and are compared to previous studies and theoretical predictions in Sect. 2.6.

2.2 High extinction clouds

2.2.1 Method: extinction mapping

The overall distribution of dust in a cloud can be traced by the extinction of background starlight at visual and near-infrared wavelengths as it passes through a cloud (Lada et al. 1994). Since extinction decreases with wavelength, observations at longer wavelengths probe deeper into the cloud and trace denser regions. Additionally the number of detectable background stars increases at these wavelengths. With the advance of infrared cameras it became possible to detect several hundreds of background stars through a cloud, allowing to convert the infrared images covering them in extinction maps of useful resolution.

The GLIMPSE survey employed the Infrared Array Cameras (Fazio et al. 2004) onboard the Spitzer Space telescope, operating at 3.6, 4.5, 5.8 and 8.0 μm. We used the data provided by the GLIMPSE I survey (release April 2005), which covered longitudes of $l = 10 - 65°$, $295 - 350°$with $b = \pm 1°$. The calibration of the data is described in Reach et al. (2005). The inner 20° of the Galactic Plane, except for the innermost $\pm 1°$, was taken from the GLIMPSE II survey (2007).

To construct the extinction maps we used the averaged (3.6 μm–4.5 μm) color excess, because the extinction law determination for these wavelengths is the most accurate of all the Spitzer bands. The averaged color excess, $< E(3.6\,\mu\mathrm{m} - 4.5\,\mu\mathrm{m}) >$, was calculated from the color excess in a large scale field (a box of size $108'' \times 108''$):

$$< E(3.6\,\mu\mathrm{m} - 4.5\,\mu\mathrm{m}) >= \\ < (3.6\,\mu\mathrm{m} - 4.5\,\mu\mathrm{m}) - (3.6\,\mu\mathrm{m} - 4.5\,\mu\mathrm{m})_0 > , \tag{2.1}$$

where the background stars are taken to be common-type K giants. Measurements of $(3.6\,\mu\mathrm{m} - 4.5\,\mu\mathrm{m})_0$ in such control fields showed that K giants have an average color of $\sim$0 mag with a dispersion of 0.2 mag. Starting from the reddening law for $< E(H - K) >$ in Lada et al. (1994), one can extend it following Indebetouw et al. (2005), and get the relation between the averaged color excess to the averaged visual extinction, $< A_V >$:

$$< A_V >= 81.8 < E(3.6\,\mu\mathrm{m} - 4.5\,\mu\mathrm{m}) > \qquad [\mathrm{mag}] . \tag{2.2}$$

The color excess map can be contaminated by embedded stars in the cloud itself or by foreground stars. The latter will increase in number as the cloud is located at a further distance. Since the foreground stars will not be reddened, they decrease the average color excess of the field. For example, if the number of foreground stars equals the number of background stars the color excess will be halved. It also means that for far away clouds the color excess will be underestimated. Rathborne et al. (2006) and Chambers et al. (2009) find signs of active massive star formation in one of our clouds. Such young red objects will contribute to the measured color excess, which will lead to an overestimation of the derived extinction. However, the selection of clouds associated with very early phases of star formation will not be affected.

In general, the limits of extinction mapping are set by the number of available background stars; their number has to be sufficient for a statistically meaningful color excess determination. Thus, the reach of the extinction method will change with Galactic latitude, because at higher latitudes the number of stars decreases. In the Galactic plane, there will be "horizon" to which one can measure a sufficient color excess, however this horizon will be far from uniform; it depends for every direction on the number of K giants in front and behind the clouds, which will differ when crossing a spiral arm or moving in towards the Galactic center.

Recently, Chapman et al. (2009) studied the changes in the mid-infrared extinction law within a large region with high resolution. They find that while in regions with a K-band extinction of $A_\mathrm{K} \leq 0.5$ mag, the extinction law is well fitted by an extinction factor, $R_\mathrm{V} = 3.1$ (Weingartner & Draine 2001), the regions with $A_\mathrm{K} \geq 1.0$ mag are more consistent with the Weingartner & Draine (2001) model of $R_\mathrm{V} = 5.5$, which uses larger maximum dust grain sizes. The high extinction clouds are by definition very dense regions for which $A_\mathrm{K} > 1.0$ mag. This means that the visual extinctions and column densities reached by the extinction mapping are a factor $\sim$1.8 higher than

estimated from Eq. 2.2, where we used $R_V = 3.1$. The near and mid-infrared extinction law is of great interest, and recently many publication appeared on the mid-infrared (Flaherty et al. 2007; Nishiyama et al. 2009; Zasowski et al. 2009) and the near-infrared Moore et al. (2005); Froebrich & del Burgo (2006); Stead & Hoare (2009) extinction law. Within the range of 3.6 and 4.5 μm, the range we used for our extinction maps, there is a reasonable agreement between the results of Indebetouw et al. (2005) and most recent studies.

2.2.2 Catalog of high extinction clouds

We made extinction maps for the complete inner part of the Galaxy with a resolution of 108″, plotted in Fig. 2.1. The mid-infrared extinction is changing with longitude and latitude, because it is sensitive to large-scale structures. Fig. 2.2 shows histograms of the average color excess in longitude and latitude. Most of the peaks in the average color excess can be associated to Galactic spiral arms. The large-scale structure of the extinction was excluded by selecting only compact high extinction regions with an color excess above 0.25 mag (equivalent to a hydrogen column density of 2×10^{22} cm^{-2}). In a second step, smaller extinction maps with a higher resolution (54″) were computed to obtain more accurate positions of the highest extinction peaks. These peaks were selected by eye, and regions with known sources, like for example HII regions and HMPOs, were discarded leaving a sample of unknown, and possibly cold and massive clouds. We studied 25 high extinction clouds (HECs) in the first Galactic quadrant. These were the clouds, visible from the northern hemisphere, with the highest extinction peaks which were not associated with HII regions from the Becker et al. (1994) survey and which had no available mm/submm maps from the literature. A complete catalog of all the high extinction clouds is given in Table A.1, where for each cloud the center position in J2000 coordinates is listed with its corresponding peak color excess.

2.3 Observations and data reduction

2.3.1 Millimeter bolometer observations and calibration

The 1.2 mm dust continuum of the selected extinction peaks was imaged with the 117-element Max-Planck Bolometer array (MAMBO-2) installed at the IRAM 30m telescope. The observations were performed in four sessions between 2006 October and 2007 March. The MAMBO passband has an equivalent width of approximately 80 GHz centered on an effective frequency of 240 GHz ($\lambda \sim 1.25$ mm). The FWHM beam size at this frequency is 10.″5. The maps were taken in the dual-beam on-the-fly mapping mode, where the telescope was scanning row by row in azimuth at a constant speed, while the secondary beam was wobbling in azimuth with a throw of 92″. The map sizes were 6′×6′, resulting in $\sim$ 10′×10′ images with a reduced sensitivity at the edges. Each scan was separated by 8″ in elevation. We used a scanning velocity of 8″ s^{-1} with a wobbler rate of 2 Hz. The observation time per map was $\sim$ 27 minutes. In total 25 high extinction clouds listed in Table A.2 were observed, the respective center positions used for the observations are given in Table A.1.

The project was observed in the bolometer pool as a backup project resulting in strongly varying weather conditions from one session to another. The zenith atmospheric opacity, τ, was monitored by sky dips, performed every $\sim$1.5 hour, and varied between 0.1 and 0.5. The calibration was performed every $\sim$3 hours mainly on HII regions G34.3+0.2 and G10.2–0.4, and was found to be accurate within $\sim$10%. Pointing checks were made roughly every half hour to hour, before and usually also after each map. Bolometer observations are dominated by the sky noise, the variation of the brightness of the sky, which usually exceeds the intensity of astronomical sources. The sky noise was reduced by subtracting the correlated noise between the bolometers in the array. The average r.m.s. noise signal in the individual maps was better than $\sim$15 mJy beam^{-1} after reduction of the sky noise. The data were reduced using the MOPSI software package developed by R. Zylka.

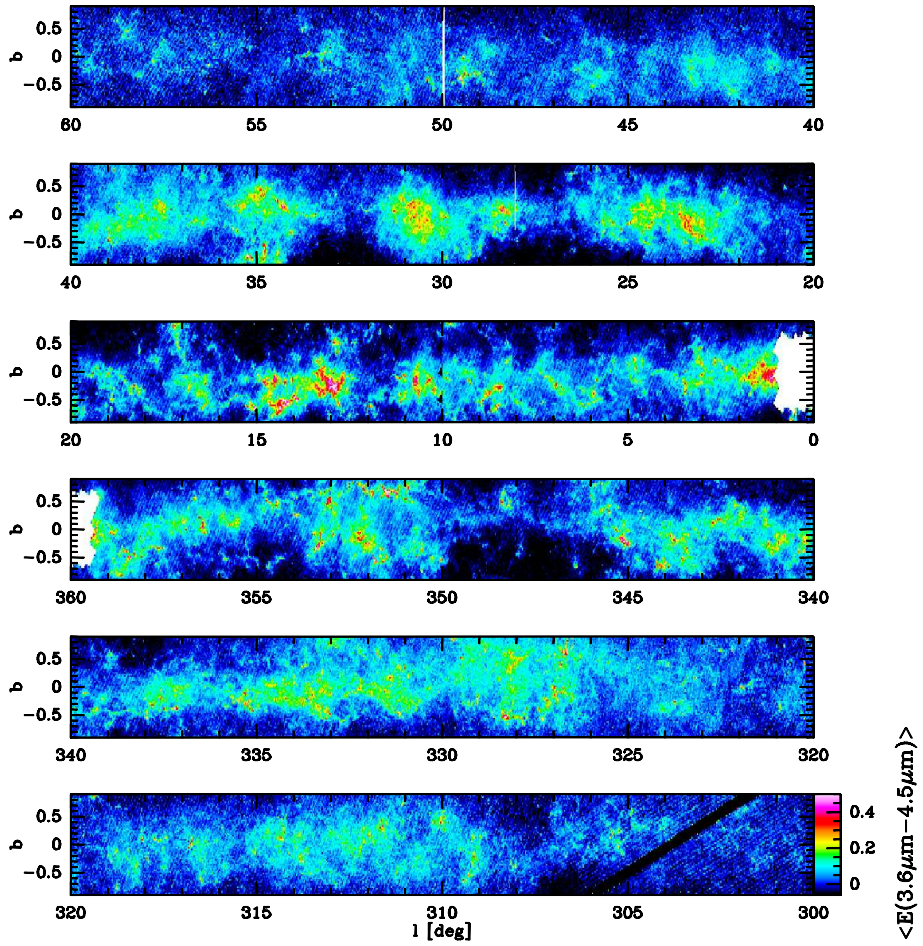

Figure 2.1: The color excess $< \mathrm{E}(3.6\mu\mathrm{m} - 4.5\mu\mathrm{m}) >$ for the first (*top three graphs*) and fourth (*bottom three graphs*) Quadrant of the Galaxy.

2.3.2 Ammonia observations

For each cloud, we selected by eye the mm emission peaks for follow-up with pointed ammonia observations. All mm emission peaks above two times the mean emission of the cloud, that is the r.m.s. emission in the cloud where we omit the bright mm peaks, were observed. When no clear emission peak was present, such as in a very diffuse cloud, the center of the diffuse emission was targeted. Even in cases where the mm emission was below 3σ, where σ is the noise in the bolometer map ($\sigma = 0.015\,\mathrm{mJy}$), we choose a few positions to observe the ammonia lines to search for a cloud so cold and diffuse that is was missed by the bolometer. For clouds that had several continuum emission peaks separated by more than $20''$ from each other, more than one position was observed, denoted by MM1, MM2 etc. Several high exinction clouds had very weak or no mm emission – in this case the name extension, which was MM1, MM2 for the mm sources, was changed to 1 or 2, e.g., G034.34–00.90 1.

The ammonia observations were performed with the MPIfR 100m Effelsberg Telescope. We observed 54 positions, given in Table A.3 and A.4, between 2007 April and 2008 December. The Effelsberg beam is $40''$ FWHM at the ammonia inversion line frequencies of $\sim$23.7 GHz. The 2007 observations used the 8192 channel AK90 auto correlator backend. The correlator was configured into eight spectral windows with 20 MHz bandwidth and 1024 channels each, where every window could be set to a different frequency. This provided the opportunity to simultaneously observe the $(J, K) = (1,1)$, (2,2) and (3,3) inversion lines of ammonia in both polarizations. The spectral resolution with this setup was $0.25\,\mathrm{km\,s^{-1}}$. The 2008 observations used the Fast Fourier Transform

Spectrometer (FFTS) with a 500 MHz bandwidth and 8192 channels. The bandwidth was sufficient to simultaneously observe the three ammonia inversion lines with a spectral resolution of 0.7 km s^{-1}. All the observations were performed in frequency switching mode with a throw of 7.5 MHz.

Data calibration

During the observations, pointings on a nearby compact continuum source were performed every hour for determining pointing corrections. For the flux calibration, we observed a well-known flux calibrator, NGC 7027 or 3C 286, in every run. The post-observational calibration to obtain the main beam brightness temperature, $T_{\rm MB}$, consisted of the opacity correction, elevation correction and flux calibration:

$$T_{\rm MB} = \frac{A \times T_{\rm ant} e^{-\tau/\sin\theta}}{G(\theta)}\,, \tag{2.3}$$

where A is a scaling factor, $T_{\rm ant}$ is the antenna temperature, τ the zenith opacity, and G the function of the gain with elevation θ.

The opacity, τ, was calculated by fitting a linear function to the system temperature against airmass ($\sin^{-1}\theta$) and taking the slope of the fit. We found a τ of 0.031 for good weather. When it was not possible to retrieve the τ by this method the average τ of 0.054 at 23 GHz was assumed (the averaged water vapor radiometer value for 2007).

For all parabolic dish telescopes the gain decreases at very low and very high elevations. We corrected for this by dividing by $G(\theta)$ taken from the Effelsberg website[1] (see Eq. 2.3), which is given by

$$G(\theta) = a_0 + a_1\theta + a_2\theta^2\,, \tag{2.4}$$

where $a_0 = 0.88196$, $a_1 = 6.6278\times10^{-3}$, $a_2 = -9.2334\times10^{-5}$ and θ the elevation. After the opacity and gain corrections, the scaling factor A was found by comparing the measured uncalibrated intensities of absolute flux density calibrator sources with the literature values calculated from the formulae given by Baars et al. (1977) for 3C 286, and Ott et al. (1994) for NGC 7027.

The calibrated spectra were baseline subtracted, and the ammonia lines were fitted by a Gaussian. Only the NH_3(1,1) line, for which the hyperfine structure was clearly detectable given the signal to noise ratios, was fitted by special routine 'method nh3(1,1)' of the GILDAS/CLASS software. This method calculates the optical depth from the hyperfine structure and returns optical depth corrected line widths. The observed ammonia parameters, such as LSR velocity, $v_{\rm LSR}$, main beam temperatures, $T_{\rm MB}$, line widths, Δv, and the main group optical depth, $\tau_{\rm main}$ are listed in Table A.5.

2.3.3 Water maser observations

Several positions with a peak in the 1.2 mm emission above twice the mean cloud emission, hence possibly harboring evolved clumps, were searched for water maser emission using the 100m Effelsberg telescope on 5 and 24 of February 2008. In total 24 positions in common with NH_3 were observed (marked in Table A.3). We performed on-off observations using the FFTS backend with a bandwidth of 20 MHz centered on 22.235 GHz. This setup afforded a high spectral resolution of 0.04 km s^{-1}, while allowing the water maser to have line widths of up to 100 km s^{-1}. The bandwidth was 270 km s^{-1} and was centered on the NH_3 $v_{\rm LSR}$ of the observed clump. We applied the same data reduction as described above in Sect. 2.3.2. for the ammonia observations. Table 2.1 lists the $v_{\rm LSR}$ and peak intensity of the water maser detections. In case of multiple maser components we give the $v_{\rm LSR}$ range.

[1] http://www.mpifr-bonn.mpg.de/div/effelsberg/calibration/1.3cmsf.html

Table 2.1: Detected water masers

HEC name		Peak Intensity (Jy beam^{-1})	$v_{\rm LSR}$ (km s^{-1})
G014.63–00.57	MM1	9.3	22
G017.19+00.81	MM2	22.3	−4–37
G022.06+00.21	MM1	11.7	42–51
G024.37–00.15	MM2	6.0	65
G024.94–00.15	MM1	6.6	52–72
G035.49–00.30A	MM1	5.6	40–77
G035.49–00.30B	MM2	2.6	40

2.4 Results

2.4.1 Kinematic distances

Accurate distance determination within the Galaxy is generally difficult. Nevertheless, the kinematic distance is commonly used as a distance measure. It is based on a model of Galactic rotation, the "rotation curve" characterized by the distance between the Sun and the Galactic Center, R_0, and the rotation velocity at the Suns orbit, Θ_0. Toward the inner part of the Galactic plane, kinematic distances are ambiguous: for a given Galactic longitude and LSR velocity, it cannot a priori be determined if the object is at the "near" or "far" kinematic distance. All extinction clouds should be at the near kinematic distance since at large distances the number of background stars decreases and the percentage of foreground stars increases making it difficult to measure any color excess. We calculated the kinematic distances for all clumps with NH_3 detections, using a program of Todd Hunter, which applies the Galactic rotation model of Fich et al. (1989) assuming a flat rotation curve, $\Theta_0 = 220\,\mathrm{km\ s^{-1}}$, and $R_0 = 8.5\,\mathrm{kpc}$. The resulting kinematic distances are given in Table A.4 and A.6.

2.4.2 Galactic scale extinction

The low resolution extinction maps show large extinction structures across the whole inner Galactic disk from 60° to −60° longitude (Fig. 2.1). In longitude, the 3° averaged distribution (Fig. 2.2, top panel) shows signs of Galactic structure, meaning that peaks in the distribution can be related to known spiral arms. The column density appears higher in the fourth quadrant, $0° > l > -60°$, than in the first, $60° > l > 0°$. Additionally, there seems to be a quasi symmetrical distribution around the Galactic Center around longitudes of ∼15°, –10°and ∼35°, –30°. In latitude (Fig. 2.2, lower panel), we found a peak towards $b \sim -0.°1$, which is also seen for the compact submillimeter sources found in the ATLASGAL survey (Schuller et al. 2009). The shift of the peak out of the midplane indicates that the Sun is located above the midplane. Similar results have been found by the studies using young open clusters and OB stars (see e.g., Joshi 2007). The FWHM of our distribution is ∼1°, while in ATLASGAL this is more narrow, ∼0.°6. If one assumes that the Galactic disk has a constant scale height, then objects closer to the Sun should have a wider latitude distribution then ones at larger distances. It therefore appears that the high extinction clouds are on average closer to the Sun than the ATLASGAL sources.

With the kinematic distances we can place our sample of clouds within a face-on view of the Galactic plane (Figure 2.3). They inhabit similar regions as IRDCs (see the IRDCs distribution by Jackson et al. 2008). The extinction method misses nearby ($d < 1\,\mathrm{kpc}$) and most of the far away ($d > 4\,\mathrm{kpc}$) clouds. The insensitivity to the latter stems from the increasing number of foreground stars at larger distances (see Sect. 2.2.1). Between distances of one and four kilo parsec the high extinction clouds agree with the IRDCs regions.

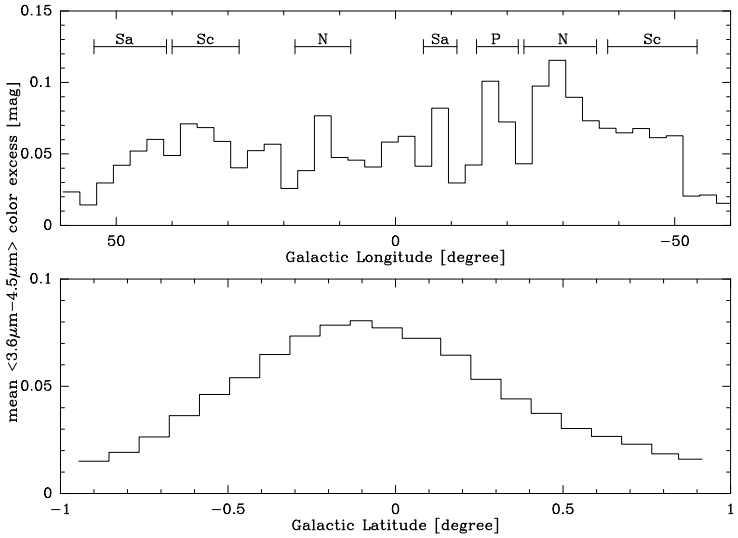

Figure 2.2: Mean color excess along Galactic longitude (*upper diagram,* bins of 3°) and Galactic latitude (*lower diagram,* bins of 0.1°). In the longitude histogram, encounters with a spiral arm are marked with letters representing N for Norma-Cygnus, Sc for Scutum-Crux, Sa for Sagittarius-Carina, and P for Perseus.

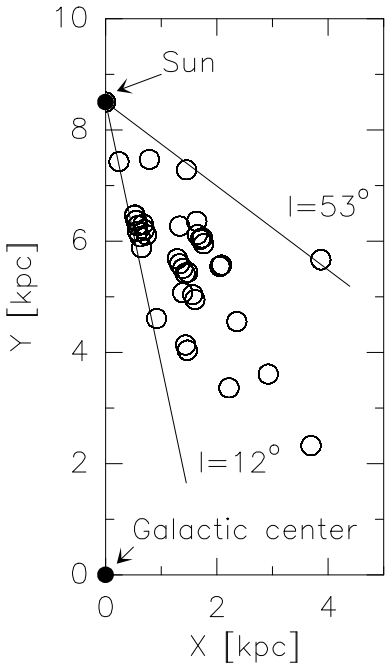

Figure 2.3: A face-on view of the Galactic Plane. The Galactic center is located at (0,0). The Galacitic longitudes of 12° and 53° are indicated by solid lines. The locations of the sample of high extinction clouds, which were studied in this chapter, are marked by open circles.

2.4.3 Extinction clouds

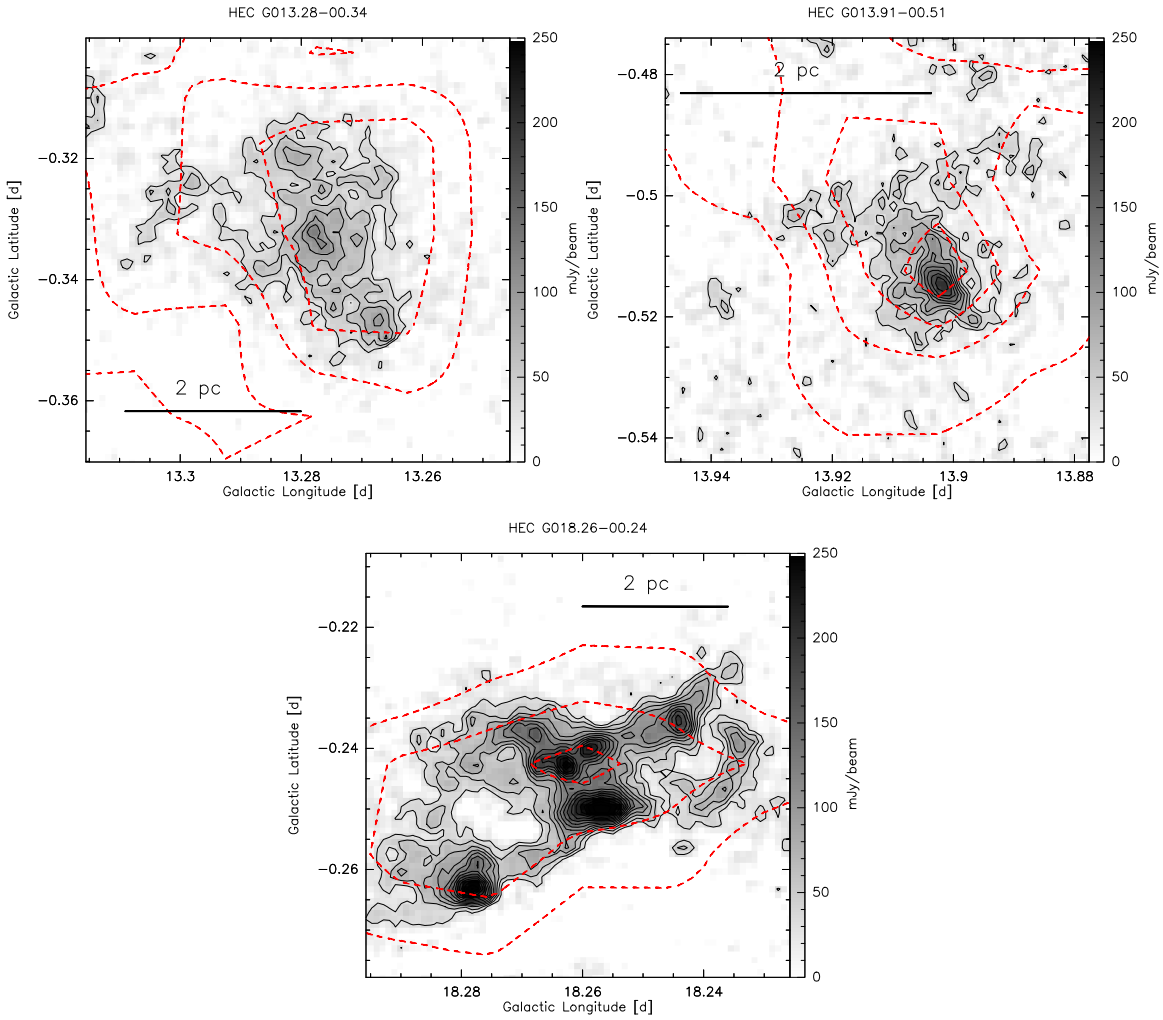

Figure 2.4: Examples of extinction maps (red dashed contour, starting at A_V=21 mag and increasing by 10 magnitudes, beam 54″) on top of the 1.2 mm emission observed with MAMBO-2 (beam 10.″5) in greyscale and solid black contours.

Millimeter continuum emission was detected in 88% of the bolometer maps. It usually followed well the 54″ resolution extinction maps (Fig. 2.4). Two examples of weak millimeter emission or non-detections are G034.03–00.33 and G034.34–00.90 (Fig. B.1). Figure B.1 shows the Spitzer/Mid Infrared Photometer (MIPS) 24 μm maps overlaid with the mm emission. While the high extinction clouds match well with 24 μm dark features, the 1.2 mm peaks often contain weak compact 24 μm emission. The bolometer maps were sensitive to structures from 10.″5 (HPBW) to $\sim$ 90″; large-scale structures are not faithfully represented due to the sky noise subtraction and chopping. We smoothed the maps, by convolving with a 20″ Gaussian beam, to study the extended cloud structure and increase the signal-to-noise toward weak and diffuse sources.

We find single clouds and clusters of clouds, for example G014.63–00.57 in Fig. B.1. Based on the kinematic distance the clouds were identified as belonging together in one large cloud, or being physically separated clouds if the difference in distance was larger than 10%. The latter clouds were marked as A, B etc. and were treated as distinct clouds throughout the thesis. For the total integrated flux of the cloud (Table A.2), we defined a cloud edge at a threshold of 3σ (of the smoothed map) and integrated all the emission within this region using the Gildas Software

package GREG. The corresponding radius of the cloud, $\sqrt{A/\pi}$ with A the area of the cloud, is given in arcseconds and parsecs (using the kinematic distance) in Table A.2. The average cloud radius was 0.6 pc. Certain clouds have spherical shapes, for example G013.28–00.34, however, most are filamentary, as can be seen in G024.94–00.15 or G016.93+00.24. Cloud sizes are very diverse depending on the geometry; there are elongated structures up to several parsecs in length. The number of clumps per cloud varies from five (in G018.26–00.24, Fig. B.1) to one or none in very diffuse clouds (G034.85+00.43, Fig. B.1). We used the SIMBAD database to investigate if our clouds contain signs of star formation, such as maser emission, HII regions and IRAS sources.

2.4.4 Clumps in high extinction clouds

To study the clumps we used the unsmoothed maps, as the extended structure surrounding the clump complicates the definition of source edge and confuses Gaussian fitting routines. We removed the extended emission from the map by applying a median filter with a box size of 63″ (6 × beamsize) using the MIRIAD task 'immedian'. After median removal, the source-find algorithm of MIRIAD, 'sfind', was run on these images, delivering 2D Gaussian fits, the peak flux and the integrated fluxes of the clumps. The median removal should strip the low density mass reservoir which surrounds the denser part of the clump.

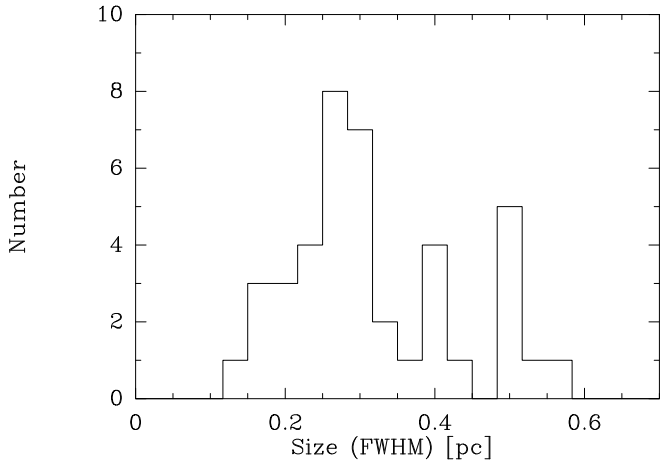

Figure 2.5: Number distribution of 1.2 mm clumps with size determined from the Gaussian fits (geometric mean of the FWHM of the major and minor axis) and converted to physical units using the near kinematic distance.

First, we selected the peaks in the mm emission by eye, and then we took the parameters for the FWHM size, the integrated flux and peak flux of the clump from 'sfind'. The observed parameters of the clumps are presented in Table A.3. The clumps have sizes of 10″–30″ or 0.11–0.72 pc, peaking around 0.25 pc (Fig. 2.5). Most of the clumps are resolved with the 10.″5 beam of the 30m telescope. The (physical) clump size follows a linear trend with distance (Fig. 2.6, right panel). At far distances we observe only larger, hence brighter clumps, which is expected for our sensitivity limited selection. The angular sizes, however, are more equally distributed (see Table A.3). For several clouds with very weak mm emission the selected position was not the mm emission peak, but the emission center. In such clouds 'sfind' did not find any clumps; these positions without clumps are listed in Table A.4.

Ammonia emission was detected toward 94% of the observed positions. Figure 2.7 shows the spectra of the $NH_3(1,1)$, $NH_3(2,2)$ and $NH_3(3,3)$ transitions toward two compact clumps representing typical values for an early stage where the clump is cold (14 K, G016.93+00.24 MM1) and a more evolved stage, where the temperature has increased (19 K, G017.19+00.81 MM2). In the early stage $NH_3(3,3)$ is not detected while for the warmer clump it is clearly present. The results of the ammonia observations are summarized in Table A.5. The main beam brightness temperatures of the $NH_3(1,1)$ lines are, after baseline removal, between 0.5 and 4.0 K. The baseline rms is ∼0.2 K,

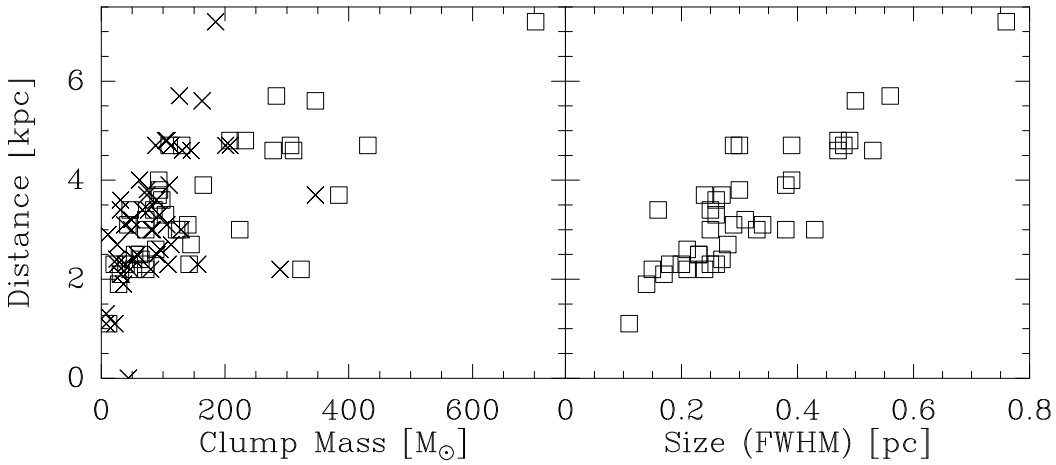

Figure 2.6: Distance as a function of clump mass (*left*) and size (*right*). In the left panel, the clump mass based on the Gaussian fitting is marked by squares, and the clump mass within 0.25 pc around the center of a clump is indicated by crosses. There is a linear correlation with distance for the mass and the size. The most massive clumps are at large distances, whereas almost no low-mass clumps are found at distances larger than 4 kpc, which can be expected for a sensitivity limited selection of clouds.

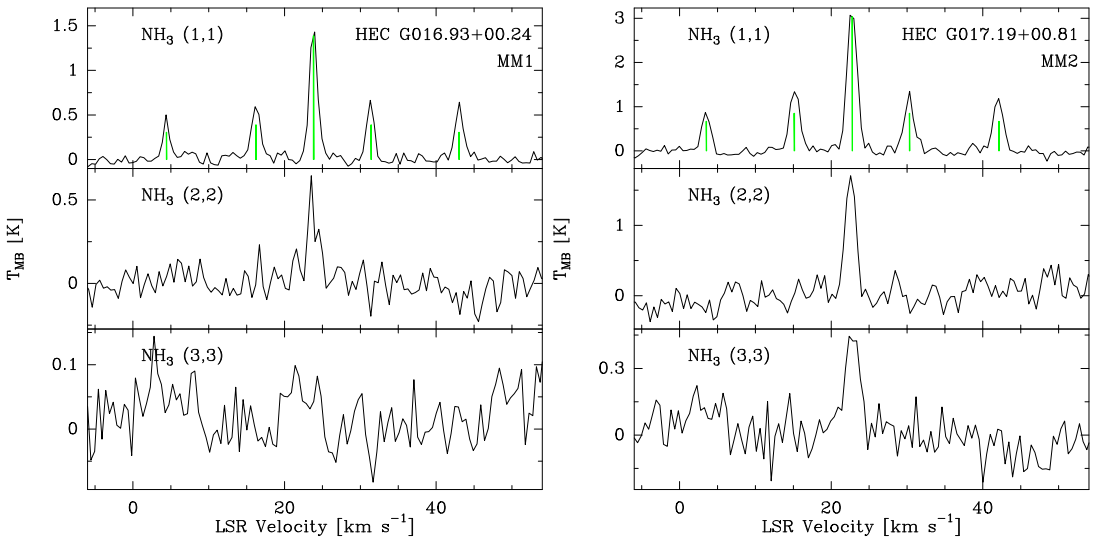

Figure 2.7: The $NH_3(1,1)$, $NH_3(2,2)$ and $NH_3(3,3)$ spectra taken with the Effelsberg 100m telescope toward two HEC clumps. The green lines indicate the theoretical intenstity of the hyperfine lines given the intensity of the main line.

but several spectra are more noisy. The line widths from the main component of the $NH_3(1,1)$ ranges between 0.7–2.8 km s^{-1}, yielding an average of 1.4 km s^{-1}(Fig. 2.8) . These line widths are far above a thermal linewidth, which would be around 0.23 km s^{-1} for temperatures of ∼18 K . For most of the sources, the $NH_3(1,1)$ and $NH_3(2,2)$ lines are both detected, while the $NH_3(3,3)$ line is often very weak or not present. The $NH_3(2,2)$ and $NH_3(3,3)$ lines are on average both wider than the main $NH_3(1,1)$ line. This implies that these lines do not trace exactly the same volume of gas, meaning that the beam filling factor is not identical.

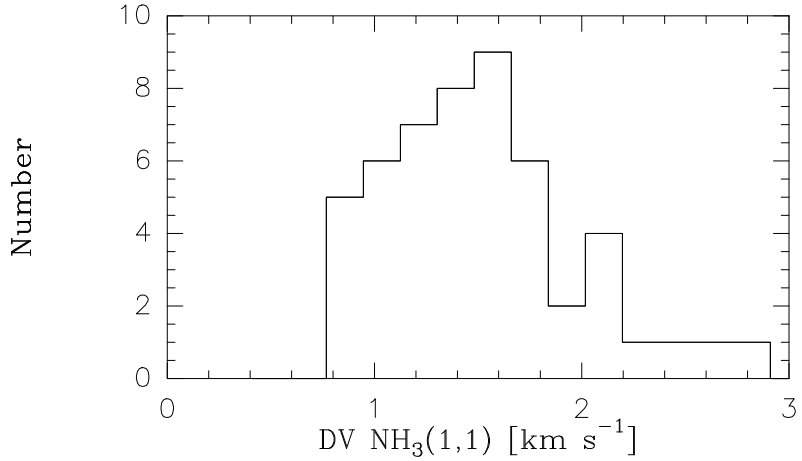

Figure 2.8: Number distribution of the $NH_3(1,1)$ line widths of the 1.2 mm clumps. There is a clear peak around ∼1.4 km s^{-1}.

2.5 Analysis

2.5.1 Extinction masses

Since the color excess, or extinction, is a direct measure of the amount of column density in a region, we could derive extinction masses. One magnitude of visual extinction, A_V, is related to a hydrogen column density, $N_{\rm H_2}$, according to Bohlin et al. (1978); Frerking et al. (1982) by

$$A_V = \frac{N_{\rm H_2}}{0.94 \times 10^{21}} \quad [\rm mag]\,. \tag{2.5}$$

Multiplying by the mass of a hydrogen atom, $m_{\rm H}$, the mean molecular weight, $\mu = 2.33$, and the cloud area, A, one arrives at the extinction mass:

$$M_{\rm ext} = 3.7 \times 10^{26} \mu m_{\rm H} < E(3.6\,\mu{\rm m} - 4.5\,\mu{\rm m}) > \left(\frac{A}{\rm pc^2}\right) \quad [\rm M_\odot]\,. \tag{2.6}$$

The extinction mass is independent of temperature, but it still depends on the distance via the cloud area A. We derive extinction masses for the clouds from ∼30 to 6500 $\rm M_\odot$ (Table A.2).

2.5.2 Column densities and visual extinction

As mm emission from cool clouds is usually optically thin, the column density and the mass of a cloud are well sampled by the observed flux density. The beam averaged hydrogen column density, $N_{\rm H_2}$, is given by Motte et al. (2007)

$$N_{\rm H_2} = \frac{F^p_{\rm 1.2mm}}{\Omega m_{\rm H} \mu \kappa_{\rm 1.2mm} B_{\rm 1.2mm}(T_{\rm dust})}\,, \tag{2.7}$$

where $F^p_{1.2\mathrm{mm}}$ is the peak flux, Ω the beam solid angle, $\kappa_{1.2\mathrm{mm}}$ the dust opacity at 1.2 mm per unit mass column density, assuming a gas-to-dust ratio of 100, $B_{1.2\mathrm{mm}}(T_{\mathrm{dust}})$ the (full) Planck function at the dust temperature and m_H and μ as defined before. The column density depends strongly on the dust properties: the dust opacity, κ_λ and the emission coefficient, β, are related as $\kappa_\lambda = \kappa_0(\frac{\lambda}{\lambda_0})^{-\beta}$ [$\mathrm{cm^2 g^{-1}}$]. We considered two different opacities; $\kappa_{1.2\mathrm{mm}} = 0.4\,\mathrm{cm^2 g^{-1}}$ after Hildebrand (1983) and $\kappa_{1.2\mathrm{mm}} = 1.0\,\mathrm{cm^2 g^{-1}}$ taken from Ossenkopf & Henning (1994), Table 1 column 6, for dust grains with thin ice mantles. The emission coefficient was kept at $\beta = 2$, the advocated value for cold dust clumps (Hill et al. 2006). The dust opacities differ by a factor 2.5, meaning the κ of Hildebrand (1983) results in 2.5 times larger column densities than the opacity of Ossenkopf & Henning (1994). In this work we used the dust opacity of Ossenkopf & Henning (1994), $\kappa_{1.2\mathrm{mm}} = 1.0\,\mathrm{cm^2 g^{-1}}$. For the dust temperature we assumed the rotational temperature derived from ammonia (see Section 2.5.5). Since the clumps have high densities, collisions will dominate over radiative processes and the temperature exchange between dust and gas will be efficient. In sources without NH_3 detection we assumed a dust temperature of 16 K, which was the average NH_3 rotational temperature. For clumps which have an embedded protostar the NH_3 rotational temperature, derived on a $40''$ scale, might underestimate the dust temperature leading to an overestimation of the derived masses and column densities.

We found clumps with column densities of the order of 10^{22}–$10^{23}\,\mathrm{cm^{-2}}$ (Table A.6). We derived corresponding peak visual extinction values by applying Eq. 2.5. The peak fluxes, column densities and peak visual extinction of Table A.6 correspond to the positions listed in Table A.3. The clumps have peaks in A_V from 31 to 280 mag, with an average value of 75 mag. These values are much higher than the mean visual extinction reached by the extinction method for this selected sample, which is between 16–47 mag. This is expected because the peak values are larger than the mean and with the limited resolution of $54''$ higher extinction peaks (as found for example in IRDCs) are missed. Additionally, also the temperature might play a role, since the derivation of the A_V from the mm emission depends on temperature while the extinction method does not.

2.5.3 Masses from 1.2 mm emission

The clump mass can be derived from the 1.2 mm emission by (Hildebrand 1983; Motte et al. 2007):

$$M_{1.2\mathrm{mm}} = \frac{F^i_{1.2\mathrm{mm}} d^2}{\kappa_{1.2\mathrm{mm}} B_{1.2\mathrm{mm}}(T_{\mathrm{dust}})}\,, \tag{2.8}$$

where $F^i_{1.2\mathrm{mm}}$ is the integrated flux density of the clump, d the distance, and $\kappa_{1.2\mathrm{mm}}$, $B_{1.2\mathrm{mm}}$ and T_{dust} as defined before. The measured flux density can be contaminated by free-free emission, if there is an ionizing source present. Since our sample contained very young objects, we can neglect such contamination. The derived masses depend strongly on temperature and distance; a 10% closer distance decreases the mass by 20%, a 10% decrease in temperature increases the mass by 17%. Nevertheless, the largest uncertainty in the mass derivation is caused by the dust properties, as described in the previous section.

The majority of the clumps have masses between 12–700 $\mathrm{M_\odot}$, and are located at distances between 2–5 kpc (see the squares in the left panel of Fig. 2.6 and Table A.6). We find no low-mass clumps ($M < 100\,\mathrm{M_\odot}$) further than 4 kpc, which is an bias of our extinction method (discussed in Sect. 2.6.4). Almost all high mass clumps ($M > 100\,\mathrm{M_\odot}$) are located at distances larger than 4 kpc.

A second method was used as a comparison for the clump masses to check if the source finding algorithm was biased to a source size (and hence clump mass). Based on the (near) kinematical distances, we defined circles of 0.25 pc diameter for each source. Then, we derived the integrated flux, $F_{0.25\mathrm{pc}}$ and the mass, $M_{0.25\mathrm{pc}}$ for the region within this circle (see Tables A.3, A.4 and A.6). The crosses in the left panel of Fig. 2.6 show $M_{0.25\mathrm{pc}}$ as a function of the distance. The clump masses within 0.25 pc show a similar behavior as the clump masses determined by Gaussian fits. On a larger scale, the cloud mass was derived from the 1.2 mm emission according to Eq. 2.8 using the integrated flux down to 3σ. The cloud diameters are of order $\sim 90''$, so after resampling the extinction map, it was possible to compare the cloud masses derived by extinction with the masses

from the 1.2 mm emission. We find the extinction masses to be larger by a factor ~ 1.3 than the masses derived from the dust continuum maps (see Fig. 2.9). This is expected, since the bolometer filters out large-scale structures by the sky noise subtraction and chopping. The cloud masses derived from the 1.2 mm emission and the extinction are listed in Table A.2.

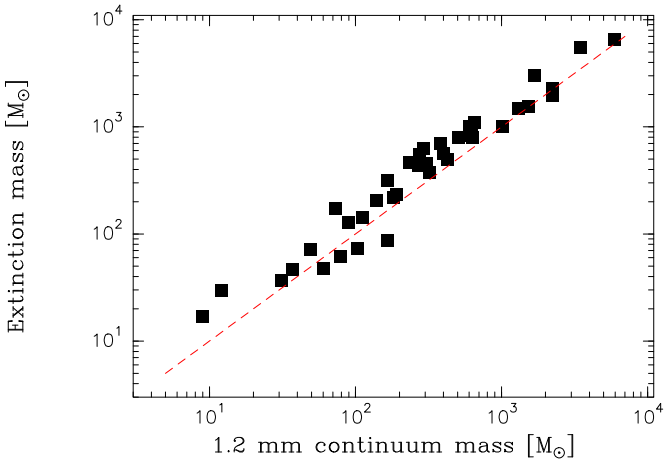

Figure 2.9: The cloud masses estimated from the color excess versus the masses estimated from the 1.2 mm bolometer maps. The red dashed line is a help line indicating the trend in which both mass estimates are equal.

Finally, we estimated the volume-averaged gas density of the clumps, $n_{\mathrm{H_2}}$, following Motte et al. (2007):

$$n_{\mathrm{H_2}} = \frac{M}{\frac{4}{3}\pi R^3 \mu m_{\mathrm{H}}}\,, \tag{2.9}$$

where M is the clump mass, R the clump radius given by the geometrical mean of the semi major and semi minor axis from the Gaussian fit, and μ and m_{H} as defined before. The average gas density is $\sim 2 \times 10^5\,\mathrm{cm}^{-3}$, the individual results are given in Table A.6.

2.5.4 Virial masses

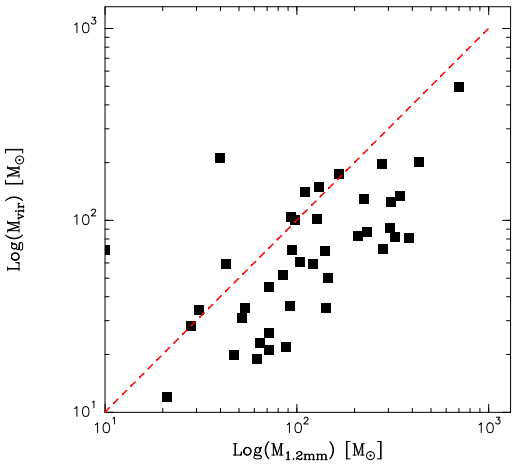

Figure 2.10: Virial clump masses versus the 1.2 mm continuum clump masses. The red dashed line indicates the trend where the virial parameter is unity.

The thermal line widths are usually one order of magnitude smaller than the observed NH_3 line

widths, which indicates that the observed line widths are dominated by turbulence, hence contain information of the average kinetic energy within a clump.

Given a line width of an optically thin line and a clump radius, the virial mass, $M_{\rm vir} = k_1\sigma^2 R/G$, can be calculated (MacLaren et al. 1988). Here σ is the three dimensional root-mean-square velocity, R the clump radius, k_1 a density distribution constant, and G the gravitational constant. For a constant density distribution $k_1 = 5/3$. After the conversion of σ to the observable FWHM line width Δv, $\sigma^2 = (3/8\ln 2)\Delta v^2$ (Rohlfs & Wilson 2004), the virial mass can be written as:

$$M_{\rm vir} = 210 \times \big(\frac{\Delta v}{\rm km\,s^{-1}}\big)^2 \big(\frac{R}{\rm pc}\big) \quad [{\rm M}_\odot]\,. \tag{2.10}$$

The resultant virial masses, $M_{\rm vir}$, are listed for each clump in Table A.6. The virial parameter is defined as $\alpha = \frac{M_{\rm vir}}{M}$ (Bertoldi & McKee 1992). For $\alpha < 1$, the clumps are dominated by gravity, however with $\alpha >> 1$, the clumps are confined by surface pressure and self-gravity is unimportant. Most clumps in high extinction clouds have clump masses larger than their virial masses (see Fig. 2.10), indicating that possibly most clumps are dominated by gravity and are collapsing.

2.5.5 Temperatures

The ammonia molecule, described thoroughly by Ho & Townes (1983), is often used as a molecular cloud thermometer (Danby et al. 1988). Its energy levels are parameterized by the J and K quantum numbers, measuring, respectively, the magnitude of the total angular momentum and its component along the symmetry axis. Each set of rotational transitions is arranged into so-called K-ladders, levels of fixed K-value. From the symmetry of the electric dipole moment of the molecule, all dipole transitions with nonzero ΔK are forbidden, meaning that the K-ladders are independent of each other. The lowest transitions of each K-ladder are metastable, and can be excited via collisions. Additionally, NH_3 also undergoes vibrational motion from the tunneling of the nitrogen atom through the hydrogen plane, which splits the rotational energy levels into inversion doublets.

The inversion transitions are further split into 5 quadrupole hyperfine lines, which allow the calculation of the optical depth (see the hyperfine lines in the NH_3(1,1) transition in Fig. 2.7). Typical values of the optical depth were between 1–3, showing that ammonia is optically thick in most cases. With the optical depth known, the rotational temperature, $T_{\rm rot}$, follows from the ratio of the peak intensities of NH_3(1,1) and NH_3(2,2) lines after Mangum et al. (1992):

$$T_{\rm rot} = -41.5\big[\ln\big[-\frac{0.283\Delta v_{22}}{\tau_{\rm main}\Delta v_{11}}\ln\big[1-\frac{T_{22}}{T_{11}}(1-e^{-\tau_{\rm main}})\big]\big]\big]^{-1} \quad [{\rm K}]\,, \tag{2.11}$$

where $\tau_{\rm main}$ is the main group optical depth of NH_3(1,1), Δv_{11}, Δv_{22}, T_{11}, T_{22} are the line widths and the peak intensities of the (main component) NH_3(1,1) and NH_3(2,2) lines, respectively.

The line width ratio in this equation is debatable. Observations show that the NH_3(1,1) and NH_3(2,2) line widths are dominated by turbulence. If one assumes that both transitions arise from the same region, they experience the same turbulence, and the line widths are equal, $\Delta v_{22} = \Delta v_{11}$. In this case, the linewidth ratio drops out of the equation, which becomes the equation from Ho & Townes (1983). We observed slightly larger NH_3(2,2) line widths for several clumps, probably since this transition has a higher energy and is therefore more sensitive to warmer and more turbulent regions. The NH_3(2,2) line widths are therefore more sensitive to the peak temperature, determined by the turbulent outliers. We considered it reasonable to use Δv_{22} =Δv_{11}, since it would give an 'average' of the NH_3(2,2) turbulence, and hence an 'average' rotational temperature of that region. The two methods yield very similar results; the Ho & Townes (1983) temperatures were slightly lower ($\Delta T_{\rm rot} \simeq 1$K) than when using the formula of Mangum et al. (1992).

The clumps are on average cold ∼16 K. The temperatures range from 10 to 25 K. For such low temperatures, the kinetic temperature is well approximated by $T_{\rm rot}$ (Walmsley & Ungerechts 1983; Danby et al. 1988).

We derived column densities of the $NH_3(1,1)$ line (after Mangum et al. 1992):

$$N_{(1,1)} = 6.60 \times 10^{14} \Delta v_{11} \tau_{\rm main} \frac{T_{\rm rot}}{\nu_{11}} \quad [{\rm cm}^{-2}], \tag{2.12}$$

where ν_{11} is the frequency of the $NH_3(1,1)$ transition, and Δv_{11}, $\tau_{\rm main}$, and $T_{\rm rot}$ as defined before. From this we estimated the total ammonia column density (following Li et al. 2003):

$$N_{\rm NH_3} = N_{(1,1)} \Big[1 + \frac{1}{3} e^{23.1/T_{\rm rot}} + \frac{5}{3} e^{-41.2/T_{\rm rot}} + \frac{14}{3} e^{-99.4/T_{\rm rot}} \Big] \quad [{\rm cm}^{-2}]. \tag{2.13}$$

The averaged ammonia column density for the clumps is $3.1 \times 10^{15}\,{\rm cm}^{-2}$. The NH_3 rotational temperatures and column densities for all clumps are given in Table A.6 together with the other parameters derived in this Section.

2.6 Discussion

2.6.1 High extinction structures

Thanks to the high resolution Spitzer IRAC data, the extinction method allows to follow the mass distribution from Galactic size-scales down to single clouds. High extinction traces Galactic structure (see the Galactic distribution of the color excess in Fig. 2.2), similar to the CO survey of the Galactic plane (Dame et al. 1987) and the dust continuum surveys, ATLASGAL at 850 μm (Schuller et al. 2009) and BOLOCAM at 1.1 mm (Rosolowsky et al. 2009). In addition, the distribution of 6.7 GHz Class II methanol masers traces high-mass star-forming regions and, thus, Galactic structure (Pestalozzi et al. 2005). All these surveys, except for the methanol masers, peak toward the Galactic Center. The extinction maps miss the inner 1° around the Galactic Center, since the Spitzer IRAC data were not publicly available for this region at the time. However, a rising trend toward the Galactic Center was observed. The extinction distribution indicates that the column densities are higher towards the fourth quadrant, $0° > l > -60°$. We find no evidence for this from the CO distribution, nor from the methanol masers. Only the ATLASGAL survey (Schuller et al. 2009) hints at a similar distribution, but needs to be extended in longitude range for giving conclusive evidence.

The next eye-catching features in the extinction distribution were two bumps, peaking roughly around longitudes of $\sim 40°$and $-30°$(see Fig. 2.2), which were confirmed by the methanol maser distribution (Pestalozzi et al. 2005). We identified several spiral arms by comparing our results to the Galactic models of Vallée (2008). In Fig. 2.2, each spiral arm traced by a maximum in the extinction distribution is marked. We can trace the tangential point of the Sagittarius-Carina arm at $l \sim 50°$, the tangential points of the Scutum-Crux arm at $l \sim 35°$and $l \sim -45°$, the beginning of the Norma-Cygnus arm on the near end of the Galactic bar $l \sim 10°$, the beginning of the Sagittarius-Carina arm at the far end of the Galactic bar $l \sim -5°$, the beginning of the Perseus arm $l \sim -20°$and the tangential point of the Norma-Cygnus arm at $l \sim -30°$. Several of these features are also seen in the ATLASGAL survey, and to a lesser extend in the CO distribution. Hence, the total extinction distribution seems to agree with results of previous studies, and tracks large scale mass structures.

The combination of submillimeter dust continuum emission and extinction maps extends the size scales down to clump sizes of fractions of parsecs. In Table 2.2 the mean masses, sizes and volume densities for different size-scales of complexes, clouds and clumps are compared. Complexes are the low density ($A_{\rm V} > 21$ mag or $N_{\rm H_2} > 2 \times 10^{22}\,{\rm cm}^{-2}$) regions surrounding the cloud. In general, the masses and sizes decrease towards the smaller scales, while the volume density increases as expected. The cloud masses derived from the extinction are higher than from the mm emission, as discussed in Sect. 2.5.3. The complexes and the clouds are confined by the pressure of the surrounding medium rather than by gravity. This is based on their virial masses, where we used

for the line width estimate the ^{13}CO data from the Galactic Ring Survey (GRS) (Jackson et al. 2006). The ^{13}CO is a probe of the low density material and the GRS resolution of 47″ the line width is close to a cloud-scale average. Most of the clumps inside the clouds are, however, bound objects for which $M_{\rm vir} < M_{1.2\,\rm mm}$.

Table 2.2: Mean properties of high extinction complexes, clouds and clumps

Size scale	Method	Mass ($M_\odot$)	Size (pc)	Volume density (cm^{-3})
complex[a]	extinction	4000	2.8	6×10^3
clouds	extinction	910	1.2	2×10^4
clouds	1.2 mm emission [b]	700	1.2	1×10^4
clumps	1.2 mm emission [c]	130	0.3	2×10^5

[a]Note: the high extinction complexes should be treated as a indication; the regions were chosen by eye to be a connected extinction patch.
[b]smoothed maps by 20″ Gaussian
[c]unsmoothed maps

2.6.2 Evolutionary sequence

Our observations suggest different classes of clouds and in the following we discuss their possible relation to different evolutionary stages. Clouds, which either have no clumps or clumps of which the peak in the mm emission is less than twice the mean emission in the cloud, were defined as diffuse clouds – this definition is based on the morphology and therefore different from the "classical diffuse clouds" defined by $A_{\rm V} < 1$ mag (Snow & McCall 2006). Clouds which contain clumps with a higher contrast, above twice the mean cloud emission, were considered to be peaked clouds. If the peak flux was above thrice the mean emission and there were two or more clumps the cloud was classified as a multiply peaked cloud. The ratio of the clump peak emission to the mean emission of the cloud is given in Table A.2 together with the classification. The mean physical properties such as temperature, masses, column densities and line widths are put together in Table 2.3 for the three classes.

Diffuse clouds are the most likely candidates to form, or harbor, starless clumps, which are expected to be cold, more extended and more massive. The clump, or cloud, consists of low column density material and contains no massive compact object. Indeed, for very diffuse clouds, the source find algorithm yielded few clumps. On the smoothed maps, the algorithm returned values which were close to cloud size-scales without much substructure. This supports the idea that these diffuse clouds represent the earliest stage in which few condensations have formed and gravitational collapse has not yet started. More evidence for the young nature of diffuse clouds was found in the 24 μm MIPS data: generally the (smoothed) dust emission followed the 24 μm-dark regions and only a few 24 μm sources of $\sim$100 MJy sr^{-1}, located within 20″ of mm peak, were found toward the clouds. In two cases 24 μm source $>$ 100 MJy sr^{-1} were found the edge of the cloud, at $\sim$1′ from the mm peak. Examples are G012.73–00.58, G013.28–00.34 and G034.85+00.43 (see Fig. B.1).

As the first clumps become more compact and their mm peak flux rises above twice the mean emission of cloud, in the *peaked cloud* stage, the clump is accreting material from a lower density reservoir or envelope surrounding it, and consequently the temperature and turbulence rise. Since star formation is a process which is dynamic and includes feedback and triggering, already in this early stage a cloud can contain more than one clump, though possibly the other peaks barely stick out above the mean mm emission of the cloud. The peaked clouds are generally dark at 24 μm, except for a bright 24 μm source located within 20″ of the mm peak (see G013.91–00.51, G016.93+00.24 and G053.81–00.00 in Fig. B.1). The peak flux of the 24 μm sources is on average $\sim$ 250 Mjy sr^{-1}, higher than for the diffuse clouds.

After more accretion from the reservoir, the clump will have a much higher mm peak flux compared to the initial stage, reaching at least trice the mean emission of the cloud. The clump

mass will have decreased toward the more evolved stage, since not all of the mass reservoir will not be accreted onto the clump, as the star formation efficiency is apparently less then 100%. The column density, temperature and turbulence will increase even further than in the peaked cloud stage. While in the peaked stage, there were few clouds which had multiple clumps, in the more evolved stage one expects to find more clouds with multiple clumps. Most of these clumps should be well above the mean emission of the cloud. In these *multiply peaked clouds*, the clumps will be in different cloud stages of evolution depending on the initial conditions of the clump. Also not all clumps will form high-mass stars so they will have different properties. And indeed, several clumps in the multiply peaked clouds show bright, $\gtrsim 500\,\mathrm{Mjy\ sr^{-1}}$, 24 μm emission, indicating a protostar, within $10''$ or less of the mm peak, while other clumps are infrared dark. Such clouds with clumps in various phases are not completely infrared dark, since the dust is locally heated from the already hot HMPO or UCHII region. Examples for multiply peaked clumps are shown in Fig. B.1: G014.63–00.57, with the very bright component MM1 and the cloud G018.26–00.24 with five clumps.

Additionally, one can check the evolutionary stage by searching for signs of star formation like water masers, Class II methanol masers, shocks etc. Table 2.3 also contains entries for such star formation tracers. Water masers are thought to be caused by outflows during (low and high-mass) star formation (Menten 1996). The Class II methanol masers are uniquely associated with high-mass star formation, and are usually found prior or coexistent with an H II region (Menten 1991; Ellingsen 2006; Pestalozzi et al. 2007). While the water masers are found towards both the peaked and the multiply peaked clouds, the methanol masers are only found toward the latter class. Another indication for star formation comes from gas excited by shocks, such as $H_2(v{=}0{-}0)$, $S(9,10,11)$ or $CO(v{=}1{-}0)$ gas. The IRAC 4.5 μm band contains both these transitions, and can therefore be used to search for ongoing star formation. The close association of the extended 4.5 μm objects with Class II methanol masers, found by Cyganowski et al. (2008), suggests that they might trace ongoing *massive* star formation. We find two multiple peaked clouds in our sample that contain such an extended 4.5 μm source, of which one also contains Class II methanol masers.

The peaked and multiply peaked clouds show active star formation, while the diffuse clouds do not. Possibly, these clouds might not form stars or will not have column densities high enough to form massive stars. However, some like G013.28–00.34 seem to be forming clumps which might evolve into active star-forming clumps. Table 2.3 shows that the clumps temperatures are very similar, especially in the case of peaked and the multiply peaked clouds; the diffuse clouds stand out with their temperature of $13.5 \pm 1.5\,\mathrm{K}$ against the average temperature of all clouds $16 \pm 1.8\,\mathrm{K}$. As star formation produces stars in a large range of masses, so cluster-forming regions or clumps within one cloud are expected to have different column densities and temperatures. Given the range of column densities for the clumps $3 - 30 \times 10^{22}\,\mathrm{cm^{-2}}$ not all clumps might evolve into clusters with massive stars, even if mass accretion is still continued from the low density material surrounding the clump.

2.6.3 Comments on individual sources

We performed a systematic search using the SIMBAD Astronomical Database of our cloud to find signs of star formation such as maser emission, H II regions and IRAS sources. We discuss here several diffuse, peaked and multiply peaked high extinction clouds, which are representative examples of typical clouds in our sample. Additionally, several unique and interesting clouds are mentioned.

G013.28–00.34

The cloud G013.28–00.34, with its one centrally located clump MM1, is a good example of a cloud in a very early phase of protocluster formation. This clump has a low column density $3 \times 10^{22}\,\mathrm{cm^{-2}}$ and contains less than 5% of the total cloud mass. Likely, this clump did not yet start to collapse, since from the virial mass we know that the clump is confined by gas pressure. Additionally, the clump contains no 24 μm emission, which is a further evidence for stage prior to star formation.

Table 2.3: Mean physical properties of the clumps and star formation indicators in diffuse, peaked and multiply peaked clouds.

	Diffuse	Peaked	Multiply peaked
Mass ($M_\odot$)	*230*[a]	185	150
Size (pc)	*0.52*[a]	0.36	0.30
$N_{\mathrm{N_{H_2}}}$ (10^{22}cm^{-2})	*4.5*[a]	5.5	8.5
T_{rot} (K)	13.5	15.7	17.5
Δv (km s^{-1})	1.2	1.4	1.6
IRDC corr.[b] (within 2′)	83%	50%	70%
24μm[c] (within 1′)	17%	83%	100%
Ext. 4.5μm [d] (within 1′)	none	none	29%
Masers[e] (within 1′)	none	H_2O 25%	H_2O 57% CH_3OH 29%

[a]As most diffuse clouds contained no clumps, we derived the sizes from the smoothed bolometer maps of the diffuse clouds. These are therefore not properties of the clumps in diffuse clouds, but properties of the diffuse clouds themselves.
[b]Catalogs of Simon et al. (2006a) and Simon et al. (2006b).
[c]> 100 MJy sr^{-1}
[d]Extended 4.5μm sources from the catalog of Cyganowski et al. (2008)
[e]H_2O: Jaffe et al. (1981) and this work, CH_3OH: Szymczak et al. (2000)

The moderate NH_3 line widths of 1.6 km s^{-1} indicate a source of turbulence or large scale motions, however, without an NH_3 map of the cloud it is impossible to isolate the source for the turbulence.

G013.91–00.51

In the cloud G013.91–00.51 the 1.2 mm emission follows an infrared dark patch. The one clump in this cloud which is three times above the mean emission is located close by two infrared emission peaks and can be possibly triggered by the star formation in these infrared bright sites. The clump is very massive, 145 $M_\odot$, and cold. The virial mass is 50 $M_\odot$ suggesting a collapse.

G014.63–00.57

Cloud G014.63–00.57 is nested around two bright infrared sources. The 1.2 mm peak fluxes are high, especially for clumps close to the border of the infrared sources. The brightest clump, MM1, contains a compact bright infrared source, IRAS 18164–1631, with a flux density at 25 μm $F_{25\mu\mathrm{m}} = 23$ Jy (Helou & Walker 1988) and has wide NH_3 line widths of 1.8 km s^{-1} indicating large turbulence. Additionally, water masers were observed towards this clump (Jaffe et al. 1981) and Cyganowski et al. (2008) showed that there is extended 4.5 μm emission – a further indication for outflows. All evidence points to a state of ongoing star formation for the MM1 clump. The other clumps of G014.63–00.57 are still infrared dark. The MM1 and MM2 clumps have the theoretically required column density of 1×10^{23} cm^{-2} for massive star formation (see Sect. 2.6.6).

G016.93+00.24

In G016.93+00.24 the 1.2 mm emission followed the infrared dark filament. In the west end of the filament, the 1.2 mm peak, MM1, is a few arc seconds offset from a infrared bright emission peak. The NH_3 line widths are relatively narrow, 0.9 km s^{-1}, and the temperature is low 14 K, which suggests that the clump is in a very early phase with little turbulence.

G017.19+00.81

The multiple peaked cloud G017.19+00.81 harbors several clumps, which are all at a kinematic distance of 2.3 ± 0.2 kpc, arranged in an infrared dark arc (Figs. B.1 and 2.11). Such a morphology

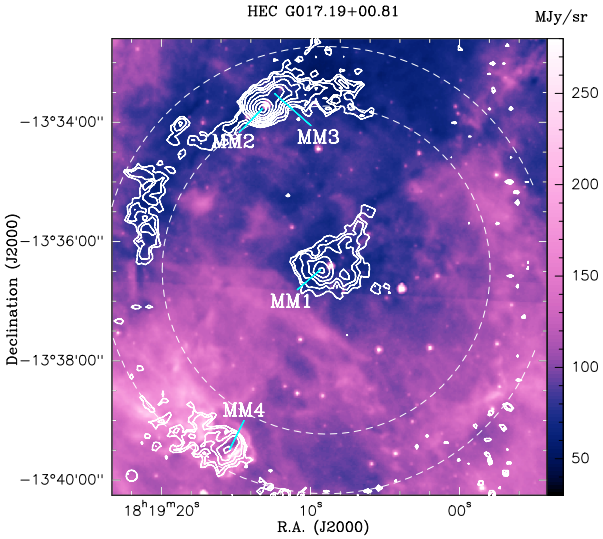

Figure 2.11: A Spitzer GLIMPSE 8.0 μm image of cloud G017.19+00.81 overlaid with the 1.2 mm emission in white contours starting at 2σ ($\sigma = 0.015$ mJy) and increasing by $\sqrt{2}$. All clumps are at the same kinematic distance of 2.3 ± 0.2 kpc. One parsec corresponds to $1.5'$ in this image. The dashed circles guide the eye to the arc-like structure, which is infrared dark in the north-east and infrared bright in the south west.

might point to triggered star formation. The location of this cloud, on the edge of the bright HII region M16, the Eagle nebula, suggests that we are observing the next episode of star formation in this region. However, G017.19+00.81 differs from the classical triggered star formation scenario described by Zavagno et al. (2005). First, the absence of an HII region in the center of the arc; no radio emission was detected neither in the 20 cm MAGPIS survey (Helfand et al. 2006), nor in the 21 cm VLA survey (Condon et al. 1998), nor in the 6 cm Parkes survey (Haynes et al. 1979) – the object was not covered by the 5 cm VLA survey (Becker et al. 1994). Second, an arc triggered by an HII region is expected to be infrared bright, whereas G017.19+00.81's arc is partially infrared dark.

The clumps in the cloud have similar temperatures and sizes. The upper two left clumps, MM2 and MM3, represent most of the mass in this cloud, whereas the southern MM4, shows the largest amount of turbulence. Towards the MM2 clump we observed water masers, within a beam of $40''$. It is coincident with a bright 24 μm source indicating a protostar. MM2 seems to be an evolved clump, where star formation is just beginning. Additionally, the column density of this clump theoretically allows high-mass star formation. The MM4 clump is located nearby an HII region, which might cause the wide line width of 2.8 km s^{-1} and high degree of turbulence. Nearby ($1'$) there is an infrared-bright source, IRAS 18164–1340, which is only detected at long mid-infrared wavelengths of 100 μm ($F_{100\mu m} = 770$ Jy, Helou & Walker 1988). We performed a more detailed study of this region; a molecular line survey with IRAM 30m and an interferometer study with the SMA (Rygl et al., in preparation).

G018.26–00.24

G018.26–00.24 is a cloud with five 1.2 mm peaks located northward of an infrared bright region, with several HII regions and water maser detections. There are several infrared sources present in the cloud, however the most mm emission peaks are infrared dark. MM3 is an exception, here the infrared peak is just a few arc seconds from the mm peak. MM1 has the largest separation from the infrared bright region. This clump has the highest column density and the narrowest line width of the five clumps in this cloud. The overall cloud shape suggests that the gas and dust was collected by a driving force south-west of the cloud, possibly the infrared bright source at ($\alpha = 18^{\rm h}25^{\rm m}02\overset{s}{.}8, \delta = -13°09'30''$, J2000).

G022.06+00.21

G022.06+00.21 contains one clump with a bright mm peak, MM1, and second clump with a weaker peak, MM2. MM1 is coincident with IRAS 18278–0936 ($F_{25\mu m} = 12$ Jy, Helou & Walker 1988), has 6.7 GHz methanol masers (Szymczak et al. 2000) and extended 4.5 μm emission (Cyganowski et al. 2008), and has a sufficient column density for high-mass star formation. Additionally, we observed also water masers towards MM1, within a beam of 40″. MM1 is a relatively warm clump, 25 K, with ongoing star formation suggested by the masers and outflow tracers. MM2 is more quiescent and coincident with a weak infrared source.

G024.37–00.15

G024.37–00.15 contains two clumps, one infrared bright, MM1, and one infrared dark, MM2. MM1 coincides with the bright IRAS source 18337–0743 ($F_{25\mu m} = 47$ Jy, Helou & Walker 1988), and has a wide linewidth 2.1 km s^{-1}. The MM2 core is in an earlier state of star formation, exhibiting SiO emission (Beuther & Sridharan 2007) and water masers.

G024.61–00.33

In G024.61–00.33, the strongest mm emission peak, MM1, is coincident with IRAS 18346-0734 ($F_{25\mu m} = 25$ Jy, Helou & Walker 1988) and nearby, separated by $\sim 30''$, Szymczak et al. (2000) detected 6.7 GHz methanol masers. The second clump, MM2, is infrared dark.

G024.94–00.15

The mm emission follows closely the infrared dark filament in cloud G024.94–00.15. The clumps, MM1 and MM2, are located near weak infrared sources. We found water maser emission toward MM1, within a beam of 40″, indicating early phases of star formation.

G030.90+00.00 A, B, C, and D

G030.90+00.00 consists of several high extinction clouds at very different distances (Fig. B.1). It is located at the tangential point of the Scutum-Crux spiral arm ($v_{\rm LSR} \sim 105\,{\rm km\,s^{-1}}$), where it overlaps with the Sagittarius-Carina ($v_{\rm LSR} \sim 35$ and $\sim 75\,{\rm km\,s^{-1}}$) (Vallée 2008). The Scutum-Crux arm connects at this longitude of 30° with the Galactic bar, a region with highly shocked gas and explosive star formation (Garzon et al. 1997), featuring additionally the mini-starburst region W 43. We found one clump, MM2, which, considering the kinematic distance at 7.2 kpc, is located on the end of the bar.

G034.77–00.81

G034.77–00.81 is a cloud with very diffuse 1.2 mm emission located in a infrared dark part of the sky. By smoothing with a 20″ Gaussian the extended emission became more evident. We detected weak $NH_3(1,1)$ emission toward the center of the extended emission. The ammonia emission indicates that there is a dense region in this cloud, however, it has too low column density or is too extended to be detected by MAMBO-2. Such clouds as G034.77–00.81 could be the most early stages of within our sample.

G035.49–00.30 A and B

Cloud G035.49–00.30 A contains one clump, MM1, coincident with a bright infrared source. In the nearby G035.49–00.30 B we found five clumps located in an elongated infrared dark cloud with several weak infrared sources. We detected water maser emission towards MM1 and MM3, within a beam of 40″. MM1 is the most evolved clump, with ongoing star formation. MM3 should be in a earlier stage of star formation, since the peak of the mm emission is infrared dark.

2.6.4 Comparison with infrared dark clouds

Recent studies have shown that IRDCs generally have a filamentary shape and a high column density of $\sim 10^{23}\,\mathrm{cm}^{-2}$ (Carey et al. 1998, 2000; Rathborne et al. 2006). IRDCs which are very compact or have large aspect ratios might not be detected in the extinction maps because of the limited resolution. The extincion method is more sensitive to the more extended and therefore on average lower column density material than generally found in IRDCs. However, the follow-up study of the 1.2 mm emission maps with MAMBO is sensitive enough to reach the typical IRDC column densities, allowing a comparison between the properties of the high extinction clouds and the IRDCs.

We find that almost 70% of the high extinction clouds have also IRDC characteristics using the Catalog of IRDC candidates from Simon et al. (2006a). This overlap caused that we incidentally studied the same source as Rathborne et al. (2006), namely G035.49–00.30 (listed as MSXDC G035.39–00.33 in the paper by Rathborne et al. 2006), allowing a direct comparison. Given the size of our bolometer map, we identified the same clumps within this cloud. Taking into account different analysis methods, we find similar fluxes and masses as Rathborne et al. (2006).

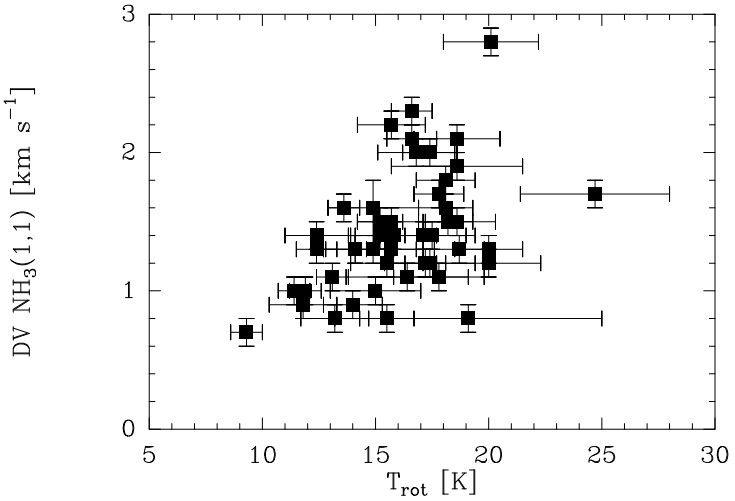

Figure 2.12: The $NH_3(1,1)$ line width as a function of the NH_3 rotational temperature. Linear regression finds a weak trend, correlation coefficient of 0.46, of increasing line widths with temperatures.

In general, the temperature and the level of turbulence (line withs) of the clumps in high extinction clouds was similar to values found for IRDCs (Pillai et al. 2006). Figures 2.12 and 2.13 show that the turbulence tends to increase with ammonia column density and temperature, which is similar for IRDCs (Pillai et al. 2006). The masses and volume averaged densities of the clumps in our sample are similar to the averaged values for clumps in IRDCs (referred to as "cores" in Rathborne et al. 2006). However, the high extinction method is biased at large distances toward more massive clumps. Comparing with the IRDCs sample of Rathborne et al. (2006) our sample is missing low-mass clumps ($M_{\mathrm{clump}} < 100\,\mathrm{M}_{\odot}$) at large distances ($d > 4\,\mathrm{kpc}$), see the left panel of Fig. 2.6. However, our goal, to search for high-mass molecular clouds, is not affected.

Although, the majority of the high extinction clouds is infrared dark, there are a number of infrared bright sources. Especially amongst the multiply peaked clouds, we find several cases of already ongoing star formation via detections of HII regions, water and Class II methanol masers and extended 4.5 μm emission. Since we did not require the high extinction clouds to be infrared dark, the method is also sensitive to the evolved stages of star formation. In addition, the color excess selection is sensitive to embedded young stars with a color excess of their own.

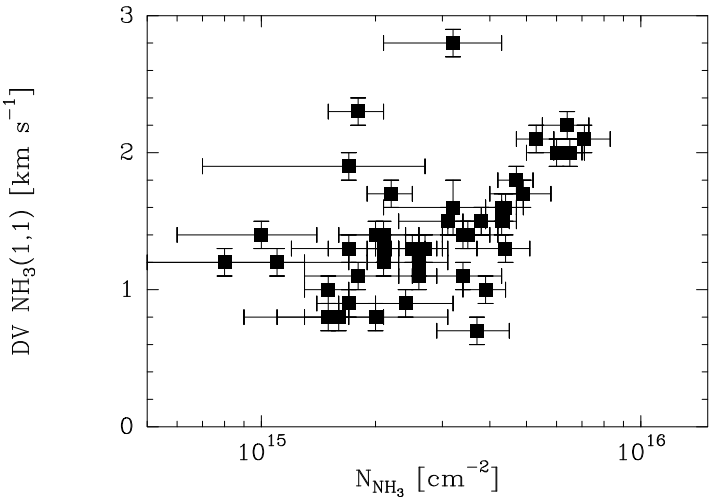

Figure 2.13: The $NH_3(1,1)$ line width as a function of the NH_3 column density. In general, larger line widths are found for higher NH_3 column densities with a correlation coefficient of 0.53.

2.6.5 Comparison with more evolved objects

Later stages of massive star formation are the HMPOs and the UCHII regions. Since these objects are usually still embedded in their natal cloud, they emit most strongly in the millimeter to infrared. Additionally, UCHII regions emit free-free emission, which is detectable at radio frequencies. Most red and bright IRAS sources are such embedded stages of evolved star (or cluster) formation (Wood & Churchwell 1989). Ammonia observations of HMPOs and UCHII regions show that they are usually warm ($T \geq 22\,\mathrm{K}$, Sridharan et al. 2002; Churchwell et al. 1990) and very turbulent (line widths of 2–3 $\mathrm{km\,s^{-1}}$). Water and Class II methanol masers are observed towards these regions (Walsh et al. 1998), indicating outflows and infrared radiation, respectively.

The high extinction clumps have lower temperatures and narrower line widths. Many of the more evolved clumps in high extinction clouds have their peak of mm emission close to bright infrared sources. In several cases the two emission peaks even coincide. For three such cases, G014.63–00.57 MM1, G017.19+00.81 MM2, and G022.06+00.21 MM1, we find slightly higher rotational temperatures, respectively 18, 19 and 25 K, and detections of water masers reminiscent of outflows in the early phase of star formation.

The clump masses in the high extinction clouds are almost one order magnitude lower than the masses of HMPOs (Beuther et al. 2002a). Likely, by removing the median emission before performing the source extraction, the low column density mass reservoir of the clump is subtracted resulting in less massive clumps than in the HMPO studies. Also the HMPOs are on average larger with an average FWHM of 0.5 pc, than the sizes of our clumps ($\sim$0.3 pc).

In most of our clumps the ammonia column densities were of an order of magnitude higher than those for HMPOs. As a clump forms proto stellar objects, the temperature and line widths increase, while the clump will start losing its envelope, which will decrease the ammonia column density on clump size-scales. Similar behavior of temperature, line width and ammonia column density is also observed for IRDCs (Pillai et al. 2006).

2.6.6 Comparison with theoretical models

There are two competing models to explain the formation of massive stars, core accretion (McKee & Tan 2003; Krumholz et al. 2005, 2009) and competitive accretion (Klessen et al. 1998; Bonnell et al. 2001; Bonnell & Bate 2002, 2006). They differ primarily in how the mass is collected which will ultimately make the massive star. In the first model, Core Accretion, a massive star forms in a massive core, hence the mass reservoir of the core determines the mass of the star. In the second theory, a clump of gas will fragment into many low-mass objects containing masses around the

thermal Jeans mass. The accretion will continue in this N-body system, where the overall system potential funnels gas down to the center of the potential, to be accreted by the massive stars forming there. A powerful way to distinguish between these scenarios are better determinations of the massive cores within the clumps. For the core accretion model these cores should be distributed similar to a stellar mass function. The degree of mass segregation of the cores in a clump and the limit of fragmentation will test the competitive accretion model. Such massive core studies require a resolution much higher than this study; they have to resolve the clumps into cores. Several studies on fragmentation were recently carried out using the Plateau du Bure or the SMA interferometers (Beuther et al. 2007; Rathborne et al. 2007, 2008; Zhang et al. 2009; Swift 2009). They show that the 1.2 mm clumps fragment into smaller cores, but cannot tell at what level the fragmentation halts. With the advent of ALMA, the limit of fragmentation will finally come within observational reach.

Simulations of core accretion models by Krumholz & McKee (2008) put forward a minium column density of $1\,\mathrm{g\,cm^{-2}}$ for massive star formation. For reference, this corresponds to $4750\,\mathrm{M_\odot\,pc^{-2}}$ or $N_{\mathrm{H_2}} = 2.7 \times 10^{23}\,\mathrm{cm^{-2}}$. This limit would imply that only one clump from the high extinction clouds can form massive stars, namely G014.63–00.57 MM1. We note here that Krumholz & McKee (2008) use a $\kappa_{1.2\mathrm{mm}} \sim 0.4\,\mathrm{cm^2\,g^{-1}}$, while we used $\kappa_{1.2\mathrm{mm}} \sim 1.0\,\mathrm{cm^2\,g^{-1}}$. This would decrease the minimum column density to $1 \times 10^{23}\,\mathrm{cm^{-2}}$, and four clumps would theoretically be able to form massive stars. Of these four clumps, only one, G014.63–00.57 MM2, is infrared dark. The other three clumps are infrared bright, indicating that they already commenced forming stars. It suggests that the theoretical column density limit is too high for the very initial stages of star cluster forming clumps.

2.7 Summary

We made infrared extinction maps of the first and fourth Galactic quadrant, compiling a catalog of compact high extinction features. We studied 25 high extinction clouds in detail, using IRAM 30m bolometer observations and pointed ammonia observations with the Effelsberg Telescope. The main results of this chapter can be summarized as:

1. Using the average color excess of the Spitzer 3.6–4.5 μm IRAC bands, we are able to trace high density structures across the Galactic plane. The extinction selected clouds are found on distances between 1–7 kpc. Most of them are concentrated in the range of 1–4 kpc, and trace the same regions of the Galactic plane as IRDCs.

2. The extinction method is more sensitive to large scale lower column density clouds than the bolometer observations of 1.2 mm emission, which resulted in a few non detections of clouds in the mm emission despite a mean visual extinction of ∼30 magnitudes from the extinction map. In general, there is a good correlation between the cloud masses derived from the extinction maps and from the 1.2 mm emission.

3. From the 1.2 mm emission, we have found clumps with column densities of 3×10^{22}–$3 \times 10^{23}\,\mathrm{cm^{-2}}$ and masses of 12–400 $M_\odot$. Evidently, not all clumps found by high extinction will be able to form massive stars. It is expected for cluster-forming regions to produce low and high-mass stars, thus to have a wide range in masses.

4. High extinction clouds contain a wide range of evolutionary stages. 70% of the high extinction clouds is associated with infrared dark clouds, however several clouds show more evolved stages of ongoing (massive) star formation. Several different classes of clouds are proposed:

   - Diffuse clouds have no signs of masers, HII regions or extended 4.5 μm objects, which are the general signposts of star formation. The 1.2 mm emission shows no mm peaks above twice the mean emission of the cloud. These clouds are cold, 13.5 K, and the line widths far above the thermal value mark the importance of turbulence. The observations suggest that the diffuse clouds are in an early phase, where the accretion of gas and

dust into clumps might be on the verge of beginning or might never reach the necessary column density to form stars. When the clumps manage to accrete more matter so the mm emission exceeds twice the mean cloud emission are the next (peaked) stage.

- During the peaked stage already some clouds show more than one clump, which indicates that star formation can start in different regions in the same cloud at different times.
- Multiply peaked clouds show many signs of ongoing star formation, such as detections of masers, H II regions or extended 4.5 μm objects. Several clumps are infrared bright show generally slightly higher temperatures and turbulence than diffuse or peaked clouds. Clumps within a cloud are not necessary in the same state, and will likely not all form massive stars. We find four clumps that satisfy the theoretical column density requirement for high-mass star formation.

CHAPTER 3

Molecular line study of clumps in high extinction clouds

3.1 Tracers of star formation

Star formation takes place through many different stages of temperature, density and size scales (see for a review Evans 1999). The growing body of observations acquired by generations of astrophysical and laboratory work, makes it possible to use molecules as probes to study these environments. We studied the molecular emission toward the sample of high extinction clouds, whose bolometer and ammonia observations were discussed in Chapter 2. Based on those results, three categories were defined: the diffuse, peaked, and multiply peaked clouds, in order of evolution. In this Chapter we aim to improve our understanding of these classes by using molecular probes of various densities, large scale motions such as infall and outflows, heating sources and depletion.

The kinematics of the lower density material of the clumps was probed with CO transitions to find outflows or signs of infall. Additionally CO is a molecule which depletes as the clump becomes more dense for a temperature of $\sim$15 K (Bergin & Langer 1997), and the level of depletion shows if the clump is young or if it consists of already more processed material.

The higher density components of the clumps were studied with N_2H^+ and $H^{13}CO^+$. N_2H^+ is known to be a reliable probe of cold gas with lower depletion than most other species (Tafalla et al. 2002). The hyperfine structure of this molecule also allows to determine its excitation temperature and column density.

Molecular line observations help to understand whether the compact clumps are places of ongoing star formation and already contain massive young stellar objects (YSOs), or if the star formation is in an earlier pre-protocluster phase. YSOs will exhibit outflows which can be detected with the CO and SiO observations. An early phase of heating by the YSOs can be detected in the clumps by observations of H_2CO and CH_3CN, of which the latter will allow rotional temperature estimates of the hot phase from the emission in different K ladders. We already know that some of the clumps are associated with bright 24 μm MIPS emission which is an additional, but not sufficient, indication of the presence of YSOs (see Fig. B.1).

Crucial for understanding massive star formation is observational evidence for the infall of matter. In low-mass star-forming regions such as the Bok globule B335 this has been already observed in line profiles (Zhou et al. 1993). The number of infall studies for candidate high-mass

stars (Wu et al. 2005; Fuller et al. 2005; Beltrán et al. 2006) are few, however it is currently increasing rapidly. We studied the infall of material using optically thick molecular lines to find infall velocities and to distinguish clumps without indications of YSO from those in starless and prestellar phases. Additionally, we searched for indications for outflows with the silicate bearing species SiO, a good shock tracer (Schilke et al. 1997).

The Effelsberg observations (Chapter 2) showed that almost all clumps show $NH_3(1,1)$ emission, indicating the presence of high density gas, where this molecular survey can be used to pinpoint their evolutionary stage. We observed all the positions which contained $NH_3(1,1)$ emission with the IRAM 30m telescope in lines listed in Table 3.1. Next, a subsample of these sources was observed at APEX in higher J transitions. The APEX targets included mostly active and evolved sources, which are expected to emit strongly at these higher energy transitions, but a few diffuse and peaked clouds were added to serve as a comparison between the three categories of clouds. The line data was interpreted using the RADEX radiative transfer code (van der Tak et al. 2007) to arrive at models of the physical parameters of the clumps.

In summary, we observed molecules which probe the various stages of evolution and provide estimations of the temperature and density:

Molecule	Information on
$C^{18}O$(2–1)	total gas column density, depletion
CO(2–1), CO(3–2), HCO^+(1–0), HCO^+(4–3)	infall, outflow
$H^{13}CO^+$(1–0)	systemic velocity of dense gas
CH_3CN(5–4), H_2CO(4–3)	YSOs, rotational temperature
SiO(2–1)	outflows and YSOs
N_2H^+(1–0)/N_2H^+(3–2), HCO^+(1–0)/HCO^+(4–3)	indication of density and kinetic temperature (RADEX)

The results of the line observations can then be compared with results from similar surveys towards other samples, e.g. the study of line emission towards IRDCs and other massive star-forming regions by Ragan et al. (2006); Motte et al. (2007); Pillai et al. (2007); Pirogov et al. (2007); Purcell et al. (2009), the survey of methanol maser sources by Purcell et al. (2006), the high-mass protostellar objects survey by Fuller et al. (2005); Beuther & Sridharan (2007) and similar work towards hot molecular cores by Araya et al. (2005) and UCHII regions by Churchwell et al. (1992). This comparison will allow to assess the differences in evolutionary stages covered by the surveys.

The observations and data reduction are described in Sect. 3.2. The next section, Sect. 3.3, gives the results of the infall study, the derived temperature and density estimates, the search for young stellar objects, and the depletion study. These results are interpreted in light of an evolutionary sequence of the three classes of clouds in the Discussion (Sect. 3.4). The chapter ends with a summary in Sect. 3.5.

3.1.1 Temperature definitions

There are several kinds of temperature mentioned in this chapter, so for clarity we define them here. A system is said to be in thermodynamic equilibrium (TE) when the radiation field of that system is described by the Planck function, which depends only on the thermodynamic temperature of the system:

$$B_\nu(T) = \frac{2h\nu^3}{c^2}\frac{1}{e^{h\nu/kT}-1}\,. \tag{3.1}$$

Here B is the specific intensity of blackbody radiation, ν the frequency, T the temperature, h the Planck constant, c the speed of light, and k the Boltzmann constant. In a thermodynamic equilibrium radiative transitions, resulting from emission or absorption of photons, are relatively unimportant and collisional excitation and deexcitation by the thermal gas are dominant. When

a system is only locally dominated by particle collisions it will locally have one temperature – such a system is in local thermodynamic equilibrium (LTE). The difference between LTE and TE is the radiation field. In TE also the photons are in equilibrium since they obey the Planck function, while in LTE there is no equilibrium between the photons and the (massive) particles. The velocity distribution, $f(v)$, of particles in LTE (or TE) is given by the Maxwellian distribution, which depends only on the particles mass m and the kinetic temperature $T_{\rm kin}$:

$$f(v) = \frac{4}{\sqrt{\pi}}\Big(\frac{m}{2kT_{\rm kin}}\Big)^{3/2} v^2 e^{-mv^2/2kT_{\rm kin}} \,. \tag{3.2}$$

Therefore, $T_{\rm kin}$ is a measure of the average kinetic, or translational, energy associated with the disordered microscopic motions of atoms and molecules. One can try to indirectly approximate the $T_{\rm kin}$, by measuring the excitation temperature or the rotational temperature.

The excitation temperature $T_{\rm ex}$ is given by comparing the populations of two energy levels as described in the Boltzmann equation:

$$\frac{n_u}{n_l} = \frac{g_u}{g_l} e^{-\frac{h\nu_{ul}}{kT_{\rm ex}}} \,, \tag{3.3}$$

where n_i is the population of i-th state, g_i the statistical weight of the i-th state, ν_{ij} the frequency of the transition between the state i and j, h the Planck constant, and k the Boltzmann constant. The upper energy level is denoted by u, the lower by l. The excitation temperature has only a physical meaning in LTE when it equals the kinetic temperature.

Rotational transitions are described by two quantum numbers, J the total angular momentum quantum number and K the projection of the angular momentum on the symmetry axis of the molecule. A J level can be splitted in different K levels (a K ladder) for asymmetric molecules. The rotational temperature, $T_{\rm rot}$, is given by comparing the populations between two or more rotational transitions. Especially for symmetric top molecules, which have many rotational transitions in a large range of energies that lie in a small range of frequencies. They can therefore easily be observed simultaneously with one telescope and the rotational temperature can be estimated from the ratios of the various line strengths. For example in CH_3CN the populations within the K ladder of a given rotational transition, $(J+1,K)\rightarrow(J,K)$, are solely determined by collisions, which allows to determine $T_{\rm rot}$ from the relative strengths of the different K levels. Ammonia is another example, but for which one does not take the rotational transitions, but the inversion transitions ($J = K$). These are meta-stable transitions excited only by collisions, therefore the ratio between two inversion transitions yields $T_{\rm rot}$ (see also Sect. 2.5.5). For a medium in LTE, the rotational and excitational temperature equal the kinetic temperature, $T_{\rm ex} = T_{\rm rot} = T_{\rm kin}$.

3.2 Observations and calibration

3.2.1 IRAM 30m telescope

The spectral line survey of the clumps in high extinction clouds was performed with the IRAM 30m telescope during four nights, between June 6–9, 2007. We exploited the possibility of the AB receivers to observe simultaneously at two frequencies, one at ∼100 GHz and the other at ∼230 GHz. With two different receiver setups we could observe a total of seven molecular lines listed in Table 3.1. Two transitions, SiO(2–1) and $H^{13}CO^+$(1–0), could be observed simultaneously since they are separated by only 100 MHz. The high-frequency transitions, CO(2–1) and $C^{18}O$(2–1), were observed in both setups, which increased the signal-to-noise by $\sqrt{2}$. For the ∼100 GHz lines we used the VESPA backend with a bandwidth of 40 MHz and a channel spacing of 0.02 MHz and with a bandwidth of 120 and 160 MHz using a channel spacing of 0.04 MHz, corresponding to a resolution for the respective channels spacing of 0.08 km s^{-1} and 0.16 km s^{-1}. The two wider bandwidths were necessary to allow SiO(2–1) and $H^{13}CO^+$(1–0) to be observed together in the 160 MHz bandwidth, and for the broad line-profile of CH_3CN(5–4) to fit within the 120 MHz band. For the ∼230 GHz lines of ^{12}CO(2–1) and $C^{18}O$(2–1), which both have very wide line profiles,

we used the 1 MHz backend, which offers a bandwidth of 512 MHz and a spectral resolution of 1.5 km s^{-1}. Table 3.1 gives an overview of the bandwidth and spectral resolution for each transition. We observed in position switching mode, where the off position was located 800″ away.

During the observations we performed a pointing check every 1.5 hours on a nearby quasar or the HII regions G10.6–0.4 or G34.3+0.2. The pointing was found to be accurate within 4″. The focus check was usually performed on Jupiter or quasar 3C273 at the beginning of each observing run. The opacity at 230 GHz was variable from excellent winter weather conditions $\tau = 0.1$ to average summer conditions of $\tau = 0.5$. The system temperatures at 230 GHz ranged between 270–920 K. At 100 GHz the opacity ranged between 0.04–0.1 and the system temperatures were between 87–173 K.

The IRAM 30m telescope has a system to calibrate the observed output counts to an antenna temperature, $T_{\rm A}^{\star}$, by using two loads of known temperature, the hot load and the cold load. The $T_{\rm A}^{\star}$ temperature is the brightness temperature of an equivalent source which fills the entire 2π radians of the forward beam pattern of the telescope. This can be converted to a main beam brightness temperature, $T_{\rm MB}$, by multiplying by the ratio of the forward efficiency, $F_{\rm eff}$, and the main beam efficiency, $B_{\rm eff}$:

$$T_{\rm MB} = \frac{F_{\rm eff}}{B_{\rm eff}} \times T_{\rm A}^{\star}\,. \tag{3.4}$$

A list of the efficiencies for each transition is supplied in Table 3.1.

3.2.2 APEX telescope

The Atacama Pathfinder EXperiment (APEX) operates a 12m submillimeter telescope, located on the Chajnantor plateau in the Atacama desert in Chile. Its 5100m altitude location was chosen for the excellent atmospheric conditions, which are much needed for submillimeter observations, since at lower altitudes or in a wet atmosphere the water opacity strongly deteriorates the observations. The observations were carried out with the double side band receiver APEX-2A in several runs between June 10 and November 2, 2007. The receiver was equipped with two Fast Fourier Transform Spectrometer (FFTS) backends. The signal and image sidebands are separated by 12 GHz. We used two setups in our observations, which are described in Table 3.1. Each FFTS 'group' has a bandwidth of 1 GHz, and 8192 channels, which corresponds to a velocity resolution of ∼0.12–0.15 km s^{-1} for lines between 285–350 GHz. Each observation was performed with on-off iterations using three subscans, integrating in total between 90–230 seconds on source. From the IRAM 30m observations, which were carried out before the start at APEX, it was clear that the CO off positions often still contained some signal, which confuses the spectral line results and is undesirable. Therefore the APEX off-positions were used much further out at 1800″, which in most cases were free of emission.

The APEX calibration is very similar to that used at the IRAM 30m, since the telescope calibration unit also contains a hot and cold load. Before each run the focus was calibrated using a planet, usually Jupiter. Pointings were made once every three hours on nearby HII regions like Sgr B2(N). The Precipitable water vapor ranged between 1.44 to 2.80 mm, while the system temperatures ranged from 190–300 K at 280 GHz and 410–575 K for 356 GHz.

3.2.3 Data reduction

Further processing of the data, such as smoothing (spectral averaging) to increase the signal to noise and baseline subtraction were done in CLASS (Pety 2005). For most lines Gaussian fitting was performed to retrieve the basic line parameters, such as $v_{\rm LSR}$, line widths and line intensities. For the line profiles presenting hyperfine structure (hfs), we used "method hfs" which allows additionally the derivation of the optical depth of the main hfs component. The spectral plots were also prepared in CLASS.

Table 3.1: Molecular lines and frequencies

Molecule	$J+1 \rightarrow J$	Frequency (GHz)	Bandwidth (MHz)	Resolution (km s^{-1})	Beam ($''$)	1σ r.m.s[a] (K)	$n_{\rm crit}$[b] (cm^{-3})	$B_{\rm eff}$	$F_{\rm eff}$
				IRAM 30m telescope					
$H^{13}CO^+$	1–0	86.8	160	0.16	29	0.06	1.7×10^5	0.78	0.98
SiO	2–1	86.8	160	0.16	29	0.07	7.3×10^5	0.78	0.98
HCO^+	1–0	89.2	40	0.08	28	0.10	1.8×10^5	0.78	0.98
CH_3CN	5–4	92.0	120	0.16	27	0.09	4.7×10^5	0.78	0.98
N_2H^+	1–0	93.2	40	0.08	27	0.11	1.6×10^5	0.78	0.98
$C^{18}O$	2–1	219.6	512	1.5	12	0.12	9.2×10^3	0.62	0.94
^{12}CO	2–1	230.54	512	1.5	11	1.3	1.1×10^4	0.58	0.92
				APEX telescope					
N_2H^+	3–2	279.5	1000	0.15	22	0.23	3.0×10^6	0.73	0.97
H_2CO	4_{04}–3_{03}[c]	290.6	1000	0.15	22	0.20	9.2×10^6	0.73	0.97
HCO^+	4–3	356.7	1000	0.12	18	0.47	9.1×10^6	0.73	0.97
CO	3–2	345.8	1000	0.12	18	1.1	3.5×10^4	0.73	0.97

[a] The given r.m.s. noise is after smoothing several velocity channels.
[b] Calculated from the collision rates at $T = 20\,\mathrm{K}$ from the LAMBDA molecular database (Schöier et al. 2005).
[c] In subscript are listed the K doublets.

3.3 Results

An overview of all the detected lines is given in Table C.1.

3.3.1 Infall

An infall signature can be recognized in a line profile having a double peaked structure, where the intensity of the blue peak exceeds the intensity of the red peak (Leung & Brown 1977; Zhou et al. 1993; Myers et al. 1996; Mardones et al. 1997; Evans 1999). This assumes that, both, the infall velocity and the excitation temperature rise toward the center. The blue peak originates in the rear part and the red peak in the front part of the infalling shell (see Figure 3.1). Going from the line center toward the wings translates into going from the cold and slowly infalling material in the outer edge of the clump to the warm inner part with higher infall velocities. The opacity of the front shell is responsible for diminishing the red part of the line emission hence creating a blue excess. While for the rear end one observes the hot plus the cold contribution, in the front shell the emission from the hot inner part is absorbed by the colder outer part and the main contribution is the optically thick outer part with low excitation temperatures. A larger opacity of the front shell increases the depth of the self absorption dip. The systemic velocities at the rear and front end will also change, since the opacity changes with emission region: for very opaque material the rear systemic velocity increases, while the front infall velocity decreases. Thus, with increasing opacity, the double peaked profile is blue shifted to lower LSR velocities. In addition, an increase in the infall velocity, $v_{\rm in}$, can cause the red peak to diminish – at very large values of $v_{\rm in}$ the red peak can even dissappear and become a red "shoulder". A red excess, on the contrary to the discussed blue excess, is usually connected with an expansion or outflow. Alternatively, it could also be caused by an outwards moving blob of matter, instead of large scale outward motion (Evans 1999). Infall profiles can be studied using optically thick spectral lines. The observed line profiles can, in addition to large scale motions such as infall, also be influenced by abundance changes though the clouds. Hence it is desired to investigate infall using several molecules. To probe different depths in the clouds and thereby possible different infall velocities we used lines with different critical densities: ^{12}CO(2–1), ^{12}CO(3–2), HCO^+(1–0) and HCO^+(4–3).

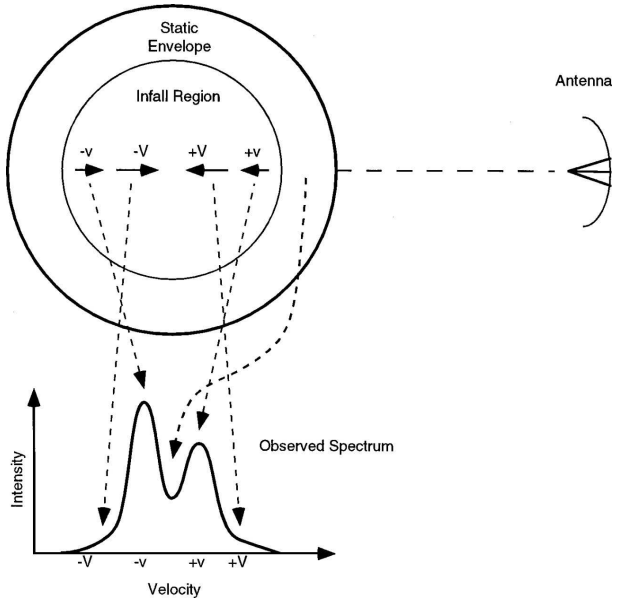

Figure 3.1: A sketch, taken from Evans (1999), showing the origin of the various parts of the line profile for a cloud undergoing inside-out collapse. The infall velocities increase toward the center of the clump. The static envelope produces the self absorption dip. The blue and red peaks come from the rear and front part of the infalling envelope. The center part of the shell, which collapses with faster velocities, produces the wide line wings.

^{12}CO line profiles

We started the study with the ^{12}CO(2–1) and ^{12}CO(3–2) lines, whose critical densities are around $1 \times 10^4\,\mathrm{cm}^{-2}$ (Table 3.1). There is a caveat with regard to the observations of ^{12}CO lines; since the ^{12}CO molecule is a common component of the ISM, the off-position[1] is not necessarily free of its emission. This results in artificial absorption lines in the spectrum as demonstrated in Fig. 3.2. To avoid this, one can observe with two different off-positions and/or use different ^{12}CO transitions. Since higher transitions have a higher critical density, they are less common in the ISM. We employed this strategy, and observed, in addition to the ^{12}CO(2–1) line with IRAM 30m,the ^{12}CO(3–2) line with APEX using different off-positions. Because of the molecules' ubiquity and low critical density, ^{12}CO observations pick up emission from various Galactic arms. This manifests itself in the spectrum by more than one peak at various LSR velocities. For example, source G013.91–00.51 MM1 in Fig. 3.2 shows two additional peaks in ^{12}CO(2–1) and ^{12}CO(3–2), while molecules that are less common or have a higher critical density, such as the isotopologue C^{18}O(2–1) or H^{13}CO$^+$(1–0), show just one emission peak.

We searched for infall signatures by comparing the position of the emission peak of ^{12}CO(2–1) and ^{12}CO(3–2) with that of the optically thin C^{18}O(2–1) line. When the optically thick peak was shifted to bluer velocities with respect to the C^{18}O the source was marked a blue excess source or blue source. A source with a red shifted peak was marked a red source. In general both the ^{12}CO transitions showed similar behavior (see Table C.2). Four examples of infall and outflow signatures are presented in Fig. 3.3. When the peaks of the optically thick and thin lines were at the same velocity, nothing could be inferred. Many ^{12}CO lines had wider line profiles than the C^{18}O lines. Where the ^{12}CO profile was significantly broader than that of the C^{18}O we say that ^{12}CO has "wings". We found ^{12}CO wings ranging from 10 to almost 50 km s^{-1}. Line width broadening is partially due to a high optical depth, which is higher for ^{12}CO than for C^{18}O. However, the line wings are dominated by gas emitting at many different velocities. This can happen if gas in the clump undergoes strong and dominant motions, such as large scale infall or outflow.

[1]The off-position is an observation of 'blank' sky which is used to remove the instrumental bandpass

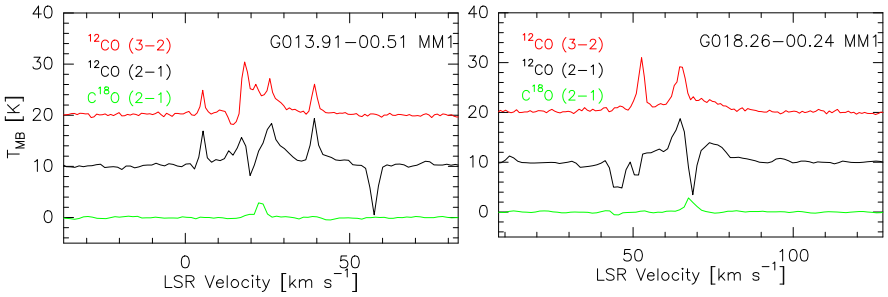

Figure 3.2: Examples of a contaminated off-position for the ^{12}CO(2–1) line profile: there are absorption valleys, that are not present in the higher transition or in the isotopologue, so likely these are artefacts. Additionally there are various peaks at different LSR velocities indicating that there is confusion of several emission regions in the line of sight.

The results on ^{12}CO are given in Table C.2. For the lower transition presence of wings and their width are given. The ^{12}CO line profiles were taken as first indications of infall or outflow, because of the trouble with the off position, a deeper study was done with the HCO$^+$(1–0) and H^{13}CO$^+$(1–0) lines, reported in the next section.

The skewness parameter δv

The optically thick HCO$^+$(1–0) line profiles were used for an in depth study of infall and outflow motions in the clumps. We used the optically thin H^{13}CO$^+$(1–0) line as an indicator of the systemic velocity of clump. Examples of HCO$^+$(1–0) line profiles are shown in Fig. 3.4. For half of the clumps the HCO$^+$(1–0) line showed a double peaked profile with a self absorption dip. Here the ratio of the two intensity peaks, $\frac{T_{\rm blue}}{T_{\rm red}}$, was used to check whether the source showed blue or a red excess in the emission.

When the HCO$^+$(1–0) line profile showed only one peak, we compared the position of this peak with the velocity position of the optically thin H^{13}CO$^+$(1–0) line. The measure of this shift in velocity is called the skewness parameter. Following the method outlined in Mardones et al. (1997) the skewness parameter δv, is defined as

$$\delta v = \frac{v_{\rm thick} - v_{\rm thin}}{\Delta v_{\rm thin}}\,, \tag{3.5}$$

where $v_{\rm thick}$ and $v_{\rm thin}$ are the LSR velocities of the peaks of the optically thick and thin lines, respectively; $\Delta v_{\rm thin}$ is the line width of the optically thin line. The line width and LSR velocity of the H^{13}CO$^+$(1–0) line were retrieved by Gaussian fits (Table C.3). For the optically thick HCO$^+$(1–0) line, the profiles often showed non-Gaussian shapes; therefore the position of the peak was determined by hand (also given in Table C.3). After Mardones et al. (1997) we adopt the definition of significant blue and red sources, namely for the former if $\delta v \leq -0.25$, and the latter when $\delta v \geq 0.25$.

The skewness parameter was determined for the HCO$^+$(1–0), HCO$^+$(4–3) and ^{12}CO(3–2) lines (listed in Table C.2). For all molecules the values ranged between –1.5 and 1.5. Literature values also fall in this range, –0.5 for UCHII regions (Wyrowski et al. 2006), –1.5 to 1 for HMPOs (Fuller et al. 2005), –1 to 2 for Extended Green Objects (EGOs, Chen et al. 2009), which are objects undergoing shocks, and –0.5 for the cluster forming clump G24.4 (Wu et al. 2005). Cross correlations of the skewness between the three different molecules (Fig. 3.5) shows that the HCO$^+$(4–3) line is the least sensitive to infall and or outflow. This is possibly an optical depth effect, since the infall profile is expected to arise in a low density environment ($n < 10^4\,{\rm cm}^{-3}$) where the optical depth of the HCO$^+$(4–3) line is much smaller than that of the HCO$^+$(1–0) line. Most of the HCO$^+$(4–3) lines' δvs are $< |0.25|$, while the other two species exhibit a range of skewness. For the HCO$^+$(1–0) and ^{12}CO(3–2) lines, the skewness seems to be correlated, which makes the infall determination based on these two molecules more reliable.

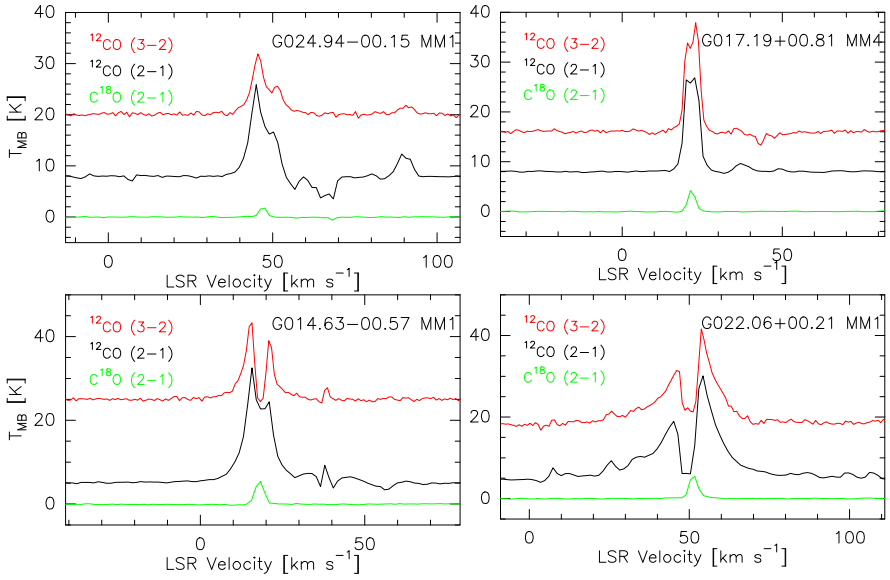

Figure 3.3: Four examples of infall/outflow signatures of the ^{12}CO line profiles. Green marks C^{18}O(2–1) which is optically thin, and is used to indicate the systemic velocity and the shift in the ^{12}CO(2–1) and/or ^{12}CO(3–2) emission shown in black and red, respectively. The panels show infall (*left top and bottom*) and outflow (*right top and bottom*). The profiles show various degrees of self-absorption and various ranges of the wings.

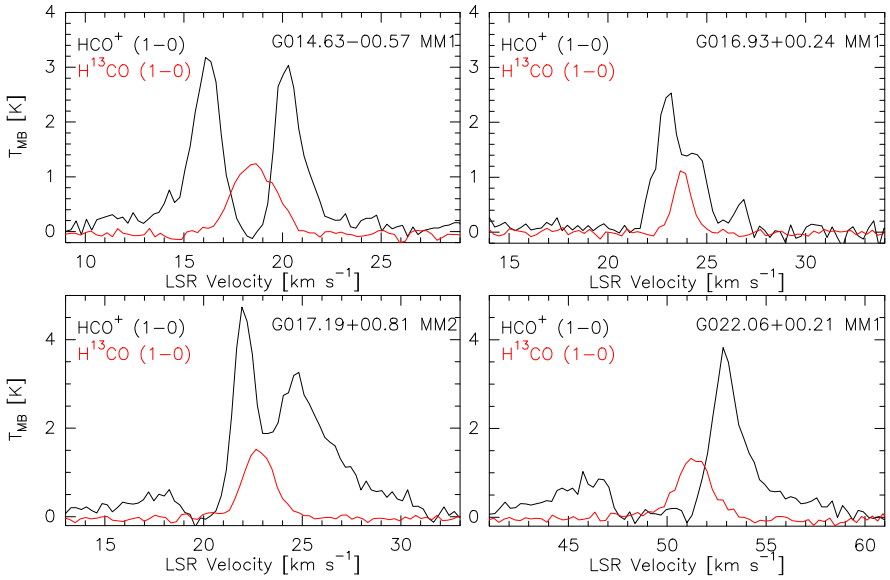

Figure 3.4: Four examples of infall/outflow signatures of the HCO$^+$(1–0) line profile. Red marks H^{13}CO$^+$(1–0) which is optically thin, and marks the systemic velocity of the dense gas. Compared to this the shift of the peak of the HCO$^+$(1–0) emission, in black, becomes clear. The panels show infall (*top right, bottom left*), outflow (*bottom right*) and a case of central self absorption where both peaks are equal (*top left*). The profiles show various degrees of self-absorption.

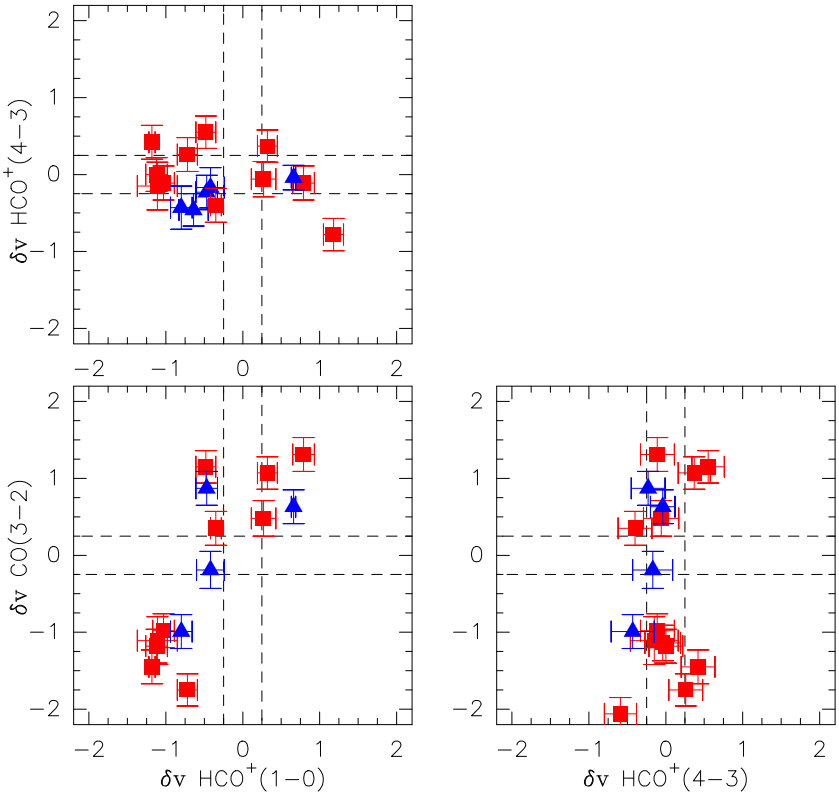

Figure 3.5: The skewness parameter of the HCO^+(1–0) line versus that of the HCO^+(4–3) and ^{12}CO(3–2) lines. The dashed lines mark the boundary of significant excess at $\delta v > |0.25|$. The blue triangles represent clumps in peaked clouds, while the red squares represent sources in multiply peaked clouds.

Table 3.2: Distribution of the skewness parameter per molecule

Transition	$N_{\rm blue}$	$N_{\rm red}$	$N_{\rm tot}$	E	P	$< \delta v >$
HCO^+(1–0)	24	14	47	0.22	0.07	−0.26
HCO^+(4–3)	5	4	18	0.06	0.50	−0.11
^{12}CO(2–1)^a	24	11	35	0.37	0.02	-
^{12}CO(3–2)	8	7	16	0.06	0.50	−0.31

^{a}The numbers of the ^{12}CO(2-1) transition serve only as an indication

The excess parameter which shows the behavior of the average blue wing over red wing excess, is defined as $E = (N_{\rm blue} - N_{\rm red})/N_{\rm tot}$, where $N_{\rm red}$ is the number of red sources, $N_{\rm blue}$ the total number of blue and $N_{\rm tot}$ the total number of all sources (Mardones et al. 1997). Table 3.2 lists the excess parameter and average skewness parameter per transition. Each transition is accompanied by a probability P of the distribution between the blue and red excess being by change. A small P means that the distribution is real and could not happen at random. We calculated the probability that the number of blue sources was equal or higher than observed was by chance by using the binomial test:

$$P = \binom{n}{k} p^k q^{(n-k)}\,, \tag{3.6}$$

where n the the total number of blue and red sources, k the number of blue sources, and p and q are both 0.5. To retrieve the possibility of the number of blue sources *equal or higher* than observed one adds all possibilities $P(n, k, p) + P(n, k{+}1, p) + ..$ until $k = n$.

The number of blue sources in the higher transitions, ^{12}CO(3–2) and HCO^+(4–3), has a probability of 50% to arise by chance, which is not significant. For the lower transitions, however, the values of 7% and 2% indicate a non random distribution of blue and red sources. The result of the ^{12}CO(2–1) line should be treated with care, as not the same definitions of blue and red sources apply. Because of the large uncertainty with the off-position and the high probability of confusing various ^{12}CO(2–1) line components within the line of sight δv would have been very uncertain. The ^{12}CO(2–1) emission was classified to be blue or red skewed based on the peak emission with respect to C^{18}O(2–1) line without the calculation of δv. Therefore, the numbers in Tables 3.2 and C.2 have to be taken just as indications. Additionally, the probability P of the ^{12}CO(2–1) line is artificially low since there were no sources which are neither blue or red. In conclusion, the HCO^+(1–0) line seems to be the best indicator of a significant blue excess. The excess parameter of the HCO^+(1–0) line is similar to values found in a previous survey by Fuller et al. (2005) of high mass protostellar objects reaching excesses of 0.29 and 0.31. Low mass studies also report similar numbers (Mardones et al. 1997; Evans 2003).

HCO^+(1–0) and HCO^+(4–3)

Figure 3.6 shows the spectra of both HCO^+ transitions overplotted for two sources. The HCO^+(1–0) and HCO^+(4–3) critical densities differ almost by a factor 100, and therefore the medium will become optically thick to the higher transitions deeper inside the cloud (or closer to the infall center). We compared our data to the infall model of Myers et al. (1996), which assumes that the density decreases outwards as $n \propto r^{-3/2}$, the excitation temperature increases at small radii, $T_{\rm ex} \propto^{-1/2}$, and that the infall speed decays at large radii as $v \propto r^{-1/2}$. The optical depth for the front shell decreases when reaching the edge of the clump (at radius R_0) as $\tau \propto r^{-1/2} - R_0^{-1/2}$, while for the rear shell the optical depth is minimal in the inner part of the clump and increases toward the clump edge on the far side of the clump, $\tau \propto R_0^{-1/2} - r^{-1/2}$. Based on these assumptions, the model of Myers et al. (1996) and Zhou et al. (1993) predicts the following for the double peaked spectral line:

1. The main beam temperature, $T_{\rm MB}$, $T_{\rm MB}(HCO^+(4–3)) > T_{\rm MB}(HCO^+(1–0))$

2. The level of the self absorption is larger for the HCO^+(1–0) line than for the HCO^+(4–3) line since $\tau(HCO^+(1–0)) > \tau(HCO^+(4–3))$

3. The difference between the red and the blue peak, $v_{red} - v_{blue}$ is larger for the lower transition, since the optical depth is smaller for the higher transition, however if the HCO^+(4–3) emission is originating from much smaller radii of the clump than the lower transition this will not be true, since the infall speed will be higher there.

4. The blue and red peaks of the higher transition should be redshifted, because of the lower opacity of this transition

Less than half of our sources had a double peaked spectrum in both transitions. For those which have, generally all four conditions were met – however not for all. Figure 3.6 shows two examples, G014.63–00.57 MM1 for which the model predictions are correct, and G024.94–00.15 MM1 where we see that $T_{MB}(HCO^+(4–3)) < T_{MB}(HCO^+(1–0))$ and that the assumption of the increasing excitation temperature at small radii was not correct. Condition no. 4 was not easy to verify because of the limited velocity resolution and was generally not found to be true for both the red and blue peak. Possibly, the optical depth effects which cause predictions no. 3 and 4 are confused – these two effects can interfere with each other. We conclude that the predictions no. 1–3 of the model agree well with the general trend.

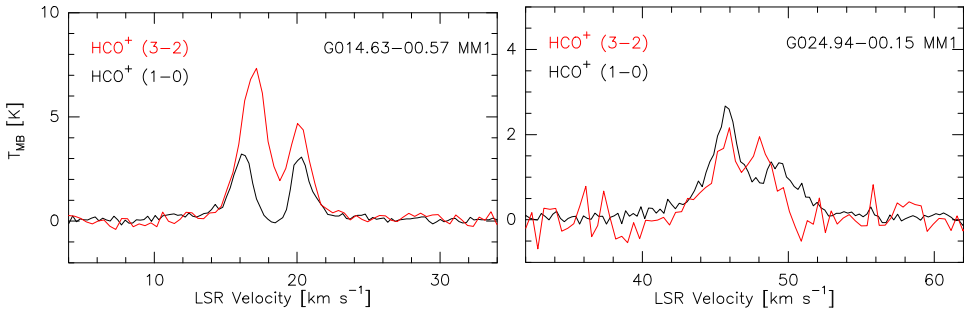

Figure 3.6: HCO^+(1–0) and HCO^+(4–3) spectra for an clump in a multiply peaked cloud (*left*) and a clump in a peaked cloud (*right*).

3.3.2 Temperature and density

N_2H^+(1–0) and N_2H^+(3–2)

The N_2H^+(1–0) and N_2H^+(3–2) rotational transitions have hyperfine structure arising from the interaction between the molecular electric field gradient and the electric quadrupole moments of the two nitrogen nuclei (Caselli et al. 1995). The N_2H^+(1–0) rotational transition is split into seven hyperfine components. The three main hyperfine groups were well-resolved in our observations, and for a few sources we could retrieve all seven components. In the higher transition we were barely able to retrieve even the hyperfine structure, except for one source with a low optical depth. Figure 3.7 shows the spectra of the (1–0) transition for an optically thick and an optically thin case and two spectra of the higher transition.

For fitting the N_2H^+(1–0) transitions we took the hyperfine structure into account using the "method hfs" in CLASS. Besides line widths and integrated intensities, this method also provides the main group optical depth of the lines, based on the intensity ratio of the hyperfine components. The total optical depth τ_{tot} can be calculated from the main hfs group optical depth τ_{main} as $\tau_{tot} = 1.8\tau_{main}$ for the N_2H^+(1–0) line. We calculated the column density of N_2H^+, $N_{N_2H^+}$, following Benson et al. (1998)

$$N_{N_2H^+} = 3.3 \times 10^{11} \frac{\tau_{tot} \Delta v T_{ex}}{1 - e^{-4.47/T_{ex}}} \quad [cm^{-2}], \tag{3.7}$$

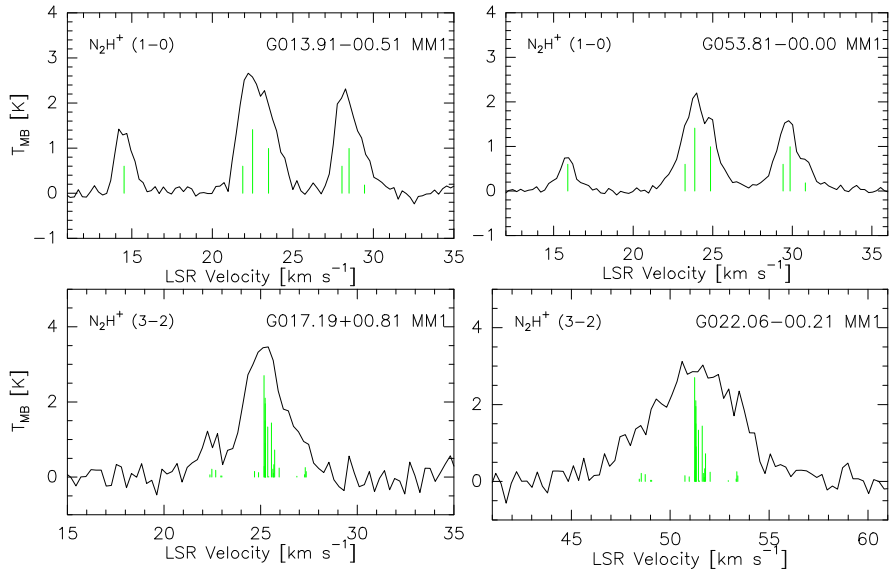

Figure 3.7: $N_2H^+(1–0)$ (*top*) and $N_2H^+(3–2)$ (*bottom*) line profiles. The top left plot shows an optically thick $N_2H^+(1–0)$ transition with $\tau_{\rm tot} = 5.3$, while in the top right plot the spectrum is optically thin with $\tau_{\rm tot} = 0.5$.

where Δv is the linewidth obtained from the hyperfine fit and $T_{\rm ex}$ is the excitation temperature calculated by:

$$T_{\rm ex} = \frac{\int T_{\rm MB,main} {\rm d}v}{\tau_{\rm main}(1 - e^{-\tau_{\rm main}})} + 2.7 \quad [{\rm K}]\,. \tag{3.8}$$

Here $\int T_{\rm MB,main} {\rm d}v$ is the integrated intensity of the main component, $\tau_{\rm main}$ the optical depth of the main component, and the background temperature is 2.7 K. The results of the fits, the integrated intensity, including the hyperfine components, total optical depth, and line width, are placed together with the excitation temperature and the column density in Table C.4. For sources with $\tau_{\rm tot} < 0.4$ the $T_{\rm ex}$ values were much higher than the kinetic temperatures which ranged between 10 and 30 K (based on the rotational temperature $T_{\rm rot}$ derived from NH_3). Because of the large relative errors in optical depth for these sources, these excitation temperatures were not reliable. The excitation temperatures generally ranged from 3 to 37 K averaging on 9.5 K. The low average indicates the limited number of sources with $T_{\rm ex} > 20\,K$; G017.19+00.81 MM1, MM2 and MM3 have 37, 28, and 30 K respectively. The difference between the $T_{\rm ex}$ determined here and the $T_{\rm rot}$ determined by ammonia is that the $T_{\rm ex}$ is influenced by the filling factor f, while the rotational temperature is an intrinsic temperature (independent of f since it is solely determined by line ratios). From the ratio of the two temperatures one can determine the average filling factor:

$$f = \frac{< T_{\rm ex,\,N_2H^+} >}{< T_{\rm rot,\,NH_3} >} = \frac{9.5}{16.0} = 0.59\,. \tag{3.9}$$

This filling factor can be interpreted by a source size that is smaller than the beam or by the source being clumpy instead of centrally condensed. Alternatively, when the $N_2H^+(1–0)$ line is subthermally excited (explained below) the excitation temperature of that transition will be lower mimicking the behavior of a small filling factor.

Table C.5 lists the $N_2H^+(3–2)$ parameters obtained by Gaussian fits. We did not observe the hyperfine structure as clearly as in the lower transition and could therefore not determine the optical depth (see bottom panels of Figure 3.7).

At densities lower than the critical density the population of the lower and the higher energy level is not balanced: collisions do not manage to populate the upper level and the system is in non-LTE. In this case the excitation temperature will be lower than the kinetic temperature.

Excitation at densities lower than the critical density is called subthermal excitation. In a non-LTE system the ratios of line intensities deviate from the LTE predictions and become a function of density, column density, temperature and optical depth. We studied the line ratios of two pairs of molecules N_2H^+(1–0)/N_2H^+(3–2) and $H^{13}CO^+$(1–0)/HCO^+(4–3) and combined this with a non-LTE radiative transfer modeling using RADEX (van der Tak et al. 2007). This is a non-LTE radiative transfer code and by using its molecular database (Schöier et al. 2005) one can estimate the density n_{H_2}, kinetic temperature T_{kin}, column density of the molecule N_{mol}, and τ (total optical depth).

Figure 3.8 shows the integrated intensities of the two N_2H^+ transitions plotted against each other. To identify the clumps from different classes of high extinction clouds (diffuse, peaked and multiply peaked, see Sect. 2.6.2 for the definition), we use differently colored symbols for each class in the graphs shown throughout this chapter. By this we visualize the (possible) behavior of the plot with evolution – the results for different classes of clouds are summarized in the Discussion. The integrated intensity, $\int T_{MB} dv$, of the lower transition, N_2H^+(1–0), exceeded that of N_2H^+(3–2) by an average of:

$$\frac{<\int T_{MB} dv(N_2H^+(1-0))>}{<\int T_{MB} dv(N_2H^+(3-2))>} = 2.9 \pm 0.1\,. \tag{3.10}$$

There are three sources which lie outside the average ratio, these are the more evolved sources (G014.63–00.57 MM1, G017.19+00.81 MM2 and G022.06+00.21 MM1), which are bright at 24 μm and contain water masers.

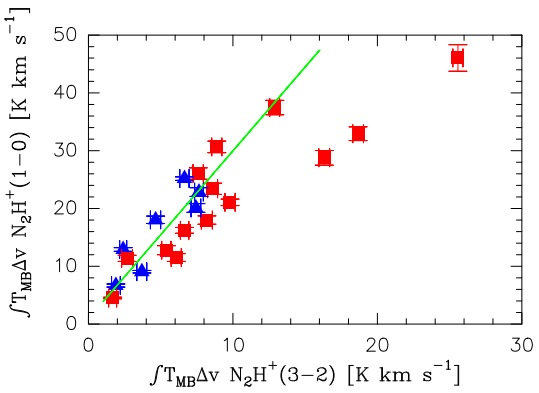

Figure 3.8: A plot of the N_2H^+(1–0) and N_2H^+(3–2) integrated intensities against each other. The blue triangles represent clumps in peaked clouds, while the red squares represent sources in multiply peaked clouds. The green solid line marks the trend of the observed ratio of 2.9.

By forming this ratio it is implicitly assumed that the source fills the beam, which is possibly untrue since we found a filling factor of 0.6 toward the lower transition. For the higher transition, the APEX beam is slightly smaller making a filling factor of unity plausible. Taking the filling factor of the N_2H^+(1–0) line into account, the ratio will be increased by a factor 1/0.6 to result in 4.8.

We estimated the behavior of the N_2H^+(1–0)/N_2H^+(3–2) line ratio and the opacity of N_2H^+(1–0) against N_{mol} and n_{H_2} for kinetic temperatures of 15, 20 and 25 K, which seem plausible compared with the NH_3 rotational temperatures. The results are shown in Fig. 3.9 for the average N_2H^+(1–0) line width of 1.6 kms^{-1} and for that of the N_2H^+(3–2) line (3.0 kms^{-1}). The N_2H^+(1–0) line width is an intrinsic line width, while for the higher transition it is not since the optical depth could not be determined. Therefore, the narrower N_2H^+(1–0) line width is expected to be more accurate. Each panel in Fig. 3.9 shows three regimes: the subthermal region at low densities, the thermal excitation region at high density and the transition region in between. While for both the thermal and subthermal region the optical depth is just proportional to column density, in the transition region it becomes a more complex function. This complexity enters via the change of the T_{ex} with increasing density. For the observed N_2H^+(1–0) optical depth, which ranged between 0.5–5.5 and

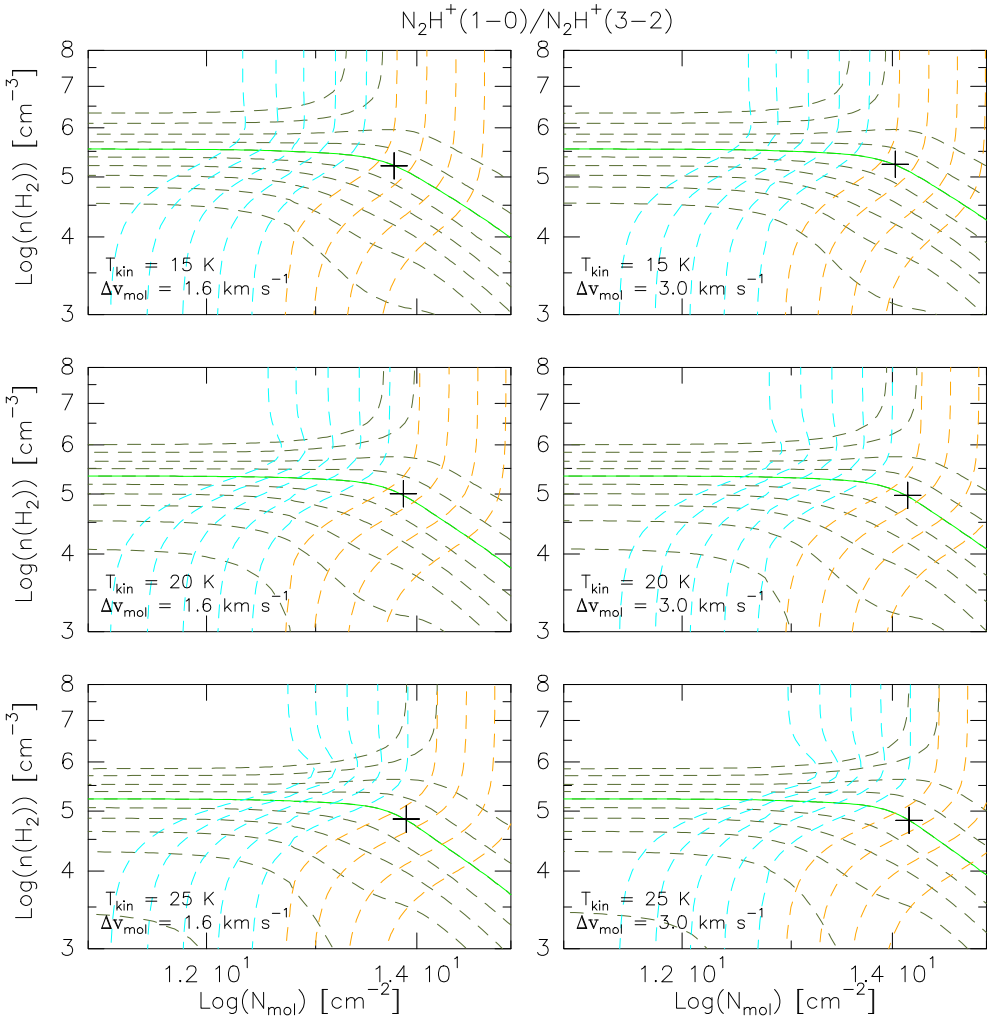

Figure 3.9: N_2H^+(1–0) and N_2H^+(3–2) integrated intensities as a function of volume density and column density for different kinetic temperatures and line widths. Lines of increasing ratio (by a factor of $\sqrt{2}$)are indicated by dashed green lines, increasing towards lower volume densities. The average ratio of 2.90 is a solid green line. The optical depth of N_2H^+(1–0) marked by dashed lines increasing from left to right in the graph, is blue and orange for the optically thin and thick emission, respectively. The first blue contour starts at 1/16 and increases by factors of two till one, then the orange contour continues from two by factors of two. The averaged observed optical depth was three, and the intersection of this τ with the observed ratio is marked by a black cross. $N_{\rm mol}$ represents the column density of the molecule, here N_2H^+, and $\Delta v_{\rm mol}$ the line width.

averaged around 3, the column densities of both N_2H^+ transitions are roughly between 7×10^{13} and $1 \times 10^{14}\,{\rm cm}^{-2}$ for $T_{\rm kin}$ of 15, 20 and 25 K. Rising $T_{\rm kin}$ increases the column density for a given optical depth. When we compare the column density determined by the radiative transfer, which is an intrinsic column density, $N_{\rm intrinsic}$, and the observed column density, $N_{\rm obs}$, which is a beam average and therefore affected by the filling factor, we find the filling factor f to be:

$$f = \frac{< N_{\rm obs} >}{< N_{\rm intrinsic} >} = \frac{3 \times 10^{13}}{7 \times 10^{13}} = 0.43\,. \qquad (3.11)$$

We used the column density for $T_{\rm kin} = 15\,K$ since that is closest the the average $T_{\rm rot}$ of 16 K. The hydrogen volume density $n_{\rm H_2}$ is roughly around $1 \times 10^5\,{\rm cm}^{-3}$ and decreases with rising temperatures. Considering the effect of the filling factor on the ratio, then only for $T_{\rm kin} = 15\,{\rm K}$ $n_{\rm H_2}$

stays at $1 \times 10^5\,\mathrm{cm}^{-3}$, for higher kinetic temperatures the volume density drops below that.

We calculated the average abundance, χ, of N_2H^+ by comparing $N_{N_2H^+}$ to the hydrogen column density, N_{H_2}, measured from the 1.2 mm continuum (Chapter 2):

$$\chi(N_2H^+) = \frac{< N_{N_2H^+} >}{< N_{H_2} >} = \frac{7 \times 10^{13}}{7 \times 10^{22}} = 1 \times 10^{-9}\,. \tag{3.12}$$

The true abundance is likely to be slightly lower, since the N_{H_2} is a beam averaged column density and contains an unknown filling factor. Taking this into account the abundance is in agreement with the value of Pirogov et al. (2007) for high-mass star-forming cores and the results of Ragan et al. (2006) for IRDCs.

Second, the line ratio of N_2H^+(1–0)/N_2H^+(3–2) and the τ of the N_2H^+(1–0) line was estimated for several values of $N_{mol} = 1 \times 10^{13}, 5 \times 10^{13}$ and $1 \times 10^{14}\,\mathrm{cm}^{-2}$, inspired by the first calculation (Fig. 3.9). Figure 3.10 shows the results for the two line widths. The line ratio behaves almost constantly for all temperatures, and prefers a volume density around $1 \times 10^5\,\mathrm{cm}^{-3}$. The observed average value for the N_2H^+(1–0) optical depth ($\tau = 3$) and the line ratio coincide, in Fig. 3.10 at column densities of $5 \times 10^{13} - 1 \times 10^{14}\,\mathrm{cm}^{-2}$.

$H^{13}CO^+$(1–0) and HCO^+(4–3)

For the second line ratio $H^{13}CO^+$(1–0)/HCO^+(4–3) we found that the HCO^+(4–3) integrated intensity often exceeded the that of $H^{13}CO^+$(1–0) (see Figure 3.11); the average ratio was

$$\frac{\int T_{MB} \mathrm{d}v(H^{13}CO^+(1-0))}{\int T_{MB} \mathrm{d}v(HCO^+(4-3))} = 0.34 \pm 0.05\,. \tag{3.13}$$

The sources which stand out from the average ratio (see Figure 3.11) are the same sources which had also a remarkable N_2H^+(1–0)/N_2H^+(3–2) line ratio. The $H^{13}CO^+$(1–0) and HCO^+(4–3) integrated intensities obtained by Gaussian fits, are listed in Table C.3 and C.5, respectively.

Adopting the isotopic ratio for $^{12}C/^{13}C$ of 77 (Wilson & Rood 1994), we calculated with RADEX several models using HCO^+(4–3) column densities, marked by a 12 in the subscript for ^{12}C, $N_{12} = 1 \times 10^{13},\ 5 \times 10^{13}$ and $1 \times 10^{14}\,\mathrm{cm}^{-2}$. The used $H^{13}CO^+$(1–0) column density, marked by a 13 in the subscript for ^{13}C, N_{13}, was a factor 77 lower. At these column densities the $H^{13}CO^+$(1–0) lines are optically thin. Figure 3.12 shows the RADEX results for both the N_2H^+(1–0)/N_2H^+(3–2) and $H^{13}CO^+$(1–0)/HCO^+(4–3) line ratios plotted as a function of T_{kin}, and hydrogen density, n_{H_2}. We used line widths of 1.7 and 3.0 km s^{-1}, representing the average $H^{13}CO^+$(1–0) and HCO^+(4–3) line widths, respectively. Both observed ratios intersect at densities of $3 - 10 \times 10^4\,\mathrm{cm}^{-3}$ in a temperature range between 17–40 K. The errors on the estimates of n_{H_2} and T_{kin} are large since both ratios show similar dependence on n_{H_2} and T_{kin} for a large part of the parameter space.

The intersection of both line ratios has the value of:

$$\frac{\int T_{MB} \mathrm{d}v(N_2H^+(1-0))}{\int T_{MB} \mathrm{d}v(N_2H^+(3-2))} \Big/ \frac{\int T_{MB} \mathrm{d}v(H^{13}CO^+(1-0))}{\int T_{MB} \mathrm{d}v(HCO^+(4-3))} = 9.8 \pm 0.6\,. \tag{3.14}$$

The line ratios are correlated, as shown in Figure 3.13, except for the two outliers of G034.71–00.81 MM2 (at an HCO^+line ratio of 1.2) and G018.26–00.24 MM2 (at an HCO^+ line ratio of 0.65). Both sources have follow the general trend in Figs. 3.8 and 3.11, but they have a very low N_2H^+(1–0)/N_2H^+(3–2) line ratio with respect to that of $H^{13}CO^+$(1–0)/HCO^+(4–3). The plot of both ratios against the hydrogen column density derived from the 1.2 mm continuum (right panel of Fig. 3.13) shows that the ratios increase toward lower column densities where the higher transition will become less populated. Especially the N_2H^+ ratio exhibits a strong correlation with volume density.

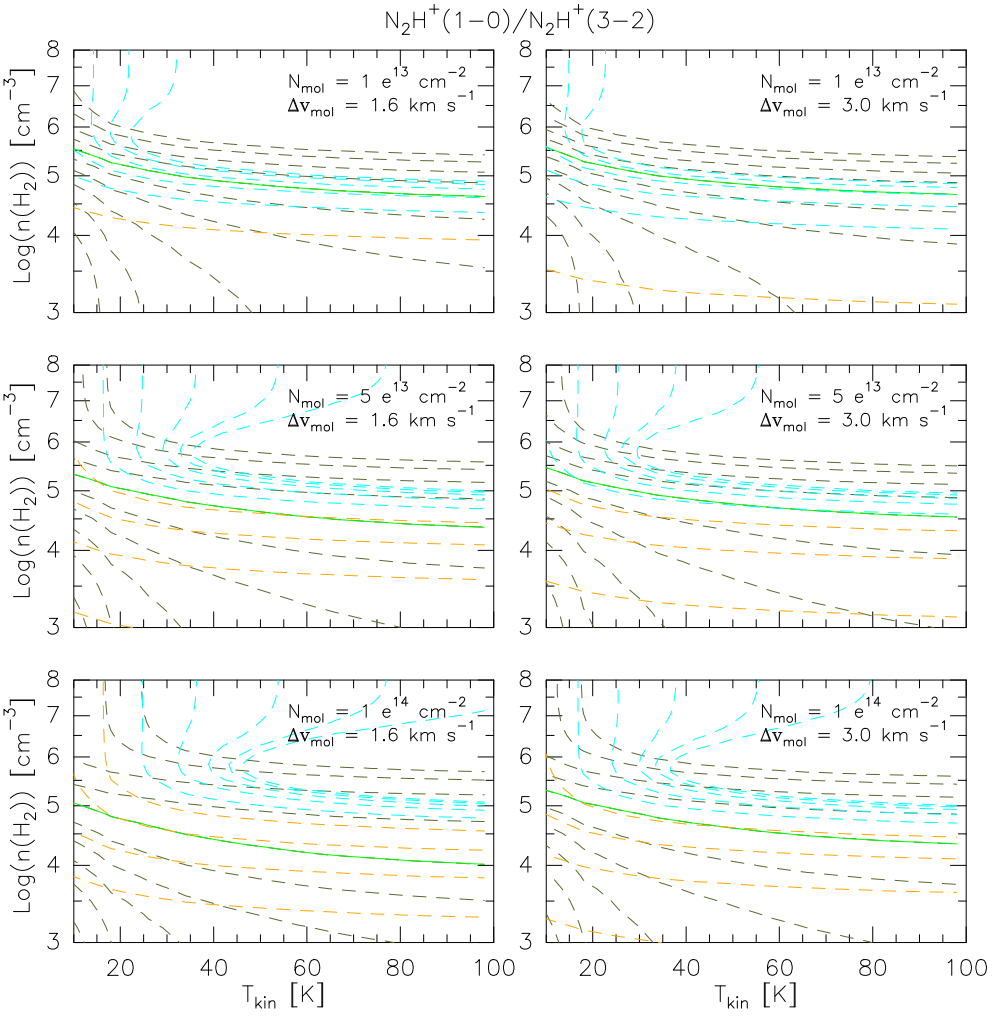

Figure 3.10: The N_2H^+(1–0) and N_2H^+(3–2) integrated intensities as a function of volume density and temperature for different column densities and line widths. Lines of increasing ratio (by a factor of $\sqrt{2}$) are indicated by dashed green lines, increasing towards lower volume densities. The average ratio of 2.90 is a solid green line. The optical depth of N_2H^+(1–0) marked by dashed lines increasing from left to right in the graph, is blue and orange for the optically thin and thick emission, respectively. The first blue contour starts at 1/16 and increases by factors of two till one, then the orange contour continues from two by factors of two. $N_{\rm mol}$ represents the column density of the molecule, here N_2H^+, and $\Delta v_{\rm mol}$ the line width.

CH_3CN

Methyl cyanide, or CH_3CN, is a symmetric top molecule. Each of its rotational levels, denoted by the total angular momentum quantum number J, is split for different projections of the angular momentum along the symmetry axis of the molecule, labeled by the quantum number K. The different K levels form K ladders. Energy levels with higher K values and cannot be excited by radiative transitions, but only by collisions. The population of one K ladder within one rotational level, $J+1 \rightarrow J$, is thus determined by collisions, and therefore closely related to the kinetic temperature and density of the region (Solomon et al. 1971). The K ladders are very closely spaced in frequency (see Table 3.3), which makes it possible to simultaneously observe them. The left panel of Fig.3.14 shows an example of a CH_3CN(5–4) spectrum, where for the various K ladders we marked their upper energy level.

Under the assumption that the CH_3CN emission is optically thin, uniformly fills the beam and

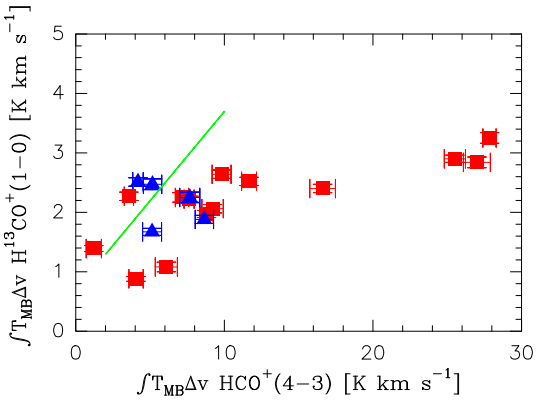

Figure 3.11: Plot of the $H^{13}CO^+(1–0)$ integrated intensity versus the $HCO^+(4–3)$ integrated intensity. The blue triangles clumps in peaked clouds and the red squares represent sources in multiply peaked clouds. The green solid line marks the trend of the observed ratio of 0.34.

Table 3.3: Observed energy levels of methyl cyanide

$J+1 \rightarrow J$	K	Frequency. (MHz)	E_u (K)	$\mu_D^2 g_K g_{nuc}(J^2-K^2)/J$ (D^2)
5–4	0	91,987.054	13.24	305.76
	1	91,985.284	20.39	293.43
	2	91,980.000	41.82	246.94
	3	91,971.374	77.53	391.00
	4	91,959.206	127.51	109.98

that all K ladders are characterized by one temperature we can derive $T_{\rm rot}$ and its total column density $N_{\rm CH_3CN}$ (see for details Araya et al. 2005). The integrated line intensity $\int T_{\rm MB}\Delta v$ is related to the column density N_u of the upper level u by:

$$\frac{N_u}{g_u} = \frac{3kJ\int T_{\rm MB}\Delta v}{8\pi^3\nu\mu_D^2 g_K g_{nuc}(J^2-K^2)} = \frac{N_{\rm CH_3CN}}{Q(T_{\rm rot})}e^{-E_u/T_{\rm rot}}\,, \tag{3.15}$$

where
- k the Boltzmann constant
- μ_D the dipole moment of the molecule
- $Q(T_{\rm rot})$ the partition function at $T_{\rm rot}$, $Q(T_{\rm rot} \simeq 3.89T_{\rm rot}^{1.5}$ (Araya et al. 2005)
- g_u the rotational degeneracy for the upper energy (J,K)
- g_K the K degeneracy
- g_{nuc} the nuclear degeneracy
- E_u the energy of the upper level (J,K)
- ν the transition frequency.

The upper energy levels and frequencies are listed in Table 3.3. The μ_D of CH_3CN is 3.91 Debye. By taking the natural logarithm and plotting it against the E_u, the slope equals $-1/T_{\rm rot}$ as is shown in Eq. 3.15. Then, using the partition function Q we can calculate $N_{\rm CH_3CN}$. The used numbers of $\mu_D^2 g_K g_{nuc}(J^2-K^2)/J$ are supplied in Table 3.3. The right panel of Fig. 3.14 gives an example of the derivation of the $T_{\rm rot}$ by this method.

For almost half of our sources we detected one or more different K levels of the $CH_3CN(5–4)$ rotational transition. All detections and the derived $T_{\rm rot}$, rotational temperature, and column density are listed in Table C.6. In general the CH_3CN lines were very weak and could easily be confused with noise. Not all the detected K levels could be used for fitting the rotational temperature, which explains why Table C.6 does not list a rotational temperature and column

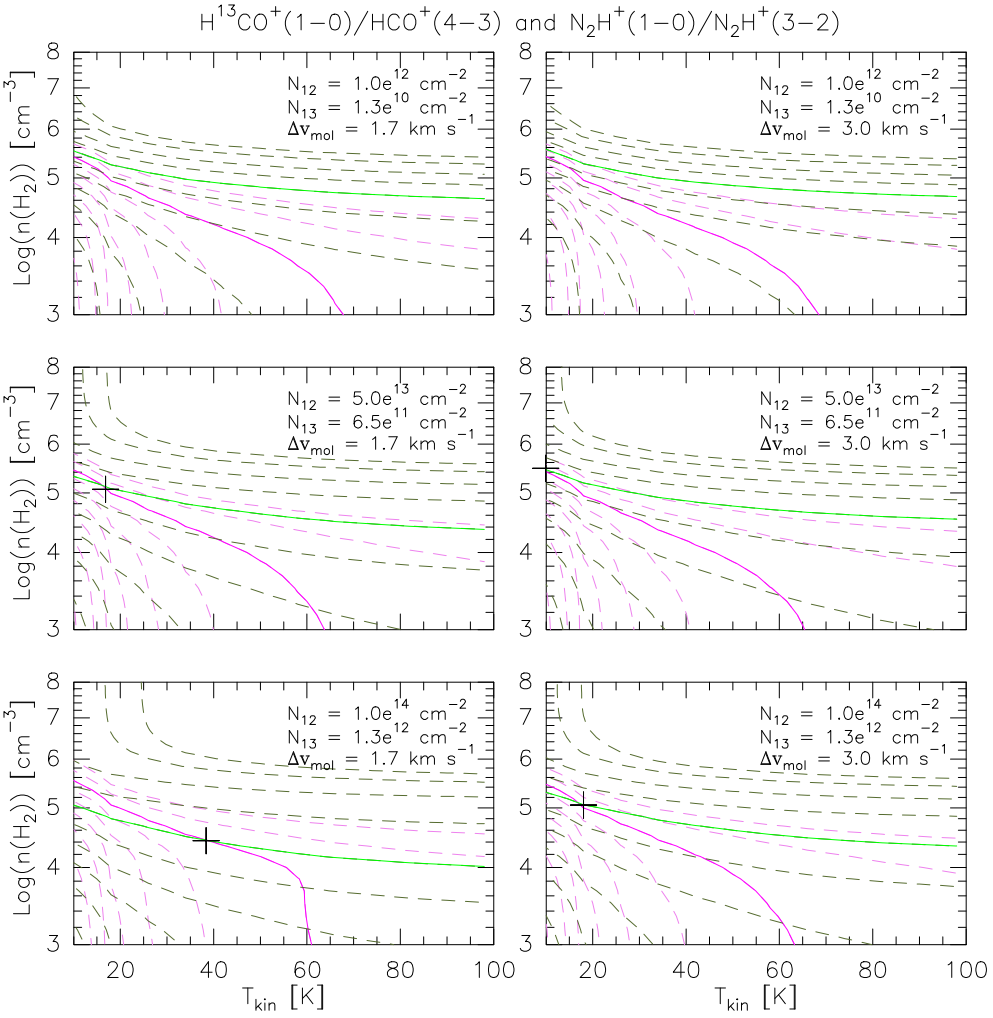

Figure 3.12: Contour plots showing the $H^{13}CO^+$(1–0)/HCO^+(4–3) line ratio in violet and the N_2H^+(1–0)/N_2H^+(3–2) line ratio in green as a function of volume density and temperature for different column densities and line widths. Both ratios increase with column density. The observed ratios are drawn by a solid line and their intersection with a black cross. N_{12} represents the column density of the used molecules except for the $H^{13}CO^+$ column density which is given by N_{13}, and $\Delta v_{\rm mol}$ is the line width.

density for all sources with CH_3CN emission. The rotational temperatures range roughly between 20–40 K for the sources with smaller (12 K) error bars. There are some outliers with $T_{\rm rot}$ as high as 70 K, however the uncertainty on these numbers is very large. For only a handful of clumps, we could calculate meaningful CH_3CN column densities. Their values were between $3-10\times10^{12}\,{\rm cm}^{-2}$ averaging on $6\times10^{12}\,{\rm cm}^{-2}$. This is lower than the $\sim 3\times10^{13}\,{\rm cm}^{-2}$ which was found by Purcell et al. (2006) in an CH_3CN survey toward more evolved sources with methanol masers, and also below the $\sim 10^{13}-10^{14}\,{\rm cm}^{-2}$ found toward hot molecular cores by Araya et al. (2005), and the $\sim 10^{14}\,{\rm cm}^{-2}$ observed toward UCHII regions by Churchwell et al. (1992). In very cold environments CH_3CN is caught in ice mantels on dust grains. Only when the presence of an YSO rises the temperature so much that these ice mantels evaporate releasing the CH_3CN into the gas phase, where one can observe it. The observations show that the CH_3CN column density increases with evolution of the YSO in the clump, resulting from an increase in the abundance by the rising temperature of the environment by the YSO. The CH_3CN results indicate that our clumps are in an earlier stage, younger than the sources with methanol masers, with hot molecular cores and UCHII regions.

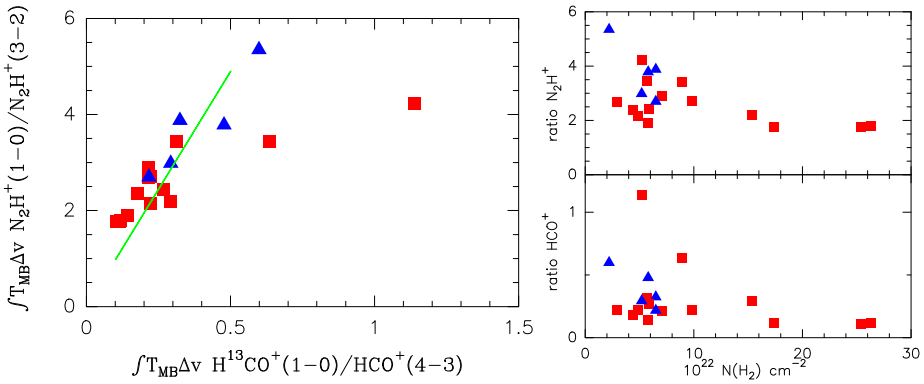

Figure 3.13: *Left:* Plot of the $H^{13}CO^+$(1–0) and HCO^+(4–3) line ratio versus that of N_2H^+(1–0) and N_2H^+(3–2). *Right:* plots of the N_2H^+(1–0)/N_2H^+(3–2) and $H^{13}CO^+$(1–0)/HCO^+(4–3) line ratios as a function of hydrogen column density. The green crosses represent sources in diffuse clouds, the blue triangles clumps in peaked clouds, and the red squares represent sources in multiply peaked clouds. The green solid line marks the trend of the observed ratio of 9.8.

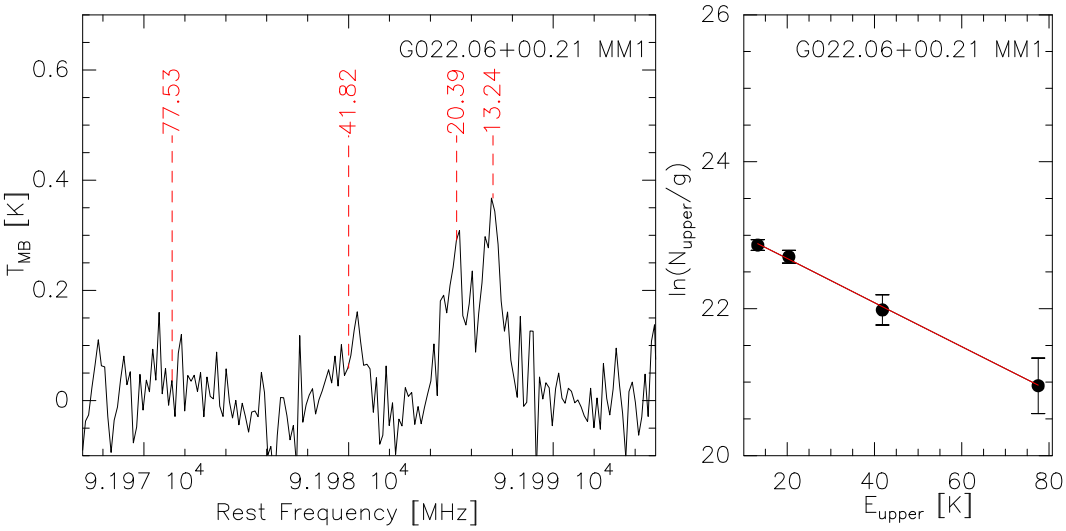

Figure 3.14: The left panel shows a CH_3CN(5–4) spectrum overplotted with the energy levels of the different K ladders. In the right panel, is plotted the fitted slope of the measured $\ln(N_{\rm upper}/g)$ against the energy of the upper level (in Kelvin). For this clump G022.06+00.21 MM1, we found a rotational temperature of 34 ± 5 K and a CH_3CN column density of $9.7 \pm 2.8 \times 10^{12}$ cm^{-2}.

Summary

Before ending this subsection, we briefly summarize the various temperature and density estimates obtained by different methods.

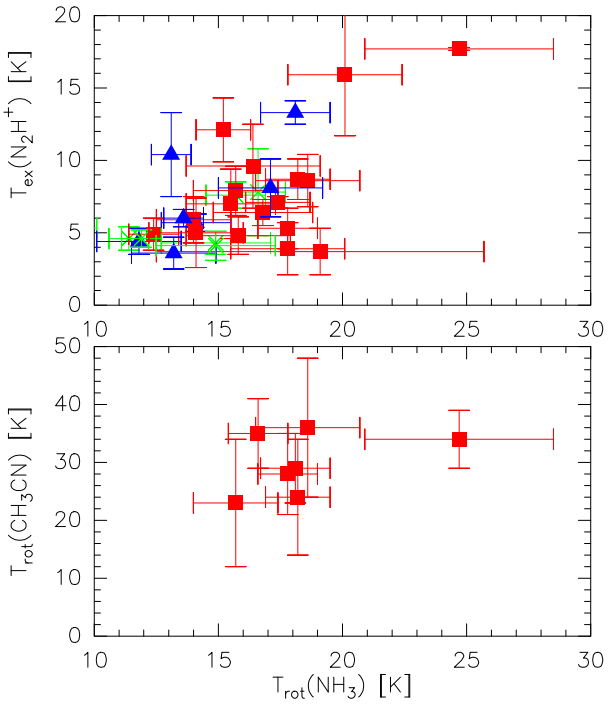

Figure 3.15: The behavior of different temperature estimates. The top graph shows the N_2H^+ excitation temperature against the NH_3 rotational temperature, the bottom graph the CH_3CN rotational temperature (for those results with error bars smaller than 12 K) against that of NH_3. The green crosses represent sources in diffuse clouds, the blue triangles clumps in peaked clouds, and the red squares represent sources in multiply peaked clouds.

Tool	Temperature (K)	Column density (cm^{-2})	n_{H_2} (cm^{-3})
1.2 mm		$3 - 30 \times 10^{22}$	$0.5 - 7 \times 10^5$
NH_3(1,1) and NH_3(2,2)	$10 - 25$	$1 - 7 \times 10^{15}$	
N_2H^+(1–0)	$3 - 35$	$3 - 130 \times 10^{12}$	
N_2H^+(1–0) and N_2H^+(3–2)		$5 - 10 \times 10^{13}$	$> 1 \times 10^5$
$H^{13}CO^+$(1–0) and HCO^+(4–3)	> 17	$5 - 10 \times 10^{13}$	$> 1 \times 10^6$
K levels CH_3CN(5–4)	$20 - 40$	$3 - 10 \times 10^{12}$	

Note that here we assume $T_{ex} = T_{rot} = T_{kin}$. Figure 3.15 shows how the CH_3CN rotational temperature and the N_2H^+(1–0) excitation temperature behave relative to the NH_3 rotational temperature. The NH_3 and N_2H^+ temperatures are simultaneously increasing, however for the CH_3CN temperature the increasing trend is very weak. Possibly this is due to large uncertainty in the temperature. In Fig. 3.15 we plotted only the results which have small (< 12 K) error bars, which shows that the number of well determined temperatures from this molecule was small. Alternatively, CH_3CN can probe a separate more compact and hot component of the clump, since CH_3CN is a tracer of hot molecular cores, while N_2H^+ and NH_3 trace mostly cold and dense regions.

3.3.3 Line width – size scale relations

Many observations of molecular lines in interstellar clouds have revealed a relation between the line width, Δv, and the size (radius R) of the cloud. Most studies (Larson 1981; Myers 1983; Dame

et al. 1986) seem to converge on a ratio:

$$\Delta v \propto R^p \,, \tag{3.16}$$

where the exponent $p = 0.5$. This ratio is valid for the total line width $\Delta v_{\rm TOT}$, which consists of a thermal $\Delta v_{\rm TH}$ and a non-thermal line width $\Delta v_{\rm NT}$:

$$\Delta v^2_{\rm TOT} = \Delta v^2_{\rm TH} + \Delta v^2_{\rm NT} = 8 \ln 2 k T_{\rm kin}/m_{\rm mol} + \Delta v^2_{\rm NT} \,, \tag{3.17}$$

where k is the Boltzmann constant, $T_{\rm kin}$ the kinetic temperature and $m_{\rm mol}$ the mass of the molecule. If the observed line width is dominated by the non-thermal component, one can treat it as the total line width. Additionally, for very narrow lines, the observed line width, $\Delta v_{\rm obs}$, needs to be corrected for the finite channel width, $\Delta v_{\rm chan}$, of the backend by subtracting the square of channel width from the square of the observed line width:

$$\Delta v = \sqrt{\Delta v^2_{\rm obs} - \Delta v^2_{\rm chan}} \,. \tag{3.18}$$

But, as the channel width is much smaller than the observed line width by almost a factor 2, this correction can be neglected.

We correlated the widths of the $H^{13}CO^+$(1–0), $C^{18}O$(2–1), and N_2H^+(1–0) lines with the width of NH_3(1,1) line. The thermal line width component for all these lines was very small. The average NH_3(1,1) line width was 1.4 km s^{-1} where the thermal line width was almost an order of magnitude smaller: 0.2 km s^{-1}. The thermal line widths for the other molecules are less than this value by almost a factor of $\sqrt{2}$ since the molecular masses are almost twice that of NH_3. We therefore used the observed line width in Equation 3.16.

The $H^{13}CO^+$(1–0) line widths usually exceeded those of NH_3(1,1) (see bottom right panel in Figure 3.16), by an average of

$$\frac{\Delta v(\mathrm{H^{13}CO^+(1-0)})}{\Delta v(\mathrm{NH_3(1,1)})} = 1.19 \pm 0.03 \,. \tag{3.19}$$

A slighter larger ratio of 1.5 has been found by Beuther et al. (2007) for clumps in (massive) infrared dark clouds. As the NH_3(1,1) transition has a smaller critical density by almost two orders of magnitude than the $H^{13}CO^+$(1–0) transition (see Table 3.1), so one would expect the NH_3 emission to be more widely spread and more sensitive to different velocity components of the gas. The difference is attributed to the non-thermal component, since as mentioned above, both line widths are dominated by the non-thermal mechanisms. Using Equation 3.16 this ratio indicates that the $H^{13}CO^+$(1–0) emission region should be 1.4 times larger than the NH_3(1,1) emission region. Beuther et al. (2007) argued that this was very unlikely based on the $n_{\rm crit}$. Recently, Purcell et al. (2009) observed the massive star-formation region NGC 3576 and made maps in many molecular transitions, amongst them $H^{13}CO^+$(1–0), NH_3(1,1), $C^{18}O$(2–1), and N_2H^+(1–1). The maps clearly show that the $H^{13}CO^+$(1–0) emission region is indeed larger than that of the NH_3(1,1) line. The ratio of 1.4 seems plausible, but it can not be confirmed by judging the maps "by eye". Alternatively, the $H^{13}CO^+$(1–0) depletion in the dense regions of the clump would lead to an increase in emission region and velocity dispersion.

After this we continued with the other line width ratios, finding:

$$\frac{\Delta v(\mathrm{N_2H^+(1-0)})}{\Delta v(\mathrm{NH_3(1,1)})} = 1.06 \pm 0.13 \tag{3.20}$$

and

$$\frac{\Delta v(\mathrm{C^{18}O(2-1)})}{\Delta v(\mathrm{NH_3(1,1)})} = 1.85 \pm 0.07 \,. \tag{3.21}$$

The top and bottom left panels in Figure 3.16 visualize behavior of the width of the N_2H^+(1–0) and $C^{18}O$(2–1) lines against the NH_3(1,1) line width. This shows that N_2H^+(1–0) and NH_3(1,1)

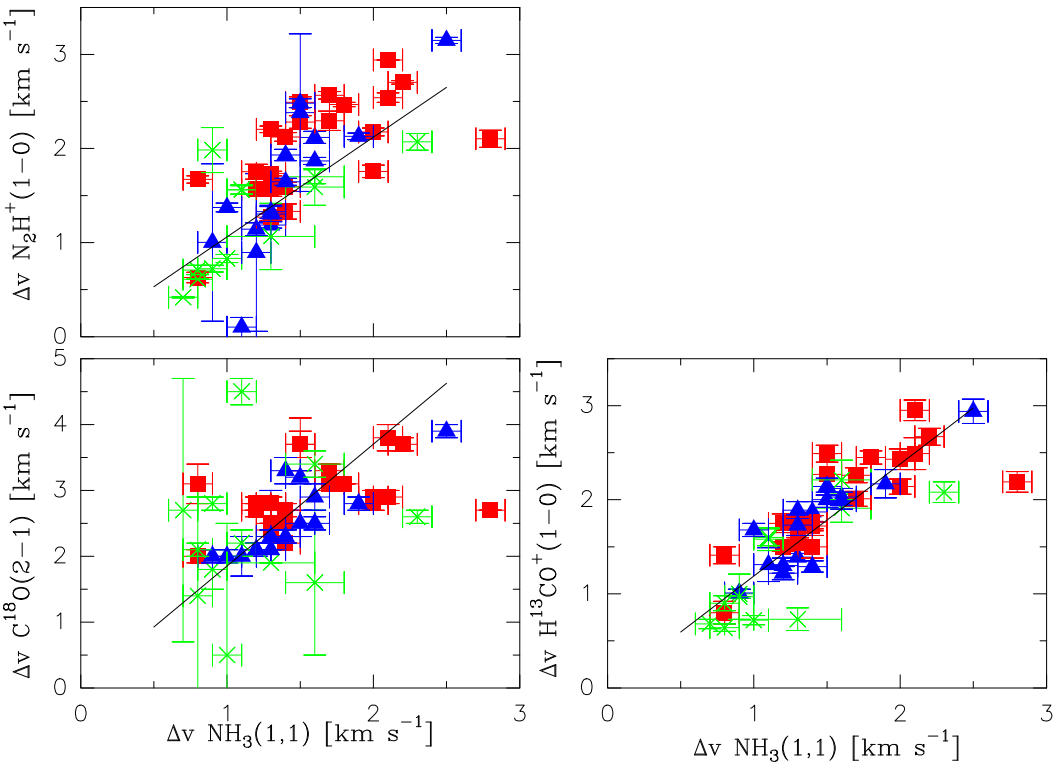

Figure 3.16: Line widths of $NH_3(1,1)$ versus those of $N_2H^+(1–0)$ (*top left*), $C^{18}O(1–0)$ (*bottom left*), and $H^{13}CO^+(1–0)$ (*bottom right*). The green crosses represent sources in diffuse clouds, the blue triangles clumps in peaked clouds, and the red squares represent sources in multiply peaked clouds. The average ratios are indicated by a solid black line.

lines have emission regions of similar size, i.e. they trace the same very dense regions, while the $C^{18}O(2–1)$ emission is four times more extended than the $NH_3(1,1)$ emission. The Purcell et al. (2009) observations support these both results. However, in star forming clouds, where turbulence plays an important role, it is obvious that line width is not only related to size scale as in Eq. 3.16. The turbulence increases toward the denser inner parts of the clumps driven by star formation activity (Ormel et al. 2005), and leads to an increase of the line width accordingly. We found some evidence for this in the NH_3 lines; the $NH_3(2,2)$ line widths were broader than those of the $NH_3(1,1)$ line, but the (2,2) line emission region was not more extended. However, for clumps without an embedded heating source the turbulence should mainly arise by external heating, and be very low in the shielded inner part of the clump. In this scenario the ammonia observations can be explained if the (2,2) line samples more the warmer outer part of the clump. Additionally to turbulence lines can also be broadened by infall and outflow motions.

3.3.4 Presence of young stellar objects

Hot molecular cores: CH_3CN and H_2CO

CH_3CN and H_2CO are usually found toward YSOs or hot molecular cores (Mangum & Wootten 1993; Olmi et al. 1996), which are warm (≥ 100 K) and dense ($\geq 10^5 - 10^6\,\mathrm{cm}^{-3}$) (Kurtz et al. 2000). Both molecules can be used as a tracer of ongoing star formation. The CH_3CN was discussed in Sect 3.3.2, where we derived the column density and rotational temperature. For the $H_2CO(4–3)$ rotational transition we observed only the $4_{04} - 3_{03}$ K doublet, since by a mistake in the center frequency of the observation the remaining K doublets of this transition were outside the bandpass. The observed main beam temperature, LSR velocities and line widths, determined from Gaussian fits, are listed in Table C.7.

To understand if YSOs are preferably present in denser, or more compact clumps, we plot in Fig. 3.17 for all clumps the size versus the column density. Apparently, YSOs are only found in regions with high column densities N_{H_2}, since CH_3CN and H_2CO are detected toward small but also large clumps. The minimal N_{H_2} for $H_2CO(4–3)$ emission to be detected is $4 \times 10^{22}\,\mathrm{cm}^{-2}$, while $CH_3CN(5–4)$ line is still found toward one less dense clump with $N_{H_2} = 3 \times 10^{22}\,\mathrm{cm}^{-2}$. For both molecules there is a general cut-off in the column density at $4 \times 10^{22}\,\mathrm{cm}^{-2}$ below which no YSOs are found. This cut-off is lower than the theoretically required column density of $1 \times 10^{23}\,\mathrm{cm}^{-2}$ to form massive stars (Krumholz & McKee 2008). Possibly, not all these YSOs are massive YSOs and will not evolve to high-mass stars, or they are still accreting and will increase their column densities in the future.

Outflow: SiO(2–1)

Apart from evidently heating their environments, (massive) YSOs drive strong molecular outflows (Beuther et al. 2002b), which remove the angular momentum away from the forming star. While in low-mass star formation mechanisms to accelerate the outflow have been proposed (Shu et al. 2000), in the high-mass scenario it is not well understood yet.

Interstellar dust grains are largely made of silicates (Draine 2003). The only way to free Si-bearing species into the gas phase is when an outflow or jet clashes into the ambient gas and dust and destroys the dust grains (Schilke et al. 1997). The SiO molecule is then believed to be produced in the gas phase. By its formation history SiO is associated to ongoing star formation. Observations support this, since SiO is more common to more active (or evolved) sources, while very weak toward quiescent (hence early) sources (Beuther & Sridharan 2007). Naturally, one also expects to observe wide line widths. We found line widths from $1\,\mathrm{km\ s}^{-1}$ for very weak SiO detections up to $26\,\mathrm{km\ s}^{-1}$ for stronger ones. The individual values for all detections are given in Table C.7 along with the main beam temperatures and LSR velocities. The noise level of the SiO observations was a 1σ r.m.s. of 0.07 K, which is comparable to previous studies of SiO(2–1) in massive star-forming region of Beuther & Sridharan (2007) and Motte et al. (2007), which reached a r.m.s. of 0.02 K and 0.10 K, respectively.

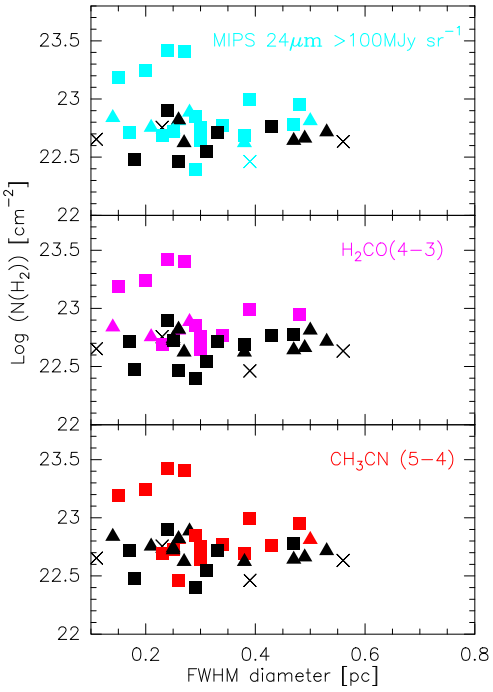

Figure 3.17: The high extinction clumps placed in a diagram of column density versus the FWHM diameter (in pc). The detections of $H_2CO(4–3)$, $CH_3CN(5–4)$, and MIPS 24μm emission are marked in color, black symbols are non-detections. The crosses mark the clumps in diffuse clouds, triangles clumps in peaked clouds and squares clumps in multiply peaked clouds.

SiO(2–1) emission was widely detected toward sources with infall signatures as is illustrated in the left panel of Figure 3.18. We find that 70% of the SiO detections are sources which have a negative skewness parameter, δv, in $HCO^+(1–0)$ (see Sect. 3.3.1). The residual 20% are sources exhibiting an expansion, and 10% are sources showing neither expansion nor infall. To check if SiO emission is stronger for more evolved sources, we looked at the behavior of SiO with hydrogen column density N_{H_2} (determined from the 1.2 mm continuum in the previous Chapter). The right panel of Figure 3.19 shows that the SiO is almost equally distributed over the N_{H_2} range of 1–10$\times 10^{22}$ cm^{-2}. Of the four sources with $N_{H_2} > 1 \times 10^{23}$ two (G014.63–00.57 MM1 and G017.19+00.81 MM2) have the strongest SiO line fluxes of our sample, while the SiO emission of the remaining clumps (G022.06+00.21 MM1 and G014.63–00.57 MM2) was just average or below average. The SiO emission was detected toward all multiply peaked clouds, while just toward three peaked clouds (25%) and only two diffuse clouds (18%), singling out the multiply peaked clouds

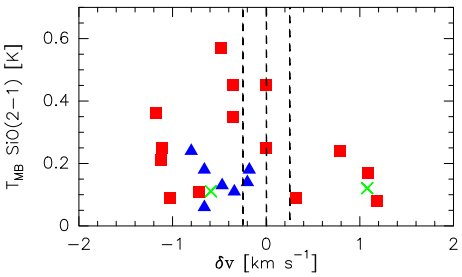

Figure 3.18: SiO detections against the skewness parameter δv. The skewness parameter which is significant if $|\delta v| > 0.25$, marked by the outer dashed lines. A negative δv indicates infall, while a positive δv outflow or expansion. The green crosses represent sources in diffuse clouds, the blue triangles clumps in peaked clouds, and the red squares represent sources in multiply peaked clouds.

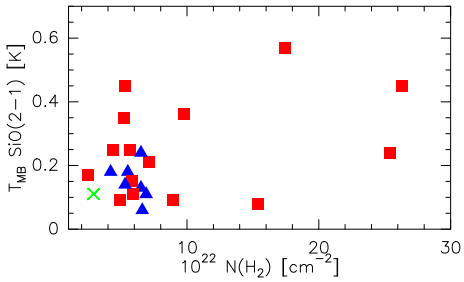

Figure 3.19: *Right:* SiO line detections against the hydrogen column density $N_{\mathrm{H_2}}$. The green crosses represent sources in diffuse clouds, the blue triangles clumps in peaked clouds, and the red squares represent sources in multiply peaked clouds

as active regions of star formation.

A handful sources was left that contained no evidence of an YSO. Of these sources, one third shows infall in the HCO^+(1–0) line profile indicating that these are in a *prestellar phase*, one third is expanding according to the skewness parameter, and the last third shows no infall nor outflow. The latter are the *starless* clumps or clouds.

3.3.5 Depletion

As a clump contracts, the level of depletion of C-bearing molecules like CO or CS increases (Bergin & Langer 1997), so the depletion in a clump can be used as a time marker. Tafalla & Santiago (2004) found for core L1521E in the Taurus molecular cloud a negligible level of depletion. They argue that this is a very young core which has not begun contracting yet. Other evidences such as a low N_2H^+(1–0) abundance (N_2H^+ is a late type molecule, since to form N_2H^+ one needs to first form molecular nitrogen from atomic nitrogen, see Aikawa et al. 2003) and a cold temperature (10 K) agree with this hypothesis. Observations of massive protostellar objects (Purcell et al. 2009) and clumps in IRDCs (Pillai et al. 2007) show depletion of CO, indicating that the clumps in these objects are already in a state of collapse, and that a chemically earlier stage to these objects is still to be found.

We used $C^{18}O$, a less common isotopologue of ^{12}CO, to measure the depletion in the clumps of the high extinction clouds. The line profile of $C^{18}O$ consisted of one Gaussian peak without any wings or self absorption, on the contrary to those of ^{12}CO (see Figure 3.3). This is an indication that the $C^{18}O$(2–1) emission has a low, or moderate optical depth, which would agree with previous observations that derived the $C^{18}O$ optical depths by comparing with $C^{17}O$ (Crapsi et al. 2005; Pillai et al. 2007). Therefore, in this work we will assume that the $C^{18}O$(2–1) line is optically thin. The $C^{18}O$(2–1) line profiles were fitted with a Gaussian. Table C.8 lists the found integrated intensities, LSR velocities and line widths.

The total column density, N_{tot}, of an optically thin line can be calculated as follows:

$$N_{\mathrm{tot}} = \frac{3h}{8\pi^3 S\mu_D^2}\,\frac{Q(T_{\mathrm{ex}})}{g_u g_K g_{nuc}}\,\frac{e^{E_u/kT_{\mathrm{ex}}}}{e^{h\nu/kT_{\mathrm{ex}}}-1}\,\frac{\int T_{\mathrm{MB}}\Delta v}{J_\nu(T_{\mathrm{ex}})-J_\nu(2.73)}\,, \tag{3.22}$$

where
- h the Planck constant
- S the line strength
- $Q(T_{\mathrm{ex}})$ the partition function at T_{ex}, $Q(T_{\mathrm{ex}}) \simeq 0.38(T_{\mathrm{ex}}+0.88)$
- $J_\nu(T)$ $\frac{h\nu/k}{e^{h\nu/kT}-1}$,

while the other parameters are used as defined before in Sect. 3.3.2. The properties of the $C^{18}O$ J=2→1 transition are: $S = J_u/(2J_u+1) = 0.4$, with J_u the upper J level, $\mu_D = 0.1098$ Debye $= 0.1098\times10^{-18}$ e.s.u., $g_u = 2J_u+1 = 5$, $g_K = 1$, $g_{nuc} = 1$, $E_u = k\times 15.81$ erg and $\nu = 219.56$ GHz. The following assumptions were made; a beam filling factor of unity, which is likely for a beam of

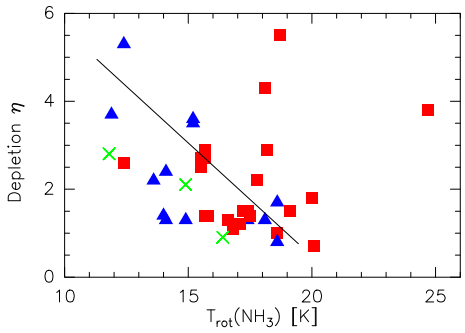

Figure 3.20: The $C^{18}O$(2–1) depletion versus the rotational temperature derived from NH_3. The green crosses represent sources in diffuse clouds, the blue triangles clumps in peaked clouds, and the red squares represent sources in multiply peaked clouds. The black line marks the trend of an increase in depletion with colder temperatures, after excluding the top right three sources from the multiply peaked clouds.

11″ and clumps which have an average size of 20″ in the 1.2 mm continuum. Second, we assume LTE and equate the excitation temperate to the rotational temperature, $T_{\rm rot}$, derived from the NH_3(1,1) and NH_3(2,2) transitions. In very dense and cold regions, where NH_3 inversion transitions are dominated by collisional rather than radiative excitations and de-excitations, $T_{\rm rot}$ is a good measure for the kinetic temperature of the system (Walmsley & Ungerechts 1983; Danby et al. 1988). The background temperature was taken at 2.73 K. With the total column density of $C^{18}O$, $N_{\rm C^{18}O}$, known, we calculated $\chi_{\rm C^{18}O}$, the abundance of $C^{18}O$ relative to H_2, by comparing it to the hydrogen column density, $N_{\rm H_2}$, derived from the 1.2 mm emission in Chapter 2.

$$\chi_{\rm C^{18}O} = \frac{N_{\rm C^{18}O}}{N_{\rm H_2}} \,. \tag{3.23}$$

The canonical number for $\chi_{\rm C^{18}O}$ is 1.7×10^{-7} measured in the nearby ISM (Frerking et al. 1982). At larger distances towards the Molecular Ring and the Galactic center this value is expected to be higher (Wilson & Rood 1994) which would increase the depletion. The ratio between the observed abundance, $\chi_{\rm obs}$, and the canonical value for the abundance, $\chi_{\rm canonical}$ then resulted in η the depletion factor:

$$\eta = \frac{\chi_{\rm canonical}}{\chi_{\rm obs}} \,. \tag{3.24}$$

The $N_{\rm C^{18}O}$, $N_{\rm H_2}$ from the 1.2 mm, $\chi_{\rm C^{18}O}$ and η are listed in Table C.9. $C^{18}O$ appears to be depleted in most of the clumps, with an average level of 2.3, which is slightly lower than what is found in clumps of IRDCs ($\eta = 2-10$, Pillai et al. 2007). Depletion or freezing out is enhanced at lower temperatures. To find if we observe such a trend we plot in Fig. 3.20 the depletion against the rotational temperature. The diffuse and peaked clouds (green crosses and blue triangles) indeed follow this trend, as well as a part of the multiply peaked clouds (red squares). The outliers are G17.18+0.8 MM2, G14.63–00.6 MM1 and G22.06+0.1 MM1, which all three have dust column densities above $10^{23}\,{\rm cm}^{-2}$ and water masers. Possibly these sources were heated so fast by the embedded YSO that the CO was not freed into the gas phase yet.

Since in the above treatment we assumed the $C^{18}O$(2–1) line to be optically thin, we would underestimate the true column density if the emission is optically thick by a factor $\tau/(1-e^{-\tau})$. To calculate the optical depth, τ, we assumed for $N_{\rm tot}$ the number obtained from Eq. 3.22 and used the general formula for the total column density, which is valid for the optically thin and thick regime:

$$N_{\rm tot} = \frac{3h}{8\pi^3 S \mu_D^2} \frac{Q(T_{\rm ex})}{g_u g_K g_{nuc}} \frac{e^{E_u/kT_{\rm ex}}}{e^{h\nu/kT_{\rm ex}}-1} \int \tau \Delta v \,, \tag{3.25}$$

where all the quantities are as defined above. Figure 3.21 shows that the resulting optical depth

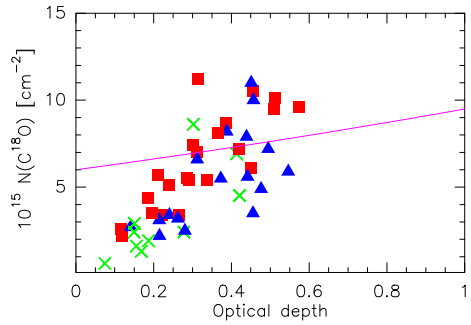

Figure 3.21: The $C^{18}O$(2–1) optical depth versus the $C^{18}O$(2–1) column density in the optically thin limit. The purple line indicates the slope of $\tau/(1-e^{-\tau})$. The green crosses represent sources in diffuse clouds, the blue triangles clumps in peaked clouds, and the red squares represent sources in multiply peaked clouds.

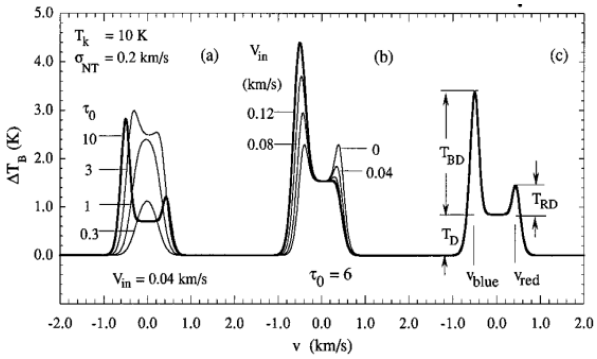

Figure 3.22: Figure, taken from Myers et al. (1996), showing the model line profiles as function of (a) increasing optical depth and (b) infall speed. The parameters to calculate the infall speed are defined in (c). The $\sigma_{\rm NT}$ in the figure refers to the non-thermal line width.

against the $C^{18}O$ column density derived for the optically thin limit. The slope of $N_{\rm C^{18}O}$ with τ is much steeper than a factor $\tau/(1-e^{-\tau})$, which is what one would expect if optical depth effect were playing a strong role, and we therefore conclude that such effects are limited. The calculated optical depths ranged between 0.1–0.5 which would lead to a possible underestimation of the real column density by 5–22%. With this accuracy of 20% our depletion detections are significant since the average depletion factor η was 2.3.

3.4 Discussion

3.4.1 Infall velocities

In Sect. 3.3.1 we determined by binomial tests that the HCO^+(1–0) line was the best of the available molecular transitions to study the infall. For the double peaked sources in the HCO^+(1–0) line profile with a blue excess pointing to a systemic infalling motion, we derived the infall velocity $v_{\rm in}$ according to Myers et al. (1996). This assumed a clump with a density profile, and an increasing infall speed towards the center. It assumes that the opacity of the front shell decreases with radius, while the opacity of the rear shell increases with radius. Then, for a total optical depth of $\tau \gtrsim 3$, the optical depth, infall velocity and line width (of an additional optically thin line) determine the spectral line profile as can be seen in Fig. 3.22. If one assumes that $v_{\rm in} \ll \Delta v_{\rm thin}\sqrt{2\ln\tau}$, where $\Delta v_{\rm thin}$ is the line width of the optically thin line, than one can insert the formulas of front and rear optical depths (see Eq. 1a and 1b in Myers et al. 1996) in the radiative transfer equation for

Table 3.4: Infall velocities, mass infall rates, and time scales for the blue excess sources

Source		$v_{\rm in}$ (km s^{-1})	$\dot{M}_{\rm in}$ (10^{-3}M$_\odot$ yr^{-1})	$\tau_{\rm in}$ (10^5 yr)	$\tau_{\rm ff}$ (10^5 yr)
Diffuse clouds					
G013.28–00.34...	MM1	0.45(0.15)	0.6	1.6	1.5
G013.97–00.44...	MM1	0.32(0.13)	-	-	-
Peaked clouds					
G013.91–00.51...	MM1	2.71(0.10)	8.6	0.17	0.70
G024.94–00.15...	MM1	1.38(0.12)	3.4	0.31	0.74
	MM2	1.08(0.13)	2.2	0.39	0.78
G030.90+00.00...	MM2	1.57(0.15)	90.2	0.08	1.5
G035.49–00.30...	MM1	1.81(0.13)	4.1	0.24	0.78
	MM2	0.50(0.10)	8.6	0.08	0.85
G053.81–00.00...	MM1	4.82(0.10)	6.3	0.04	0.55
Multiply peaked clouds					
G017.19+00.81...	MM2	2.08(0.20)	9.7	0.15	0.42
	MM3	6.65(0.13)	11.5	0.06	0.85
G018.26–00.24...	MM3	5.46(0.18)	14.4	0.09	0.80

the double peaked line profile (see Eq. 2 in Myers et al. 1996). This leads to the following formula for the infall velocity:

$$v_{\rm in} = \frac{\Delta v_{\rm thin}^2}{v_{\rm red} - v_{\rm blue}} \ln\left(\frac{1 + e^{T_{\rm blue}/T_{\rm dip}}}{1 + e^{T_{\rm red}/T_{\rm dip}}}\right) \tag{3.26}$$

where $v_{\rm red}$ and $v_{\rm blue}$ are the LSR velocities of red and blue peaks, whose main beam temperatures are given by $T_{\rm red}$ and $T_{\rm blue}$, respectively, and $T_{\rm dip}$ is the main beam temperature of the dip between the two peaks (see Fig. 3.22, however the naming in this figure is different from our naming; $T_{\rm red}$ is $T_{\rm RD}$; $T_{\rm blue}$ is $T_{\rm BD}$; $T_{\rm dip}$ is $T_{\rm D}$). All these quantities refer to the spectral shape of the optically thick line, except for $\Delta v_{\rm thin}$. With the volume density of the clump $n_{\rm H_2}$ and clump size R, the infall velocity can be converted to a mass infall rate $\dot{M}_{\rm in}$ (after Myers et al. 1996):

$$\dot{M}_{\rm in} = 4\pi R^2 n_{\rm H_2} \mu m_{\rm H} v_{\rm in}\,, \tag{3.27}$$

where $\mu = 2.33$ the mean molecular weight and $m_{\rm H}$ the mass of an hydrogen atom.

For low-mass star formation the mass infall rates are between $\sim 10^{-5}\,{\rm M}_\odot$ yr^{-1} (Palla & Stahler 1993) and $\sim 10^{-6}\,{\rm M}_\odot$ yr^{-1} (Whitney et al. 1997). This is too low to form high-mass stars, since their prestellar phase is much shorter – less then 3×10^4 yr according to Motte et al. (2007) compared to $\sim 3 \times 10^5$ yr for low-mass stars (Kirk et al. 2005). Theoretical models predict for high-mass stars $\dot{M}_{\rm in}$ of 10^{-3} (McKee & Tan 2003; Banerjee & Pudritz 2007). Observations of massive cores or clumps find mass infall rates of $10^{-3} - 10^{-4}\,{\rm M}_\odot$ yr^{-1} (Fuller et al. 2005; Peretto et al. 2006) and even higher ($10^{-2} - 10^{-4}\,{\rm M}_\odot$ yr^{-1} , Beltrán et al. 2006, 2008). Our mass infall results, plotted in Table 3.4, fall in the range of these observed values for massive star-forming clumps. Combined with the masses determined from the 1.2 mm continuum we calculated an infall time scale, $\tau_{\rm in} = \frac{M}{\dot{M}}$ yr and the free fall time scale, $\tau_{\rm ff} = 3.3 \times 10^7 n^{-1/2}$ yr. In general, the free-fall time scale was longer than the infall time scale – for some sources with a high infall rate the difference was up to an order of magnitude. This indicates that the infall speeds calculated in Eq. 3.26 are overestimated. A possible explanation is that the continuum emission, from which we derive the free-fall time scale, sees densities between $10^4 - 10^5\,{\rm cm}^{-3}$, while the HCO$^+$(1–0), with a critical density of $2 \times 10^5\,{\rm cm}^{-3}$, sees only the high density component of the gas. This high density gas resided closer to the infall center where the infall velocities are higher than in the averaged gas content which is sampled by the continuum emission.

In the next section we review these results for the different types of clouds.

3.4.2 Evolutionary sequence

In the previous Chapter, three classes of high extinction clouds were defined, based on the contrast of the clump to the cloud in the 1.2 mm continuum. Here we review all the results of this chapter in light of the hypothetical evolutionary sequence from the quiescent diffuse clouds to the peaked ones, and finally to the multiply peaked clouds.

Diffuse clouds

For this class more than half of the investigated sources were not clumps, but positions of diffuse emission of the cloud. The infall study found a slight excess of blue sources, indicating infall, but the binomial test showed that this result is not significant (see Table 3.5). Two of the three clumps in diffuse clouds, G013.28–00.34 MM1 and G030.90+00.00 MM3, have significant infall characteristics from the profile of the HCO^+(1–0) line – possibly when the clump is formed the infall of material starts and can be detected from the profiles. In the more diffuse places of the cloud – those without clumps – the infall did not start yet, and may possibly never begin. The derived infall velocities and mass infall rates were both low, 0.4 km s^{-1} and 0.6×10^{-3} M$_\odot$ yr^{-1}, respectively. SiO emission, indicative of outflows (see Sect 3.3.4), was found toward two diffuse sources, G013.28–00.34 MM1 and G025.79+00.81 MM1. While G013.28–00.34 MM1 has an infall profile in HCO^+(1–0), G025.79+00.81 MM1 showed outflow or expansion (see Fig. 3.18).

Table 3.5: Infall properties from the HCO^+(1–0) line profile for different classes of clouds

Class	$N_{\rm blue}$	$N_{\rm red}$	$N_{\rm tot}$	E	P	$< \delta v >$
Diffuse	4	2	8	0.25	0.34	−0.001
Peaked	11	2	17	0.53	0.01	−0.63
Multiply peaked	9	8	20	0.05	0.50	−0.72

The N_2H^+(3–2) and HCO^+(4–3) lines were observed for one diffuse cloud, G034.85+00.43, and yielded only non-detections. With only upper limits for one source, it is difficult to extract a meaning for a whole class of clouds, and therefore we did no RADEX calculations for the diffuse clouds. The averaged observed N_2H^+ column density was 1.3×10^{13} cm^{-2}, which still includes a filling factor. If we take the averaged filling factor, determined in Eq. 3.11 then $N_{\rm N_2H^+} = 3 \times 10^{13}$ cm^{-2}, lower then in the more evolved classes.

One can find indirect evidence of high temperatures by looking for molecules such as CH_3CN and H_2CO that are characteristic for YSOs. In the diffuse clouds we found two tentative detections of the CH_3CN(5–4) line and no detections of the H_2CO(4–3) line. The CH_3CN(5–4) detections were too weak to allow the derivation of a significant rotational temperature. These weak and non-detections point to a cold nature of the diffuse clouds, which agrees with the NH_3 results in Chapter 2.

In diffuse clouds the NH_3(1,1), N_2H^+(1–0), $H^{13}CO^+$(1–0), and $C^{18}O$(2–1) line widths are narrower than those of peaked and multiply peaked clouds. If one ignores the turbulence in the line width ratio, then the increasing line width can be interpreted as an increase in size (discussed in Sect. 3.3.3). Diffuse clouds, which have a lower $n_{\rm H_2}$ than the more peaked or multiply peaked clouds, show as expected weaker emission in molecules with high critical densities, such as N_2H^+, NH_3, and $H^{13}CO^+$.

The depletion in diffuse clouds was on average not significantly lower than in peaked or multiply peaked clouds, and therefore we could not use the depletion as a time marker in the clump evolution. However, the ratio of $C^{18}O$ and N_2H^+ can approximate the evolution as well. In the early stages, $C^{18}O$ should not be depleted yet, while N_2H^+, which takes some time to form, is still expected to be weak (Tafalla & Santiago 2004). Therefore the ratio of $C^{18}O/N_2H^+$ is high for young sources, while low for more evolved clumps. Figure 3.23 shows that while most of the diffuse clouds have low N_2H^+(1–0) intensities, not all of them have a high ratio of $C^{18}O$ to N_2H^+.

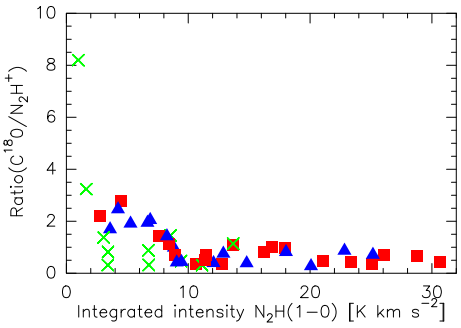

Figure 3.23: The ratio of the integrated intensities of $C^{18}O(2–1)/N_2H^+(1–0)$ versus the $N_2H^+(1–0)$ integrated intensity. The green crosses represent sources in diffuse clouds, the blue triangles clumps in peaked clouds, and the red squares represent clumps in multiply peaked clouds.

Peaked clouds

In the peaked clouds the distribution of blue and red sources from the $HCO^+(1–0)$ line profile favored significantly the blue sources with infall. The excess parameter was 0.53 with the possibility for this distribution to arise by chance of only 1%. There is a notable difference in the increase of the infall velocities and rates between the peaked clouds and the diffuse clouds. Toward the peaked clouds infall velocities of $\sim 1.7\,\mathrm{km\ s^{-1}}$ and infall mass rates of $4.5 \times 10^{-3}\,\mathrm{M_\odot\ yr^{-1}}$ were found. Here we excluded G035.49–00.30 MM2, G053.81–00.00 MM1, and G030.90+00.00 MM2 for which the infall time scale was more than one order of magnitude smaller than the free-fall time scale making the infall rate untrustworthy. All the SiO detections of clumps in peaked clouds coincide with sources that show infall (Fig. 3.18). The strong correlation between the infall characteristics and SiO outflows shows that accretion is accompanied by collimated outflows which lead to an enhancement of SiO. This correlation does not exist for the earlier nor latter classes.

The RADEX radiative transfer calculations were performed for the peaked clouds, using the averaged values for the $N_2H^+(1–0)$ line properties for this class: $\Delta v = 1.6\,\mathrm{km\ s^{-1}}$, $\tau = 3.1 \pm 0.62$ and $T_{\mathrm{kin}} = T_{\mathrm{rot}} = 15\,K$ (the average NH_3 temperature for the peaked clouds for which we could measure the τ and T_{ex}). From the intersection of the ratio and opacity in the left top panel of Fig. 3.24 the intrinsic $N_{\mathrm{N_2H^+}}$ was found to be $5 \times 10^{13}\,\mathrm{cm^{-2}}$ with a $n_{\mathrm{H_2}}$ of $1 \times 10^5\,\mathrm{cm^{-3}}$. Adding the information from the $H^{13}CO^+(1–0)/HCO^+(4–3)$ ratio in Fig.3.25, where the HCO^+ column density (N_{12} in the Fig. 3.25) was taken to be equal to the $N_{\mathrm{N_2H^+}}$. The $H^{13}CO^+(1–0)$ column density (N_{13} in the Fig. 3.25) then followed by dividing that result by the abundance ratio of $^{12}C/^{13}C$. The resulting $n_{\mathrm{H_2}}$ was $6 \times 10^4\,\mathrm{cm^{-3}}$ and the kinetic temperature was found to be spread in a range of 18–27 K. This is higher then the kinetic temperature estimates from the NH_3 data, which are more accurate. A different $N_{\mathrm{HCO+}}$ would have changed the temperature results – and since we had to guess the column density of HCO^+ there is large uncertainty in the temperatures. The higher detection rate of the $H_2CO(4–3)$ and $CH_3CN(5–4)$ lines for the peaked clouds than for the diffuse clouds shows that some already contain YSOs. The averaged line widths in peaked clouds are broader than in the earlier class, likely due to an increase in turbulence from the YSOs.

Multiply peaked clouds

In the multiply peaked clouds the distribution between blue and red sources was almost equal. The possibility that a clump in the multiply peaked clouds shows infall is completely up to chance. This is expected, since these clouds host a variety of stages from clumps with still ongoing accretion to regions where the feedback from the formed young stars halts further accretion. The averaged skewness parameter was −0.72, showing that the blue sources have a much larger peak displacement than the red sources. G17.18+0.8 MM2 was the only source showing infall with a trustworthy infall time scale compared with the free-fall time scale – the infall velocity was $\sim 2.1\,\mathrm{km\ s^{-1}}$, and the infall mass rate $9.7 \times 10^{-3}\,\mathrm{M_\odot\ yr^{-1}}$. Clumps in multiply peaked clouds have the highest infall velocities and mass infall rates compared to the earlier classes. In UCHII regions, Fontani et al.

(2002) observed infall rates of the order of $10^{-2}\,M_\odot\ yr^{-1}$, which would agree with an increasing infall toward more evolved stages. While it is difficult for the infall to start if the matter is almost equally distributed over the cloud, the gravitational pull strengthens when a larger potential (clump) is formed. Most mass is accreted onto the clump in the HMPO and UCHII region stage. Many clumps in this class showed SiO emission, from low to high main beam temperatures of 0.6 K. Figure 3.18 shows that the clumps with SiO were almost equally distributed between infall and outflow characteristics determined by the skewness parameter.

For the multiply peaked clouds the N_2H^+(1–0) lines have on average a much wider line width, $\Delta v = 2.0$ km s, smaller opacity, $\tau = 2.4 \pm 0.46$, and a higher NH_3 rotational temperature $T_{\rm rot} = 18\,K$ than in the previous classes. With these averaged quantities the RADEX calculations yielded a higher intrinsic $N_{\rm N_2H^+}$ than the diffuse or peaked clouds, namely $8 \times 10^{13}\,{\rm cm^{-2}}$ and a higher volume density $n_{\rm H_2} = 2 \times 10^5\,{\rm cm^{-3}}$ (bottom left panel Fig. 3.24). The N_2H^+ ratio alone was not able to give strong boundaries on the kinetic temperature, as the ratio and the opacity are very close in the $T_{\rm kin}$ vs. $n_{\rm H_2}$ plot (bottom right panel of Fig. 3.24). Adding the $H^{13}CO^+$(1–0)/HCO^+(4–3) ratio (see the right panel of Fig. 3.25), assuming an HCO^+ column density equal to that of N_2H^+, indicated a range of temperatures of 10–30 K, shown by the variation of values for the different clumps. Event hough here the results agree with the kinetic temperatures from NH_3, the temperature estimation from RADEX carries large uncertainties as discussed above. The volume density of the multiply peaked clouds, $n_{\rm H_2} > 10^5\,{\rm cm^{-3}}$, is much larger than what was found for the peaked clouds. Multiply peaked clouds had the highest detection rate of the CH_3CN(5–4) and H_2CO(4–3) lines, indicating that this class contains the most YSOs or hot molecular cores and should have higher kinetic temperatures. The K ladders of the CH_3CN(5–4) line allowed a handful of rotational temperature estimates, ranging between 23 and 34 K (see lower panel Fig. 3.15). The increasing evidence for more YSOs is likely the reason for the broadening of the line width found toward clumps in this class (observed for the N_2H^+(1–0), NH_3(1,1), $C^{18}O$(2–1), and $H^{13}CO^+$(1–0) lines) by increasing turbulence.

Problems with the classification

In the discussion above we mentioned already how the temperature derived by RADEX did not fit with our evolutionary classes nor with the kinetic temperatures determined from NH_3(in the case of the peaked clouds). As said before, the errors in the $n_{\rm H_2}$ and $T_{\rm kin}$ estimates is large, since both ratios show similar dependence on $n_{\rm H_2}$ and $T_{\rm kin}$ for a large part of the parameter space. The uncertainty in the HCO^+ column density is an additional source of error. We could not determine this column density, as was possible for N_2H^+ because of its hyperfine structure, and therefore we only assumed it to be the same as N_2H^+. There are some other, more serious problems. The diffuse clouds are strongly under-represented in several studies in this chapter, because there are few detections since the lines are often weak. For the higher transitions observed with APEX most diffuse sources were not detected. This can be solved by re-observing these sources employing longer integration times. Additionally, as there are only three clumps found in the diffuse clouds, they have very few data points in the plots with clump sizes or hydrogen column densities $N_{\rm H_2}$ (for example 3.17, 3.19). In these plots, the clumps of the multiply peaked clouds are not well confined; they span a very wide range in column densities. It is understandable, since clumps within one cloud will be in different evolutionary stages, but the large overlap of clumps in multiply peaked clouds with the other classes makes distinction more difficult. The difference between the more evolved multiply peaked clouds is usually visible in the average quantities.

3.4.3 Starless and prestellar clumps and sources

Motte et al. (2007) showed how difficult it is to find the high mass analogies of low-mass starless cores such as L1521F (Shinnaga et al. 2004). In their study of the Cygnus X complex, they found SiO emission in all of the observed infrared-quiet massive dense cores, indicating that star-formation is already ongoing.

In the end of Sect. 3.3.4, several prestellar clumps and starless clouds were defined as clumps without any indications of YSOs and that show no infall in the HCO^+(1–0) line profile. In four of

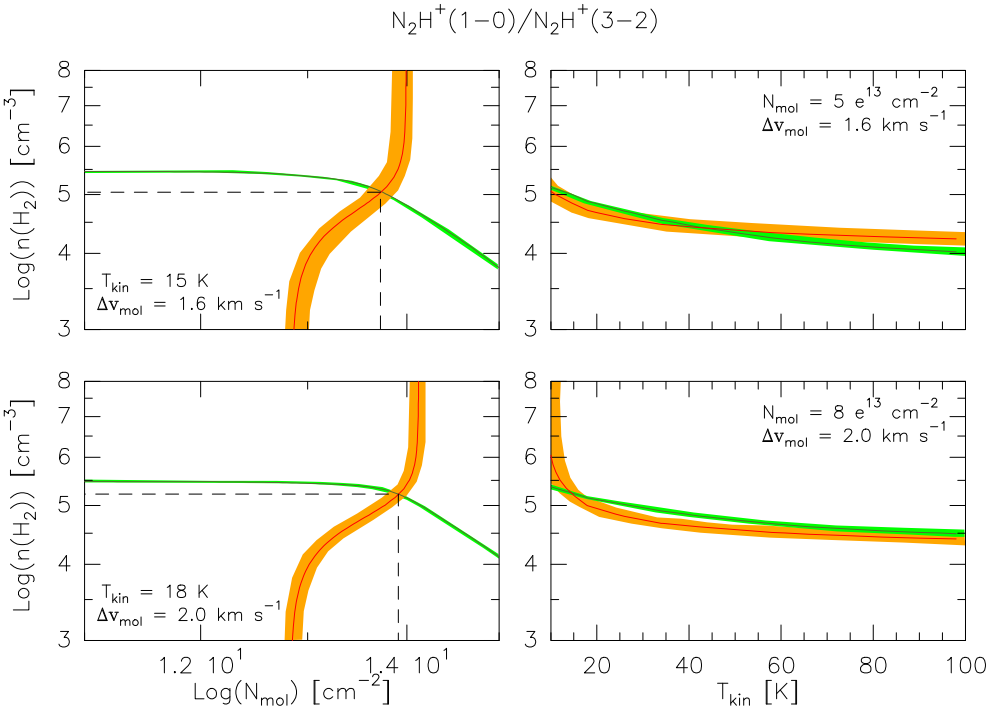

Figure 3.24: The N_2H^+(1–0)/N_2H^+(3–2) ratio as a function of column density and volume density (*left*) and kinetic temperature and volume density (*right*) shown for two classes of clouds: the peaked (*top graphs*) and the multiply peaked clouds (*bottom graphs*). In dark green the average observed ratio of the class is plotted with the dispersion in sample shown in light-green, the red line indicates the average observed opacity of the class with the dispersion of the sample shown in orange. The intersection of the ratio and opacity in the left graphs yielded the N_2H^+ column density of the class, which was used to make the right graphs. $N_{\rm mol}$ represents the column density of the molecule, here N_2H^+, and $\Delta v_{\rm mol}$ the line width.

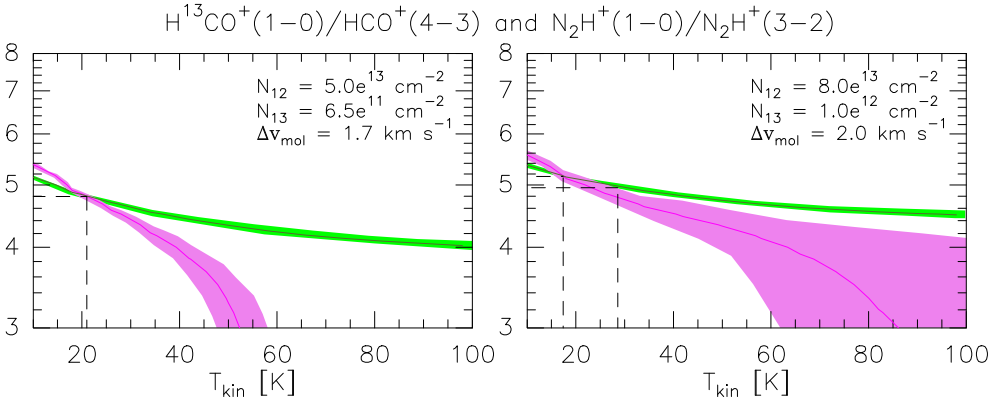

Figure 3.25: Both the N_2H^+(1–0)/N_2H^+(3–2) (dark green) and the $H^{13}CO^+$(1–0)/HCO^+(4–3) ratio (violet) plotted with their respective dispersions in light-green and lilac, as a function of kinetic temperature and volume density. The intersection is marked with black dashed lines. The left graph is for the peaked clouds, and the multiply peaked clouds are shown in the right plot. The used column densities for N_2H^+ and HCO^+ are given by N_{12} and the $H^{13}CO^+$ column density is given by N_{13}. $\Delta v_{\rm mol}$ is the line width used for all the transitions.

our six starless sources (G012.73–00.58 MM1, G024.61–00.33 MM2, G037.44+00.14 MM1 & MM2, and G050.06+00.06 MM1 & MM2) clumps were found in the 1.2 mm emission for which masses

and column densities were determined. All four have $N_{\rm H_2} \sim 3-4 \times^{22}$ cm^{-2}, masses ranging from 12 to 233 $M_\odot$ and rotational temperatures between 10–15 K. All six are dark in the 24 μm MIPS images, but G053.81–00.00 MM2 lies between two IR sources. While three are found in diffuse clouds, two are found in a peaked cloud and one is found in a multiply peaked cloud.

Six sources without any YSO evidence, but which were showing infall profiles, were named "prestellar" sources (G013.97–00.45 MM1, G014.39–00.75A MM2, G014.39–00.75B MM3, G016.93+00.24 MM1, G030.90+00.00 MM2 and G034.77–00.81 MM1). Only half of these sources contained a clump, most of them were too diffuse in the mm continuum meaning that also no masses and column densities could be determined. The three clumps have $N_{\rm H_2} \sim 5 \times^{22}$ cm^{-2}. From the MIPS images we found that half of these sources are very close to IR bright emission and that their temperatures lie between 15–20 K. All these sources are found in the diffuse and multiply peaked clouds. The virial masses for the clumps among the prestellar sources were all lighter than the clump masses determined from the mm continuum, which is an indication of gravity as the dominant force. But, also for the starless sources, the virial parameter is also pointing to gravitationally dominated clumps. Therefore it is not merely the lack of gravitational force which separates the starless from the prestellar clumps.

Since in the prestellar case, there are more infrared sources in the vicinity of the clump, these can possibly be the driving force for continuing the gravitational accretion to surpass the column densities of $3-4\times^{22}$ cm^{-2}. This implies that "stars form close to other stars" which is a well-known fact and agrees with the observed clustering of stars (see, for example, Lada & Lada 2003). The limited number of both starless and prestellar sources, compared to the 32 sources with a YSO indication, agrees with the findings of Motte et al. (2007) that the starless and prestellar phases are short and dynamic.

3.5 Summary

We performed spectral observations of several molecules using the IRAM 30m and the APEX telescopes toward a sample of high extinction clouds in various evolutionary stages. The skewness parameter was used to classify sources based on their line profiles as infall sources or outflow/expanding sources. The HCO^+(1–0) and ^{12}CO(3–2) lines were found to be more sensitive to infall and outflow than the HCO^+(4–3) line, which is possibly due to small optical depth of HCO^+(4–3) at low densities ($n_{\rm H_2} < 10^4$ cm^{-3}). Only the HCO^+(1–0) and ^{12}CO(2–1) line profiles showed a significant excess of infall sources. But, since the ^{12}CO(2–1) emission has a larger uncertainty due the off-position and confusion, the HCO^+(1–0) line profile was found to be most effective line to investigate infall profiles. In Fig. 3.18 the clumps with SiO are plotted against the skewness parameter δv, sources with $\delta v < -0.25$ have an infall signature. SiO emission, which is thought to be a tracer of shocked regions, was found be predominantly detected toward sources with infall. Such a finding is consistent for a scenario in which accretion is accompanied with collimated outflows that lead to an enhancement of SiO.

Between the three cloud classes, the peaked clouds had a significantly high excess of infall sources, while for the other classes no significant excess was found. Possibly the infall-phase is longer for the peaked clouds than in the other clouds, and therefore more easy to detect. Or maybe the infall phase has not begun in most diffuse clouds yet, and already has come to an end in some of the clumps of the multiply peaked clouds. The infall velocities, and mass infall rates, which were calculated from the spectral line shapes, showed a increasing behavior from the diffuse, peaked to the multiply peaked clouds. The mass infall rates were between 0.6 and 9.7 $M_\odot$ yr^{-1}.

From RADEX calculations we found that the ratio of the N_2H^+(1–0) to N_2H^+(3–2) integrated intensity is sensitive to volume density and can be used together with the optical depth to give good estimates of the intrinsic column density. Combining this with $H^{13}CO^+$(1–0) to HCO^+(4–3) ratio did not result in good temperatures, since the a good value for the HCO^+ column density and optical depth could not be determined. Apart from the ammonia rotational temperatures, which were determined in the previous chapter, we added several other temperature estimates in this chapter. All estimates converge one a temperature range between 10 and 40 K, where the upper level is determined by CH_3CN, a molecules usually found in hot cores and UCHII regions.

Since most temperature methods probe slightly different parts of the gas, we find that our clouds are *generally* cold. Similarly, various density estimates place the density in the order of $10^5\,\mathrm{cm}^{-3}$.

For a YSO search in the clumps of the extinction clouds, we utilized emission of CH_3CN, H_2CO and the presence of $24\,\mu$m MIPS sources. Most of the YSO are found in the multiply peaked clouds, a few was also found peaked clouds, but almost none was present in diffuse clouds. The presence of YSO does not depend on the physical size of the clump, since YSOs are found over a large of clump diameters. However, there seems to be (hydrogen) column density cutoff at $4 \times 10^{22}\,\mathrm{cm}^{-2}$ below which few or no YSOs are found. The cutoff is most clear in the H_2CO emission and least in the detection of $24\,\mu$m MIPS sources. We found that the few prestellar clumps, sources which showed no evidence for a YSO but did have infall signatures, in our sample were often located close to a infrared bright source. Possibly these infrared bright sources are the first driving mechanism for the accretion to start. The starless clumps (also few in number) were usually in an infrared dark environment. The limited number of these very early phases compared to the large number of sources with YSOs, shows that the starless and prestellar phases are very short which was also found in previous studies.

CHAPTER 4

Imaging the high extinction cloud G017.19+00.81

The G017.19+00.81 cloud is situated at the north-east edge of the bright HII region M16, the Eagle nebula (Fig. 4.1), and was, despite its proximity to this famous target, not studied before. Most studies of massive star formation in this region have focused on the prominent "Pillars of Creation" in the south (Fig. 1.1). Our new results show, that we found new massive star forming clumps in an early stage of evolution, and whose creation might be linked to the ongoing star formation in the M16 complex.

The G017.19+00.81 molecular cloud contains four massive ($M \geq 40\,M_\odot$) clumps (MM1 – MM4) which have relatively low temperatures between 17–20 K (rotational temperature from NH_3). The kinematic distances to these clumps are between 2.2–2.5 kpc, which proves the connection with the M16 nebula at 2.0 ± 0.1 kpc (Hillenbrand et al. 1993). For the rest of this chapter we assume a distance of 2.3 kpc toward all the clumps in cloud G017.19+00.81. The large scale structure of this cloud is very special: it consists of two arcs, one infrared dark in the north and an infrared bright arc in the south. Together they form a kind of annulus surrounding the central clump (top right panel in Fig. 4.1). This geometry is suggestive of a swept up dust shell caused by an central HII region. In the "collect and collapse" model of Deharveng et al. (2005) and Zavagno et al. (2006) such a shell is formed during the supersonic expansion of an HII region into its surrounding medium, where material is compressed between the ionization and shock front. In this compressed material can, in time, evolve gravitationally bound objects, which collapse to form stars. However, no radio emission, reminiscent of the free-free emission of the HII region was detected either in the 90 cm GPS survey (Brogan et al. 2006), the 20 cm MAGPIS survey (Helfand et al. 2006), the 21 cm VLA survey (Condon et al. 1998), or in the 6 cm Parkes survey (Haynes et al. 1979) – the object was not observed in the 5 GHz VLA survey by (Becker et al. 1994).

The continuum and molecular line observations of this cloud, described in the previous chapters, revealed several pieces of information, apart from the already mentioned temperature and mass. Several evidences of YSOs such as the detection of CH_3CN and H_2CO emission, and the presence of outflows by detection of SiO have been found toward all clumps except MM4. The HCO^+(1–0) line profiles tell that two clumps, MM1 and MM4, the central and the southern clump, have outflows, while the northern two, MM2 and MM3, show infall profiles. Figure 4.2 shows that MM1, MM2 and MM3 have very broad ^{12}CO(2–1) line widths of 23–30 km s^{-1}, showing that the low density

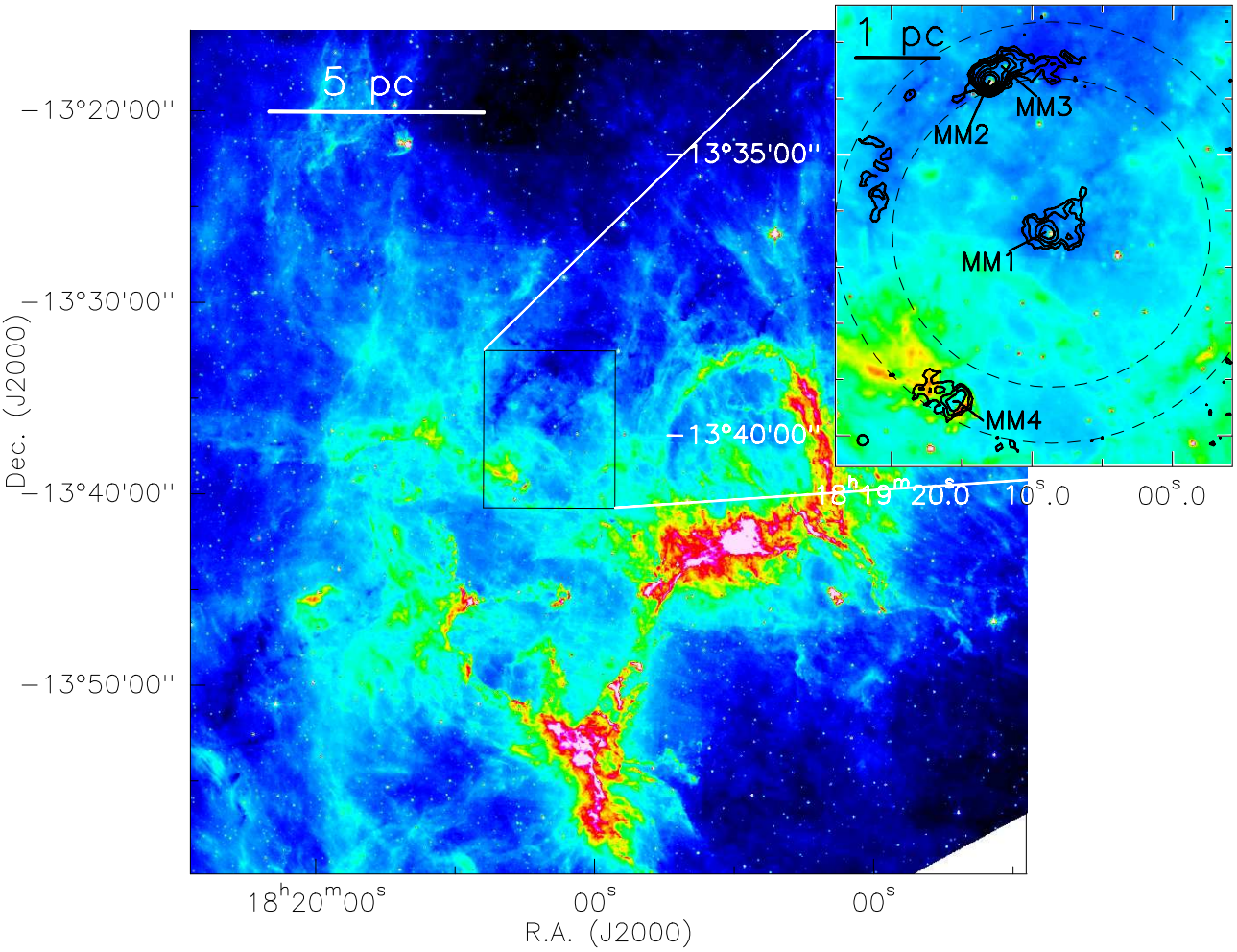

Figure 4.1: The Eagle nebula (M16) in the GLIMPSE 8.0 μm emission. The cutout box shows the location of G017.19+00.81 to the north of the "pillars of creation", which are located at $\alpha = 18^h19^m30^s$ and δ=−13°45′. Cloud G017.19+00.81 is blown up in the top right corner overlaid with the 1.2 mm continuum emission. The dashed lines serve to accentuate the possible ring-like structure. MM2 and MM3 are located in the infrared dark arc, while MM4 is close an infrared bright HII region, and the south-western part of the arc also shows infrared emission.

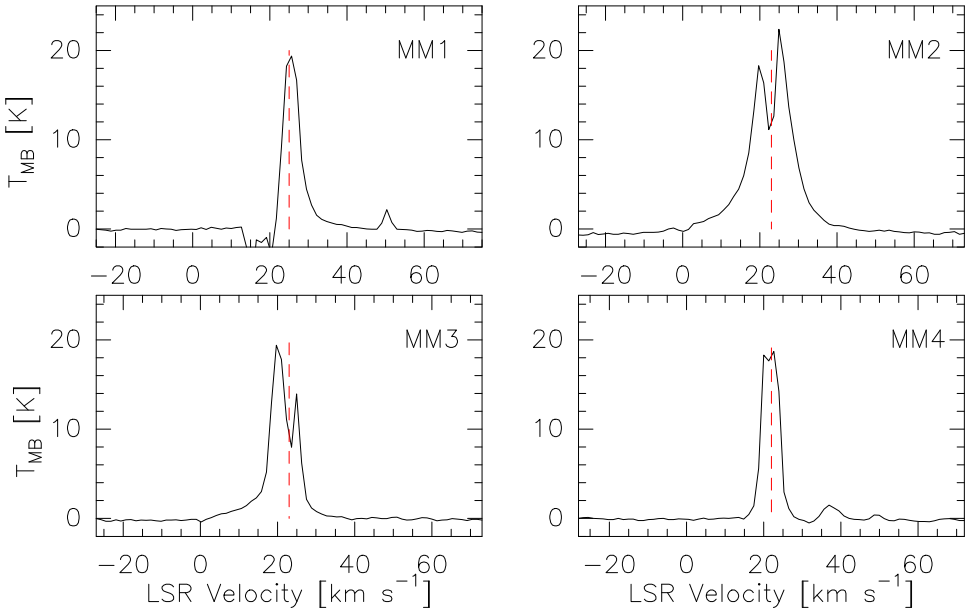

Figure 4.2: ^{12}CO(2–1) spectra observed with the 30m telescope using single pointings toward the clumps in cloud G017.19+00.81. The red dashed line indicates the $v_{\rm LSR}$ of the clump.

material traced by this molecule is pushed outward – possibly by the outflows driven by the YSO(s) inside the clump. The MM2 clump stands out by its high column density $N_{\rm H_2} = 17 \times 10^{22}\,{\rm cm}^{-2}$, the detection of water masers, and a high level of CO depletion – similar to values found in IRDC clumps (Pillai et al. 2007). Clump MM2 is one of the four clumps in the entire sample of studied high extinction clouds with large enough column density to theoretically form high-mass stars (Krumholz & McKee 2008).

Given the interesting large scale structure of the cloud, and the evidence for outflows and infall toward its clumps, we decided to improve our understanding of its kinematics and structure. By imaging the clumps with the IRAM 30m telescope ($\sim 11''$ resolution at 230 GHz) and the SMA ($\sim 7''$ resolution at 225 GHz) we had to access to information on various size scales. To probe the low-density material, the ^{12}CO(2–1) line and several isotopologues of CO were observed. Additionally, we made maps with the IRAM 30m telescope in HCO$^+$(1–0) emission, since the HCO$^+$(1–0) line profile is sensitive to infall and outflows. To have an indication of the relative ages of the clumps, we imaged the N_2H^+(1–0) line. The comparison of the correlation with the continuum emission of this high density tracer and a depletion sensitive molecule such as C^{18}O can work like a time marker in the evolution of a clump. The interferometer observation spanned a wide range in frequencies, containing several molecules associated with hot cores such as methanol, OCS and HNCO (Sutton et al. 1985; Wyrowski et al. 1999; Zinchenko et al. 2000). Also the SO molecule, which is thought to arise in shocked regions (Pineau des Forets et al. 1993) was observed simultaneously. Additionally, also methanol emission is enhanced in shocks (Jiménez-Serra et al. 2005).

The following section describes the observations and the data reduction. The imaging results of the IRAM 30m telescope are presented in Sect. 4.2 and discussed briefly in Sect. 4.3. The results SMA maps are given in Sect. 4.4 and followed by a short discussion. The whole chapter is summarized in Sect. 4.6.

Table 4.1: Molecular lines and their frequencies

molecule	$J+1 \rightarrow J$	Frequency (GHz)	BW (MHz)	Resolution (km s^{-1})	Beam[a] ($''$, $''$, $^\circ$)	$n_{\rm crit}$[b] (cm^{-3})	Beff	Feff
			IRAM 30m telescope					
HCO^+	1–0	89.2	40	0.08	28, 28, 0	1.8×10^5	0.78	0.98
N_2H^+	1–0	93.2	40	0.08	27, 27, 0	1.6×10^5	0.78	0.98
$C^{18}O$	2–1	219.6	512	1.5	11.8, 11.8, 0	9.2×10^3	0.62	0.94
^{12}CO	2–1	230.5	512	1.5	11, 11, 0	1.1×10^4	0.58	0.92
			SMA					
$C^{18}O$	2–1	219.6	1000	0.5	7.3, 6.8, 9.3[c]	9.2×10^3	-	-
SO	5_6–4_5	219.9	1000	0.5	7.2, 6.1, 6.0[c]	3.5×10^{6}[d]	-	-
^{13}CO	2–1	220.4	1000	0.5	7.2, 6.7, 9.2[c]	9.3×10^3	-	-
CH_3OH	8_{-1}–7_0, E	229.8	1000	0.5	6.9, 5.8, 8.1[c]	8.4×10^6	-	-
^{12}CO	2–1	230.5	1000	0.5	6.9, 5.8, 7.1[c]	1.1×10^4	-	-

[a]Major axis, minor axis and Position Angle (P.A.)
[b]Calculated from the collision rates at $T = 20$ K from the LAMBDA molecular database (Schöier et al. 2005).
[c]Beam size given for clump MM2.
[d]Collision rate for $T = 50$ K.

4.1 Observations and data reduction

4.1.1 Single dish imaging with IRAM 30m

The spectral line images were performed with the IRAM 30m telescope on 2007 July 10 and 11. Using the AB receivers, four spectral lines, HCO^+(1–0), N_2H^+(1–0), $C^{18}O$(2–1), and ^{12}CO(2–1) were observed simultaneously. The frequencies, spectral resolution and telescope efficiencies are listed in Table 4.1. On June 10 the weather was not good and the sky opacities were high, $\tau = 0.10$ at 90 GHz and $\tau = 0.53$ at 230 GHz, however for June 11 we experienced excellent winter weather conditions with a $\tau = 0.04$ at 90 GHz and a $\tau = 0.11$ at 230 GHz. During the observation, the pointing was checked every 1.5 hours on nearby quasars and was found to be accurate within $5''$ on June 10, and $3''$ on June 11. The focus was set on quasar 3C 273 at the beginning of each observation run. We made on the fly maps of $\sim 1' \times 1'$ size toward clumps MM1, MM2 and MM4. Clump MM3 was included in the image of MM2. The maps were made with a step of $6''$, using an integration time of 50 seconds per pointing. The total time per map was $\sim$30 minutes. The step size allowed a good sampling for the beam of ($11.8''$ FWHM) at 230 GHz. Due to a mistake in the observation script the step size clump MM1 was $12''$, similar to the beam at 230 GHz, which resulted in an undersampled map. Therefore the ^{12}CO(2–1) and $C^{18}O$(2–1) maps of this clump were smoothed to improve the sampling.

The main beam brightness temperature was obtained as described in Sect. 3.2. Further data reduction tasks, such as baseline subtraction, smoothing and imaging was done in CLASS90 which is part of the GILDAS software[1].

4.1.2 SMA interferometer maps

The Smithsonian SubMillimeter Array (SMA) consists of 8 antennas of 6 m in diameter and is located on Manua Kea, Hawaii. The interferometric observations of G017.19+00.81 were performed on 2007, September 14, in the subcompact configuration using seven antennas. The projected baselines were between 9.5 and 32 m. The data was recorded in the double side band IFs with a total bandwidth of 4 GHz. The two IFs are separated by 10 GHz and each IF consists of 24 chunks. In our observations chunk s15 of the upper side band was centered on the ^{12}CO(2–1)

[1]http://www.iram.fr/IRAMFR/GILDAS

Table 4.2: SMA pointing positions (J2000)

Pointing	R.A. (h:m:s)	Declination (°:′:″)
MM1	18:19:08.902	–13:36:29.48
MM2	18:19:12.390	–13:33:36.92
MM4	18:19:15:439	–13:39:29.61

line (230.53 GHz) resulting in a range of $\nu = 219.4 - 221.4$ GHz for the lower side band and $229.3 - 231.3$ GHz for the upper side band. The spectral resolution was $\sim$0.5 km s^{-1}. An overview of the observed molecular lines is given in Table 4.1. We observed the four clumps MM1, MM2, MM3, and MM4 in cloud G017.19+00.81. These clumps were observed in three pointings (MM2 and MM3 were observed in one pointing) listed in Table 4.2, they were part of a loop which included two gain calibrators, quasars J1833–210 and J1733–130. Uranus was used to calibrate the flux scale and the passband. Based on the documented flux of J1733–130 at 1 mm with the SMA closest to our observations, which was 1.79 ± 0.15 Jy on 2007, September 7, the flux calibration of both the lower and upper side band were found to be accurate with the error bar of 0.15 Jy, with integrated fluxes of, respectively, 1.72 Jy and 1.81 Jy. At the mean frequency of the two side bands, the field of view was 55″ and the synthesized beam size was $\sim$7″(see also Table 4.1), which translates, respectively, into 0.61 pc and 0.08 pc at a distance of 2.3 kpc. The whole calibration, the data weighting with the system temperature, the flux, bandpass, and phase calibration were done in MIR[2], which is a dedicated software package to reduce SMA data.

Afterwards, the data was exported to Miriad[3] (an image and calibration software for interferometric data) for further reduction. The outer 30 channels of each chunk or spectral window were flagged in all datasets. The calibrators were imaged to check their compactness and flux. Figure 4.3 shows images of the lower and upper side band data for J1733−130 and J1833−230. Both quasars are unresolved and compact.

To retrieve the continuum data for the sources, the channels containing spectral lines were flagged. For all clumps, the continuum was found to have an extended structure. The data were phase self-calibrated to improve the image quality and the retrieved flux, and imaged using a natural weighting scheme for maximum sensitivity. We did one or two cycles of self calibration. The position shift due to self calibration was checked and found to be less then 2″. The spectral line data were first split into smaller spectral line blocks. Then the continuum was subtracted and the rest frequency of the spectral line was inserted in the header. The lines whose emission was extended, such as ^{13}CO(2–1) and C^{18}O(2–1) lines, were imaged with a natural weighting scheme. We used the clean algorithm to get the initial model of the emission, and then used the maximum entropy algorithm with this model to deconvolve the beam pattern from the image. Since C^{18}O was also imaged with the 30m telescope, we combined the single dish and interferometric maps to improve the image sensitivity to extended structure. For compact line emission, such as from SO and CH_3OH, we used a weighting with robust parameter of 0, and used only the clean algorithm to obtain the deconvolved image.

4.2 Results from the single dish maps

4.2.1 Infall signature in HCO$^+$(1–0)

The infall signatures from the HCO$^+$(1–0) line profile as discussed in Sect 3.3.1 were based on a single pointing. Aside from infalling material on the clump, such a line profile can also be caused by large scale motions. Single dish HCO$^+$(1–0) maps allow to differentiate between the two scenarios. In Sect. 3.3.1 we found that clump MM1 and MM4 showed an outflow and MM2 and MM3 showed

[2]http://www.cfa.harvard.edu/ cqi/mircook.html
[3]http://bima.astro.umd.edu/miriad/

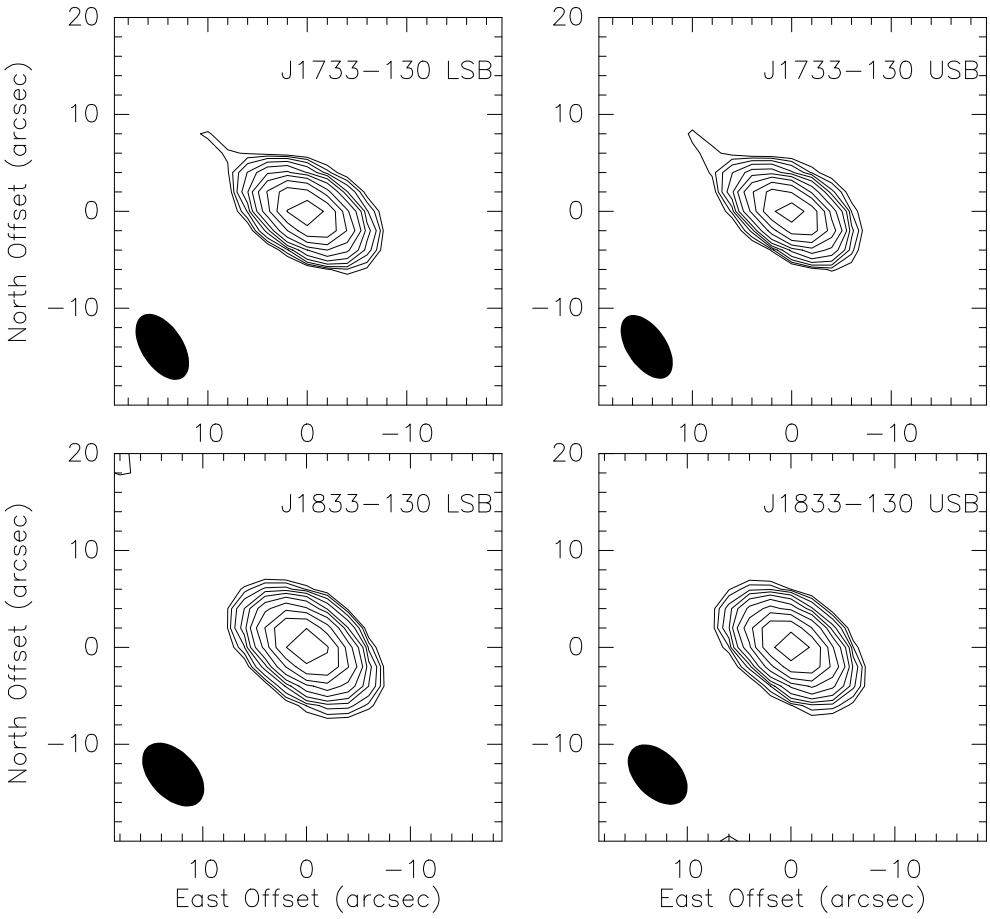

Figure 4.3: Continuum maps of the two phase calibrators used in the SMA observations. The images are centered at the positional coordinates of both quasars: α=17$^{\rm h}$:33$^{\rm m}$:02$^{\rm s}$.7, δ=−13°:04′:49.″54 for J1733–130, and α=18$^{\rm h}$:33$^{\rm m}$:39$^{\rm s}$.9, δ=−21°:03′:40.″21 for J1833–230. The contours at 0.029 mJy and increase by factors of $\sqrt{2}$.

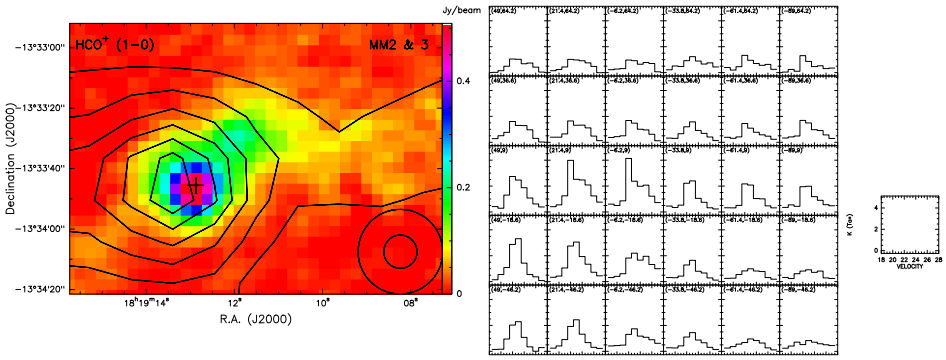

Figure 4.4: *Left:* Integrated HCO^+(1–0) intensity image of clumps MM2 and MM3 (white contours), observed with the 30m telescope, overlaid on the 1.2 mm continuum. The cross marks the center position at α=18^h:19^m:12^s.88, $\delta = -13°$: 33: 45.″6. At a distance of 2.3 kpc, 20″ correspond to 0.22 pc. *Right:* HCO^+(1–0) spectra of the region shown in the left image. The offset (in arcsec), with respect to the center position in the left image, is given in the upper left corner of each spectrum.

signs of infall. Figure 4.4 shows the integrated emission of the HCO^+(1–0) line and spectra for MM2 and MM3. The HCO^+ emission peak is offset to the east with respect to the continuum peak of clump MM2. Toward the HCO^+ peak the spectrum is double peaked with an enhanced blue peak, reminiscent of infall. In the remaining part of the cloud the line profile is single peaked, and showing no clear infall profile. It is very likely that the HCO^+(1–0) line signature results from infalling material near clump MM2. Near the second clump, MM3, there is no evident infall to be inferred from the HCO^+(1–0) spectra, there are, however, a few spectra in the top right of that map which show a slightly blue shifted emission peak.

For the clumps with an outflow signature in the HCO^+(1–0) line profile, MM1 and MM4, the integrated intensity and spectra are shown in Figure 4.5. The HCO^+(1–0) spectrum is redshifted toward the peak in the HCO^+ emission for clump MM1. The remaining part of the spectra shows no red (or blue) shifted peaks, and therefore the outflow, or expansion is associated with the clump itself. On the contrary for clump MM4, where the spectrum is changing across the map; roughly, the north-eastern part has more blue shifted spectra, while the south-western part has more redshifted ones. Likely, this is an indication for a large scale motion along the northeast-southwest axis.

4.2.2 Outflows

Similar to the infall behavior, the outflow can also be either associated to the clump or arising due to large scale motions. Figure 4.2 shows the single dish ^{12}CO(2–1) spectra toward the continuum peaks of the clumps. The line widths of MM2, MM3 and the red part of MM1 show that there is material emitting at high velocities – likely due to an outflow. However, the rather narrow line width of MM4 seems to indicate an absence of an outflow. The single dish ^{12}CO map of MM4 (Fig. 4.6) shows indeed large scale motion along a northeast-southwest axis, which is also present in the HCO^+(1–0) spectra (Fig. 4.5). The MM4 channel map (Fig. 4.6) shows that the ^{12}CO line is narrow, between 17 and 25 km s^{-1}. The blue emission peaks near the HII region at α =18^h 19^m 16.^{s}3, δ =−13° 39′ 10″, while the red emission peaks toward the southern part of the MM4 clump. We interpret the ^{12}CO emission as a result of a large scale motion likely triggered by the HII region.

Clump MM2 is an example of a localized outflow, showing a red and a blue lobe, originating close to the mm continuum peak (left panel of Fig. 4.7). Toward this clump the single dish ^{12}CO spectrum revealed very wide wings (Fig. 4.2), which is a strong indication of an outflow. In the single dish channel maps (right panel of Fig. 4.7) the broad line wings are observed to be located in blue and red lobes, and not in a large scale structure. Over a range of ±12 km s^{-1} from the central line velocity at 23 km s^{-1} one can still see emission in red and blue lobes. Interestingly,

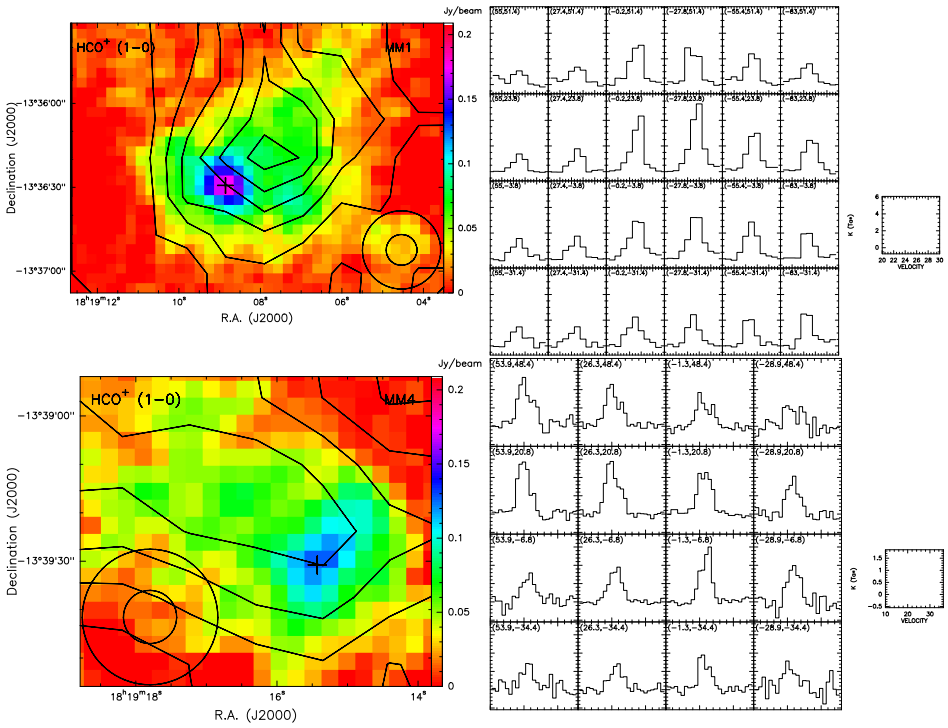

Figure 4.5: *Left:* Integrated HCO^+(1–0) intensity image of clumps MM1 (*top*) and MM4 (*bottom*) (white contours), observed with the 30m telescope, overlaid on the 1.2 mm continuum. The crosses mark the center positions of MM1 at α=18^h:19^m:$08\overset{s}{.}86$, $\delta = -13°$: 36: $29\overset{''}{.}4$ and MM4 at α=18^h:19^m:$15\overset{s}{.}43$, $\delta = -13°$: 39: $30\overset{''}{.}8$. At a distance of 2.3 kpc, 20″ correspond to 0.22 pc. *Right:* HCO^+(1–0) spectra of the region shown in the left image. The offset (in arcsec), with respect to the center position in the left image, is given in the upper left corner of each spectrum.

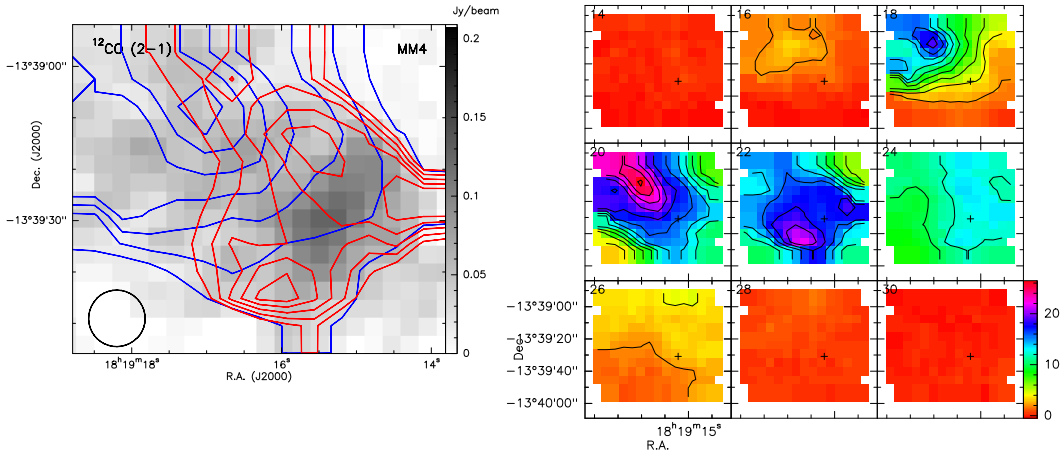

Figure 4.6: *Left:* ^{12}CO(2–1) integrated intensity map for clump MM4 with velocities [16, 22] km s^{-1} in blue and velocities [22, 27] km s^{-1} in red. At a distance of 2.3 kpc, 20″ correspond to 0.22 pc. *Right:* Channel map for clump MM4 in ^{12}CO(2–1) emission between [14,31] km s^{-1} in steps of 2 km s^{-1}. Map units are K km s^{-1}. The clump has a $v_{\rm LSR}$ of 22 km s^{-1}.

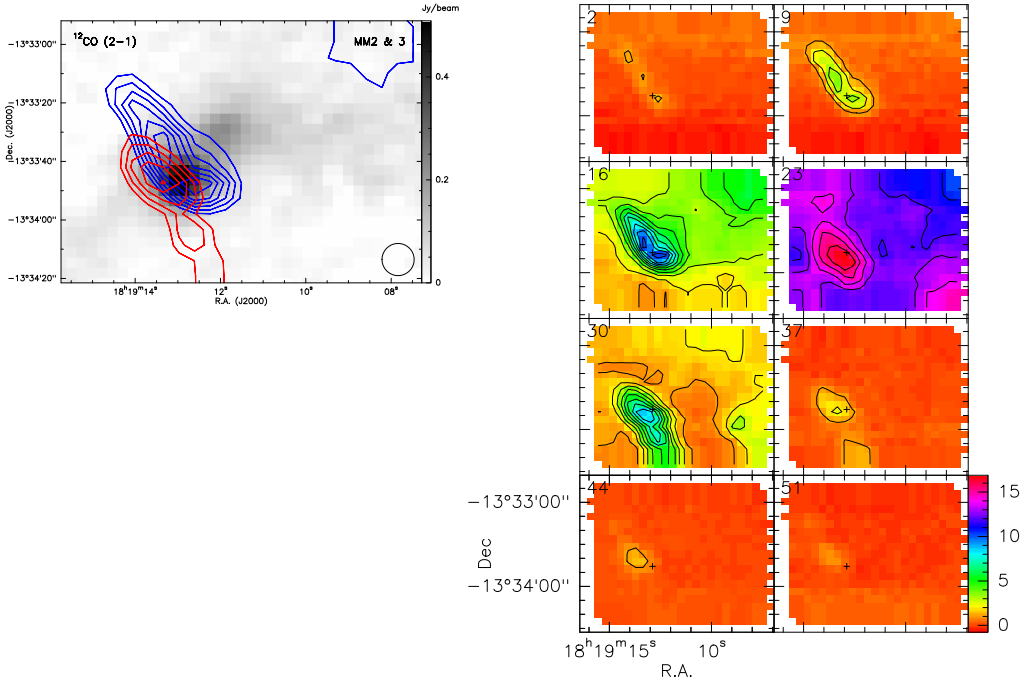

Figure 4.7: *Left:* ^{12}CO(2–1) integrated intensity map for clumps MM2 and MM3 with velocities [−8, 19] km s^{-1} in blue and velocities [27, 54] km s^{-1} in red. The contour levels start at 45 K km s^{-1} and increase with steps of 10 K km s^{-1}. At a distance of 2.3 kpc, 20″ correspond to 0.22 pc. *Right:* Channel map for clumps MM2 and MM3 in ^{12}CO(2–1) emission between [2, 54] km s^{-1} in steps of 7 km s^{-1}. Map units are K km s^{-1}. At the $v_{\rm LSR}$ of 23 km s^{-1} the ^{12}CO emission is all above 12 K.

clump MM2 shows not only a high velocity outflow, but also collapse, detected by the infall profile of the HCO$^+$(1–0) line (see Sect. 3.3.1). No high velocity ^{12}CO emission was found toward the adjacent clump MM3.

Clump MM1 is a complex case, where the single dish channel maps (left panel of Fig. 4.8) show that the blue part of the line profile only emits southeast of the mm emission, while the red line profile is very wide and concentrated on the peak of the mm continuum. The red line wing is broader then the blue one, which was already known from the single dish spectra (Fig. 4.2). The right panel of Fig.4.8 shows maps integrated over the red and blue wings. The difference in strength of the blue and the red wing is evident. The blue emission has little structure and no clear peak, even though the red emission is strong and peaked near the continuum peak. Therefore, the ^{12}CO emission can be a localized outflow from clump MM1, where the blue cone is, possibly due to a geometrical reasons, smeared out. Alternatively, there can be a large movement on a southeast to northwest axis.

4.2.3 Correlation of N_2H^+(1–0) and $C^{18}O$(2–1) with the mm continuum

Purcell et al. (2009) showed that for massive star-forming clumps, the C^{18}O(2–1) emission is more extended than the dust continuum emission, while the N$_2$H$^+$(1–0) emission follows well the continuum. N$_2$H$^+$ is a late-type molecule (Aikawa et al. 2003), since it is formed from molecular nitrogen, which first has to be formed from atomic nitrogen. Therefore, it is found only in very dense clumps with gravitational infall which already had the time for the chemistry to create N$_2$H$^+$ (Aikawa et al. 2003). The C^{18}O(2–1) line is often found to be depleted in dense clumps (Bergin & Langer 1997; Pillai et al. 2007), where the continuum and N$_2$H$^+$ actually show peaks. However in earlier stages, the depletion of C^{18}O should be still limited (Tafalla & Santiago 2004). Therefore, one might use the level of correlation of these two molecules with the continuum as a time marker.

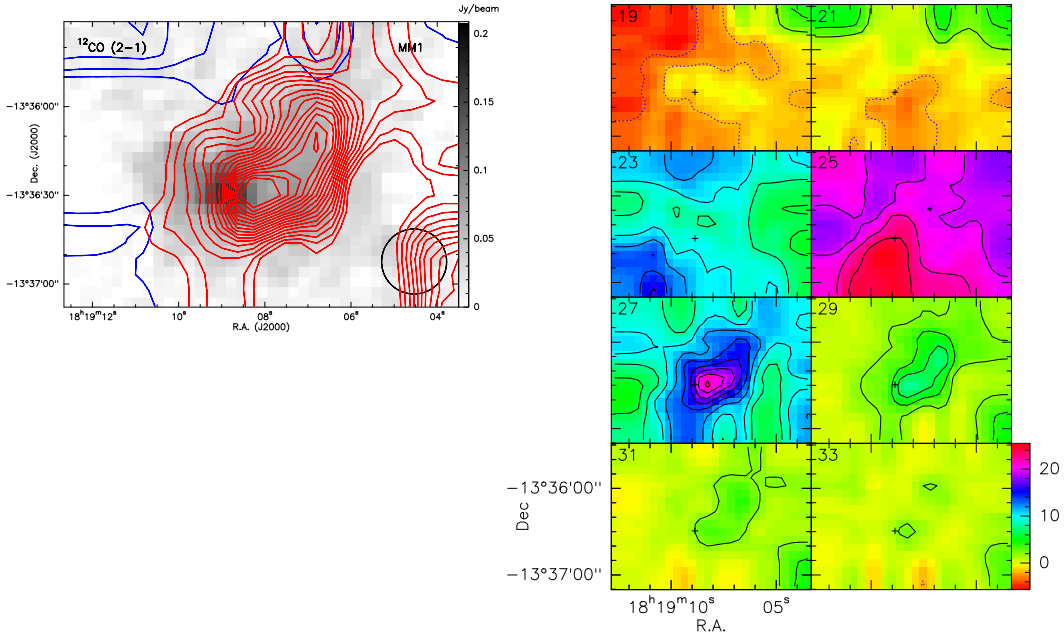

Figure 4.8: *Left:* ^{12}CO(2–1) integrated intensity map for clump MM1 with velocities [19, 23] km s^{-1} in blue and velocities [23, 32] km s^{-1} in red. The contour levels start at 17 K km s^{-1} and increase with steps of 2 K km s^{-1}. At a distance of 2.3 kpc, 20″ correspond to 0.22 pc. *Right:* Channel map for clump MM1 in ^{12}CO(2–1) emission between [19, 34] km s^{-1} in steps of 2 km s^{-1}. Map units are K km s^{-1}. The $v_{\rm LSR}$ of this clump is 25 km s^{-1}.

To correlate the mm continuum maps with the spectral line maps, they were reprojected using the spectral line as a template to have the same sampling and resolution.

The depletion results from the previous chapter served as a first indication; MM4 has the lowest depletion ($\eta = 0.7$), then with $\eta = 1.5$ follows MM1, then $\eta = 1.8$ of MM3, and finally the most depleted clump is MM2 with $\eta = 5.5$ (see Table C.9).

For clump MM4, which has seen no depletion yet, the integrated intensity maps of both molecules seem to follow the continuum emission (Fig. 4.9). Figure 4.10 shows that both molecules have good correlation with the continuum emission, the correlation of C^{18}O is even better than that of N_2H^+.

For the central clump of G017.19+00.81, MM1, the integrated line maps of N_2H^+(1–0) and C^{18}O(2–1) have some similarities: both have a clear maximum northward of the continuum peak (Fig. 4.11). Further away from this peak the two molecules behave differently, C^{18}O(2–1) seems more extended to the north, while N_2H^+(1–0) weakens as it crosses the border of the continuum emission. The correlation plot in Fig. 4.12 shows that the N_2H^+(1–0) is well correlated with the continuum emssion (top graph). For C^{18}O there seem to be two trends; several points (pixels in the map) are well correlated – they increase simultaneously, but the majority follows a flat linear trend of strong C^{18}O emission where the continuum is weak. We interpret this as two components, one which belongs to the millimeter clump – the low level of depletion of MM1 supports the idea that the C^{18}O is well correlated with the continuum – and a second large scale C^{18}O component. The latter is not correlated with the continuum, as it originates from the large scale low density regions surrounding the mm clump.

For the clumps with the highest depletion, MM2 and MM3, the N_2H^+(1–0) emission is strong and follows the continuum (left panel of Fig. 4.13). The C^{18}O has the same elongated shape as the N_2H^+ and the continuum, and the peak of C^{18}O conicides with the continuum emission peak of MM2. The C^{18}O emission is not peaked toward clump MM3. The C^{18}O emission is less concentrated on the continuum than the N_2H^+ which has a sharp increase of many contour levels near the continuum peak. The correlation plot in Fig. 4.14 confirms this; for C^{18}O only a handful

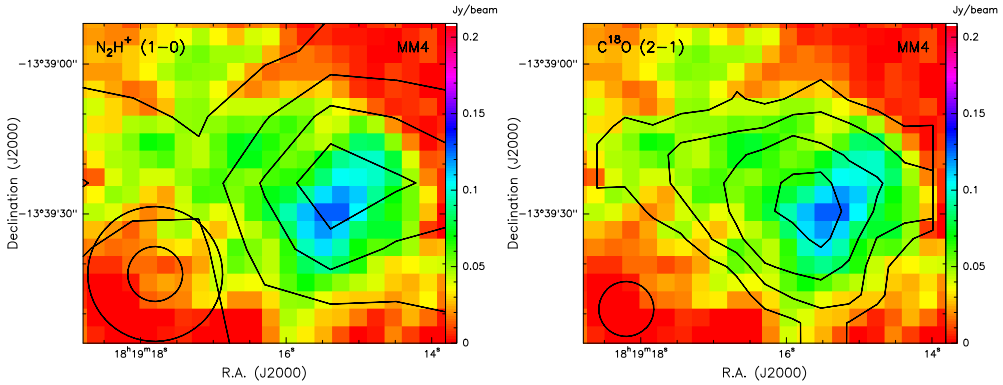

Figure 4.9: N_2H^+(1–0) and $C^{18}O$(2–1) integrated line intensities overlaid on the 1.2 mm emission for clump MM4. At a distance of 2.3 kpc, 20″ correspond to 0.22 pc. Contour levels are 0.5, 1.5 K km s^{-1} further increasing by 1 K km s^{-1} for N_2H^+ and 5, 7, 9 K km s^{-1} further increasing by 2 K km s^{-1} for $C^{18}O$.

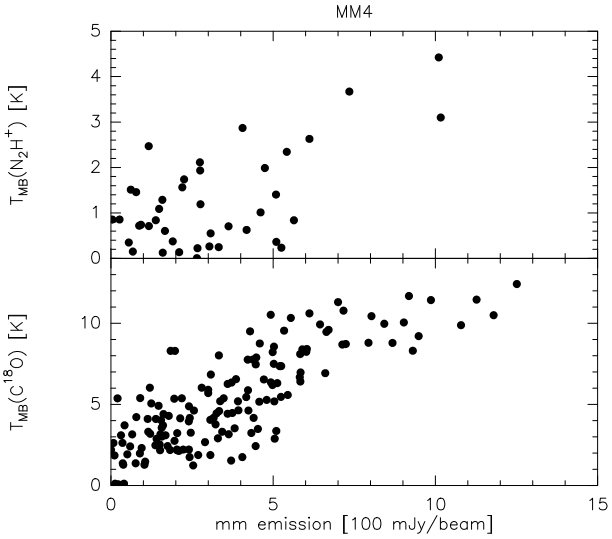

Figure 4.10: Correlation plot of the images of N_2H^+ and $C^{18}O$ with the mm continuum map for clump MM4.

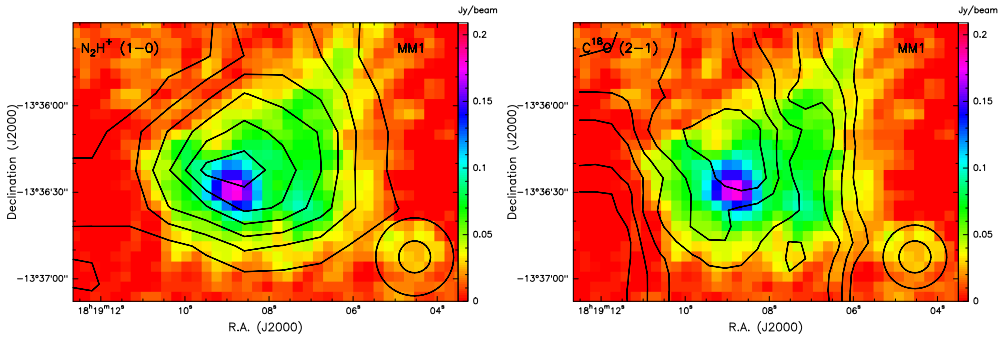

Figure 4.11: N_2H^+(1–0) and $C^{18}O$(2–1) integrated line intensities overlaid on the 1.2 mm emission for clump MM1. At a distance of 2.3 kpc, 20″ correspond to 0.22 pc. Contour levels are 3, 5 K km s^{-1} further increasing by 2 K km s^{-1} for N_2H^+ and 5, 7, 9 K km s^{-1} further increasing by 2 K km s^{-1} for $C^{18}O$.

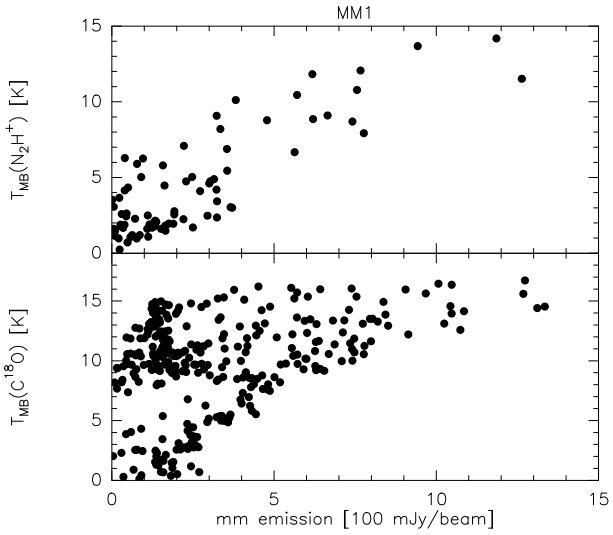

Figure 4.12: Correlation plot of the images of N_2H^+ and $C^{18}O$ with the mm continuum map for clump MM1.

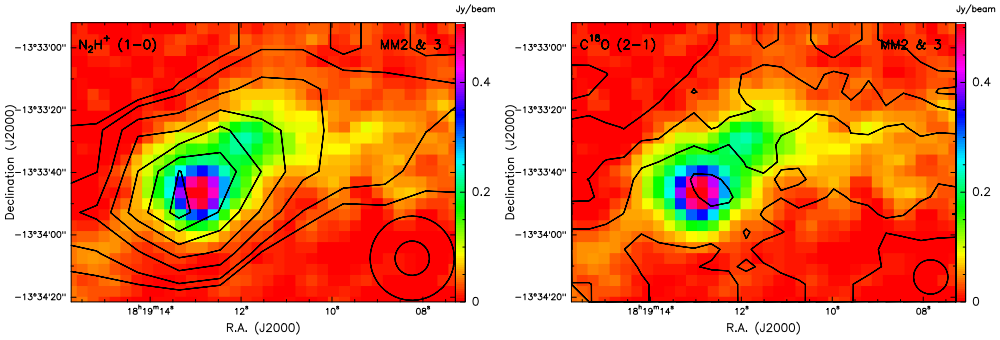

Figure 4.13: N_2H^+(1–0) and $C^{18}O$(2–1) integrated line intensities overlaid on the 1.2 mm emission for clumps MM2 and MM3. At a distance of 2.3 kpc, 20″ correspond to 0.22 pc. Contour levels are 3.6, 5.6 K km s^{-1} further increasing by 4 K km s^{-1} for N_2H^+ and 5, 7 K km s^{-1} further increasing by 2 K km s^{-1} for $C^{18}O$.

of strong intensity pixels correlate with the continuum, but the majority of pixels with a weak continuum emission have strong $C^{18}O$ emission. The N_2H^+ intensity in Fig. 4.14 correlates well with mm continuum emission.

The $C^{18}O$ depletion agrees well with the level of correlation of $C^{18}O$ with the continuum – for the high depletion clump (MM2), $C^{18}O$ does not correlate with the continuum emission, while for the low depletion clump (MM4) the correlation between $C^{18}O$ and the continuum is good. The moderate $C^{18}O$ depleted clump (MM1) sees $C^{18}O$ correlation on larger low density scales, while the toward the dense millimeter clump $C^{18}O$ is not correlated any more with the continuum – it is depleted.

4.3 Discussion of single dish maps

Clump MM4 in cloud G017.19+00.81 has a complex nature. It is located close an HII region (see Fig. 4.1) and contains a 24 μm source. Even though, N_2H^+ has already formed in this clump, there is no sign of $C^{18}O$ depletion and the $C^{18}O$ correlates well with the continuum emission. From the depletion, this clump should be "young", however the 24 μm source in this clump argues against this. Possibly, the heating from the nearby HII region caused the evaporation of CO from

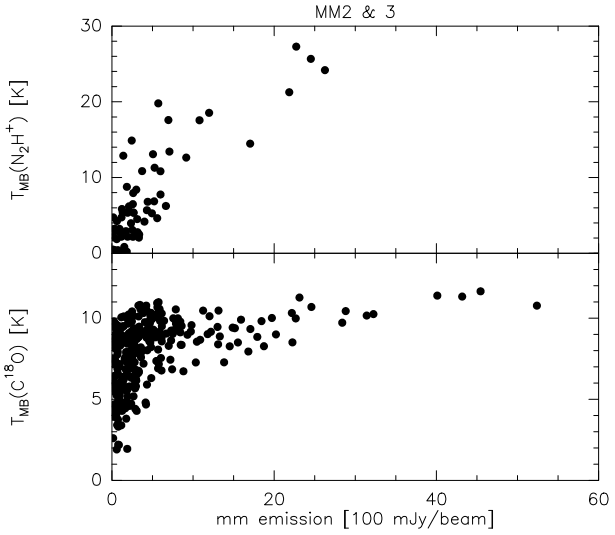

Figure 4.14: Correlation plot of the images of N_2H^+ and $C^{18}O$ with the mm continuum map for clumps MM2 and MM3.

the dust grains, or maybe the relatively high $T_{\rm rot}$ from NH_3 of 20 K is making the CO depletion more difficult. Other evidence for an "early" nature of this clump is the absence of infall in the HCO^+(1–0) line profile and outflows in the ^{12}CO(2–1) line data.

MM1, the centrally located clump, seems more evolved: we have detected a possible outflow in the ^{12}CO(2–1) line along an southeast-northwest axis, even though infall profiles are still absent. The ambivalent correlation of the $C^{18}O$ with the continuum points to still low levels of depletion, however the $C^{18}O$ does not stricktly follow the continuum.

The most evolved clump, located in the northern arc, was MM2. There is clear evidence of infall close to the continuum emission from the HCO^+(1–0) spectra, and a high velocity CO outflow along the southeast-northwest axis is detected. Also, chemically this is the most evolved clump. It has the brightest N_2H^+(1–0) line intensity of all three clumps. The $C^{18}O$ intensity does not follow the continuum emission, which agrees with the measured high level of $C^{18}O$(2–1) depletion toward the continuum clump similar to what is found in clumps in IRDCs (Pillai et al. 2007).

4.4 Results from the SMA maps

With the SMA we observed the clumps simultaneously in two wide frequency ranges of $\nu = 219.4 - 221.4$ GHz and $229.3 - 231.3$ GHz, resulting in, apart from the continuum emission, the detection of several spectral lines. A full spectrum of the SMA data is shown in Fig. 4.15 for clump MM2. Apart from the detected lines, we also marked all strong ($T_{\rm A}^* > 5$ K) transitions found toward Orion A in the molecular line survey of Sutton et al. (1985) which were not detected by our observations. Table 4.3 gives for each clump an overview of the detected lines and summarizes the non-detected lines. As most of the non-detected molecules are often observed toward hot molecular cores (Sutton et al. 1985; Wyrowski et al. 1999; Zinchenko et al. 2000) we conclude that our clumps are in an earlier evolutionary phase.

4.4.1 Dust continuum emission

The 1.3 mm emission mapped with the SMA follows well the structures revealed by the MAMBO bolometer at 1.2 mm. Figures 4.16 show overlays of the dust continuum emission by the SMA and the bolometer. For clumps MM1 and MM4 the interferometric observations show fragmentation into two or three smaller clumps. The SMA resolved the continuum emission of clumps MM2 and MM3 into two separate peaks, which was not possible with the bolometer observations alone. We

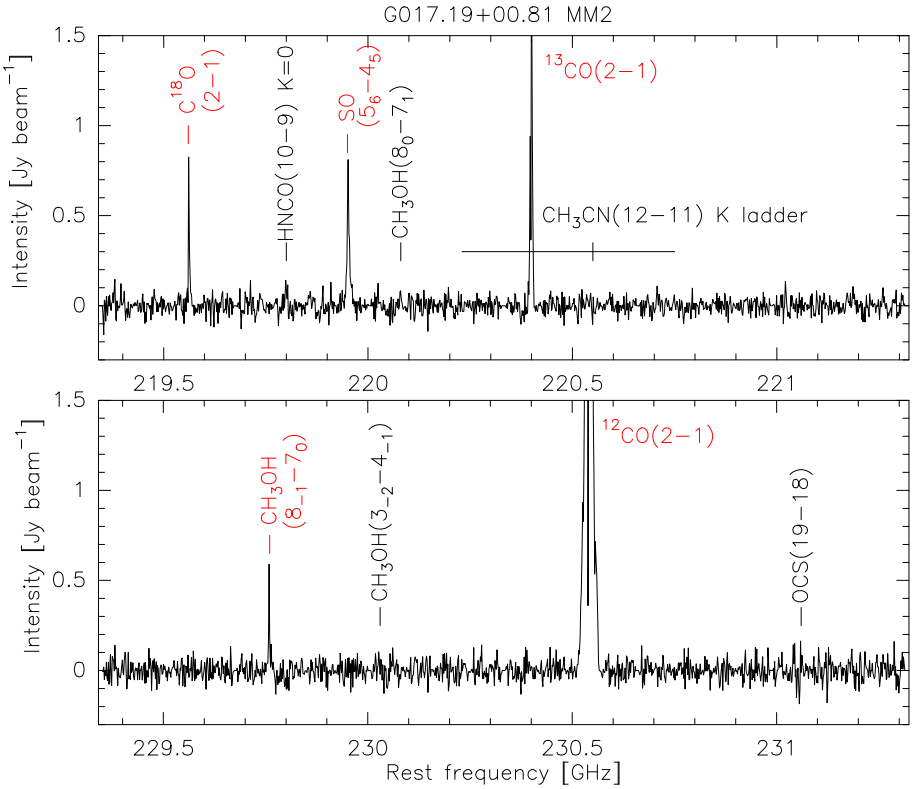

Figure 4.15: Spectra toward clump MM2 with detected lines marked in red and non-detections marked in black.

Table 4.3: Molecular line detections and non-detections

Clump	Detected molecular transitions
MM1a, b	$C^{18}O$(2–1), ^{13}CO(2–1), ^{12}CO(2–1)
MM2	$C^{18}O$(2–1), ^{13}CO(2–1), ^{12}CO(2–1)
MM3	$C^{18}O$(2–1), ^{13}CO(2–1), ^{12}CO(2–1), SO(5_6–4_5), $CH_3OH(8_{-1}–7_0)$
MM4a, b, c	$C^{18}O$(2–1), ^{13}CO(2–1), ^{12}CO(2–1)
	Non-detected moleculer transitions
all	HNCO(10_0–9_0), $CH_3OH(8_0–7_1)$, $CH_3OH(3_{-2}–4_{-1})$,CH_3CN(12–11), OCS(19–18)

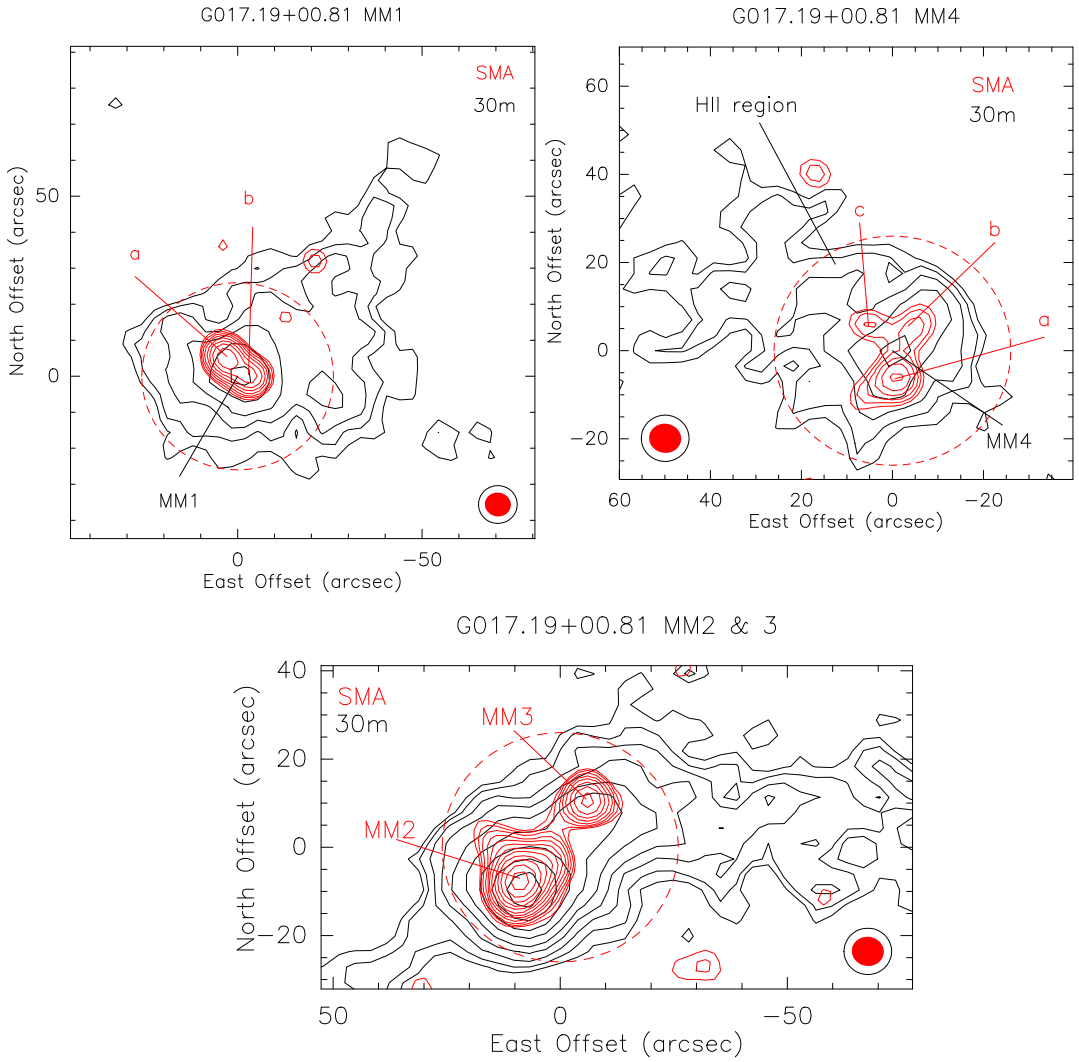

Figure 4.16: Interferometric millimeter continuum maps (red contours) overlaid on the single dish bolometer maps (black contours). The contours start at $2\sqrt{2}\sigma$, where σ is the r.m.s. noise in the map, and increase by factors of $\sqrt{2}$. The noise levels were 2 mJy beam^{-1} for the SMA maps, and 15 mJy beam^{-1} for the bolometer maps. The interferometric beam size is indicated with the red filled circle in the left or right bottom corner, the bolometer beam is indicated by a black circle. The red dashed circle indicates the size of the primary beam of the SMA. Ten arcseconds translate to 0.11 pc at a distance of 2.3 kpc. The center positions are α(J2000)=18$^{\rm h}$:19$^{\rm m}$:08$^{\rm s}$.902, δ(J2000)=−13°:36′:29″.48 for MM1, α(J2000)=18$^{\rm h}$:19$^{\rm m}$:12$^{\rm s}$.390, δ(J2000)=−13°:33′:36″.92 for MM2, and α(J2000)=18$^{\rm h}$:19$^{\rm m}$:15$^{\rm s}$.439, δ(J2000)=−13°:39′:29″.61 for MM4.

Table 4.4: Observed clump properties of cloud G017.19+00.81 from the dust continuum SMA observations

Clump	R.A. (h:m:s)	Dec. (°:′:″)	$F^{p}_{1.3\,\mathrm{mm}}$ (mJy beam^{-1})	$F^{i}_{1.3\,\mathrm{mm}}$ (mJy)	Major axis[a] (″)	Minor axis [a] (″)	P.A. (°)
MM1a	18:19:09.1	–13:36:24	48(3.7)	59	3.7/7.7	2.5/7.4	50
MM1b	18:19:08.7	–13:36:29	33(4.0)	35	2.4/7.4	0.8/6.7	27
MM2	18:19:13.0	–13:33:44	266(2.4)	414	5.4/8.6	4.8/8.4	−27
MM3	18:19:12.0	–13:33:26	66(2.8)	74	3.3/7.4	1.3/7.1	−55
MM4a	18:19:15.4	–13:39:36	24(2.0)	36	5.4/8.6	4.2/8.2	85
MM4b	18:19:15.2	–13:39:24	10(2.1)	16	7.0/9.7	2.4/7.5	−53
MM4c	18:19:15.8	–13:39:24	8(2.5)	8	-/7.0	-/6.5	41

[a]Deconvolved from the beam / not deconvolved from the beam

added for the new fragmented clumps an "a" or "b" to their names resulting in, for example MM1a. Table 4.4 shows the clump properties, such as peak flux, integrated flux and the size, obtained by two-dimensional Gaussian fits to the maps. The SMA peak fluxes are similar to those found from the single dish observations (Table A.3), after correcting for the different beam sizes.

We calculated the masses, column densities, volume densities and physical sizes of the clumps using the method outlined in Sect. 2.5.2 and 2.5.3. In the mass calculation we assumed the rotational temperature of NH_3 as the kinetic temperature. As distance estimate we used the kinematic distance determined by ammonia. The results are given in Table 4.5 together with the masses, column densities and volume densities calculated from the bolometer observations with the 30m telescope.

The masses from the interferometric data are smaller, since a significant part of the large scale emission is lostin the interferometer observations. When one compares the integrated flux of the single dish (see Table A.3) and the SMA, between 70% and 90% of the flux is lost. This is largely due to resolving out of the extended low density mass reservoir surrounding the clumps; the 30m continuum is more extended than that detected with the SMA in Fig. 4.16. The largest flux loss occurred for MM3 and MM4. In clumps MM1 and MM2 the flux loss was smaller, indicating that compared to MM3 and MM4, a larger percentage of the flux resides in the compact clump structure and less in the extended envelope. Only one clump, MM2, has a mass $M > 8\mathrm{M}_{\odot}$.

The (beam averaged) column densities were similar to the numbers derived from the single dish data for all clumps except MM2 – for this clump the column density increased by 50%. Since the only newly observed parameter which entered the column density calculation was the peak flux, this is not surprising. The clumps sizes (derived from the deconvolved major and minor axis of the Gaussian fit) were all below 0.1 pc and therefore much smaller than the sizes derived from the bolometer data of 0.2 pc (not deconvolved from the 30m telescope beam). Due to the size difference the density, $n \propto R^{-3}$, of the clumps derived from the SMA data was one or two orders of magnitude higher than the density derived from the 30m observations.

The SMA study found only one clump, MM2, with a mass $M > 8\,\mathrm{M}_{\odot}$ and a column density above $1 \times 10^{23}\,\mathrm{cm}^{-2}$, the theoretical threshold for massive star formation predicted by Krumholz & McKee (2008) based on simulations. However, some clumps might still be accreting material from the surrounding low density mass reservoir and might attain higher masses in the future. Therefore one cannot exclude massive star formation yet for the remaining clumps.

4.4.2 G017.19+00.81 MM1

Clump MM1 is situated in a infrared dark region central to the hypothetical annulus or shell. The clump hosts one 24 μm source, which is slightly offset from clump MM1b. Figure 4.17 shows the blue and red part of the high velocity ^{12}CO emission. There is at least one outflow, marked by the arrows, in eastwest direction. Possibly there is a second outflow on smaller scales in a southeast

Table 4.5: Derived clump properties of cloud G017.19+00.81

Clump	$d_{\rm kin}$ (kpc)	$T_{\rm rot}$ (K)	SMA size[b] (pc)	SMA $N_{\rm H_2}$ (10^{22}cm^{-2})	SMA $n_{\rm H_2}$ (10^5cm^{-3})	SMA M ($M_\odot$)	30m[a] $N_{\rm H_2}$ (10^{22}cm^{-2})	30m[a] $n_{\rm H_2}$ (10^5cm^{-3})	30m[a] M ($M_\odot$)
MM1a	2.5	17.2	0.04	4.9	61.6	9	4.9	1.5	54
MM1b	2.5	17.2	0.02	3.4	386.5	5	..	..	..
MM2	2.3	18.7	0.06	24.4	89.6	49	17.4	6.3	142
MM3	2.3	20.0	0.02	5.5	218.0	8	5.3	1.5	72
MM4a	2.3	20.1	0.05	2.0	8.7	4	2.9	0.8	40
MM4b	2.3	20.1	0.05	0.8	6.0	2	..	..	..
MM4c	2.3	20.1	0.08	0.7	0.7	1	..	..	..

[a]Data observed with the MAMBO bolometer for clumps MM1, MM2, MM3 and MM4.
[b]Geometrical mean of major and minor axis, deconvolved from the beam (except for MM4c)

to northwest direction around the 24 μm source. Additional evidence for shocks was found in the emission of SiO (Fig. 4.18), however other shock tracers such as SO and methanol covered by the SMA were not detected. Since these latter molecules have critical densities of $n_{\rm H_2} > 10^6\,{\rm cm^{-3}}$ the density of this region is likely to be less than that. Figure 4.19 shows the ^{13}CO and C^{18}O spectral line maps performed with the SMA. The C^{18}O line profile is $\lesssim 10\,{\rm km\ s^{-1}}$ broad and dominated by blue emission, while the ^{13}CO has much wider wings of $\sim 30\,{\rm km\ s^{-1}}$, which extend mostly to red velocities. Both, the CO isotopologues have narrower line profiles compared to the ^{12}CO(2–1) line where the red part of the line was extended over almost $50\,{\rm km\ s^{-1}}$. The maps of C^{18}O and ^{13}CO are difficult to interpret. The C^{18}O emission is very confused and shows no clear trend. The ^{13}CO peak is clearly offset from the continuum emission. Fig. 4.19 suggests that the ^{13}CO emission is blown away by the outflow, since it oriented orthogonally to the outflow direction.

4.4.3 G017.19+00.81 MM2 and 3

The ^{12}CO line profiles close to clump MM2 show extremely broad line widths extending over $70\,{\rm km\ s^{-1}}$. Figure 4.20 shows the ^{12}CO(2–1) spectrum for several positions and the integrated image of the high velocity components. The blue emission had two main outflow axes, which are marked by arrows. There is no obvious red counterpart which would belong to either of the blue outflows – the red emission is concentrated on a eastwest axis. Located 0.1 pc offset of the continuum peak of MM2, we found SO emission and a methanol line $CH_3OH(8_{-1}–7_0)\,E$ (Fig. 4.21). The images of the molecules are shown in Fig. 4.22. The offset position of these two molecules match with the peak of the blue ^{12}CO, which suggests that they are excited in the outflow shock. Jiménez-Serra et al. (2005) observed that SO, methanol and SiO are enhanced in pre- and post-shock regions. The SiO line profile, shown in Fig. 4.21, had a very wide blue line wing – which would indicate that it arises from the same region as the SO and the CH_3OH emission. Unfortunately, we have no SiO maps. The SO line profile (Fig. 4.21) is similar to that of SiO with broad blue line wings. The methanol line was located at the edge of the bandpass, so we could not see the blue part of the line profile. Possibly, this methanol line is a class I methanol maser, as was it found to be for cloud G345.01+1.79 by Val'tts (1998). As this was the only outflow for which SO and the methanol lines were detected, it is the most extreme case of our sample – it must contain densities $n_{\rm H_2} > 10^6\,{\rm cm^{-3}}$ since n_{crit} of these two molecules is of that order. We did not detect typical hot core tracers such as HNCO and OCS (see Fig. 4.15), nor did we find other methanol lines, such as the $(3_{-2} - 4_{-1})$ transition, toward clump MM2. We therefore think that the object releasing this strong outflow is still a young and cold source, which did not reach the typical hot core densities of $n_{\rm H_2} > 10^6\,{\rm cm^{-3}}$ and higher, and temperatures of $T > 100\,{\rm K}$ (Cesaroni et al. 1992, 1994).

The top panels of Fig. 4.22 show the two observed isotopologues of ^{12}CO which trace low densities. The ^{13}CO seems to follow the high velocity outflow, while the C^{18}O is extended quasi

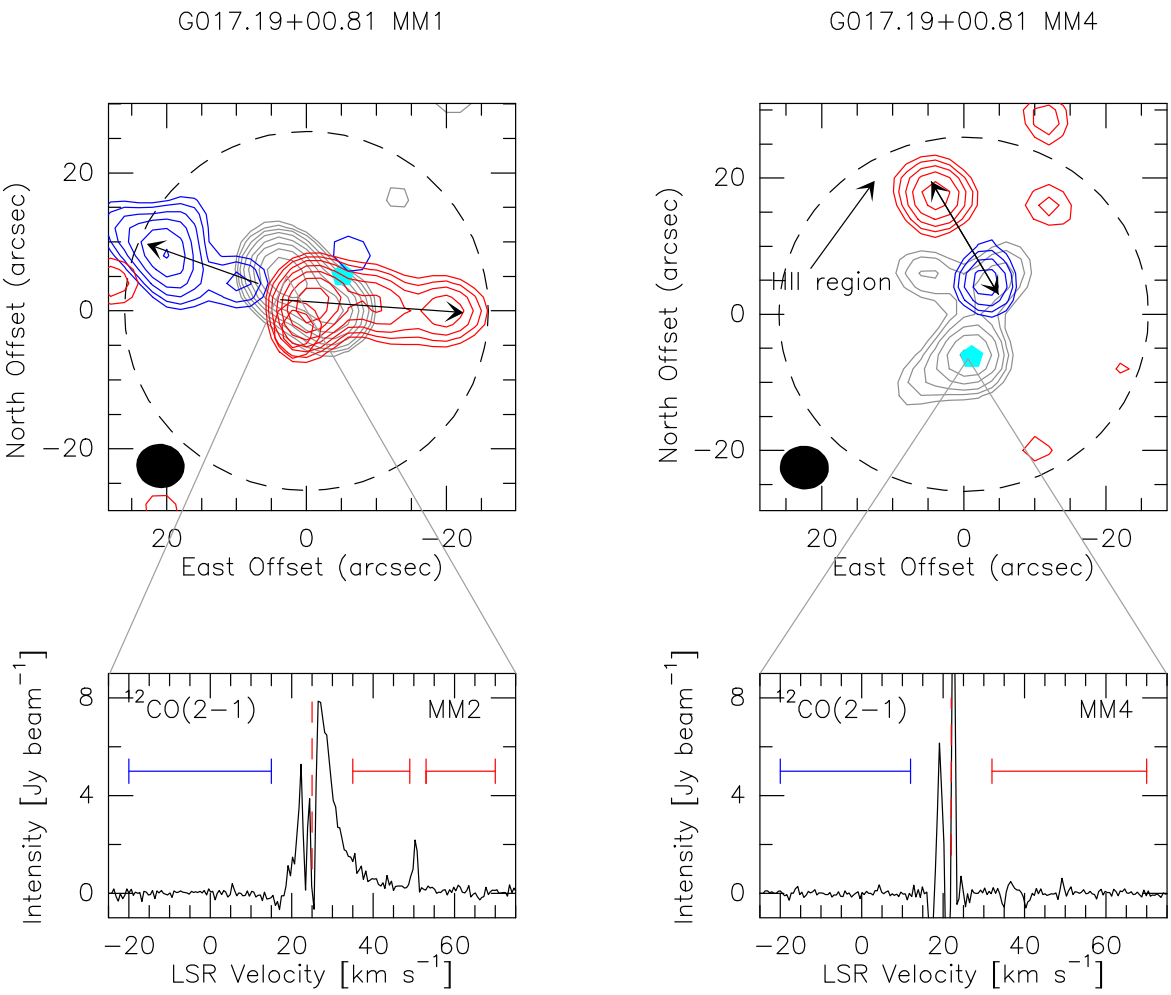

Figure 4.17: Interferometric images of ^{12}CO(2–1) emission centered on α(J2000)=18$^{\rm h}$:19$^{\rm m}$:08$^{\rm s}$.902, δ(J2000)=−13°:36′:29.″48 (*left*) and α(J2000)=18$^{\rm h}$:19$^{\rm m}$:15$^{\rm s}$.439, δ(J2000)=−13°:39′:29.″61 (*right*). The blue and red velocity ranges are marked in the spectra shown toward the peak of the mm continuum. In the background we show the SMA continuum emission. All contours start at twice the noise level in the respective map and increase by a factor of $\sqrt{2}$. The noise levels were 0.07 and 0.8 Jy beam^{-1} for ^{13}CO and C^{18}O, respectively. The ^{12}CO beam is given in the bottom left corner, and the primary beam of the SMA is indicated by the dashed black contours. 24 μm sources are highlighted by a blue pentagon and the ^{12}CO outflow is marked by black arrows. At a distance of 2.3 kpc, 10″ correspond to 0.11 pc.

spherically around MM2 – with the peak of the emission offset by 0.1 pc.

4.4.4 G017.19+00.81 MM4

Located ∼0.3 pc southwest of an HII region, MM4 is a candidate for a clump formed in the so-called collect and collapse scenario (Deharveng et al. 2005; Zavagno et al. 2006). Caused by supersonic expansion of the HII region into its surrounding medium, matter is compressed between the the ionisation and shock front. This accumulated material can, in time, evolve into gravitationally bound objects which collapse to form stars.

Figure 4.23 shows the GLIMPSE 8 μm emission in the background, overplotted with the SMA continuum and ^{12}CO isotopologues. The GLIMPSE 8 μm map reveals a pair of arc-like shapes

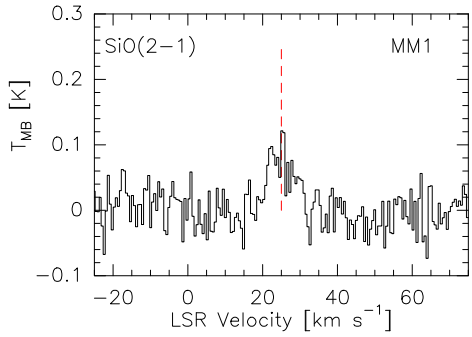

Figure 4.18: SiO spectrum toward the continuum peak MM1 done with the 30m telescope.

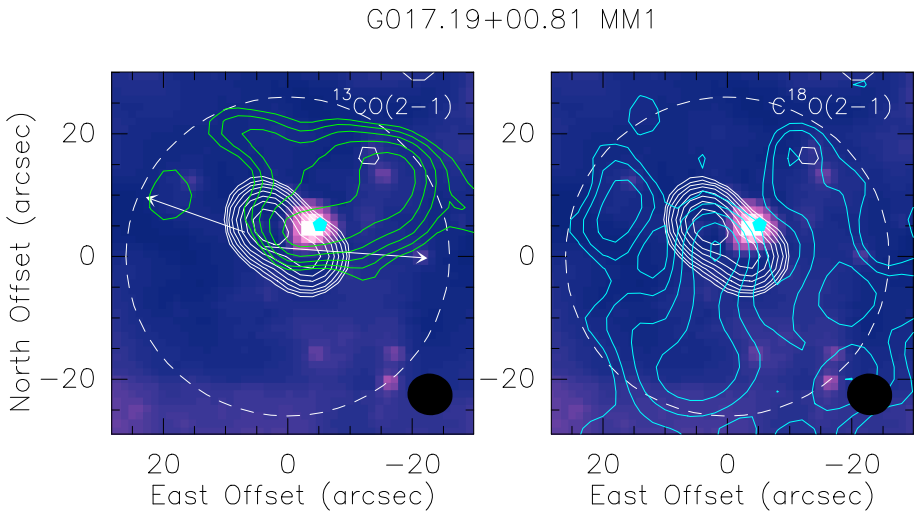

Figure 4.19: ^{13}CO(2–1) (*left*) and C^{18}O(2–1) (*right*) interferometric maps marked by green and blue contours, respectively, centered on α(J2000)=18$^{\rm h}$:19$^{\rm m}$:08$^{\rm s}$.902, δ(J2000)=−13°:36′:29.″48. The white contours show 1.3 mm continuum mapped by the SMA. The background is a GLIMPSE 8μm image. All contours start at twice the noise level in the respective map and increase by a factor of $\sqrt{2}$. The noise levels were 0.08 and 0.03 mJy beam^{-1} for MM1 and MM4, respectively. The beam of CO isotoplogues is marked in black in the bottom right corner. The primary beam of the SMA is shown by the dashed white contour. 24 μm sources are highlighted by a blue pentagon and the ^{12}CO outflow is marked by white arrows. At a distance of 2.3 kpc, 10″ correspond to 0.11 pc.

originating from the HII region, an infrared dark one followed by a infrared bright one. If the latter (western) represents a shock front, this would explain its infrared emission as arising from the collision with the ISM. The 1.3 mm continuum is found towards these 'bow shocks', with two peaks MM4b and MM4c lying in the infrared dark arc and MM4a coinciding with the outer infrared bright arc. The 24 μm infrared source located toward MM4a is probably a young stellar object. The ^{12}CO high velocity map of this region (Fig. 4.17) reveal one outflow, but it is located close to MM4b. No outflows were detected in ^{12}CO toward MM4a with the infrared bright source, and MM4a likely represents a low-mass object (see Table 4.5) in which the outflows have already stopped. There were no detections in shock tracers such as the SO and CH_3OH lines, which were also included in the SMA observations. Also in the previous observations, we found little evidence for star formation, no SiO, or H_2CO emission was detected, even though transitions of CH_3OH were observed. The emission from low density tracers such as the ^{13}CO and C^{18}O lines, plotted in Fig. 4.23, seems to follow the infrared bright bow shock. The spectrum of these molecules toward MM4a shows that both molecules have no wide line wings and emit in a limited (narrow) range of velocities. A large scale slow shock or movement would agree with this velocity range, which would

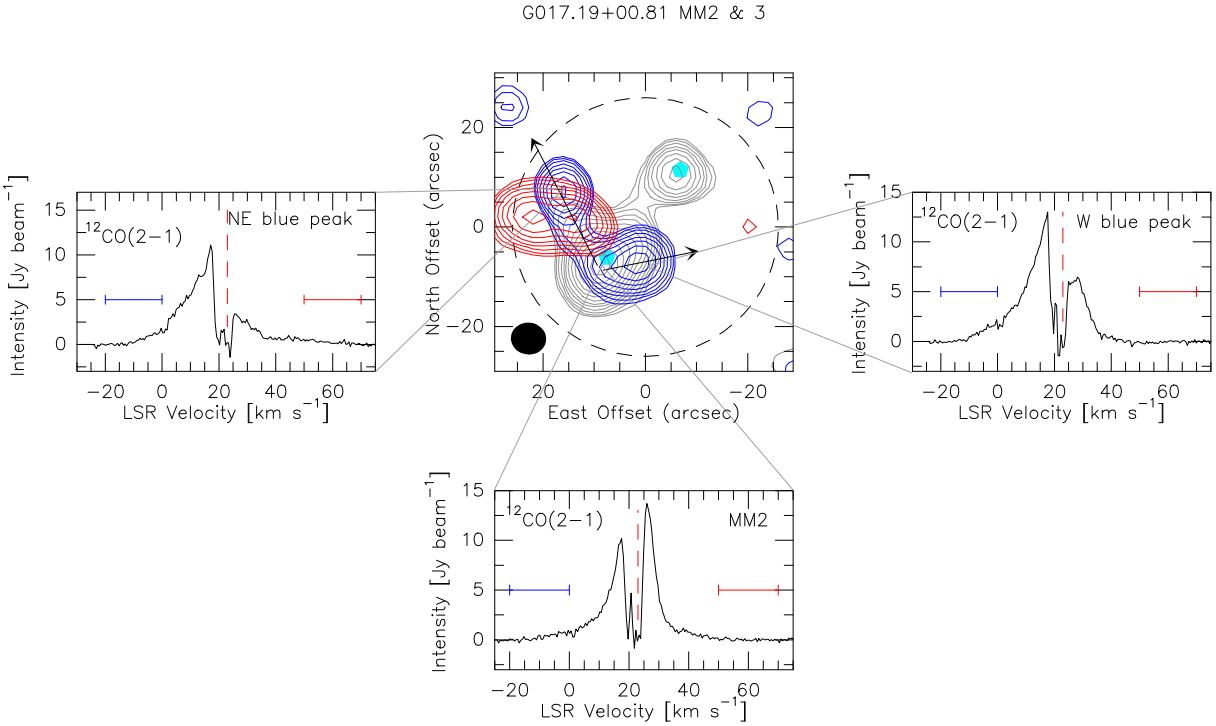

Figure 4.20: Same as Fig. 4.17, but for MM2 and centered on α(J2000)=18$^{\rm h}$:19$^{\rm m}$:12$^{\rm s}$.390, δ(J2000)=−13°:33′:36.″92.

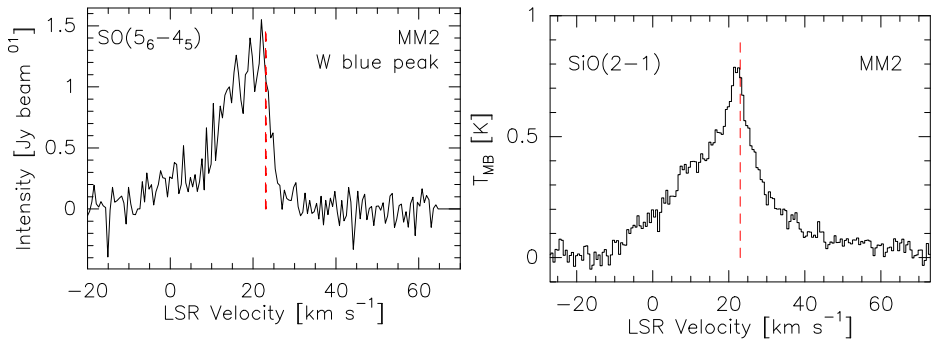

Figure 4.21: Spectra of shock-tracing molecules. *Left:* SO spectrum made with the SMA toward the outflow (the western blue ^{12}CO peak in Fig.4.17). *Right:* SiO spectrum done with the 30m telescope toward the continuum peak of MM2.

explain also why no shock tracing molecules are detected. The density of the swept up material is still low ($n_{\rm H_2} < 10^5\,{\rm cm}^{-3}$) and will possibly increase as more material is blown into this region by the radiation pressure of the HII region. In one of the infrared dark clumps, there is evidence of ongoing star formation – detectable from the ^{12}CO outflow. Since clump MM4b has only a mass of 2 $M_\odot$ it will likely only form a low-mass star.

4.5 Discussion of SMA data

The SMA resolved two of the four clumps detected with the MAMBO bolometer in to several fragments. We found evidence for outflows in high velocity ^{12}CO(2–1) lines toward MM1a and/or b, MM2 and MM4b. Some outflows arise near 24 μm sources, but also toward positions free of 24 μm emission. In all clumps, except for MM4, the outflow is also traced by SiO emission (30m

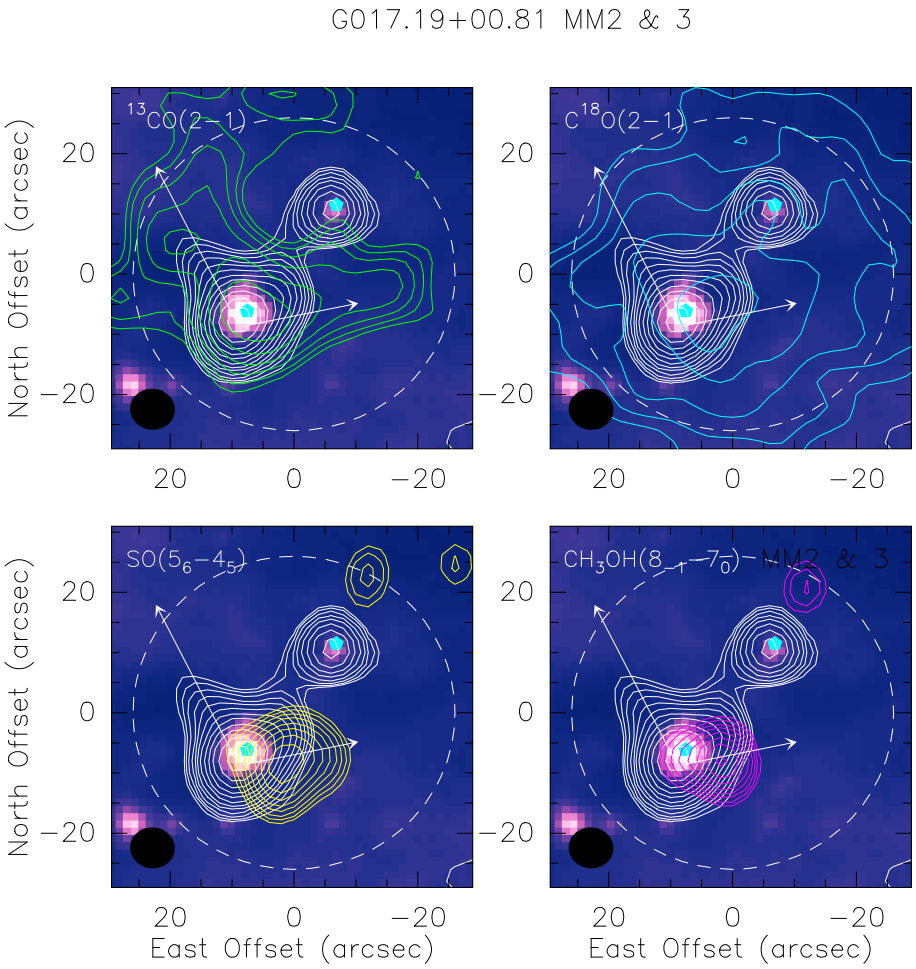

Figure 4.22: Interferometric maps of the ^{13}CO(2–1) (*top left*), C^{18}O(2–1) (*top right*), SO(5_6–4_5) (*bottom left*), and CH$_3$OH(8_{-1}–7_0) lines marked by green, blue, yellow and pink contours, respectively, centered on α(J2000)=$18^{\rm h}$:$19^{\rm m}$:$12\overset{\rm s}{.}390$, δ(J2000)=−13°:33′:36″.92. The white contours show 1.3 mm continuum mapped by the SMA. The background is a GLIMPSE 8 ,μm image. All contours start at twice the noise level in the respective map and increase by a factor of $\sqrt{2}$. The noise levels were 0.13, 1.7, 0.02, and 0.6 for ^{13}CO, C^{18}O, SO, and CH$_3$OH, respectively. The beam of the molecular maps is marked in black in the bottom left corner. The primary beam of the SMA is shown by the dashed white contour. 24 μm sources are highlighted by a blue pentagon and the ^{12}CO outflow is marked by white arrows. At a distance of 2.3 kpc, 10″ correspond to 0.11 pc.

observation, previous chapter). Apparently, in the process of star formation one can detect the outflows before any infrared emission is observed. Only for one source, we find SO emission and a methanol line connected to the blue peak of the outflow indicating that this outflow creates strong shocks which reach densities of $n_{\rm H_2} \sim 10^6\,{\rm cm}^{-3}$. This is the most massive clump, 48 $M_\odot$, where the high-velocity ^{12}CO outflows indicate that massive star formation is ongoing inside. For the other clumps it is yet unclear if they will accrete more matter and increase their column density to become massive stars or if they will form only low-mass stars.

4.6 Summary

We imaged the high infrared extinction cloud G017.19+00.81 by single dish and millimeter interferometer. We mapped the continuum emission as well as several molecular lines. Based on the

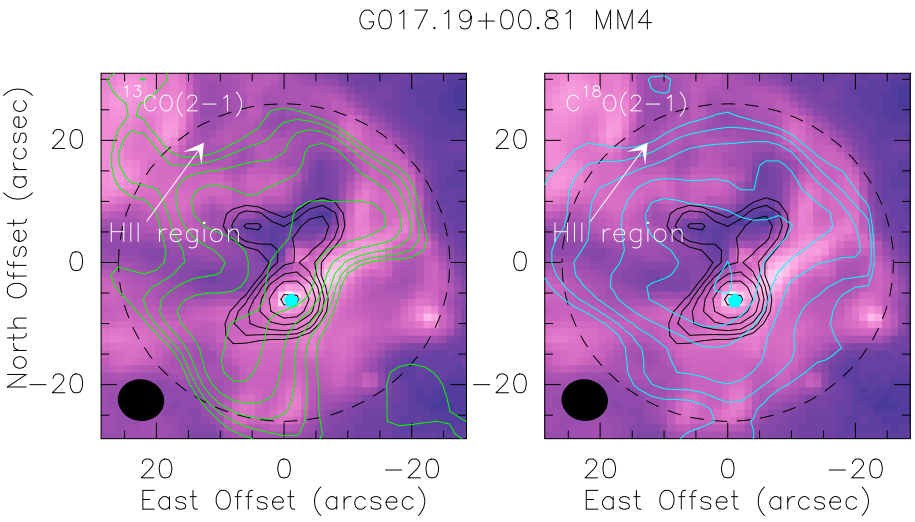

Figure 4.23: Interferometric maps of the ^{13}CO(2–1) (*left*) and C^{18}O(2–1) (*right*) lines marked by green and blue contours, respectively, centered on α(J2000)=18$^{\rm h}$:19$^{\rm m}$:15$^{\rm s}$.439, δ(J2000)=−13°:39′:29.″61. The black contours show 1.3 mm continuum mapped by the SMA. The background is a GLIMPSE 8μm image. All contours start at twice the noise level in the respective map and increase by a factor of $\sqrt{2}$. The noise levels were 0.25 and 2.1 Jy beam^{-1} for ^{13}CO and C^{18}O, respectively. The beam of CO isotoplogues is marked in black in the bottom right corner. The primary beam of the SMA is shown by the dashed white contour. 24 μm sources are highlighted by a blue pentagon and the HII region is indicated. At a distance of 2.3 kpc, 10″ correspond to 0.11 pc.

C^{18}O line, its depletion and the correlation with the continuum, and the maps in the high density tracer N_2H^+, we tried to attach a time marker to each of the clumps. The most evolved was found to be MM2 with a very high level of depletion and strong N_2H^+ emission. Clump MM1 was, based on the depletion and the correlation of C^{18}O and N_2H^+ emission, found to be younger than MM2. The age of clump MM4 is difficult to trace: even though its seems young judging by its depletion, this might not be true if the depletion of CO emission is halted by heating from the nearby HII region. In the SMA maps we found that MM4 actually consists of two infrared dark cores and one infrared bright one. The IRAM 30m telecope observations found evicence of outflows in the ^{12}CO line for clumps MM2 and MM1. HCO^+ maps confirmed a infall near clump MM2, and an outflow near clump MM1. However for clump MM4, the HCO^+ emission is experiencing larger scale motion.

The increase in angular resolution provided by the interferometer revealed fragmentation of several of the clumps. We found more ^{12}CO emission at high velocities than in the single dish maps; in almost all the clumps an outflow was detected. As outflows were also found in infrared dark clumps, it seems that in the process of star formation an outflow precedes the infrared emission. This is similar to the case of Class 0 objects in low-mass star formation (Andre et al. 2000), which are characterized as objects with centrally condensed millimeter continuum emission, while being infrared dark and having powerful jet-like outflows. For the clump MM2, with outflow velocities of ±40 km s^{-1}, we detected methanol and SO emission towards the outflow. These molecules are observed to be enhanced in shocked regions by Jiménez-Serra et al. (2005), which agrees with our observations where these molecules are not found toward the continuum emission but in the outflow.

What is the large scale structure of cloud G017.19+00.81, and do all clumps belong to it? The ^{12}CO, ^{13}CO and C^{18}O emission shows that MM4 is not part of a bubble or annulus, as hypothesized in the introduction. Clump MM4 is most likely created in a collect and collapse scenario by the nearby HII region. We interpret the structure of the single dish continuum to be part of an arc originating from the northeast and extending southward. It is unclear what drove the dust and gas

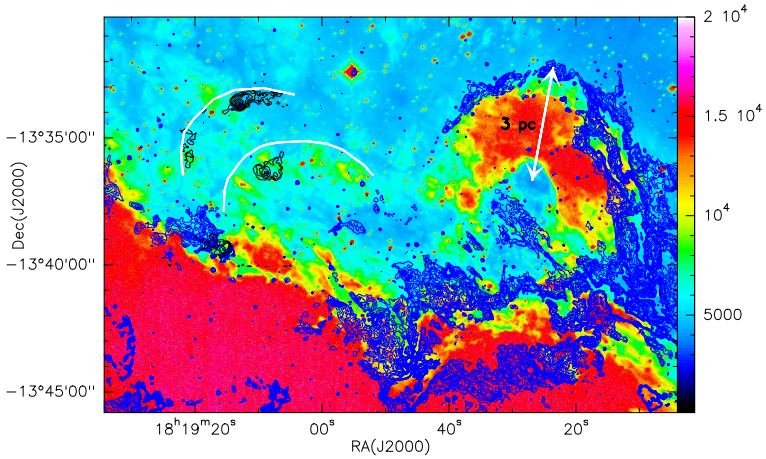

Figure 4.24: H-α image taken from the SuperCOSMOS H-alpha Survey (Parker et al., 2005) overlaid with the GLIMPSE 8 μm image in dark blue contours, and the bolometer continuum emission of cloud G017.19+00.81 with black contours. The nebula M16 contains many arc-like structures. The western arc is very large, it has a radius of 3 pc, and is observed clearly in H-α and PAH emission (8 μm). The arc-like cloud G017.19+00.81 is located in the northeast of the image and is preceded with an H-α arc in the west. Both arcs are accentuated by a white line to guide the eye.

into this filamentary arc-like shape. A similar arc is found in M16 about one minute westward of our cloud (see Fig. 4.1). A combination of an H-α map with 8 μm emission from GLIMPSE, shown in Fig. 4.24 shows that here the dust-arc was possibly created by the expansion of an HII region. The picture of an inner H-α ionization shock front with an outer shell with 8 μm emission is very similar to the expanding HII region RCW 79 described by Zavagno et al. (2006). The H-α in Fig. 4.24 shows that the infrared dark arc of G017.19+00.81 is possibly preceded by an H-α arc to the west. The H-α emission of this arc is much weaker than that of the large arc in the west. Also, the distance between the dust and the H-α is much larger for our cloud, namely $\sim$1.6 pc. However, Deharveng et al. (2009) find arc-shaped dust condensations also at distances of $\sim$1–2 pc away from the Hα emission. The central clump MM1, could be part of the rear part of the HII expansion. The slight redshift observed in all the spectral lines of ($\pm$2 km s^{-1}) toward MM1 with respect the other clumps could be explained if this clump is a part of a receding shell.

CHAPTER 5

Trigonometric parallaxes to 6.7 GHz methanol masers

Published in A&A, Volume 511, A2, as Rygl, Brunthaler, Reid, Menten, van Langevelde, & Xu (2010a)

For a proper understanding of physical properties of massive star-forming regions such as their sizes, masses and luminosities, the accurate knowledge of the distance is crucial. In this chapter we tried to obtain distances by measuring the trigonometric parallax towards several star-forming regions in the second and third Quadrant of the Galaxy.

5.1 Introduction

Accurate distances and proper motions are crucial for studies of the structure and kinematics of the Milky Way. Since we are in the Galactic plane, it is not easy to determine the spiral structure of our Milky Way (Reid et al. 2009b). Massive star-forming regions trace the spiral arms and are objects well-suited to revealing the structure of the Milky Way.

Determining the fundamental physical properties of individual objects, such as size scales, masses, luminosities, and ages, also depends critically on distance. For example, the distance to the Orion Nebula, determined by a number of trigonometric parallax measurements using radio continuum emission from stars in its associated cluster (Menten et al. 2007; Sandstrom et al. 2007), water masers (Hirota et al. 2007), and SiO masers (Kim et al. 2008), turned out to be 10% less than previously assumed, resulting in 10% lower masses, 20% fainter luminosities, and 20–30% younger ages for the stars in the cluster.

The most fundamental and unbiased method of measuring distances is the trigonometric parallax, which depends only on geometry and is therefore free of any astrophysical assumptions. To achieve the sub-milliarcsecond astrometric accuracy at optical wavelengths requires space-borne observations. The first dedicated optical satellite for this purpose was ESA's Hipparcos (Perryman et al. 1995). With its accuracy of 0.8–2 mas, it was capable of measuring distances up to $\sim$200 pc – only a small fraction of the Milky Way. A new optical astrometry satellite GAIA, to be launched in 2012, will be two orders of magnitude more accurate and push the optical parallaxes to Galactic size scales (e.g., Lindegren 2009). Despite the high accuracy, GAIA will suffer from dust extinction in the Galactic plane, in particular in the spiral arms and toward the Galactic center. Here radio astronomy can provide an important complement to GAIA, because radio wavelengths do

Table 5.1: Observation information

Program	Date	Participating Antennas[a]
EB32A	10 Jun 2006	Jb Wb Ef Mc Tr Nt Hh On Da
EB32B	18 Mar 2007	Jb Wb Ef Mc Tr Nt Hh On Cm
EB32C	17 Jun 2007	Jb Wb Ef Mc Tr Nt Hh On Cm
GB63A	31 Oct 2007	Jb Wb Ef Mc Tr Nt Hh On Y1
GB63B	16 Mar 2008	Jb Wb Ef Mc Tr Nt Hh On Y1

[a]The full names of the antennas are: Jb – Jodrell Bank; Wb – Westerbork (in single dish mode); Ef – Effelsberg; Mc – Medicina; Tr – Torun; Nt – Noto; Hh – Hartebeesthoek; On – Onsala; Da – Darnhall; Cm – Cambridge; Y1 – single EVLA antenna.

not suffer from dust extinction, and Very-Long-Baseline Interferometry (VLBI) phase-referencing techniques can provide accuracies better than 10 μas, allowing accurate distances with errors less than 10% out to 10 kpc (see for example Honma et al. 2007; Hachisuka et al. 2009; Reid et al. 2009a).

Strong and compact radio sources, such as molecular masers, are ideal targets for trigonometric parallax measurements. Masers are frequently found in (dusty) star formation regions (SFRs) and asymptotic giant branch stars. The most numerous interstellar masers are the 22 GHz water masers, followed in number by the 6.7 GHz methanol masers; to date several hundreds of these masers have been found across the Galaxy (e.g., Pestalozzi et al. 2005; Green et al. 2009). They are exclusively associated with early stages of massive star formation, observed both prior to the development of an ultra compact HII (UCHII) region and coexistent with these (Menten 1991; Ellingsen 2006; Pestalozzi et al. 2007). Maser modeling indicates that the 6.7 GHz emission is likely to be excited via radiative pumping by warm dust heated by newly formed high-mass stars (Sobolev et al. 2007).

Sources of methanol masers have long lifetimes of $\sim 10^4$ year (van der Walt 2005). Their velocity spread is typically within ± 5 km s^{-1} about the systematic velocity of the molecular core, and single maser features are usually narrow ($\sim$1 km s^{-1}). The kinematics suggest that methanol masers originate from different regions than water masers, which have wider velocity spreads and are produced in protostellar outflows (Menten 1996). To summarize, the strength, ubiquity, long lifetimes, and small internal motions make the 6.7 GHz methanol maser very suitable for astrometric purposes.

Here we present results from observations with the European VLBI Network (EVN) of eight strong methanol masers belonging to well-known massive SFRs in the outer part of the Milky Way: ON 1, L 1287, L 1206, NGC 281-W, MonR 2, S 252, S 255 and S 269. Recently, H_2O maser or 12.2 GHz methanol maser parallax measurements have been reported for three of these regions (NGC 281-W, Sato et al. 2008; S 252, Reid et al. 2009a; S 269, Honma et al. 2007), allowing a valuable cross check with our measurements. The results of this present work are crucial for star formation studies in these regions, and, together with a larger sample of parallaxes, will help to understand the structure of the Local and Perseus arms.

In paper Rygl et al. (2010a) we reported on the first parallax measurements made with the EVN. Results presented there replaced preliminary, less accurate, and less complete measurements (Rygl et al. 2008). In the next section we describe the observations and data analysis, and in Sect. 5.3 we explain the method and fitting of the parallax and proper motion. The results are then presented per source in Sect. 5.4 and discussed in Sect. 5.5. The conclusions are summarized in Sect. 5.6.

5.2 Observations and data analysis

The observations were performed with the EVN at five epochs between 2006 June, and 2008 March. The exact dates of the observations and the participating antennas are listed in Table 5.1. Each observation lasted 24 hours and made use of *geodetic-like* observations to calibrate the tropospheric

zenith delays at each antenna (see Reid & Brunthaler 2004; Brunthaler et al. 2005; Reid et al. 2009a for a detailed discussion). A typical observing run consisted of four 6-hour blocks containing ∼1 hour of geodetic-like observations, ∼10 minutes of observation of fringe finders. The remaining time was spent on maser/background source phase-referencing observations. During each run, the average on-source time per maser was between ∼0.9 and ∼1.2 hours depending on the sky position, because half of our targets were low declination sources that had a limited visibility.

Using the technique of phase referencing, each maser was observed in a cycle with two (or one) nearby (∼1°–2°separation) compact radio quasars, which were used as background sources. The sources were switched every 2 minutes. Before our EVN observations, we had used the NRAO Very Large Array under project AB1207 in A-configuration to observe several compact NVSS (Condon et al. 1998) sources within 1° from the maser source at two frequencies (8.4 and 4.8 GHz) to check their spectral index and compactness. For the best candidates, we determined their position to a sub-arcsecond accuracy to use them as a position reference in the EVN observations. Additionally, several known VLBA calibrators were used, namely: J2003+3034 and J0613+1708 (Fomalont et al. 2003), J0603+215S(9) and J0613+1306 (Ma et al. 1998), J0047+5657 (Beasley et al. 2002), J2223+6249 (Petrov et al. 2005), J0035+6130 (Petrov et al. 2006), and J0606–0724 (Kovalev et al. 2007). Table 5.2 lists the positions of the masers and their background sources.

The observations were performed with eight intermediate frequency bands (IF) of 8 MHz width, each in dual circular polarization sampled at the Nyquist rate with 2 bits per sample, yielding a recording rate of 512 Mbps. The data were correlated in two passes at the Joint Institute for VLBI in Europe (JIVE), using an integration time of 0.5 seconds, affording a field of view of 1.′2 (limited by time-averaging smearing). The maser data were correlated using one 8 MHz IF band with 1024 spectral channels, resulting in a channel separation of 7.81 kHz or 0.41 km s^{-1} at 6.7 GHz. The quasar sources were correlated in continuum mode with eight IFs of 8 MHz width with a channel separation of 0.25 MHz.

The data were reduced using the NRAO Astronomical Image Processing System (AIPS). The *geodetic-like* observations were reduced separately, and tropospheric delays were estimated for each antenna. The data were reduced following the EVN guidelines, applying parallactic angle and ionospheric delay corrections. The JIVE correlator model uses Earth's orientation parameters, which are interpolated from the appropriate daily-tabulated values, so it is not necessary to correct them after the correlation. The ionospheric delays were based on the JPL GPS–IONEX total vertical electron content maps of the atmosphere. Amplitudes were calibrated using system-temperature measurements and standard gain curves. A "manual phase-calibration" was performed to remove delay and phase differences between the IFs. The Earth rotation was corrected for with the task 'CVEL'. For each maser, a spectral channel with one bright and compact maser spot was used as the phase reference. The data was Hanning-smoothed to minimize Gibbs ringing in the spectral line data. To avoid the strong fluctuations caused by the bandpass edges, the outer two channels in each IF were discarded (following Reid et al. 2009a). The positions of the masers and background sources were extracted by fitting 2D Gaussian to the maps.

Here, we report the results on the first five sources for which we have completed the analysis: ON 1, L 1206, L 1287, NGC 281-W, and S 255. For the other sources, S 252, S 269, and MonR 2, we had problems with the calibration of the data, which were likely caused by residual atmospheric delay, so that we were unable to achieve sufficient accuracy for a parallax measurement.

5.3 Method and fitting

5.3.1 First epoch

The absolute positions of the masers were not known with milli-arcsecond accuracy before our first observation. Only after the first epoch was analyzed were accurate positions determined, which were used as correlator positions in epochs two to five. The correlator positions of the first epoch were therefore different (not so accurately centered on the maser) from the ones used in the following epochs, which were centered on the maser. In the first epoch, position errors above 0.″2 made it difficult to calibrate the phases because of a high fringe rate, which could not be

Table 5.2: Source information

Source	R.A. (J2000) (h:m:s)	Dec. (J2000) (°:′:″)	ϕ [a] (°)	P.A.[a] (°)	Brightness[b] (Jy beam^{-1})	Restoring Beam[b] (mas, mas, deg)
ON 1	20:10:09.074	+31:31:35.946	...	...	1–7	5.7×3.9, 86
J2003+3034 ...	20:03:30.244	+30:34:30.789	1.71	–124	0.124	5.3×3.7, 76
J2009+3049 ...	20:09:17.588	+30:49:24.580	0.73	–14	0.008	5.6×3.7, 88
L 1206	22:28:51.407	+64:13:41.314	...	...	0.3–1.4	5.7×4.0,−80
J2223+6249 ...	22:23:18.097	+62:49:33.805	1.53	–157	0.093	5.7×3.9,−84
J2225+6411 ...	22:25:27.993	+64:11:15.030	0.37	–96	0.002	5.6×3.8,−80
L 1287	00:36:47.353	+63:29:02.162	...	...	0.5–4.1	6.0×4.1,−57
J0035+6130 ...	00:35:25.311	+61:30:30.761	1.98	–176	0.092	6.0×4.1,−58
J0037+6236 ...	00:37:04.332	+62:36:33.310	0.88	178	0.061	5.9×4.2,−57
NGC 281-W ...	00:52:24.196	+56:33:43.175	...	...	1–12	5.7×4.2,−56
J0047+5657 ...	00:47:00.429	+56:57:42.395	0.84	62	0.142	5.6×4.0,−65
J0052+5703 ...	00:52:54.303	+57:03:31.460	0.50	–8	0.010	5.6×3.9,−62
MonR 2	06:07:47.862	–06:22:56.518	...	...	9–22	8.6×4.4, 42
J0606–0724 ...	06:06:43.546	–07:24:30.232	1.06	–165	0.135	9.0×4.1, 40
S 252	06:08:53.344	+21:38:29.158	...	...	17-44	6.4×3.9, 56
J0603+215S ..	06:03:51.557	+21:59:37.698	1.22	–73	0.019	6.7×3.8, 54
S 255	06:12:54.020	+17:59:23.316	...	...	4	6.9×3.9, 56
J0613+1708 ...	06:13:36.360	+17:08:24.946	0.87	169	0.040	7.1×3.9, 46
S 269	06:14:37.055	+13:49:36.156	...	...	0.2–1.1	6.8×3.9, 58
J0613+1306 ...	06:13:57.693	+13:06:45.401	0.73	–167	0.087	6.8×3.8, 57

[a]Separation, ϕ, and the Position Angle (east of north), P.A. , between the maser and the background source.
[b]The brightness and restoring beam (east of north) are listed for the second epoch.

interpolated correctly when applied to the data. Shifting the maser into the phase center turned out to be very time-consuming with available software because AIPS and the EVN correlator use apparent positions calculated at different times (AIPS at 0 UT of the first observing day versus the EVN correlator at the end of the first scan). Even an infinitesimally small shift in the epoch coordinate using the AIPS tasks 'CLCOR' or 'UVFIX' can result in a substantial position change and phase shifts from the old EVN apparent position to the new AIPS apparent position at 0 UT (see Sect. 5.5.7 for more details). In a parallax experiment, accurate and consistent positions throughout the experiment are crucial. Since it was difficult to calibrate the phases for masers with a large position offset or to shift these to the phase center, several sources in the first epoch could not be used for phase referencing.

5.3.2 Atmospheric delay

The observations are affected by tropospheric and ionospheric delay when the radiation transverses these atmospheric layers. This delay induces a time variable phase shift and is undesirable. At the relatively low frequency of 6.7 GHz the ionospheric delay is expected to dominate over the tropospheric delay.

Most of the ionospheric delay is removed from the data using measurements of the total electron content of the ionosphere obtained from dual-band global positioning system measurements (e.g., Ros et al. 2000). The expected residual delay is still a few centimeters, comparable to the residual tropospheric delay at the observing frequency. The ionospheric and tropospheric delay behave differently with frequency and can be isolated by determining the spectral index. However, our single frequency geodetic-like observations do not allow a separation of the ionospheric and tropospheric contributions. The measured group-delays from the geodetic blocks are interpreted as having a tropospheric origin, and the data are phase-delay-corrected accordingly. An ionospheric group delay makes a different contribution to the phase delay, so that the tropospheric correction can even deteriorate the calibration when the group delay has a partially ionospheric origin. Since the residual tropospheric delay is a few centimeters at 6 GHz and can easily be confused with an ionospheric residual, the tropospheric correction is expected to be less useful in improving the quality of calibration than at high frequencies. As a test, all data were reduced with and without a "tropospheric" delay correction. In slightly more than half of the cases, the signal-to-noise ratio improved by applying the tropospheric correction, an example is shown in Fig. 5.1, while for the remaining cases the improvement was not significant (roughly the signal-to-noise stayed constant). We noted a trend toward improvement with decreasing declination: both high declination sources, $\delta \simeq 64°$, L 1206 and L 1287 improved in 2 out of 5 epochs; NGC 281-W at $\delta \simeq 57°$improved in 3 out 5 epochs; and ON 1 at $\delta \simeq 31°$even improved in 4 out of 5 epochs. Ionospheric delay saturates at zenith angles greater than $\sim$70°. However, the tropospheric delay continues to grow rapidly at larger zenith angles and can dominate the ionospheric delay at zenith angles of $\sim 80°$(see Thompson et al. 1991).

5.3.3 Multiple maser spots

For each SFR, we found the emission to arise from a number of separate maser spots. Most of the line profiles stretched over several channels. Both spatially and/or spectrally different maser spots were considered as distinct maser components. We inspected the behavior of the proper motion for each maser spot relative to the reference spot. Maser spots with strong nonlinear proper motions or a large scatter of position about a linear fit were discarded. Only compact maser spots with well-behaved proper motions were used for the parallax fitting.

The average internal proper motion of the maser spots ranged between 0.06 and 0.23 mas yr^{-1}. Considering the distance of each maser, these proper motions correspond to 0.5–1 km s^{-1}, much lower than the internal proper motions of water masers, which can reach up to 20–200 km s^{-1} (Hachisuka et al. 2006). The only exception was ON 1, which separates into two distinct maser groups with a relative proper motion of 0.52 mas yr^{-1}, or 6.3 km s^{-1}. This particularity is discussed in Sect. 5.4.1.

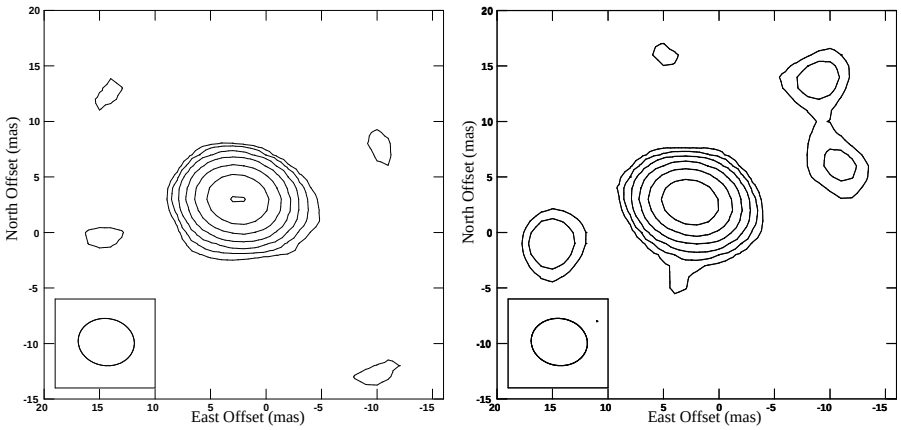

Figure 5.1: Phase-referenced images of J0035+6130 (epoch four) with the tropospheric delay correction applied (*left panel*) and without (*right panel*). The contours start at 1.3 mJy and increase by factors of 2 in both images. The signal-to-noise of the left image, 122, exceeds that of the right image, which was 91.

5.3.4 Fitting of parallax and proper motions

The parallaxes and proper motions were determined from the change in the positions of the maser spot(s) relative to the background source(s). The data were fitted with a parallax and a linear proper motion. Since the formal position errors are only based on the signal-to-noise ratios determined from the images, they do not include possible systematic errors from residual zenith delay errors or source structure changes. This leads to a high reduced χ^2 value for the fits, so we added error floors in quadrature to the positions until reduced χ^2 values close to unity were reached for each coordinate.

First, we performed parallax and proper motion fits for each maser spot relative to one background source. Then we made combined fits with respect to each background source, assuming one parallax but different proper motions for each maser spot. Finally, we repeated this combined fit for both the background sources together. The position measurements of different maser spots are not independent, since systematic errors, such as an unmodeled atmospheric delay, will affect all maser spots in a similar way. If these systematic errors dominate, this will lead to unrealistically small errors. The most conservative approach, which we adopted, is to assume that the systematic errors are 100% correlated. Then the error of the combined fit has to be multiplied by $\sqrt{N}$, where N is the number of maser spots.

However, this will overestimate the error, if significant random errors are present (e.g., owing to maser blending and structural changes over time), since the latter are not correlated between different maser spots. Random errors can be reduced by averaging the positions of the different maser spots (following the approach of Bartkiewicz et al. 2008; Hachisuka et al. 2009). We calculated the average positions with respect to each background source after removing their position offsets and proper motions. Then, we performed a parallax fit on these averaged data sets relative to each individual background source, and on both the background sources combined. This approach has the advantage that we can reduce the random errors, while leaving the systematic errors intact. In Table D.1 we list the individual parallax and proper motion fits to each maser spot, the combined fit of all the maser spots and the fit of the averaged data sets.

For most masers, we observed two background sources. Some of these background source pairs show a variation in their separation (mimicking a proper motion) of up to 1–2 mas yr^{-1} (on average this apparent movement was 0.54 mas yr^{-1}). This apparent movement is much greater than expected for extragalactic sources measured at 12 GHz, < 0.1 mas yr^{-1} (Reid et al. 2009a) or 22 GHz, < 0.02 mas yr^{-1} (Brunthaler et al. 2007). While at higher frequencies, the radio emission is typically dominated by the flat spectrum radio cores, the steep spectrum emission from the radio jets becomes stronger at lower frequencies. Thus, structure changes in these jets can lead

Table 5.3: Parallax and proper motion results

Source	π (mas)	D_π (kpc)	μ_α [a b] (mas yr^{-1})	μ_δ [b] (mas yr^{-1})
ON 1	0.389 ± 0.045	$2.57^{+0.34}_{-0.27}$	-3.24 ± 0.89[c]	-5.42 ± 0.46[c]
L 1206	1.289 ± 0.153	$0.776^{+0.104}_{-0.083}$	0.27 ± 0.23	-1.40 ± 1.95
L 1287	1.077 ± 0.039	$0.929^{+0.034}_{-0.033}$	-0.86 ± 0.11	-2.29 ± 0.56
NGC 281-W	0.421 ± 0.022	$2.38^{+0.13}_{-0.12}$	-2.69 ± 0.16	-1.77 ± 0.11
S 255	0.628 ± 0.027	$1.59^{+0.07}_{-0.06}$	-0.14 ± 0.54	-0.84 ± 1.76

[a]The proper motion, μ_α, includes the factor $\cos(\delta)$.
[b]The errors of the proper motion take the uncertainty resulting from an apparent nonzero movement between the background sources into account.
[c]For the proper motion of ON 1, we took an average of the north and south components.

to apparent motions, even if these jets are unresolved. Since we do not know which of the two background sources is responsible for this movement, the apparent movements of the background source pairs were added in quadrature to the final errors of the averaged proper motions of the masers. A summary of our parallaxes and proper motions is given in Table 5.3.

5.4 Individual sources

5.4.1 Onsala 1

The maser emission of Onsala 1 (ON 1) consists of two groups separated spatially by ∼940 mas, which have different radial velocities by 15 km s^{-1} (Fig. 5.2). The northern group, which includes the reference channel, is centered at a $v_{\rm LSR}$ of ≈ 0 km s^{-1} and the southern group at ≈ 15 km s^{-1}. Four maser spots in the northern group were suitable for parallax fitting. The masers in the southern group were not used for the parallax fit, since the phase-calibration was less accurate because of the large distance to the phase-reference center (located in the northern maser group). We find a parallax of 0.389 ± 0.045 mas, corresponding to a distance of $2.57^{+0.34}_{-0.27}$ kpc. The proper motions of the southern maser spots were fitted by assuming the parallax result of the northern group. All results are listed in Table D.1 and the parallax fit is plotted in Fig. 5.3.

For ON 1, two background sources were detected in epochs two through five (Fig. E.1). The last (fifth) epoch had poor (u, v) coverage, which resulted in very elongated synthesized beams in the east-west direction (J2003+3034, 12.1×3.7 mas^2, P.A.$\sim 87°$; J2009+3049, 11.0×3.3 mas^2, P.A.$\sim 88°$) compared to the representative numbers listed in Table 5.2. As a result, the right ascension data had a large uncertainty in epoch five. We estimated this uncertainty from fitting the variation in the background-source pair separation to be 2 mas (see Fig. 5.4). Since this was a combined error for both the background sources, the position error for each individual background source was $\sqrt{2}$ mas. We added an additional error floor of $\sqrt{2}$ mas to the error given for all the right ascension data points in the fifth epoch. The apparent movements between the two background sources, J2003+3034–J2009+3049, were 0.88 ± 0.06 mas yr^{-1} in right ascension and 0.45 ± 0.21 mas yr^{-1} in declination (Fig. 5.4).

5.4.2 L 1206

In L 1206, two maser groups were found separated by ∼100 mas. A third maser group was found northeast of the other two. This third maser group was not detected in all the epochs because of its weakness so was not used in the parallax measurements. Also the maser spot at -11.6 km s^{-1} was omitted for the same reason. The masers in L 1206 are shown with a spectrum in Fig. 5.5. The parallax fit used four compact maser spots and resulted in 1.289 ± 0.153 mas, corresponding

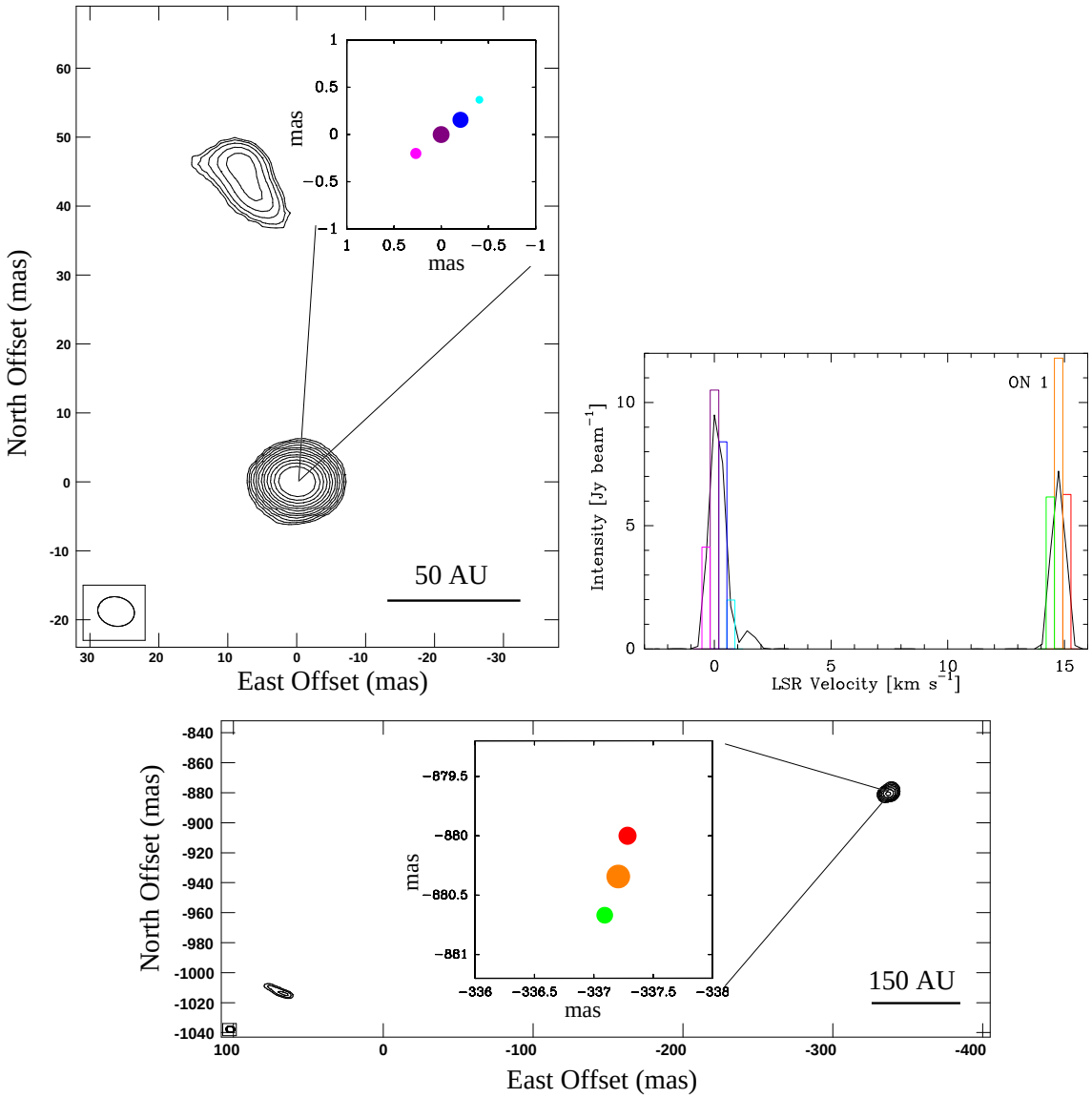

Figure 5.2: Velocity-integrated maps of the northern (*top, left*) and southern (*bottom*) maser groups in ON 1, together with the spectrum (*top, right*). Position offset (0,0) corresponds to the position listed in Table 5.2. Maser spots are indicated with color codes for different radial velocities. The areas of the colored circles and the colored histogram entries in the spectrum are scaled to the peak flux of that spot. The black line in the spectrum is the intensity of the maser within a selected surface, which is not necessarily the same as the intensity of the maser spot retrieved from a Gaussian fit. For the northern group, the contour levels start at 0.1 Jy beam^{-1} km s^{-1}, in the southern group 1.0 Jy beam^{-1} km s^{-1}, and increase by factors of $\sqrt{2}$.

to a distance of $0.776^{+0.104}_{-0.083}$ kpc. The results of the parallax and proper motion fits are displayed in Fig. 5.6 and listed in Table D.1.

Figure E.2 shows the phase-referenced images for both background sources. Only one of the two background sources, J2225+6411, was detected in the first epoch. The other background source, J2223+6249, had a much larger separation from the maser (i.e., the phase reference) and the transfer of the phase solutions to the J223+6249 data probably failed. The apparent movements between the background sources were 0.22 ± 1.45 mas yr^{-1} in right ascension and

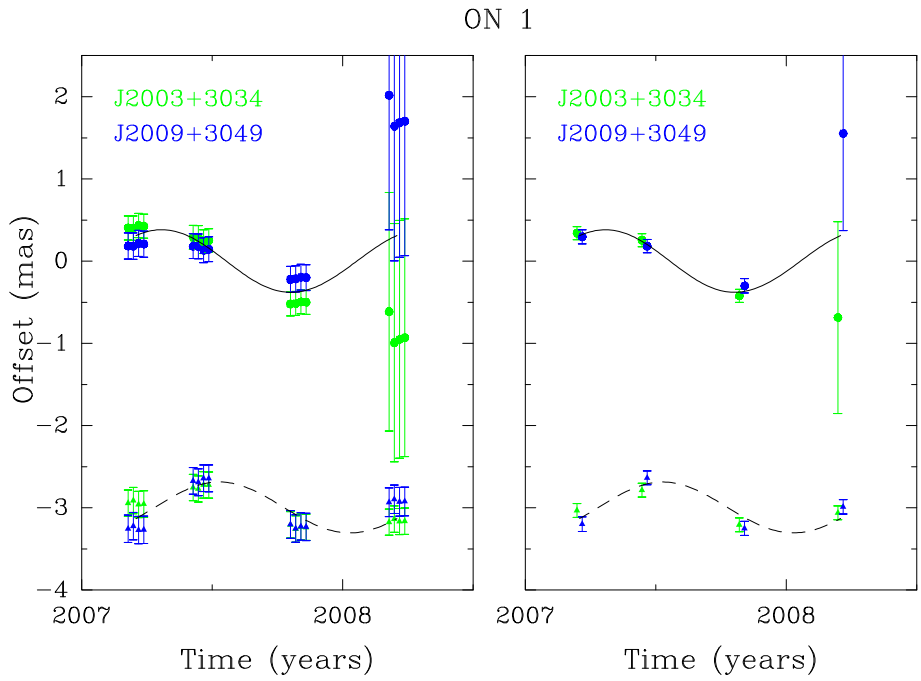

Figure 5.3: Results of the parallax fit based on four maser spots. The left graph shows a combined fit on all data, the right graph is a fit on the averaged data sets. The filled colored dots mark the data points in right ascension, while the filled colored triangles mark the declination. The solid line is the resulting fit in right ascension, the dashed line in declination. Different colors indicate a different background source.

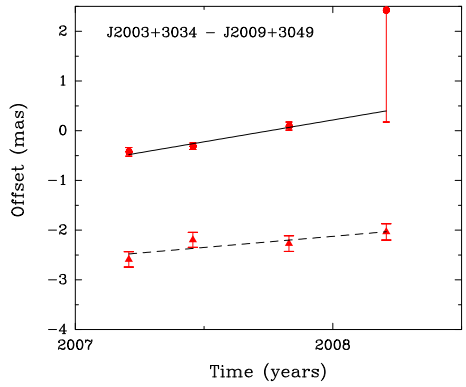

Figure 5.4: Variation of the separation between background sources J2003+3034–J2009+3049 belonging to ON 1. The solid line and the dots represent the right ascension data, while the dashed line and the filled triangles represent the declination data.

1.91 ± 1.43 mas yr^{-1} in declination (Fig. 5.7).

5.4.3 L 1287

Toward L 1287 we find three maser groups, two close together (within $\sim$ 40 mas) and the third $\sim$135 mas southward, shown with a spectrum in Fig. 5.8. A total of six maser spots from the three groups were used for the parallax fit. We report a parallax value of 1.077 ± 0.039 mas, corresponding to a distance of $0.929^{+0.034}_{-0.033}$ kpc. The results are plotted in Fig. 5.9 and listed in Table D.1.

Figure E.3 shows the phase-referenced images for both background sources. The variation of

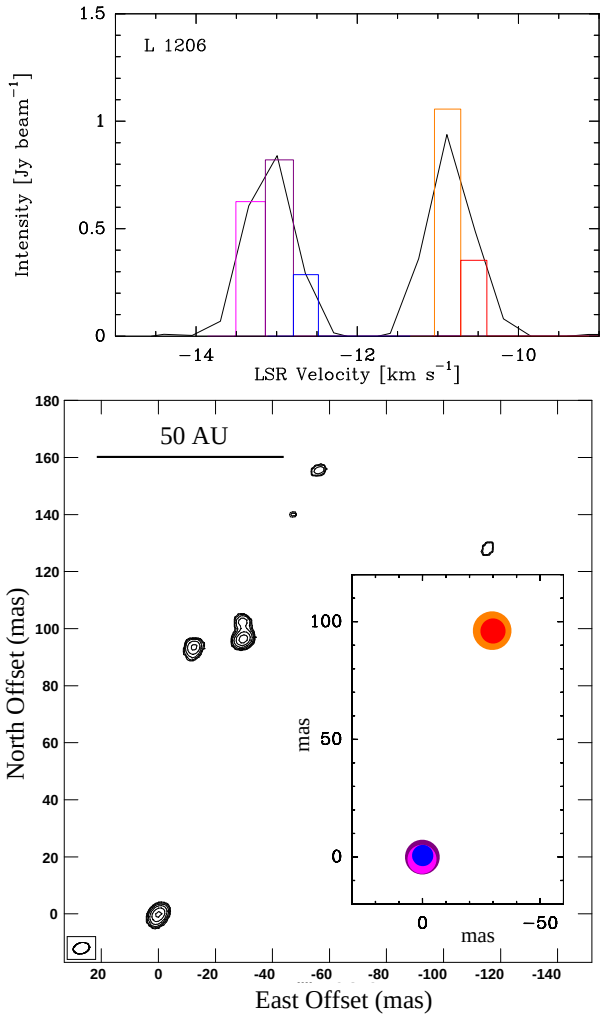

Figure 5.5: Velocity-integrated map and spectrum of L 1206. Position offset (0,0) corresponds to the position listed in Table 5.2. Maser spots are indicated with color codes for different radial velocities. The areas of the colored circles and the colored histogram entries in the spectrum are scaled to the peak flux of that spot. The black line in the spectrum is the intensity of the maser within a selected surface, which is not necessarily the same as the intensity of the maser spot retrieved from a Gaussian fit. The diffuse and weak spots were omitted, such as the spot at (−10, 95). Contour levels start at 0.1 Jy beam^{-1} km s^{-1} and increase by factors of $\sqrt{2}$.

the separation between the two background sources, J0035+6130 and J0037+6236, is shown in Fig. 5.10. Two data points appear to be outliers: the right ascension at epoch four and declination at epoch two. Increasing the data errors to 0.9 and 0.7 mas, respectively, for these outliers yields an apparent movement fit of -0.05 ± 0.12 mas yr^{-1} in right ascension and 0.54 ± 0.10 mas yr^{-1} in declination (Fig. 5.10). We investigated the visibility amplitudes as a function of (u, v) distance and found evidence of extended structure. For J0037+6236 at the fourth epoch, evidence of extended structure in the right ascension direction was found; however, for J0035+6130 at the second epoch, we found no indications of such structure.

5.4.4 NGC 281-W

We found four groups of methanol masers toward NGC 281-W, as illustrated in Fig. 5.11 together with the source spectrum. For the parallax fit we used a total of six maser spots coming from

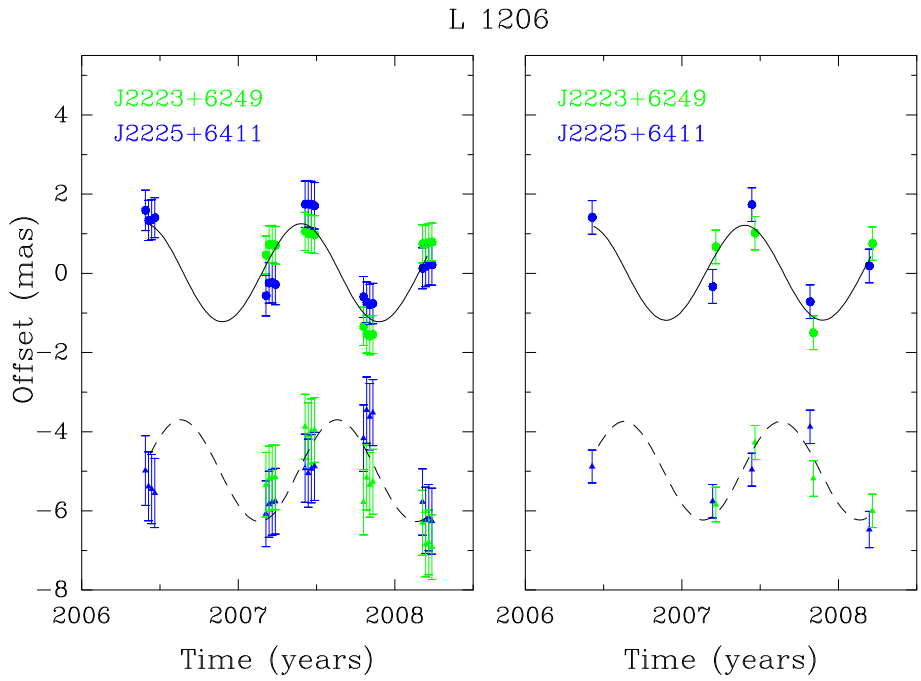

Figure 5.6: Results of the parallax fit for L 1206 based on four maser spots. The left graph shows a combined fit on all data, the right graph is a fit on the averaged data sets. The filled dots mark the data points in right ascension, while the filled triangles mark the declination. The solid line is the resulting fit in right ascension, the dashed line in declination. Different colors indicate different background sources.

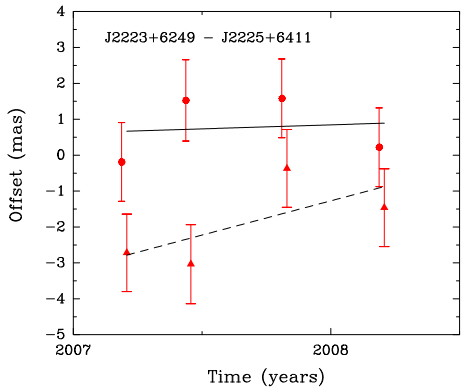

Figure 5.7: Variation of the separation between background sources J2223+6249–J2225+6411 belonging to L 1206. The solid line and the dots represent the right ascension data, while the dashed line and the filled triangles represent the declination data.

three groups, the central, southern, and southeast groups (Fig. 5.11). The weaker maser spots, like the ones located in the western group, were omitted in the parallax fitting. We find a parallax of 0.421 ± 0.022 mas corresponding to distance of $2.38^{+0.13}_{-0.12}$ kpc. The results are shown in Fig. 5.12 and listed in Table D.1.

For NGC 281-W, two background sources were detected successfully at epochs two through five (Fig. E.4). Background source J0052+5703 showed a double structure with the weaker component located ∼25 mas westward of the stronger component (Fig. E.4). The proper motion of the western component with respect to J0052+5703 was $\mu_\alpha = 0.64 \pm 0.63$ mas yr^{-1} and $\mu_\delta = -0.36 \pm 0.39$ mas yr^{-1} (Fig. 5.13), i.e, exhibiting no detectable proper motion. The apparent

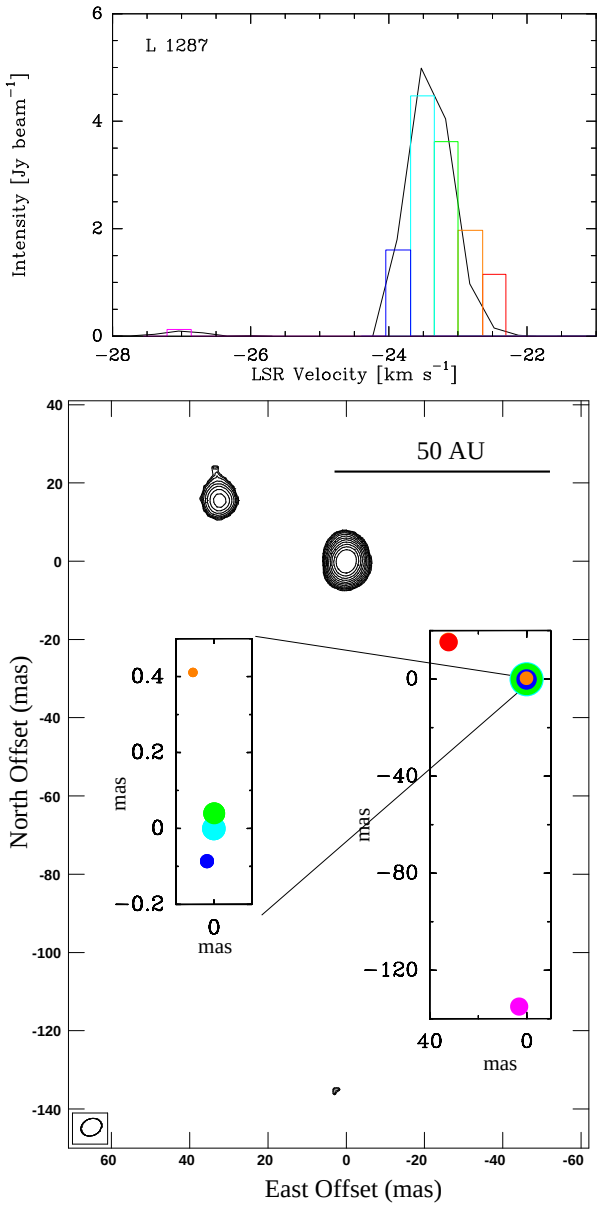

Figure 5.8: Velocity-integrated map and spectrum of L 1287. Position offset (0,0) corresponds to the position listed in Table 5.2. Maser spots are indicated with color codes for different radial velocities. The areas of the colored circles and the colored histogram entries in the spectrum are scaled to the peak flux of that spot. The black line in the spectrum is the intensity of the maser within a selected surface, which is not necessarily the same as the intensity of the maser spot retrieved from a Gaussian fit. Contour levels start at 0.05 Jy beam^{-1} km s^{-1} and increase by factors of $\sqrt{2}$.

movement between the two background sources, J0047+5657 and J0052+5703, was also close to zero: -0.16 ± 0.13 mas yr^{-1} in right ascension and -0.11 ± 0.11 mas yr^{-1} in declination.

5.4.5 S 255

For S 255, we could only use emission from one maser channel, namely the reference channel. Based on this maser spot, at 4.6 km s^{-1} (Fig. 5.14), we find a parallax of 0.628 ± 0.027 mas corresponding

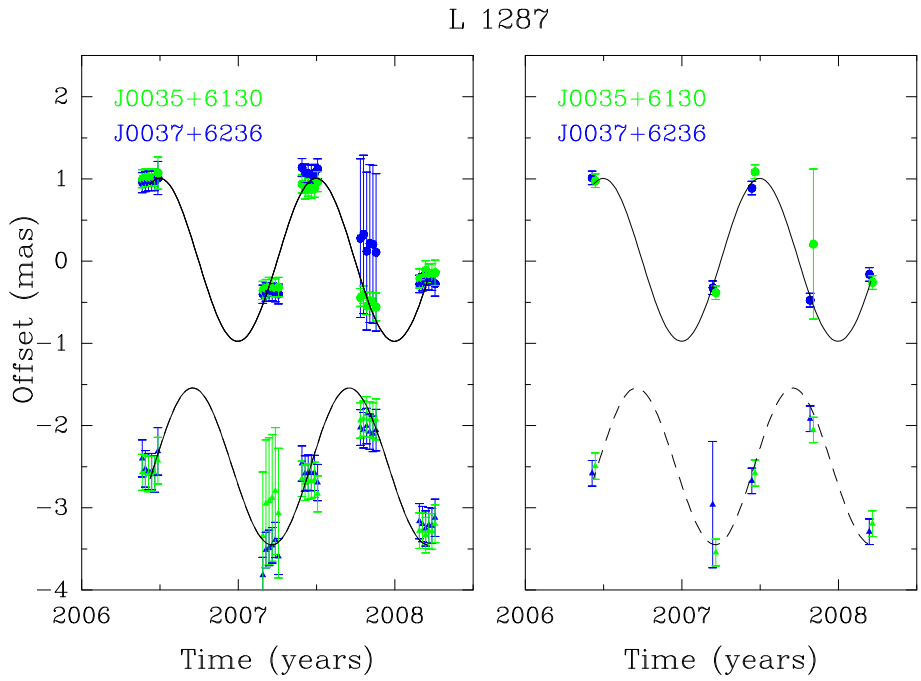

Figure 5.9: Results of the parallax fit for L1278 based on six maser spots. The left graph shows a combined fit on all data, while the right graph is a fit on the averaged data sets. The filled dots mark the data points in right ascension, while the filled triangles mark the declination. The solid line is the resulting fit in right ascension, the dashed line in declination. Different colors indicate a different background source.

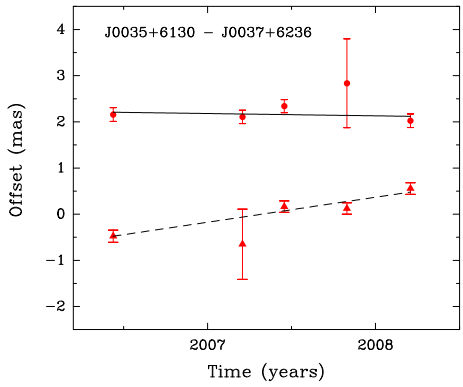

Figure 5.10: Variation of the separation between background sources J0035+6130–J0037+6236 belonging to L 1287. The solid line and the dots represent the right ascension data, while the dashed line and the filled triangles represent the declination data.

to a distance of $1.59^{+0.07}_{-0.06}$ kpc. The results are shown in Fig. 5.15 and listed in Table D.1.

We observed only one background source, J0613+1708, for S 255 (Fig. E.5), which was detected in epochs two to five. With only one background source, we could not check that its apparent movement was small, and so, conservatively, we added uncertainties of 1 mas yr^{-1} in both coordinates.

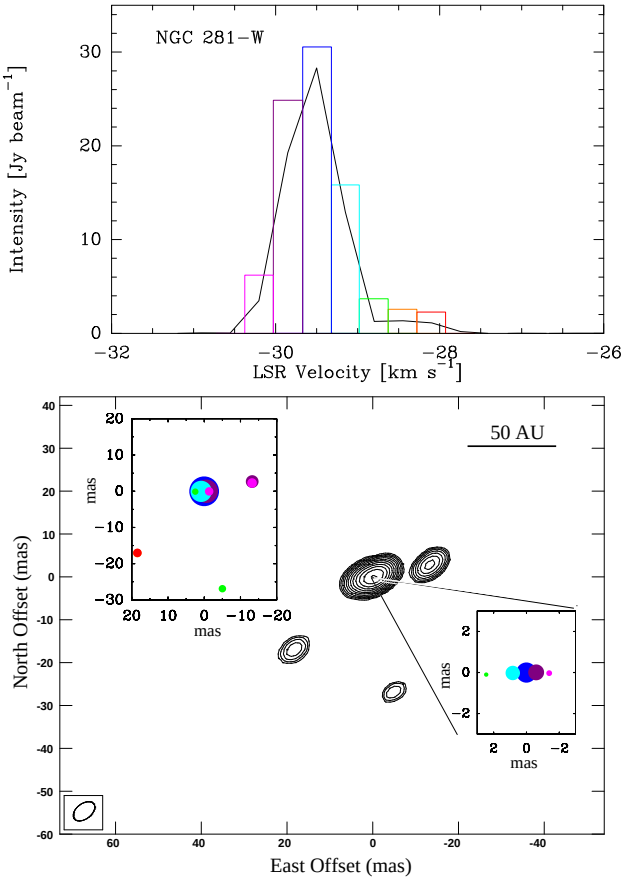

Figure 5.11: Velocity-integrated map and spectrum of NGC 281-W. Position offset (0,0) corresponds to the position listed in Table 5.2. Maser spots are indicated with color codes for different radial velocities. The areas of the colored circles and the colored histogram entries in the spectrum are scaled to the peak flux of that spot. The black line in the spectrum is the intensity of the maser within a selected surface, which is not necessarily the same as the intensity of the maser spot retrieved from a Gaussian fit. Contour levels start at 0.5 Jy beam^{-1} km s^{-1} and increase by factors of $\sqrt{2}$.

5.5 Discussion

5.5.1 Space motions

Table 5.4: Peculiar motions

Source	$R_0 = 8.5$ kpc, $\Theta_0 = 220$ km s^{-1}			$R_0 = 8.4$ kpc, $\Theta_0 = 254$ km s^{-1}		
	U (km s^{-1})	V (km s^{-1})	W (km s^{-1})	U (km s^{-1})	V (km s^{-1})	W (km s^{-1})
ON 1	18±8	−19±3	4±10	7±8	−21±3	4±10
L 1206	2±4	−16±2	0±6	−1±4	−16±2	0±6
L 1287	13±2	−18±2	−3±2	10±2	−18±2	−3±3
NGC 281-W	13±2	−3±2	−9±2	6±2	−3±2	−9±2
S 255	1±3	−4±12	3±7	2±3	−4±12	3±7

With parallax and proper motion measurements, one can calculate the full space motion of

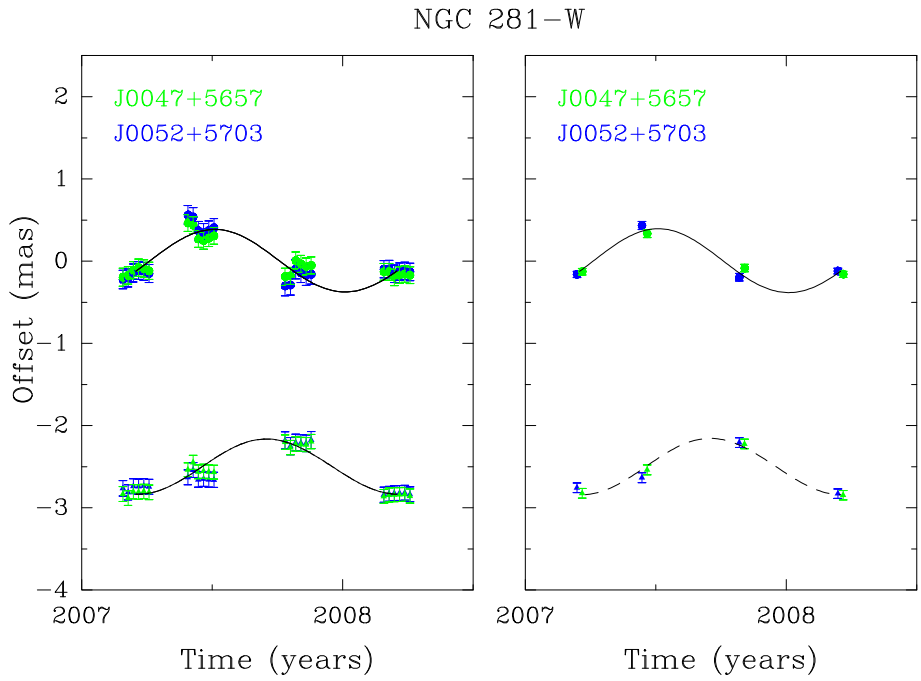

Figure 5.12: Results of the parallax fit for NGC 281-W based on six maser spots. The left graph shows a fit on all data, while the right graph is a fit on the averaged data sets. The filled dots mark the data points in right ascension, while the filled triangles mark the declination. The solid line is the resulting fit in right ascension, the dashed line in declination. Different colors indicate a different background source.

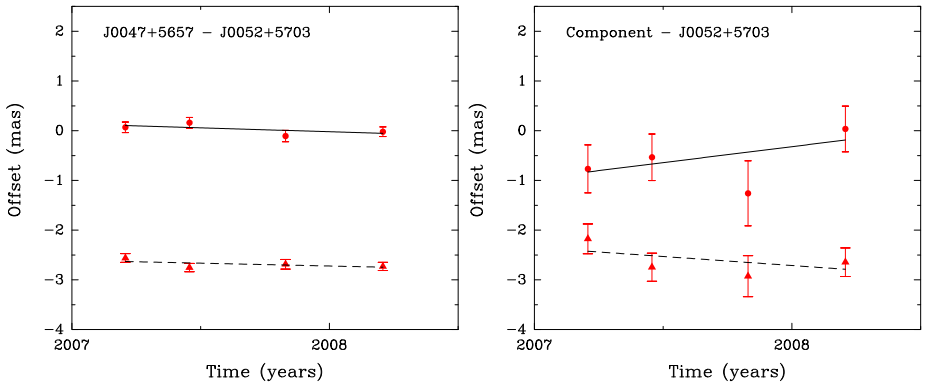

Figure 5.13: *Left:* Variation of the separation between background sources J0047+5657–J0052+5703 belonging to NGC 281-W. *Right:* The proper motion fit on the component of J0052+5703 with respect to the central source J0052+5703. The solid line and the dots represent the right ascension data, while the dashed line and the filled triangles represent the declination data.

the masers in an SFR in the Galaxy. Using an accurate model of Galactic dynamics (Galactic rotation speed, Θ_0, distance of the Sun to the Galactic center, R_0, rotation curve) for a source and removing the modeled contribution of Galactic rotation allows one to retrieve source peculiar motion relative to a circular orbit. The peculiar motion is described by the vectors U, V, and W, locally toward the Galactic center, toward the direction of rotation and toward the North Galactic Pole, respectively.

In Table 5.4, the peculiar motions of our sources are given for two different Galactic models:

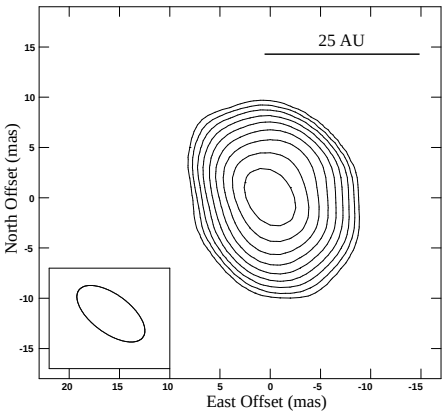

Figure 5.14: Phase-referenced image for maser S 255 at channel 4.6 km s $^{-1}$. Position offset (0,0) corresponds to the position listed in Table 5.2. Contour levels start at 0.23 Jy beam^{-1}, and increase by factors of $\sqrt{2}$.

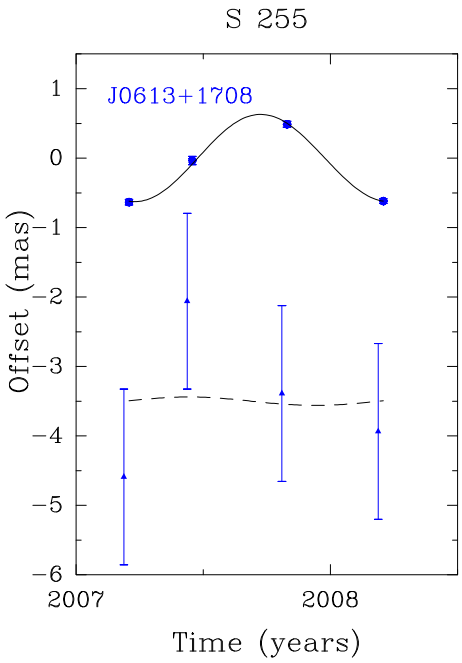

Figure 5.15: Results of the parallax fit for S 255 based on one maser spot at 4.6 km s $^{-1}$. The filled dots mark the data points in right ascension, while the filled triangles mark the declination. The solid line is the resulting fit in right ascension, the dashed line in declination.

the I.A.U. recommended values for the LSR motion $R_0 = 8.5$ kpc, $\Theta_0 = 220$ km s^{-1} in columns 2–4; a new model with $R_0 = 8.4$ kpc, $\Theta_0 = 254$ km s^{-1}, based on a large sample of trigonometric parallax measurements (Reid et al. 2009b), in columns 5–7. Both models adopt the Hipparcos values for the Solar motion (Dehnen & Binney 1998) and assume a flat rotation curve. We used the parallaxes and proper motions as are listed in Table 5.3, where the uncertainty introduced by the apparent movement of the background sources was included in the proper motion uncertainty of the source.

In Fig. 5.16 we plot the SFRs studied in this work at their determined distances with their peculiar motion in the Galactic plane, after removing the Galactic rotation. For either model, it is clear that three SFRs show a similar lag on circular rotation as the SFRs studied by Reid et al.

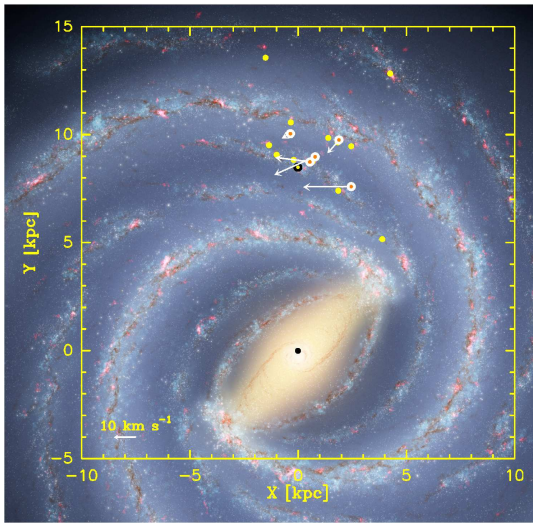

Figure 5.16: An artist's impression of a plane-on view of our Galaxy (image credit: R. Hurt NASA/JPL-Caltech/SSC), overlaid with parallax measurements of water and methanol masers between 60°< l < 240°taken from Reid et al. (2009b), in which recent parallax measurements have been put together to study the Galactic structure. The black dot marks the Galactic center, the yellow dot encircled with black the Sun, the yellow dots mark the parallaxes taken from the literature, the orange dots encircled with white, and white arrows mark the parallaxes and peculiar motions obtained in this work. The peculiar motions are shown after removing the Galactic rotation assuming the values of $R_0 = 8.4$ kpc and $\Theta_0 = 254$ km s^{-1}.

(2009b), while two have a circular rotation close to zero lag. For NGC 281-W, the zero lag can be understood from its large distance from the Galactic disk ($b \simeq -6°$) and the dominant contribution from the expanding super bubble to the peculiar motion of this SFR (see Sect. 5.5.5). For S 255, it is not clear why its circular velocity is close to Galactic rotation (Sect. 5.5.6). The motion towards the Galactic center, U, tends to be positive for most of the SFRs.

Recently, McMillan & Binney (2009) have published a reanalysis of the maser astrometry presented by Reid et al. (2009b). They fitted the data with the revised solar peculiar motion of Binney (2009), mentioned in McMillan & Binney (2009), where the V component of the solar peculiar velocity, $V_\odot$, is increased from 5.2 km s^{-1} to 11 km s^{-1}. With a larger $V_\odot$ the lag of SFRs on Galactic rotation would decrease to $\sim$ 11 km s^{-1}, which agrees with the expected velocity dispersion for young stars of $\sim$ 10 km s^{-1} (Aumer & Binney 2009). However, even when considering the revised $V_\odot$, we note that most SFRs still rotate more slowly than the Galactic rotation (by $\sim$ 11 km s^{-1}) and that their velocities are not randomly dispersed.

5.5.2 Onsala 1

Our trigonometric parallax measurement places ON 1 on a distance from the Sun of $2.57^{+0.34}_{-0.27}$ kpc, somewhat closer than the (near) kinematic distance of 3.0 kpc, based on the methanol maser line at 15 km s^{-1}. The latter assumes a flat rotation curve with as distance of the Sun to the Galactic center, $R_0 = 8.5$ kpc, and for the Galactic rotation speed, $\Theta_0 = 220$ km s^{-1}. However, it is farther than the commonly adopted (near) kinematic distance of 1.8 kpc based on formaldehyde at $v_{\rm LSR} = 11.2$ km s^{-1} (MacLeod et al. 1998) using the Galactic rotation curve of Wouterloot & Brand (1989), with $R_0 = 8.5$ kpc, $\Theta_0 = 220$ km s^{-1}. Our result resolves the near/far kinematic distance ambiguity and locates ON 1 in the Local spur consistent with the near kinematic distance.

We found different proper motions for the northern and southern maser groups (Table D.1). The resulting difference in the east-west direction was small, $\mu_\alpha = 0.18 \pm 0.24$ mas yr^{-1}, but in the north-south direction, the southern group was moving by $\mu_\delta = -0.77 \pm 0.12$ mas yr^{-1} away from

the northern group. At a distance of 2.6 kpc, this corresponds to a relative speed of 9.4 km s^{-1}.

This large proper motion may be explained by the masers being located in the molecular gas surrounding an expanding HII region, as suggested by Fish & Reid (2007) and Su et al. (2009). The HII region is located at ($\alpha = 20^{\rm h}10^{\rm m}09.^{\rm s}03$, $\delta = +31°31'35.''4$, J2000) and between the two maser groups. The radial velocity of the HII region, from the H76α recombination line, is 5.1 ± 2.5 km s^{-1} (Zheng et al. 1985). The methanol masers would be (with respect to the rest frame of ON 1 at 5.1 km s^{-1}) in a blue-shifted component at $\sim$0 km s^{-1}, northward, and a red-shifted component at $\sim$15 km s^{-1}, southward of the HII region. Also, the hydroxyl masers in ON 1 provide some confirmation of this scenario (Nammahachak et al. 2006; Fish & Reid 2007). The expansion velocities of the masers, calculated by assuming a linear expansion from the center of the HII region, would be 5.8 km s^{-1} and 3.6 km s^{-1} for the northern and southern maser groups, respectively.

5.5.3 L 1206

For L 1206, the trigonometric parallax distance, $0.776^{+0.104}_{-0.083}$ kpc, is shorter than the kinematic distance; 1.0 kpc (based on a hydroxyl maser, at $v_{\rm LSR} = -8.5$ km s^{-1}, using the Galactic rotation curve of Wouterloot & Brand (1989) with $R_0 = 8.5$ kpc, $\Theta_0 = 220$ km s^{-1}, MacLeod et al. 1998), 1.23 kpc (ammonia, $v_{\rm LSR} = -9.9$ km s^{-1}, using the Galactic rotation curve of Brand & Blitz (1993), with $R_0 = 8.5$ kpc, $\Theta_0 = 220$ km s^{-1}, Molinari et al. 1996) and 1.4 kpc (6.7 GHz methanol, flat rotation curve, $R_0 = 8.5$ kpc, $\Theta_0 = 220$ km s^{-1}). Our result places L 1206 in the Local spur. Cep A, a nearby (3.°8 separation, P.A. 126 °) star-forming region, is located at a distance of 700 ± 39 pc, as determined by a parallax measurement of 12.2 GHz methanol masers (Moscadelli et al. 2009). The L 1206 SFR therefore seems to be in the same part of the Local arm as Cep A. L 1206 is a dark cloud with an infrared source, IRAS 22272+6358A, which coincides with the methanol maser emission and a 2.7 mm dust continuum peak (Beltrán et al. 2006). Since neither 2 cm nor 6 cm radio emission is detected (Wilking et al. 1989; McCutcheon et al. 1991), L 1206 is thought to be in a young phase prior to the formation of an HII region. Beltrán et al. (2006) report large CO outflows, and put the systemic velocity of the ambient medium between [−13.5, −8.5] km s^{-1}, consistent with our systemic velocity range of [−13.3, −10.9] km s^{-1}.

5.5.4 L 1287

The parallax for L 1287 sets it at a distance of $0.929^{+0.034}_{-0.033}$ kpc. This is close to the photometric distance of $\sim$850 pc from (Yang et al. 1991), which placed L 1287 in the Local arm. However, the kinematic distance based on the methanol maser line would place L 1287 at 2 kpc in the Perseus arm.

Methanol masers in the dark cloud L 1287 are located at the base of the bipolar CO outflow (Yang et al. 1991) originating in the main core of the cloud. The infrared point source (IRAS 00338+6312) in the center of the core indicates a protostellar object surrounded by cold, high density NH_3 (1,1) gas (Estalella et al. 1993).

5.5.5 NGC 281-W

There are numerous distance estimates for NGC 281-W in the literature. Optical photometry places the cloud between 2 and 3.68 kpc (Sharpless 1954; Cruz-González et al. 1974; Henning et al. 1994; Guetter & Turner 1997), while the kinematic distance is 3 kpc (Lee & Jung 2003), based on a $v_{\rm LSR} = -30$ km s^{-1}, using the Galactic rotation curve of Clemens (1985) and $R_0 = 8.5$ kpc, $\theta_0 = 220$ km s^{-1}. The radial velocity of the methanol maser line at −29 km s^{-1}, assuming a flat Galactic rotation curve, and $R_0 = 8.5$ kpc, $\theta_0 = 220$ km s^{-1}, would place NGC 281-W at 2.5 kpc.

Recently, Sato et al. (2008) reported a water maser parallax value of 0.355 ± 0.030 mas, measured with the VERA interferometer, corresponding to a distance of 2.82 ± 0.24 kpc. We measured a parallax of 0.421 ± 0.022 mas, arriving at a distance of $2.38^{+0.13}_{-0.12}$ kpc. These distance measurements agree with Sato et al. (2008) within 2σ of the joint uncertainty. Also, our proper motion agrees within 1σ with the proper motion by Sato et al. (2008), and our radial velocity ($v_{\rm LSR} \sim -29$ km s^{-1})

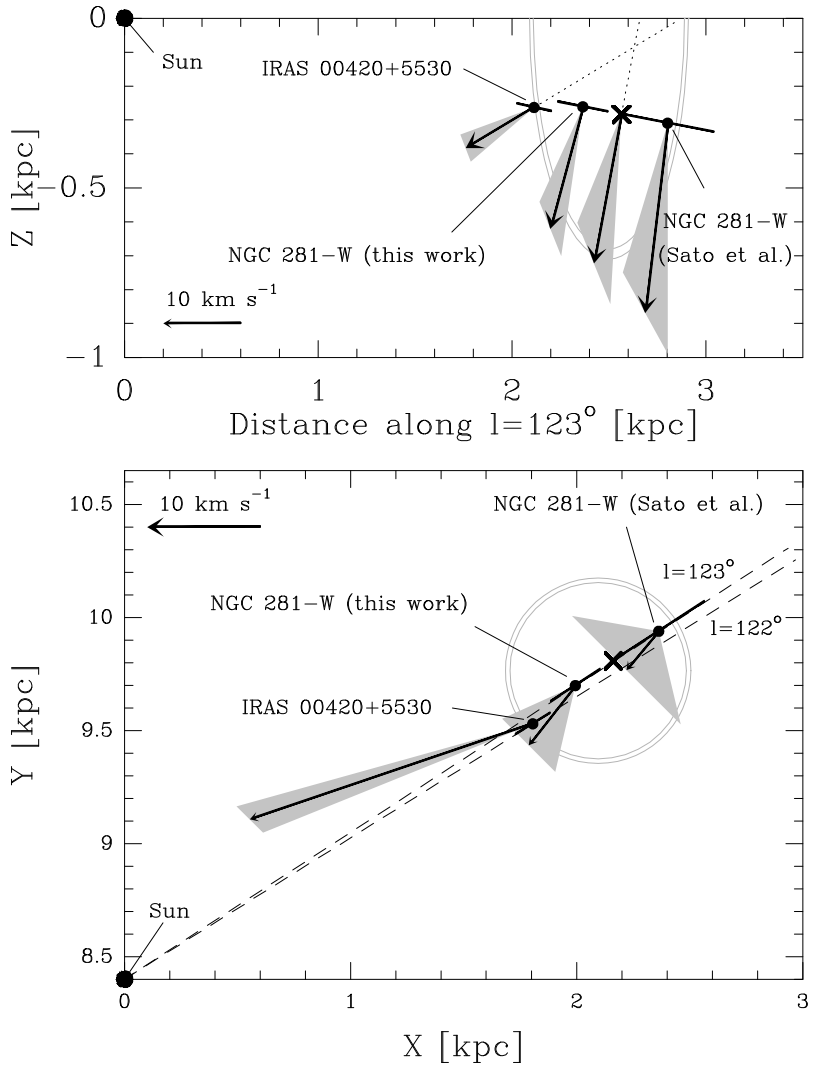

Figure 5.17: Lower panel: a face-on view of the Galactic plane. The Galactic longitudes of NGC 281-W ($l \simeq 123°$) and IRAS 00425530 ($l \simeq 122°$) are indicated by dashed lines. The top panel shows a cross-section of the Galactic plane along the Galactic longitude of NGC 281-W (123°). The vertical coordinate of this plot is the direction perpendicular to the Galactic plane. We plot NGC 281-W and IRAS 00420+5530 as black dots, together with the respective distance error. Black arrows show the peculiar motion of the source after removing the Galactic rotation ($R_0 = 8.4$ kpc, $\Theta_0 = 254$ km s^{-1}). The errors in peculiar motion are indicated by the gray cones. The light-gray circles mark the super bubble with the center of the bubble at a distance of 2.5 kpc and a radius of 0.4 kpc, adopted after Sato et al. (2008). The cross marks the averaged distance of 2.58 kpc. The dotted lines show the backward prolongation of the proper motion of NGC 281-W and IRAS 00420+5530.

is close to that of the water masers ($v_{\rm LSR} \sim -31\,{\rm km\ s^{-1}}$). It is unlikely that the water and methanol masers originate at such different depths into the SFR that it would affect the distance. For example, in the SFR W3(OH), the water and methanol maser parallaxes are in good agreement (Xu et al. 2006; Hachisuka et al. 2006).

NGC 281-W is an SFR that lies near the edge of a super bubble in the Perseus arm (Megeath et al. 2003; Sato et al. 2007). Our slightly shorter distance would change the position of NGC 281-W on this super bubble. Another SFR located on this bubble has a parallax determined distance: IRAS 00420+5530 at 2.17 ± 0.05 kpc (Moellenbrock et al. 2009). This allows to compare the distances and peculiar motions of both SFRs, and check whether the expanding super bubble, with the expansion center at 2.5 kpc adopted after Sato et al. (2008), can be responsible for the peculiar motions of both of them. We calculated the peculiar motions of IRAS 0042+5530 after Moellenbrock et al. (2009) and NGC 281-W after Sato et al. (2008) and our results. The bottom panel of Fig. 5.17 shows the peculiar motions in a face-on view of the Galactic plane. From the figure can be seen that the U component of NGC 281-W, representing the vector toward the Galactic center, is positive and non-zero in both our study and the work of Sato et al. (2008). This means that NGC 281-W is moving toward the Galactic center, which is the expected movement for the near side of an expanding bubble. In the top panel of Fig. 5.17 the peculiar motions of both SFRs are shown projected on a cross-section of the Galactic plane along the longitude of NGC 281-W, $l = 123°$. The average distance to NGC 281-W based on Sato et al. (2008) and this work, $2.58^{+0.27}_{-0.23}$ kpc, is marked in this panel as a cross. If we prolong the peculiar motion backwards of both IRAS 00420+5530 and the average result for NGC 281-W, they intersect at a distance from the Sun of 2.65 kpc and at a Galactic latitude of $\sim -0.°1$. This suggests that, if indeed both SFRs are expanding linearly from one expansion center, the expansion center is offset from the previously assumed position. However, this offset center of expansion is difficult to understand when looking at the peculiar motion of both SFRs in the Galactic plane (Fig. 5.17, bottom panel), since the motion does not seem to originate in one mutual expansion center; hence, it is difficult to pinpoint the characteristics of the super bubble if the peculiar motions and distances of only two SFRs are all that are known.

5.5.6 S 255

For S 255, the parallax distance, $1.59^{+0.07}_{-0.06}$ kpc, is much closer than the commonly used photometric distance of 2.5 kpc (Moffat et al. 1979; Blitz et al. 1982). S 255 is an individual HII region, associated with a complex of HII regions. The methanol maser emission coincides with a filament of cold dust and molecular gas between two HII regions, S 255 and S 257. Minier et al. (2007) studied the star formation in this filament, which they propose is possibly triggered by the compression of the filament by the two HII regions. They find several molecular clumps in this filament. At distance of ≈ 2.5 kpc, the masses of the clumps, determined from the submillimeter dust continuum, are around $300\,{\rm M_\odot}$ (Minier et al. 2007). However, if we place S 255 at the parallax determined distance of 1.6 kpc, the clump masses would drop by 60% to $\sim 120\,{\rm M_\odot}$.

5.5.7 Shifting of source position

In AIPS a position shift of a source can be performed with 'CLCOR'. Usually one shifts the epoch (J2000) coordinate. CLCOR calculates from the new epoch coordinate the new apparent coordinate and imposes an apparent coordinate shift between the old apparent coordinate and the new one. The EVN correlator calculates the apparent positions at the end of the first scan. However, in AIPS the apparent position is defined at 0 UT of the first day of the observation. Hence, even a zero-shift results in shifting by the difference of the two apparent coordinates. Therefore, using the EVN apparent coordinates one cannot shift the source position just by the requested amount, but rather by the requested amount plus that difference. When imposing a shift one always ends up with the AIPS apparent positions. For consistency one then should reduce all the data for all the epochs using the AIPS apparent positions instead of the EVN ones. Although it should be possible to correct for this difference in registration, it would have required a software effort beyond the

scope of the current project. Therefore we chose to discard some of the first-epoch data.

To avoid these problems one should use the same correlator positions for all epochs. When the maser position is not yet accurately known, one can use a short pre-correlation of a part of the data which will allow to image the maser and determine its position with mas accuracy. This new position can then be used for the full correlation of the dataset.

5.6 Summary

We measured parallaxes of 6.7 GHz methanol masers using the EVN towards five SFRs, achieving accuracies approaching 20 μas. The primary results are summarized as follows.

1. We report trigonometric parallaxes for five star-forming regions, the distances to these sources are $2.57^{+0.34}_{-0.27}$ kpc for ON 1, $0.776^{+0.104}_{-0.083}$ kpc for L 1206, $0.929^{+0.034}_{-0.033}$ kpc for L 1287, $2.38^{+0.13}_{-0.12}$ kpc for NGC 281-W, and $1.59^{+0.07}_{-0.06}$ kpc for S 255.

2. Galactic star-forming regions lag circular rotation on average by $\sim$17 km s^{-1}, a value comparable to those found recently by similar studies (Reid et al. 2009b).

3. Individual 6.7 GHz methanol maser spots are stable over a period of < 2 years for most of the maser spots. The internal motions of the maser spots are weak ($\sim 0.5 - 1$ km s^{-1}) and rectilinear.

4. Measurements at 6.7 GHz are less disturbed by the troposphere, as expected. However, the ionospheric delay cannot be ignored and is likely not to be completely removed by using the JPL GPS–IONEX maps to calculate propagation delays. Continuum measurements of background sources show that most of them have significant structure that is evident from the large (up to 1–2 mas) apparent movements between pairs of background sources. This additional uncertainty from the apparent movement does not prohibit a determination of the proper motion; however, it encreases its error bars. The parallax uncertainty can be affected as well, if the cause of the apparent movement between the background sources are internal structure changes, which do not need to be linear. Two background sources should be a minimum for astrometric measurements at 6.7 GHz, so three or more background sources are recommended.

CHAPTER 6

Summary

6.1 High extinction clouds

We made for the first time infrared extinction maps using Spitzer mid-infrared data of the first and fourth Galactic quadrant and compiled a catalog of compact high extinction features. 25 newly found high extinction clouds were studied in detail. First by using the IRAM 30m bolometer observations of the dust continuum emission and pointed ammonia observations with the Effelsberg 100m telescope. Then these clouds were observed in a molecular line survey with the IRAM 30m and the APEX telescopes. Finally, one extinction cloud was studied in more detail using single dish mapping with the IRAM 30m telescope and SMA interferometer observations to investigate its spatial distribution and kinematics.

The extinction-selected clouds are found at kinematic distances between 1–7 kpc. Most of them are concentrated in the range of 1–4 kpc, and trace the same regions of the Galactic plane as infrared dark clouds. The extinction method is more sensitive to large scale low column density clouds than the bolometer observations at 1.2 mm emission, which resulted in a few non detections of clouds in the mm emission despite a mean visual extinction of ∼30 magnitudes from the extinction map. In general, there is a good correlation between the cloud masses derived from the extinction maps and from the 1.2 mm emission. From the 1.2 mm emission maps, we have found clumps with column densities of 3–30 $\times$ 10^{22} cm^{-2} and masses of 12–400 $M_{\odot}$. Rotational temperatures of ammonia show that these clumps are cold, $T_{\rm rot}$ 10–25 K. Given the found clump masses, not all clumps in the high extinction clouds will be able to form massive stars. It is expected for cluster-forming regions to produce low and high-mass stars, thus to have a wide range in masses.

High extinction clouds contain a wide range of evolutionary stages. 70% of the high extinction clouds are associated with infrared dark clouds, however several clouds show more evolved stages of ongoing (massive) star formation. Three different classes of clouds are proposed:

- Diffuse high extinction clouds have no signs of masers, H II regions or extended 4.5 μm objects, which are general signposts of star formation. The 1.2 mm emission shows no mm peaks above twice the mean emission of the cloud. These clouds are cold (with an average temperature of 13.5 K) and line widths far above the thermal value mark the importance of turbulence. The observations suggest that the diffuse clouds are in an early phase, where the accretion of gas and dust into clumps is either on the verge of beginning or might never reach the necessary column density to form stars.

- When the clumps manage to accrete more matter so that the mm emission exceeds twice the mean cloud emission they enter the next (peaked) stage. During the peaked stage already some clouds show more than one clump, which indicates that star formation can start in different regions of the same cloud at different times.

- Multiply peaked clouds show many signs of ongoing star formation, such as detections of masers, H II regions or extended 4.5 μm objects. Several clumps are infrared bright and show generally slightly higher temperatures and turbulence than diffuse or peaked clouds. Clumps within a cloud are not necessary in the same state, and will likely not all form massive stars. We find four clumps that satisfy the theoretical column density requirement for high-mass star formation.

In the molecular line survey we classified sources to show infall or expansion based on the profile of the HCO^+(1-0) line. For the peaked clouds we find a significant excess of infall sources, while for the other two classes no such excess was found. Either the infall phase lasts longer for the peaked clouds than for the other classes, or, in the diffuse clouds the infall did not start yet, and in the multiply peaked clouds – which host clumps in various stages – there are already clumps in which the feedback from YSOs will have halted further accretion. The infall velocities and mass infall rates, derived from the line profiles, follow the proposed evolutionary sequence - they increase from the diffuse to the multiply peaked clouds. The derived mass infall rates ranged between 0.6 and $9.7 \times 10^{-3}\,M_\odot\ yr^{-1}$, which is much higher that what is found for low-mass stars and agrees with previous high-mass studies.

Investigations of the volume and column densities and temperatures via other molecular transitions confirmed the results from the initial ammonia and 1.2 mm continuum observations. High extinction clouds contain cold (10 K <T< 40 K) and dense ($n_{H_2} \sim 10^5\,cm^{-2}$) clumps. Most of these clumps contain evidence for YSOs, based on the presence of 24 μm sources, CH_3CN or H_2CO emission. The presence of a YSO does not depend on the physical size of the clump, since YSOs are found over the whole range of clump diameters. However, there seems to be a (hydrogen) column density cutoff at $4 \times 10^{22}\,cm^{-2}$, below which less or no YSOs are found. The cutoff is most clear in the H_2CO emission and least in the detection of 24 μm sources. We found in our sample only a few prestellar clumps, sources which showed no evidence for a YSO but did have infall signatures. These prestellar clumps are often located close to infrared bright sources. Possibly these provide the first trigger to start the gravitational collapse of the clump. This agrees with our observation that starless clumps, which show no evidence of YSOs nor infall, are usually in an infrared dark environment. We find much less starless and prestellar clumps than clumps with a YSO. This is possibly an indication of the short timescales associated with the starless and prestellar phases, which was already observed by Motte et al. (2007) for the Cygnus X region.

We imaged cloud G017.19+00.81, which is located close the active star-forming nebula M16. The cloud consists of a central clump and two arcs, visible in the 1.2 mm emission imaged with the bolometer, and contained in total four clumps all at the same distance as M16. With the single dish maps we explored the spatial correlation of N_2H^+(1-0) and $C^{18}O$(2-1) emission with the continuum emission as a time marker. The results agree with the observed $C^{18}O$ depletion. Early clumps have few depletion and weak N_2H^+(1-0) emission, both, the N_2H^+ but especially the $C^{18}O$ emission correlates well with the continuum. Late clumps have high depletion levels and strong N_2H^+(1-0) emission, and while the N_2H^+ emission correlates well with the continuum emission, the $C^{18}O$ emission does not – it is probably depleted from the gas phase. The increase in resolution by imaging with an interferometer revealed fragmentation in two of the clumps on scales of ∼0.05 pc. We found more ^{12}CO emission at high velocities than with the single dish observations – in almost all clumps an outflow was detected. As outflows were also found in infrared dark clumps, it seems that in the process of star formation an outflow precedes the infrared emission. Cloud G017.19+00.81 contained one clump, whose density already satisfies the $1 \times 10^{23}\,cm^{-2}$ threshold for massive star formation (Krumholz & McKee 2008). We detected a methanol line at 229.8 GHz and SO emission toward its outflow. Apparently, during massive star formation the outflows can be strong enough to shock material to densities $n_{H_2} > 10^6\,cm^{-3}$ – based on the critical densities of these molecules.

Not all the clumps of cloud G017.19+00.81 belong to one shell or bubble process. The most southern clump is likely created in a collect and collapse scenario from the nearby HII region. The remaining arc-shaped structure is possibly formed by an expanding HII region. H-α images, from the Super COSMOS H-alpha Survey, showed a weak H-α emission arc that could be responsible for the shape of cloud G017.19+00.81. Which young star is the origin of the ionizing emission is difficult to find, since the M16 nebula is a active star-forming region with many candidates.

In summary, our selection of a new sample of high extinction clouds was successful in revealing molecular clumps in the earliest stages of (massive) star formation.

6.2 Methanol masers

Emission from the 6.7 GHz methanol maser transition is very strong, is relatively stable, has small internal motions, and is observed toward numerous massive star-forming regions in the Galaxy. We performed high-precision astrometry using this maser transition to obtain accurate distances to their host regions. Eight strong masers were observed during five epochs of VLBI observations with the European VLBI Network between 2006 June, and 2008 March.

Individual 6.7 GHz methanol maser spots are stable over a period of < 2 years for most of the maser spots. The internal motions of the maser spots are small ($\sim 0.5 - 1$ km s^{-1}). As expected, measurements at 6.7 GHz are less disturbed by the troposphere than higher frequency observations. However, the ionospheric delay cannot be ignored and is likely not to be completely removed by using the JPL GPS–IONEX maps to calculate propagation delays. Continuum measurements of background sources show that most of them have significant structure that is evident from the large (up to 1–2 mas) apparent motions between pairs of background sources. This additional uncertainty from the apparent motion does not prohibit a determination of the proper motion; however, it increases its error bars. The parallax uncertainty can be affected as well, if the cause of the apparent motion between the background sources are internal structure changes, which do not need to be linear. Two background sources should be a minimum for astrometric measurements at 6.7 GHz, but three or more background sources are recommended.

We report trigonometric parallaxes for five star-forming regions, with accuracies as good as ~ 22 μas for sources with declinations $> 17°$. Distances to these sources are $2.57^{+0.34}_{-0.27}$ kpc for ON 1, $0.776^{+0.104}_{-0.083}$ kpc for L 1206, $0.929^{+0.034}_{-0.033}$ kpc for L 1287, $2.38^{+0.13}_{-0.12}$ kpc for NGC 281-W, and $1.59^{+0.07}_{-0.06}$ kpc for S 255. The distances and proper motions yield the full space motions of the star-forming regions hosting the masers, and we find that these regions lag circular rotation on average by $\sim$17 km s^{-1}, a value comparable to that found recently by similar studies.

6.3 Outlook

The temperature structure of clouds reveals if they are heated from the inside, most likely by protostars, or if they are heated from the outside by, for example, cosmic rays. The latter type of cloud is a very promising candidate to harbor the cold early stages of massive star formation. Ammonia maps are a good tool to study the temperature structure of the high extinction clouds. We have already acquired Very Large Array (VLA) and Effelsberg ammonia maps, that are waiting to be reduced and combined. The observations included clouds from all three classes of HECs, to see if the temperature structure changes for different classes.

Another aim is to widen our "Galactic" view of the high extinction clouds. We want to complement the first Quadrant sources, studied in this thesis, with high extinction clouds in the fourth Galactic Quadrant. The latter have lower declinations and are visible only from the southern hemisphere. These "southern" HECs were already observed with the APEX telescope, using the LABOCA bolometer to study the continuum emission and several molecular lines for obtaining, amongst others, the kinematic distances.

A good knowledge of the early diffuse clouds is very important for the evolutionary scenario. However, in several molecular transitions these clouds were so weak that many were not detected.

By reobserving these sources, using longer integration times, we want to gather more information to understand if these diffuse HECs are the precursors of peaked and multiply peaked HECs.

Cygnus X is a molecular cloud complex in the Galaxy, which harbors various famous massive star-forming regions such as W 75 and DR 21. It has been targeted by many star formation studies (e.g., Schneider et al. 2006; Motte et al. 2007; Kirby 2009; Schneider et al. 2010) that assume the Cygnus X complex to be at the photometric distance of 1.7 kpc, which was determined for the OB2 association (Knödlseder 2000). However, it is uncertain if the whole complex is at the same distance. In 2009 we started the parallax measurements using 6.7 GHz methanol masers to accurately determine the distance to Cygnus X. This region has five strong 6.7 GHz methanol masers, which were all detected on milli arcsecond scales with the EVN. Compared to the previous observations, we will improve our accuracy because of i) a larger number of epochs, ii) better coverage of the peaks of the parallax signal, and iii) probably a large number of usable spots in W 75N. Thus, we expect to reach an accuracy of better than $\sim 30\,\mu$as, which corresponds to error bars of 5% at a distance of 1.7 kpc.

APPENDIX A

Tables to Chapter 2

Table A.1: Catalog of high extinction clouds (HECs) with the peak color excess (C.E.), $E<(3.6\,\mu\mathrm{m}-4.5\,\mu\mathrm{m})>$

HEC name	R.A. (h:m:s) (J2000)	Dec. (°:′:″) (J2000)	C.E. (mag)	HEC name	R.A. (h:m:s) (J2000)	Dec. (°:′:″) (J2000)	C.E. (mag)
1st quadrant clouds				*1st quadrant clouds*			
G011.09–00.54	18:12:01.2	–19:36:07	0.40	G024.07+00.18	18:34:32.8	–07:47:49	0.28
G012.54–00.35	18:14:15.8	–18:14:11	0.29	G024.18+00.03	18:35:17.0	–07:46:11	0.27
G012.65–00.17	18:13:49.6	–18:02:53	0.45	G024.37–00.15	18:36:16.5	–07:40:56	0.32
G012.73–00.58	18:15:33.2	–18:08:45	0.29	G024.43–00.24	18:36:42.2	–07:40:06	0.31
G012.89+00.48	18:11:52.7	–17:31:27	0.55	G024.50+00.09	18:35:39.2	–07:27:13	0.27
G013.28–00.34	18:15:40.8	–17:34:32	0.57	G024.61–00.33	18:37:21.6	–07:33:08	0.31
G013.38–00.27	18:15:38.8	–17:27:26	0.47	G024.64+00.15	18:35:41.4	–07:18:22	0.38
G013.91–00.51	18:17:34.8	–17:06:07	0.58	G024.82–00.11	18:36:57.6	–07:16:02	0.26
G013.97–00.45	18:17:27.6	–17:01:34	0.51	G024.94–00.15	18:37:19.4	–07:10:34	0.35
G014.33–00.65	18:18:55.4	–16:48:12	0.53	G025.15–00.28	18:38:09.6	–07:02:52	0.32
G014.39–00.75	18:19:24.1	–16:47:34	0.42	G025.63–00.12	18:38:30.1	–06:32:55	0.32
G014.45–00.09	18:17:06.1	–16:25:37	0.50	G025.79+00.81	18:35:26.6	–05:58:57	0.19
G014.63–00.57	18:19:13.6	-16:29:56	0.57	G028.53+00.21	18:42:39.1	–03:49:20	0.30
G014.72–00.21	18:18:04.7	–16:14:47	0.46	G030.48–00.38	18:48:20.1	–02:21:16	0.29
G015.09–00.60	18:20:14.0	–16:06:38	0.33	G030.62+00.18	18:46:34.4	–01:58:31	0.31
G015.21–00.62	18:20:33.2	–16:00:37	0.40	G030.73+00.12	18:47:00.0	–01:54:22	0.32
G015.51–00.42	18:20:23.8	–15:39:22	0.31	G030.90+00.00	18:47:43.1	–01:48:24	0.30
G016.33–00.55	18:22:27.7	–14:59:20	0.31	G031.05+00.27	18:47:02.7	–01:33:08	0.30
G016.37–00.21	18:21:18.7	–14:48:01	0.36	G034.03–00.33	18:54:36.9	+00:49:43	0.30
G016.54–00.39	18:22:19.1	–14:43:50	0.28	G034.11+00.06	18:53:22.0	+01:04:37	0.30
G016.81–00.33	18:22:35.9	–14:27:46	0.30	G034.34–00.90	18:57:12.8	+00:50:40	0.30
G016.93+00.24	18:20:46.0	–14:05:28	0.30	G034.35–00.72	18:56:35.7	+00:56:11	0.34
G017.19+00.81	18:19:12.9	–13:35:18	0.37	G034.71–00.63	18:56:55.6	+01:17:44	0.41
G018.11–00.30	18:25:00.0	–13:18:15	0.26	G034.77–00.81	18:57:40.0	+01:15:57	0.39
G018.15–00.39	18:25:24.8	–13:18:34	0.28	G034.85+00.43	18:53:23.6	+01:54:07	0.34

Table A.1: continued.

HEC name	R.A. (h:m:s) (J2000)	Dec. (°:′:″) (J2000)	C.E. (mag)	HEC name	R.A. (h:m:s) (J2000)	Dec. (°:′:″) (J2000)	C.E. (mag)
G018.26–00.24	18:25:05.3	–13:08:26	0.40	G034.98+00.30	18:54:06.3	+01:57:43	0.31
G018.48–00.18	18:25:16.9	–12:54:56	0.26	G035.19–00.75	18:58:13.9	+01:40:07	0.59
G018.63–00.06	18:25:09.3	–12:43:43	0.29	G035.49–00.30	18:57:10.4	+02:08:27	0.38
G018.84–00.49	18:27:05.1	–12:44:30	0.29	G036.42–00.15	18:58:20.4	+03:02:04	0.27
G018.87–00.42	18:26:54.1	–12:41:05	0.27	G037.26+00.09	18:59:01.9	+03:53:40	0.36
G018.99–00.03	18:25:42.8	–12:23:51	0.48	G037.44+00.14	18:59:09.6	+04:04:18	0.28
G019.29+00.06	18:25:56.6	–12:05:11	0.32	G037.48+00.07	18:59:29.3	+04:05:03	0.29
G019.37–00.03	18:26:26.1	–12:03:31	0.36	G037.54+00.20	18:59:08.7	+04:11:44	0.29
G019.62–00.66	18:29:12.2	–12:07:52	0.30	G037.65+00.12	18:59:38.5	+04:15:22	0.29
G019.89–00.54	18:29:16.5	–11:50:27	0.27	G038.93–00.36	19:03:40.9	+05:10:19	0.48
G019.91–00.79	18:30:14.3	–11:56:07	0.25	G044.30+00.03	19:12:17.0	+10:07:02	0.31
G020.10–00.70	18:30:14.1	–11:43:18	0.26	G046.33–00.24	19:17:05.9	+11:47:23	0.32
G022.06+00.21	18:30:40.5	–09:34:11	0.35	G048.90–00.27	19:22:08.9	+14:02:57	0.41
G022.57–00.02	18:32:25.6	–09:13:08	0.26	G049.39–00.31	19:23:16.0	+14:27:17	0.34
G022.85–00.45	18:34:30.3	–09:10:11	0.28	G049.48–00.38	19:23:40.6	+14:30:25	0.60
G022.96+00.03	18:32:59.5	–08:51:08	0.26	G050.06+00.06	19:23:13.0	+15:13:28	0.36
G022.98–00.19	18:33:49.6	–08:55:50	0.26	G050.39–00.41	19:25:34.4	+15:17:32	0.35
G023.09–00.15	18:33:53.3	–08:49:05	0.30	G053.14+00.07	19:29:18.0	+17:56:08	0.46
G023.25–00.36	18:34:54.9	–08:46:36	0.32	G053.21–00.09	19:30:01.7	+17:55:28	0.34
G023.29–00.06	18:33:56.7	–08:36:09	0.35	G053.24+00.06	19:29:31.8	+18:01:14	0.57
G023.35–00.21	18:34:34.5	–08:37:04	0.35	G053.57+00.06	19:30:12.6	+18:18:35	0.37
G023.38–00.12	18:34:19.2	–08:32:53	0.41	G053.63+00.03	19:30:26.3	+18:20:40	0.33
G023.44–00.06	18:34:13.1	–08:27:47	0.31	G053.81–00.00	19:30:54.4	+18:29:32	0.41
G023.45–00.51	18:35:52.4	–08:39:48	0.28	G058.48+00.42	19:39:01.4	+22:46:46	0.30
G023.47+00.09	18:33:43.9	–08:22:18	0.27	G059.79+00.06	19:43:13.2	+23:44:22	0.29
G023.57+00.12	18:33:48.9	–08:16:00	0.26	G059.63–00.18	19:43:47.6	+23:28:45	0.30
G024.02+00.14	18:34:34.9	–07:51:38	0.26				
4th Quadrant clouds				*4th Quadrant clouds*			
G300.91+00.88	12:34:13.0	–61:55:39	1.00	G333.20–00.36	16:21:03.0	–50:29:19	0.43
G305.36+00.19	13:12:33.8	–62:35:12	0.58	G333.22–00.41	16:21:19.3	–50:30:37	0.46
G309.13–00.14	13:45:14.1	–62:21:36	0.52	G333.31–00.36	16:21:32.2	–50:24:41	0.51
G309.37–00.12	13:47:18.1	–62:17:35	0.22	G333.47–00.15	16:21:18.9	–50:08:51	0.44
G309.42–00.62	13:48:37.0	–62:46:00	0.51	G333.49–00.24	16:21:46.8	–50:12:19	0.57
G310.22+00.39	13:53:21.6	–61:36:15	0.66	G333.60–00.22	16:22:09.9	–50:06:32	0.44
G311.57+00.31	14:04:24.5	–61:19:45	0.53	G333.66+00.37	16:19:50.9	–49:38:47	0.68
G311.60+00.41	14:04:25.5	–61:13:36	0.50	G333.75–00.33	16:23:17.6	–50:04:46	0.56
G311.95+00.15	14:07:48.4	–61:22:56	0.49	G333.76+00.35	16:20:25.0	–49:35:26	0.54
G312.11+00.27	14:08:47.1	–61:13:09	0.47	G334.20–00.20	16:24:42.2	–49:39:56	0.43
G313.26–00.72	14:20:34.2	–61:47:42	0.48	G334.45–00.24	16:25:58.1	–49:31:03	0.50
G313.72–00.29	14:22:57.1	–61:13:49	0.69	G335.06–00.42	16:29:22.5	–49:11:57	0.77
G314.21+00.21	14:25:18.8	–60:35:22	0.70	G335.25–00.30	16:29:38.2	–48:59:04	0.68
G314.27+00.09	14:26:07.4	–60:40:48	0.67	G335.28–00.13	16:29:00.9	–48:50:43	0.69
G314.31+00.12	14:26:21.3	–60:38:31	0.58	G335.44–00.23	16:30:07.0	–48:47:56	0.82
G316.45–00.63	14:44:46.4	–60:29:47	0.47	G337.15–00.39	16:37:46.4	–47:38:49	0.79
G316.73+00.06	14:44:28.6	–59:45:12	0.49	G337.45–00.40	16:39:00.2	–47:26:07	0.45
G316.77–00.02	14:45:02.6	–59:48:25	0.89	G337.50–00.19	16:38:18.9	–47:15:09	0.48
G317.70+00.11	14:51:11.0	–59:16:52	0.53	G337.77–00.34	16:40:00.7	–47:08:50	0.53
G317.88–00.26	14:53:46.2	–59:31:40	0.89	G337.93–00.51	16:41:23.3	–47:08:51	0.64
G318.05+00.09	14:53:43.9	–59:08:36	0.90	G339.26–00.41	16:46:01.8	–46:04:40	0.53

Table A.1: continued.

HEC name	R.A. (h:m:s) (J2000)	Dec. (°:′:″) (J2000)	C.E. (mag)	HEC name	R.A. (h:m:s) (J2000)	Dec. (°:′:″) (J2000)	C.E. (mag)
G318.78–00.17	14:59:40.2	–59:02:11	0.84	G339.58–00.13	16:46:00.1	–45:38:54	0.52
G320.19+00.85	15:05:20.9	–57:28:03	0.76	G339.62–00.12	16:46:05.1	–45:37:07	0.41
G321.93–00.01	15:19:42.4	–57:18:40	1.06	G340.06–00.24	16:48:14.9	–45:21:32	0.47
G322.16+00.64	15:18:33.9	–56:38:03	0.67	G340.26–00.24	16:48:59.8	–45:12:03	0.57
G323.19+00.15	15:26:47.7	–56:29:15	0.64	G340.77–00.12	16:50:18.0	–44:44:05	0.44
G323.72–00.28	15:31:44.6	–56:32:20	0.515	G340.93–00.23	16:51:21.4	–44:40:36	0.61
G325.51+00.42	15:39:08.4	–54:55:47	0.57	G341.12–00.42	16:52:51.9	–44:39:26	0.60
G326.40+00.93	15:41:58.5	–53:59:04	0.86	G341.12–00.42	16:52:51.6	–44:39:17	0.61
G326.47+00.70	15:43:16.2	–54:07:35	0.80	G341.21–00.24	16:52:25.3	–44:28:11	0.47
G326.47+00.88	15:42:29.3	–53:59:03	0.95	G342.57+00.18	16:55:21.5	–43:09:13	0.56
G326.62+00.61	15:44:26.9	–54:06:02	0.95	G343.40–00.33	17:00:21.5	–42:49:13	0.52
G326.77–00.12	15:48:22.3	–54:35:29	0.85	G343.75–00.16	17:00:48.1	–42:26:19	0.56
G326.80+00.37	15:46:24.8	–54:10:57	0.67	G343.76–00.15	17:00:49.1	–42:25:24	0.56
G326.95–00.16	15:49:30.7	–54:30:42	0.44	G343.84–00.08	17:00:45.1	–42:19:04	0.66
G326.97–00.02	15:49:01.0	–54:23:15	0.77	G344.10–00.65	17:04:03.9	–42:27:36	0.81
G327.16–00.24	15:50:59.1	–54:26:28	0.46	G344.21–00.61	17:04:14.8	–42:21:09	0.44
G327.29–00.58	15:53:05.3	–54:37:13	0.46	G344.99–00.23	17:05:10.4	–41:29:38	0.87
G327.40–00.41	15:52:57.9	–54:25:05	0.68	G345.00–00.23	17:05:12.5	–41:29:35	0.50
G327.85–00.56	15:56:01.5	–54:15:02	0.53	G345.04–00.21	17:05:15.2	–41:26:59	1.20
G328.06+00.38	15:53:02.6	–53:23:27	0.55	G345.26–00.04	17:05:14.5	–41:10:16	0.80
G328.11+00.61	15:52:20.6	–53:11:00	0.46	G345.49+00.31	17:04:29.1	–40:46:27	0.64
G328.26–00.53	15:58:01.3	–53:57:44	0.56	G345.50+00.34	17:04:24.5	–40:44:38	1.21
G328.81+00.64	15:55:46.8	–52:43:01	0.80	G345.67+00.34	17:04:58.5	–40:36:44	0.82
G329.03–00.20	16:00:30.6	–53:12:37	0.93	G348.18+00.47	17:12:10.4	–38:31:19	0.95
G329.06–00.30	16:01:06.9	–53:16:05	0.67	G350.02–00.51	17:21:39.5	–37:35:45	0.95
G329.46+00.51	15:59:38.0	–52:23:28	0.60	G350.52–00.36	17:22:27.3	–37:05:32	0.79
G329.72+00.81	15:59:37.6	–51:59:53	0.60	G350.69–00.48	17:23:26.9	–37:01:05	0.52
G330.78+00.25	16:07:09.3	–51:42:48	1.01	G350.94+00.75	17:19:06.7	–36:07:04	0.45
G330.87–00.37	16:10:17.6	–52:06:33	1.10	G350.94+00.66	17:19:30.2	–36:09:52	0.83
G330.99+00.34	16:07:45.7	–51:30:39	0.55	G350.96+00.55	17:19:58.7	–36:12:56	0.57
G331.25–00.44	16:12:23.9	–51:53:57	0.49	G351.16+00.71	17:19:53.7	–35:57:29	0.62
G331.38+00.15	16:10:27.1	–51:23:04	0.55	G351.25+00.66	17:20:23.3	–35:54:39	0.82
G331.41–00.36	16:12:48.9	–51:44:25	0.64	G351.44+00.66	17:20:54.7	–35:45:11	0.92
G331.53–00.08	16:12:09.7	–51:27:08	0.50	G351.47–00.45	17:25:30.5	–36:21:33	0.75
G331.63+00.53	16:09:58.6	–50:56:03	0.48	G351.52–00.56	17:26:07.7	–36:22:40	0.40
G331.71+00.59	16:10:04.2	–50:50:23	0.73	G351.53–00.56	17:26:06.6	–36:22:05	1.30
G332.15+00.05	16:14:26.3	–50:55:29	0.50	G351.59–00.36	17:25:26.9	–36:12:41	0.65
G332.19-00.02	16:14:58.1	–50:56:49	0.43	G351.78–00.54	17:26:44.9	–36:09:17	0.58
G333.02+00.76	16:15:20.8	–49:48:32	0.50	G351.81+00.65	17:21:59.2	–35:27:34	0.94
G333.08–00.56	16:21:22.0	–50:42:51	0.59	G351.96–00.27	17:26:08.4	–35:51:15	0.71
G333.19–00.09	16:19:47.5	–50:18:26	0.56				

Table A.2: Properties of the high extinction clouds

HEC name		Radius [1] ($''$/pc)	$< A_V >_{\rm ext}$ (mag)	$< N_{\rm H_2} >_{\rm ext}$ (10^{22} cm^{-2})	F^i (Jy)	$M_{\rm ext}$ ($M_\odot$)	$M_{1.2\,\rm mm}$ ($M_\odot$)	Clump/Cloud [2] (mJy beam^{-1}/mJy)	Class
G012.73–00.58...		109/0.26	32	3.0	1.89	119	109	63/52	diffuse
G013.28–00.34...		59/1.15	42	3.9	3.85	3,039	1,693	129/66	diffuse
G013.91–00.51...		49/0.65	44	4.2	2.84	1,015	602	203/66	peaked
G013.97–00.45...		52/0.6	22	2.1	2.29	457	308	99/56	diffuse
G014.39–00.75...	A	62/0.66	34	3.2	4.88	507	796	64/195	peaked
	B	25/0.31	16	1.5	0.69	86	165	103/66	diffuse
G014.63–00.57...		98/1.04	35	3.3	17.47	2,084	1,822	907/96	multiply p.
G016.93+00.24...		52/0.61	32	3.0	2.20	632	294	118/56	peaked
G017.19+00.81...		71/0.79	34	3.2	6.78	1,258	785	547/63	multiply p.
G018.26–00.24...		85/1.93	32	3.0	11.27	6,540	5.896	317/92	multiply p.
G022.06+00.21...		45/0.81	28	2.6	4.05	1,000	1,018	1151/72	multiply p.
G023.38–00.12...		68/1.84	29	2.8	5.16	5,498	3,470	211/67	peaked
G024.37–00.15...		43/0.81	26	2.5	0.56	921	561	168/52	multiply p.
G024.61–00.33...		40/0.61	25	2.4	1.78	496	424	214/69	multiply p.
G024.94–00.15...		49/0.79	32	3.0	2.17	1,095	650	160/62	peaked
G025.79+00.81...		38/0.63	24	2.3	1.05	494	351	-/46	diffuse
G030.90+00.00 ...	A	36/0.80	24	2.2	1.45	826	619	188/61	peaked
	B	39/1.35	20	1.8	1.57	1,960	2,232	157/57	peaked
	C	30/0.83	21	2.0	0.83	799	636	129/71	diffuse
	D	14/0.17	22	2.1	0.17	37	31	115/68	diffuse
G034.03–00.33...		6/-	21	1.9	0.02	-	-	-/60	diffuse
G034.34–00.90...		-/-	-	-	-	-	-	-/-	diffuse
G034.71–00.63...		51/0.74	31	3.0	3.05	968	642	206/54	multiply p.
G034.77–00.81...		9/0.13	32	3.0	0.05	30	12	-/-	diffuse
G034.85+00.43...		16/0.29	37	3.5	0.17	171	73	-/43	diffuse
G035.49–00.30...	A	19/0.34	11	1.1	0.39	73	103	198/58	peaked
	B	63/0.91	33	3.1	4.1	1,495	1,300	118/56	peaked

[1] Size is the square root of the area divided by π. For the conversion to parsecs we use the kinematic distance based on $NH_3(1,1)$.

[2] Peak of the 1.2 mm emission in the clump and the mean 1.2 mm emission of the cloud without the clumps.

Table A.2: continued.

HEC name		Radius[1] ($''$/pc)	$< A_V >_{\rm ext}$ (mag)	$< N_{\rm H_2} >_{\rm ext}$ (10^{22} cm^{-2})	F^i (Jy)	$M_{\rm ext}$ (M$_\odot$)	$M_{1.2\,\rm mm}$ (M$_\odot$)	Clump/Cloud[2] (mJy beam^{-1}/mJy)	Class
G037.44+00.14...	A	26/0.16	33	3.1	0.58	47	37	-/67	diffuse
	B	9/0.11	25	2.4	0.05	17	9	-/54	diffuse
G050.06+00.06...		51/1.18	29	2.8	2.92	2,257	2,227	140/54	peaked
G053.81–00.00...		40/0.37	31	2.9	1.54	236	192	140/56	peaked

Notes. The first two columns give the HEC name and the subgrouping of clouds based on the kinematic distance, the following columns represent (in order of appearance): radius of the cloud, average visual extinction derived from the extinction maps, average hydrogen column density derived from the extinction maps, integrated 1.2 mm flux, cloud mass derived from the extinction maps, cloud mass derived from the 1.2 mm, clump peak flux and median cloud flux, class of HEC.

Table A.3: Positions (J2000) and fluxes of the clumps from the 1.2 mm continuum data

HEC name		R.A. (h:m:s)	Declination (°:′:″)	F^p (mJy beam^{-1})	F^i (mJy)	$F^i_{0.25\mathrm{pc}}$ (mJy)	Major Axis (arcsec)	Minor Axis (arcsec)	P.A. (deg)	H_2O[1]
G012.73–00.58...	MM1	18:15:41.3	–18:12:44	42(8)	165	316	28.4	15.2	26.9	..
G013.28–00.34...	MM1	18:15:39.9	–17:34:37	59(12)	212	141	22.7	17.5	–49.6	–
G013.91–00.51...	MM1	18:17:34.8	–17:06:52	142(15)	685	535	27.3	17.1	–22.2	–
G014.39–00.75A..	MM1	18:19:19.0	–16:43:49	142(17)	503	456	27.1	14.4	57.1	–
G014.39–00.75B..	MM3	18:19:33.3	–16:45:01	81(9)	259	377	21.5	16.4	6.7	..
G014.63–00.57...	MM1	18:19:15.2	-16:29:59	689(8)	3,111	2.780	28.5	17.5	10.3	+
	MM2	18:19:14.3	–16:30:41	332(9)	584	650	16.2	12.0	–57.3	..
	MM3	18:19:02.9	–16:30:29	112(11)	269	276	21.5	12.3	–42.0	..
	MM4	18:19:20.5	–16:31:42	86(9)	215	265	22.1	12.5	–49.3	..
G016.93+00.24...	MM1	18:20:50.8	–14:06:01	76(11)	357	296	27.2	19.1	–80.4	..
G017.19+00.81...	MM1	18:19:08.9	–13:36:29	120(10)	386	409	21.6	16.4	65.3	..
	MM2	18:19:12.9	–13:33:46	475(11)	1,304	1,430	17.8	16.9	87.8	+
	MM3	18:19:12.1	–13:33:32	157(11)	725	1,080	31.3	16.2	–72.9	..
	MM4	18:19:15.2	–13:39:29	87(10)	426	407	28.2	19.1	–42.0	..
G018.26–00.24...	MM1	18:25:11.8	–13:08:04	257(16)	666	438	19.4	14.7	26.5	–
	MM2	18:25:06.4	–13:08:51	221(17)	887	429	31.2	14.2	30.2	–
	MM3	18:25:05.6	–13:08:20	152(16)	231	201	14.8	11.3	–42.8	..
	MM4	18:25:04.5	–13:08:27	133(14)	211	168	16.7	10.5	47.7	..
	MM5	18:25:01.8	–13:09:06	141(19)	559	291	24.1	18.1	64.6	..
G022.06+00.21...	MM1	18:30:34.7	–9:34:46	995(14)	2,019	1,820	15.6	14.3	70.6	+
	MM2	18:30:38.5	–9:34:29	166(15)	259	208	14.6	11.8	64.0	..
G023.38–00.12...	MM1	18:34:23.5	–8:32:20	171(15)	521	246	22.3	15.1	29.1	..
G024.37–00.15...	MM1	18:36:27.8	–7:40:24	133(12)	529	350	26.8	14.4	33.0	–
	MM2	18:36:18.3	–7:41:00	94(11)	254	202	17.3	15.1	42.7	+
G024.61–00.33...	MM1	18:37:23.1	–7:31:39	147(8)	655	496	25.3	19.4	84.2	–
	MM2	18:37:21.3	–7:33:07	75(8)	276	187	26.1	15.6	20.6	–
G024.94–00.15...	MM1	18:37:19.7	–7:11:41	133(15)	350	318	19.4	13.2	–32.8	+
	MM2	18:37:12.2	–7:11:23	114(15)	278	218	19.2	12.4	23.2	–

[1] Water maser; '+'means a detection, '–' a non-detection and '..' not observed.

Table A.3: continued.

HEC name		R.A. (h:m:s)	Declination (°:′:″)	F^p (mJy beam^{-1})	F^i (mJy)	$F^i_{0.25\mathrm{pc}}$ (mJy)	Major Axis (arcsec)	Minor Axis (arcsec)	P.A. (deg)	H_2O[1]
G030.90+00.00A..	MM1	18:47:28.9	–1:48:07	141(10)	728	307	32.1	17.7	–2.5	..
G030.90+00.00B..	MM2	18:47:41.9	–1:52:13	116(19)	494	130	26.9	17.4	43.7	–
G030.90+00.00C..	MM3	18:47:48.2	–1:51:30	98(20)	369	164	24.3	17.1	–10.5	–
G030.90+00.00D..	MM4	18:47:51.5	–1:49:24	106(10)	260	279	20.9	13.0	32.4	..
G034.71–00.63...	MM1	18:56:48.3	1:18:49	148(9)	1,174	678	36.0	24.3	2.2	–
	MM2	18:56:58.2	1:18:44	79(11)	368	250	30.2	17.1	-81.7	..
	MM3	18:57:06.5	1:16:52	60(11)	203	179	23.9	15.6	78.9	–
G035.49–00.30A..	MM1	18:57:05.2	2:06:29	180(11)	374	339	16.8	13.6	–38.8	+
G035.49–00.30B..	MM2	18:57:08.4	2:09:01	76(10)	204	139	19.1	15.5	28.0	–
	MM3	18:57:08.1	2:10:47	73(14)	437	279	33.3	19.9	–1.6	+
	MM4	18:57:09.0	2:08:23	60(10)	178	118	24.1	13.5	–1.4	..
	MM5	18:57:06.7	2:08:27	62(10)	211	154	26.4	14.3	–28.9	..
	MM6	18:57:11.5	2:07:27	55(11)	274	184	29.0	19.1	–6.1	..
G050.06+00.06...	MM1	19:23:12.4	15:13:35	89(8)	332	167	26.9	15.4	43.1	–
	MM2	19:23:09.2	15:12:42	84(9)	246	157	30.5	14.8	83.0	..
G053.81–00.00...	MM1	19:30:55.7	18:29:55	106(11)	226	291	16.5	14.3	–50.8	–

Notes. The first two columns give the HEC name and the millimeter clump number, the following columns represent (in order of appearance): right ascension, declination, 1.2 mm peak flux, integrated 1.2 mm flux, integrated 1.2 mm flux within 0.25 pc radius, clump major axis, clump minor axis, position angle and water maser detection.

Table A.4: Positions (J2000) and determined properties toward the positions without clumps

HEC name		R.A. (h:m:s)	Declination (°:′:″)	$d_{\rm kin}$ (kpc)	$F^{i}_{0.25\rm pc}$ (mJy)	$M_{0.25pc}$ ($M_\odot$)	$T_{\rm rot}$ (K)	$N_{\rm NH_3}$ (10^{15} cm^{-2})
G012.73–00.58...	MM2	18:15:32.7	–18:10:15	1.1	178	8	11.4(0.7)	..
G013.97–00.45...	MM1	18:17:16.5	–17:01:16	2.4	189	25	16.6(0.9)	..
G014.39–00.75A..	MM2	18:19:17.4	–16:44:04	2.1	382	32	20.0(2.3)	..
G023.38–00.12...	MM2	18:34:20.4	–8:33:16	5.6	..	44	17.8(2.0).	..
G025.79+00.81...	MM1	18:35:20.5	–5:56:36	3.4	196	77	13.1(0.7)	..
	MM2	18:35:26.3	–5:59:21	3.4	63	31	..	..
G034.03–00.33...	MM1	18:54:25.1	0:49:56	..	..	..	..	..
	2	18:54:39.2	0:51:37	..	..	..	..	..
G034.34–00.90...	1	18:57:16.5	0:50:48	..	..	..	..	
G034.77–00.81...	MM1	18:57:40.7	1:16:09	2.9	49	11	..	..
G034.85+00.43...	MM1	18:53:23.2	1:53:16	3.6	73	31	13.2(1.5)	..
G037.44+00.14A..	MM1	18:59:14.0	4:07:37	1.3	163	8	..	..
G037.44+00.14B..	MM2	18:59:10.2	4:04:32	1.7	130	?	..	..

Notes. The first two columns give the HEC name and the millimeter clump number, the following columns represent (in order of appearance): right ascension, declination, kinematic distance, integrated 1.2 mm flux within 0.25 pc radius, mass within 0.25 pc radius, rotational temperature from NH_3, and NH_3 column density.

Table A.5: Observed ammonia parameters with uncertainties (in parenthesis) from hyperfine and Gaussian fits with CLASS

HEC name		$NH_3(1,1)$				$NH_3(2,2)$		$NH_3(3,3)$	
		v_{LSR} ($km\,s^{-1}$)	T_{MB} (K)	Δv ($km\,s^{-1}$)	τ_{main}	T_{MB} (K)	Δv ($km\,s^{-1}$)	T_{MB} (K)	Δv ($km\,s^{-1}$)
G012.73–00.58..	MM1	6.48(0.01)	1.3(0.3)	0.7(0.1)	4.1(0.4)	0.2(0.1)	0.8(0.1)	..	..
	MM2	6.19(0.01)	1.8(0.3)	1.0(0.1)	1.3(0.1)	0.3(0.1)	1.6(0.2)	..	..
G013.28–00.34..	MM1	41.30(0.06)	3.2(0.7)	1.6(0.2)	1.8(0.5)	1.3(0.3)	1.6(0.2)	..	..
G013.91–00.51..	MM1	22.94(0.02)	2.5(0.3)	1.3(0.1)	1.8(0.3)	0.8(0.2)	1.3(0.2)	..	..
G013.97–00.45..	MM1	19.76(0.02)	1.4(0.2)	2.3(0.1)	0.7(0.1)	0.5(0.1)	3.0(0.1)	0.3(0.1)	4.5(0.3)
G014.39–00.75A..	MM1	17.84(0.04)	1.0(0.1)	1.2(0.1)	0.8(0.4)	0.4(0.1)	2.9(0.4)	0.1(0.1)	3.0(0.9)
	MM2	17.49(0.03)	1.1(0.1)	1.2(0.1)	0.5(0.3)	0.6(0.1)	2.2(0.3)	0.2(0.1)	2.9(0.5)
G014.39–00.75B..	MM3	21.29(0.03)	1.5(0.2)	0.9(0.1)	2.3(0.5)	0.4(0.1)	1.3(0.4)	..	..
G014.63–00.57..	MM1	18.75(0.01)	4.0(0.4)	1.8(0.1)	2.2(0.1)	2.4(0.1)	2.4(0.1)	1.2(0.1)	2.7(0.1)
	MM2	18.45(0.02)	3.0(0.3)	1.3(0.1)	1.8(0.2)	1.3(0.1)	1.8(0.1)	0.4(0.1)	2.4(0.4)
	MM3	17.64(0.04)	1.0(0.2)	1.4(0.1)	2.1(0.4)	0.5(0.1)	1.9(0.2)	0.2(0.1)	1.5(0.3)
	MM4	19.13(0.05)	0.6(0.2)	0.8(0.1)	2.0(0.9)	0.4(0.1)	1.0(0.3)	..	..
G016.93+00.24..	MM1	23.80(0.01)	1.5(0.1)	0.9(0.1)	1.7(0.2)	0.5(0.1)	1.7(0.3)	..	..
G017.19+00.81..	MM1	25.04(0.01)	3.2(0.1)	1.2(0.1)	1.5(0.1)	1.5(0.1)	1.5(0.1)	0.2(0.1)	2.5(0.7)
	MM2	22.75(0.01)	3.1(0.1)	1.3(0.1)	1.3(0.1)	1.7(0.2)	1.6(0.1)	0.5(0.1)	2.3(0.3)
	MM3	22.73(0.01)	3.1(0.2)	1.3(0.1)	1.6(0.1)	2.0(0.2)	1.5(0.1)	0.5(0.1)	2.4(0.2)
	MM4	21.64(0.06)	0.5(0.1)	2.8(0.1)	0.9(0.3)	0.3(0.1)	3.6(0.3)	0.2(0.1)	2.6(0.4)
G018.26–00.24..	MM1	68.07(0.01)	2.6(0.1)	1.5(0.1)	2.4(0.2)	1.6(0.1)	2.3(0.1)	0.6(0.1)	2.8(0.3)
	MM2	67.75(0.02)	2.6(0.1)	2.0(0.1)	2.8(0.1)	1.7(0.2)	2.6(0.2)	0.3(0.1)	2.8(0.3)
	MM3	68.32(0.01)	3.6(0.7)	2.2(0.1)	2.6(0.1)	1.8(0.1)	2.7(0.1)	0.6(0.1)	3.3(0.1)
	MM4	68.31(0.02)	3.4(0.4)	2.1(0.1)	2.2(0.1)	1.8(0.1)	2.8(0.1)	0.8(0.1)	2.9(0.2)
	MM5	66.28(0.03)	1.9(0.2)	2.0(0.1)	2.6(0.2)	1.1(0.1)	2.0(0.2)	0.2(0.1)	5.0(1.1)
G022.06+00.21..	MM1	51.17(0.02)	1.8(0.1)	1.7(0.1)	1.9(0.2)	1.5(0.1)	2.2(0.2)	0.5(0.1)	3.6(0.3)
	MM2	51.45(0.02)	1.1(0.1)	1.2(0.1)	1.9(0.3)	0.5(0.1)	2.9(0.5)	0.1(0.1)	5.3(1.0)
G023.38–00.12..	MM1	98.42(0.02)	1.7(0.1)	1.6(0.1)	2.3(0.2)	1.1(0.1)	1.9(0.1)	0.2(0.1)	3.4(0.3)
	MM2	98.86(0.02)	1.0(0.1)	1.1(0.1)	1.4(0.3)	0.5(0.1)	1.1(0.1)	..	..
G024.37–00.15..	MM1	58.83(0.03)	0.9(0.1)	2.1(0.1)	2.8(0.3)	0.6(0.1)	2.6(0.2)	0.2(0.1)	4.2(0.4)
	MM2	55.96(0.03)	1.3(0.1)	1.5(0.1)	2.2(0.3)	0.6(0.1)	2.0(0.3)	0.1(0.1)	3.2(1.0)
G024.61–00.33..	MM1	42.80(0.02)	1.3(0.1)	1.4(0.1)	1.2(0.2)	0.6(0.1)	1.5(0.2)	0.1(0.1)	4.9(1.1)

Table A.5: continued.

HEC name		$NH_3(1,1)$				$NH_3(2,2)$		$NH_3(3,3)$	
		v_{LSR} ($km\,s^{-1}$)	T_{MB} (K)	Δv ($km\,s^{-1}$)	τ_{main}	T_{MB} (K)	Δv ($km\,s^{-1}$)	T_{MB} (K)	Δv ($km\,s^{-1}$)
	MM2	43.58(0.01)	1.9(0.1)	0.8(0.1)	1.7(0.2)	0.8(0.1)	1.3(0.1)	0.2(0.1)	3.6(0.8)
G024.94–00.15..	MM1	47.10(0.01)	2.8(0.1)	1.5(0.1)	2.3(0.1)	1.3(0.2)	1.9(0.2)	0.4(0.1)	2.4(0.3)
	MM2	48.03(0.02)	1.8(0.1)	1.4(0.1)	2.2(0.2)	0.8(0.1)	2.1(0.2)	0.2(0.1)	3.7(0.7)
G025.79+00.81..	MM1	49.70(0.01)	2.0(0.1)	1.1(0.1)	2.1(0.1)	0.6(0.1)	1.7(0.2)	..	..
	MM2	49.81(0.02)	0.9(0.2)	0.9(0.1)	1.3(0.4)	..	..	..	..
G030.90+00.00A..	MM1	74.82(0.03)	1.6(0.1)	1.5(0.1)	1.7(0.3)	0.9(0.1)	2.0(0.1)	0.3(0.1)	2.1(0.4)
G030.90+00.00B..	MM2	109.55(0.06)	1.4(0.1)	2.5(0.1)	1.9(0.3)	..	..	..	..
G030.90+00.00C..	MM3	93.78(0.03)	1.2(0.1)	1.1(0.1)	2.7(0.4)	0.7(0.2)	2.3(0.4)	0.1(0.1)	1.7(0.9)
G030.90+00.00D..	MM4	37.61(0.05)	0.8(0.1)	1.0(0.1)	1.9(0.8)	..	..	..	..
G034.71–00.63..	MM1	44.61(0.02)	1.7(0.1)	1.7(0.1)	1.1(0.1)	0.8(0.1)	2.2(0.2)	0.3(0.1)	4.4(0.3)
	MM2	45.43(0.02)	1.9(0.4)	1.3(0.1)	3.0(0.3)	0.6(0.1)	1.5(0.1)	0.2(0.1)	6.4(0.8)
	MM3	46.16(0.02)	1.1(0.1)	1.4(0.1)	0.6(0.2)	0.4(0.1)	1.3(0.2)	..	..
G034.77–00.81..	MM1	43.36(0.08)	0.6(0.1)	1.6(0.2)	0.5(0.7)	..	..	..	..
G034.85+00.43..	MM1	55.52(0.03)	1.1(0.3)	0.8(0.1)	1.8(0.5)	0.3(0.1)	0.8(0.1)	..	..
G035.49–00.30A..	MM1	55.23(0.06)	0.7(0.1)	1.9(0.1)	0.7(0.4)	0.3(0.1)	2.2(0.4)	0.2(0.1)	4.1(0.6)
G035.49–00.30B..	MM2	45.31(0.01)	2.7(0.3)	1.0(0.1)	3.5(0.3)	0.8(0.1)	1.3(0.1)	0.1(0.1)	2.4(1.2)
	MM3	45.71(0.02)	2.1(0.1)	1.6(0.1)	2.5(0.2)	0.8(0.1)	1.6(0.1)	0.1(0.1)	1.9(0.7)
G037.44+00.14A..	MM1	18.37(0.02)	1.3(0.2)	0.8(0.1)	0.6(0.3)	0.4(2.0)	0.5(2.2)	..	..
G037.44+00.14B..	MM2	40.17(0.11)	0.4(0.1)	1.3(0.3)	0.5(1.1)	..	..	..	..
G050.06+00.06..	MM1	54.11(0.03)	0.9(0.1)	1.3(0.1)	1.5(0.3)	0.3(0.1)	1.3(0.3)	..	..
	MM2	54.53(0.03)	0.8(0.1)	1.3(0.1)	1.2(0.3)	0.2(0.1)	3.2(0.7)	..	..
G053.81–00.00..	MM1	24.13(0.02)	1.3(0.1)	1.4(0.1)	1.3(0.2)	0.3(0.1)	3.1(0.9)	..	..

Table A.6: Properties of the clumps derived from NH_3 and the 1.2 mm continuum

HEC name		$d_{\rm kin}$ (kpc)	A_V (mag)	$FWHM$ (pc)	$N_{\rm H_2}$ ($10^{22}\,{\rm cm^{-2}}$)	$n_{\rm H_2}$ ($10^5\,{\rm cm^{-3}}$)	$M_{1.2\,\rm mm}$ ($\rm M_\odot$)	$M_{0.25pc}$ ($\rm M_\odot$)	$M_{\rm vir}$ ($\rm M_\odot$)	$T_{\rm rot}$ (K)	$N_{\rm NH_3}$ ($10^{15}\,{\rm cm^{-2}}$)
G012.73–00.58..	MM1	1.1	47	0.11	4.5	2.8	12	22	6	9.3(0.7)	3.7(0.8)
G013.28–00.34..	MM1	4.0	31	0.39	2.9	0.5	93	62	104	14.9(2.0)	3.2(1.1)
G013.91–00.51..	MM1	2.7	82	0.28	7.7	2.2	145	113	50	14.1(1.3)	2.5(0.5)
G014.39–00.75A..	MM1	2.2	61	0.21	5.7	2.0	52	47	31	17.4(2.0)	1.1(0.6)
G014.39–00.75B..	MM3	2.5	61	0.23	5.7	1.8	62	90	19	11.8(1.5)	2.4(0.8)
G014.63–00.57..	MM1	2.2	280	0.24	26.3	7.7	323	289	82	18.1(1.3)	4.7(0.5)
	MM2	2.2	164	0.15	15.4	7.3	72	80	26	15.7(1.1)	2.7(0.4)
	MM3	2.1	55	0.17	5.2	2.2	31	32	34	15.8(1.9)	3.4(0.8)
	MM4	2.3	32	0.18	3.0	1.2	21	26	12	19.1(5.9)	2.0(1.1)
G016.93+00.24..	MM1	2.4	44	0.27	4.2	1.1	64	53	23	14.0(1.3)	1.7(0.3)
G017.19+00.81..	MM1	2.5	52	0.23	4.9	1.5	54	58	35	17.2(0.9)	2.1(0.2)
	MM2	2.3	186	0.20	17.4	6.3	142	156	35	18.7(1.1)	2.1(0.2)
	MM3	2.3	56	0.25	5.3	1.5	72	108	45	20.0(1.5)	2.6(0.3)
	MM4	2.3	31	0.26	2.9	0.8	40	39	211	20.1(2.1)	3.2(1.1)
G018.26–00.24..	MM1	4.7	104	0.39	9.8	1.8	306	201	91	18.2(1.1)	4.3(0.4)
	MM2	4.7	95	0.48	8.9	1.3	431	208	201	17.4(1.2)	6.5(0.6)
	MM3	4.7	76	0.29	7.1	1.7	130	113	150	15.7(1.5)	6.4(0.9)
	MM4	4.7	61	0.30	5.7	1.3	110	88	140	16.6(1.1)	5.3(0.6)
	MM5	4.6	63	0.47	6.0	0.9	278	145	197	16.8(1.7)	6.0(1.0)
G022.06+00.21..	MM1	3.7	270	0.27	25.4	6.8	384	346	81	24.7(3.3)	4.9(0.9)
	MM2	3.7	84	0.24	7.9	2.4	92	74	36	15.5(1.6)	2.6(0.5)
G023.38–00.12..	MM1	5.6	70	0.50	6.5	0.9	346	163	134	18.1(1.2)	4.4(0.5)
G024.37–00.15..	MM1	3.9	52	0.38	4.9	1.1	165	110	174	18.6(1.9)	7.1(1.2)
	MM2	3.8	47	0.30	4.4	1.2	94	74	70	15.7(1.5)	3.8(0.7)
G024.61–00.3.3.	MM1	3.1	63	0.34	5.9	1.2	140	106	69	17.5(1.9)	2.0(0.4)
	MM2	3.2	38	0.31	3.5	0.8	72	49	21	15.5(1.2)	1.5(0.2)
G024.94–00.15..	MM1	3.3	69	0.26	6.5	2.0	104	94	61	15.2(1.0)	3.8(0.4)
	MM2	3.4	59	0.25	5.5	1.8	85	67	52	15.2(1.1)	3.5(0.5)
G030.90+00.00A..	MM1	4.6	55	0.53	5.2	0.7	311	131	125	18.6(1.7)	3.1(0.6)
G030.90+00.00B..	MM2	7.2	61	0.76	5.8	0.5	702	736	497	..	..

Table A.6: continued.

HEC name		$d_{\rm kin}$ (kpc)	A_V (mag)	$FWHM$ (pc)	$N_{\rm H_2}$ ($10^{22}\,{\rm cm^{-2}}$)	$n_{\rm H_2}$ ($10^{5}\,{\rm cm^{-3}}$)	$M_{1.2\,\rm mm}$ ($\rm M_\odot$)	$M_{0.25pc}$ ($\rm M_\odot$)	$M_{\rm vir}$ ($\rm M_\odot$)	$T_{\rm rot}$ (K)	$N_{\rm NH_3}$ ($10^{15}\,{\rm cm^{-2}}$)
G030.90+00.00C..	MM3	5.7	46	0.56	4.3	0.5	283	126	71	16.4(2.4)	3.4(0.9)
G030.90+00.00D..	MM4	2.6	101	0.21	9.5	3.2	49	95	22	..	..
G034.71–00.63..	MM1	3.0	61	0.43	5.8	1.0	224	129	130	17.8(1.1)	2.2(0.3)
	MM2	3.0	55	0.33	5.2	1.1	122	83	59	12.4(0.9)	4.4(0.7)
	MM3	3.1	26	0.29	2.5	0.6	43	38	59	17.1(1.9)	1.0(0.4)
G035.49–00.30A..	MM1	3.6	71	0.26	6.6	1.8	98	89	100	18.6(2.9)	1.7(1.0)
G035.49–00.30B..	MM2	3.0	57	0.25	5.3	1.5	72	49	26	11.9(0.7)	3.9(0.5)
	MM3	3.0	44	0.38	4.2	0.8	127	81	102	13.6(0.7)	4.3(0.4)
	MM4	3.0	39	0.26	3.7	1.0	54	36	..	..	..
	MM5	3.0	40	0.28	3.8	1.0	64	46	..	..	..
	MM6	3.0	36	0.34	3.3	0.7	83	55	..	..	..
G050.06+00.06..	MM1	4.8	47	0.47	4.4	0.7	208	104	83	14.9(2.2)	2.1(0.6)
	MM2	4.8	49	0.49	4.6	0.7	233	106	87	14.1(1.7)	1.7(0.5)
G053.81–00.00..	MM1	1.9	74	0.14	6.9	3.6	28	36	28	12.4(1.4)	2.1(0.5)

Notes. The first two columns give the HEC name and the millimeter clump number, the following columns represent (in order of appearance): kinematic distance, visual extinction derived from the mm emission, size FWHM (the geometric mean of the major and minor axis), hydrogen column density, hydrogen density, clump mass from the 1.2 mm emission, clump mass with 0.25 pc (also from the 1.2 mm emission), virial mass of the clump, NH_3 rotational temperature and NH_3 column density

APPENDIX B

Images of high exctinction clouds

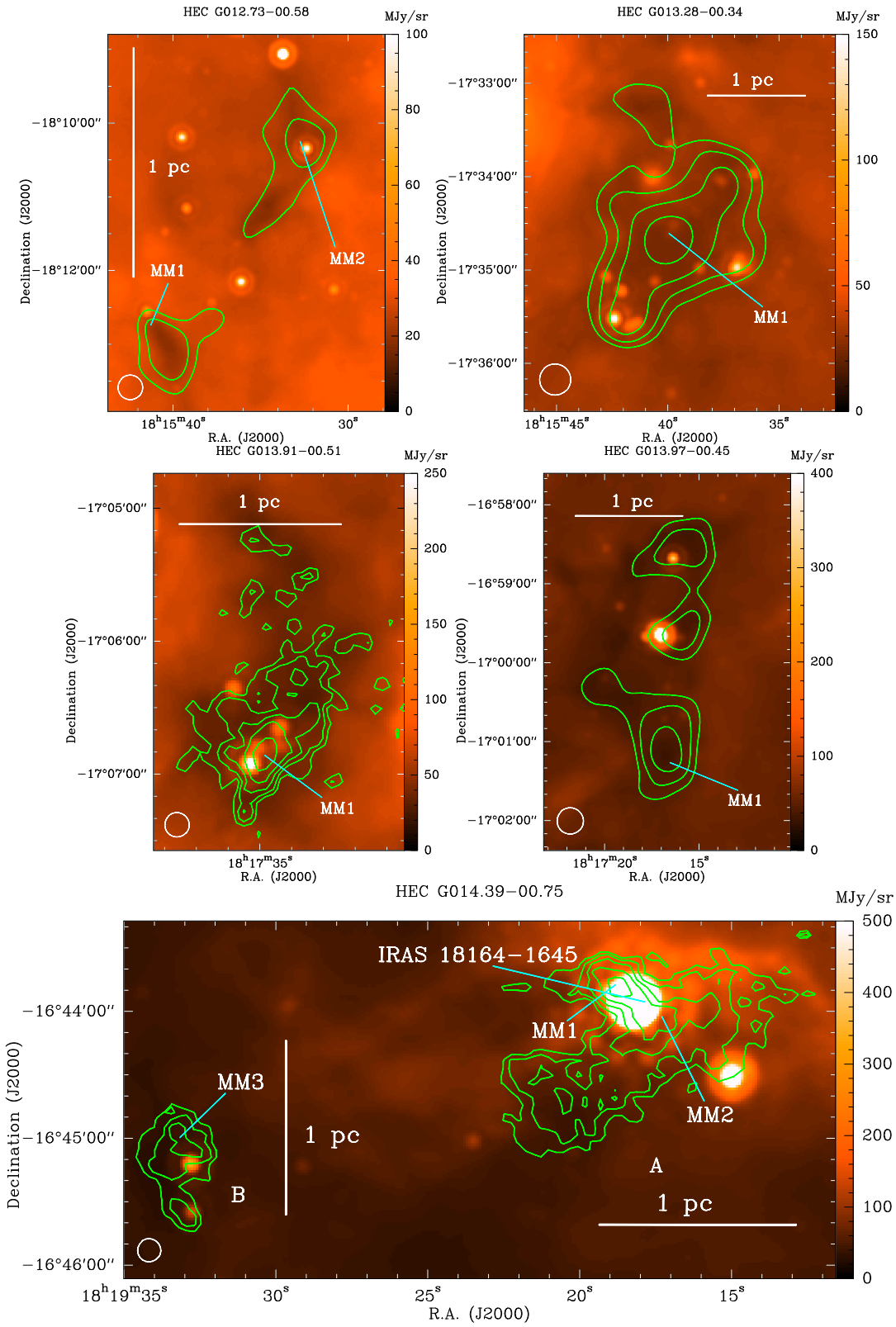

Figure B.1: MIPSGAL 24 μm images overlaid with the 1.2 mm continuum emission contours starting at $2\sqrt{2}\sigma$ and increasing by factors of $\sqrt{2}$. The 1.2 mm clumps are labeled with their designation (as listed in Table A.3, A.6 and A.5). In the bottom-left corner we indicate the original MAMBO beam at 1.2 mm (10.″5), or the smoothed beam (20″) when a smoothed map is shown. Additionally, 6.7 GHz methanol masers (cyan triangles), water maser (blue squares), HII regions (green pentagons with black contours) and IRAS sources are marked in the images. For the clouds where a kinematic distance was derived, the physical scale of the cloud is indicated by a bar of one parsec.

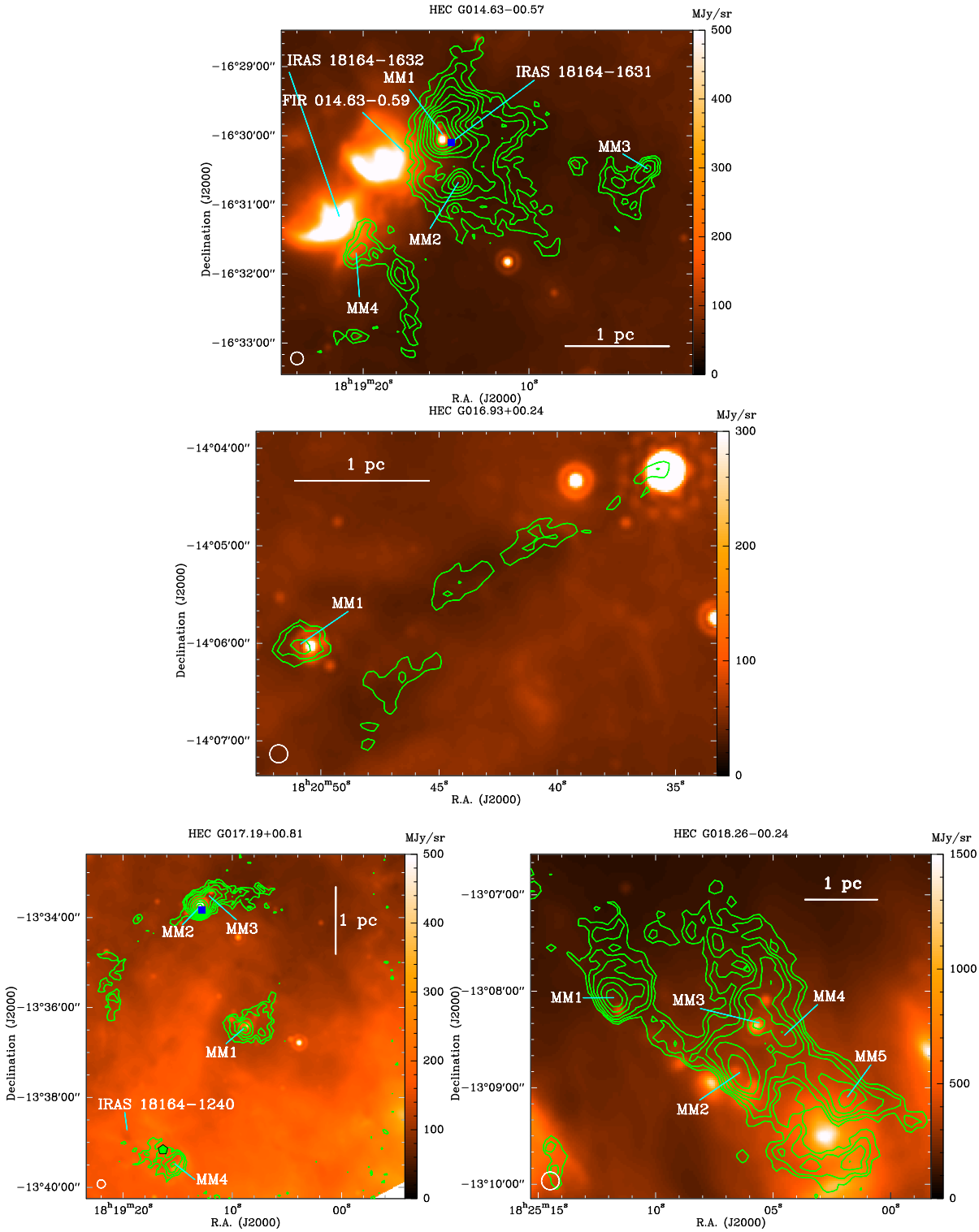

Figure B.1: –*Continued.*

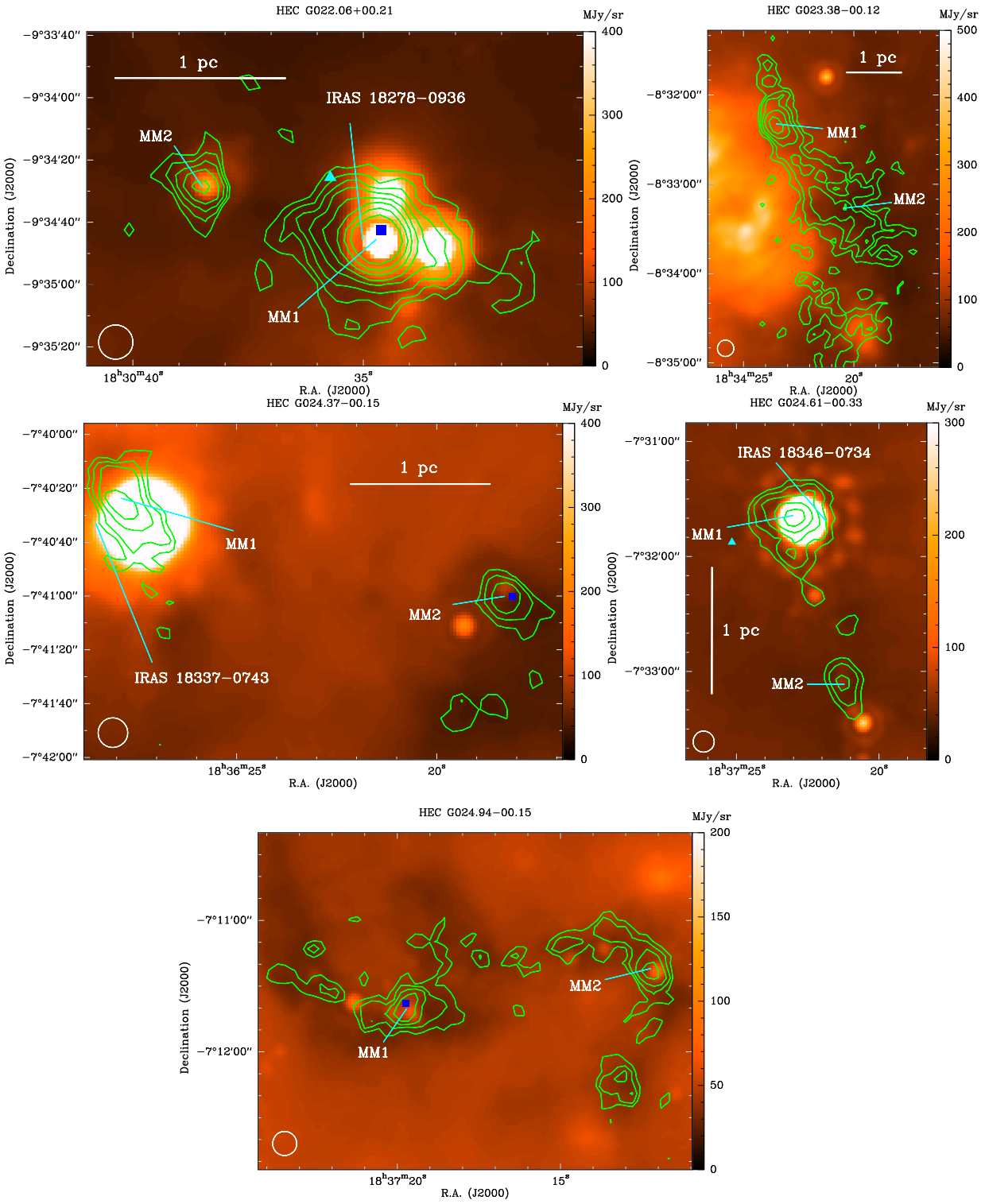

Figure B.1: *–Continued.*

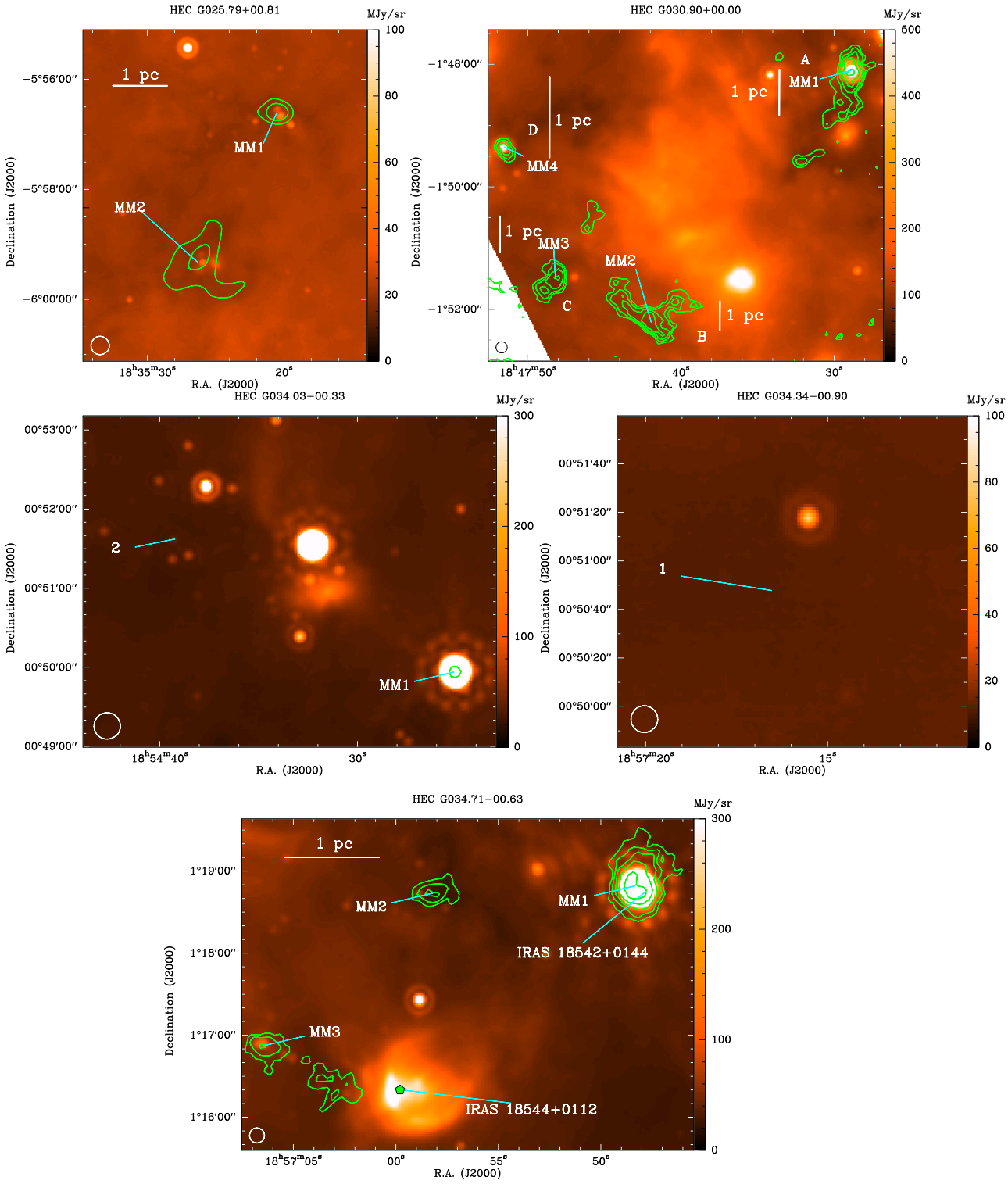

Figure B.1: –*Continued.*

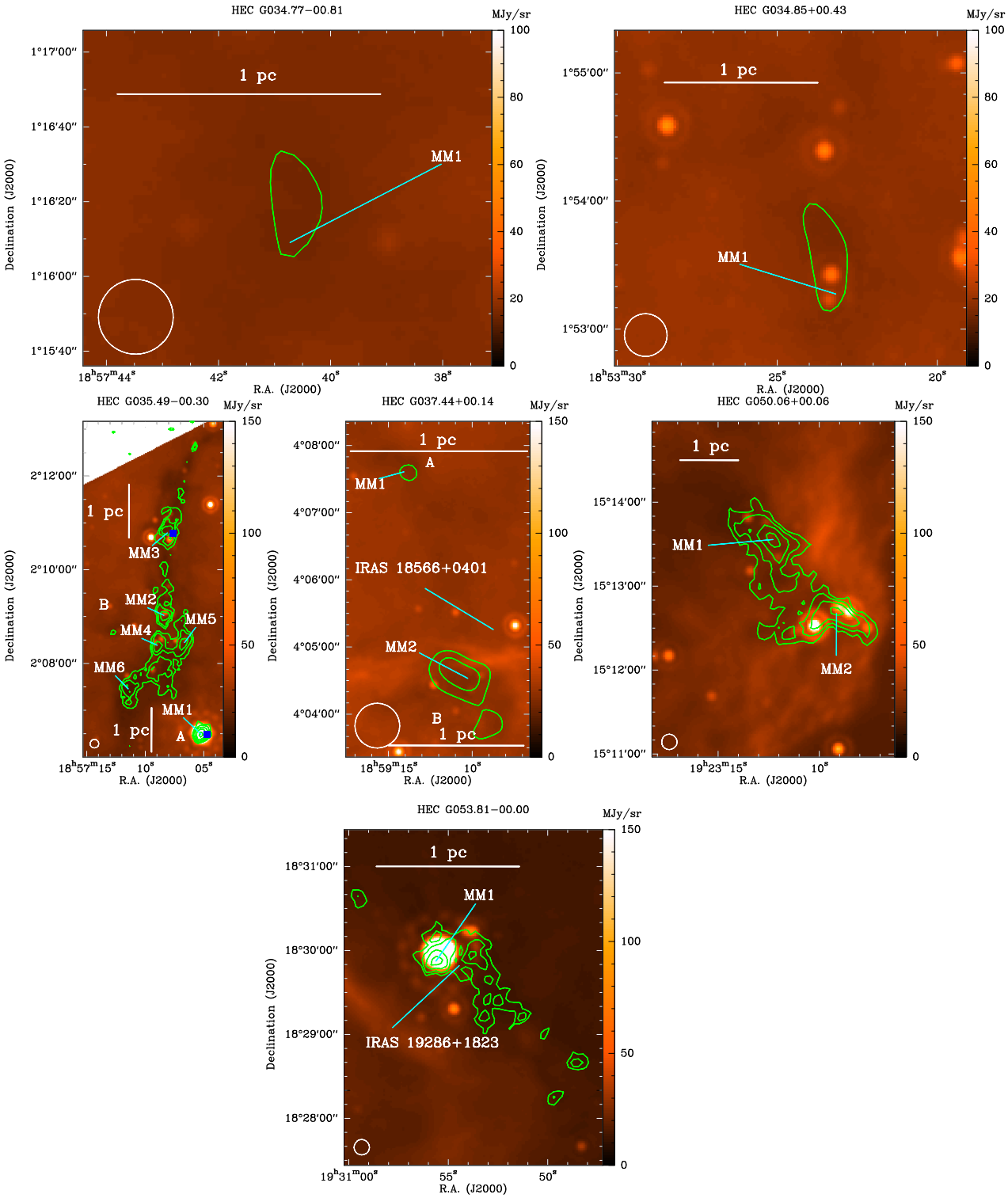

Figure B.1: –*Continued.*

APPENDIX C

Tables to Chapter 3

Table C.1: Molecular line survey overview: '√' for a detection, '-' for a non-detection and '..' when not observed.

HEC name		HCO^+ (1–0)	$H^{13}CO^+$ (1–0)	HCO^+ (4–3)	N_2H^+ (1–0)	N_2H^+ (3–2)	SiO (2–1)	CH_3CN (5–4)	H_2CO (4–3)	CO (2–1)	$C^{18}O$ (2–1)	CO (3–2)
G012.73–00.58...	MM1	√	√	..	√	..	-	-	..	√	-	..
	MM2	√	√	..	√	..	-	-	..	√	√	..
G013.28–00.34...	MM1	√	√	..	√	..	√	-	..	√	√	..
G013.91–00.51...	MM1	√	√	√	√	√	-	-	√	√	√	√
G013.97–00.45...	MM1	√	√	..	√	..	-	-	..	√	√	..
G014.39–00.75A..	MM1	√	√	..	√	√	-	-	√	√	√	..
	MM2	√	√	..	√	..	-	-	..	√	√	..
G014.39–00.75B..	MM3	√	√	..	√	..	-	-	..	√	√	..
G014.63–00.57...	MM1	√	√	√	√	√	√	√	√	√	√	√
	MM2	√	√	√	√	√	√	-	√	√	√	√
	MM3	√	√	..	√	..	-	-	..	√	√	..
	MM4	√	√	..	√	..	-	-	..	√	√	..
G016.93+00.24...	MM1	√	√	..	√	..	-	-	..	√	√	..
G017.19+00.81...	MM1	√	√	√	√	√	√	-	√	√	√	√
	MM2	√	√	√	√	√	√	√	√	√	√	√
	MM3	√	√	..	√	..	√	-	..	√	√	..
	MM4	√	√	√	√	√	-	-	-	√	√	√
G018.26–00.24...	MM1	√	√	√	√	√	√	√	√	√	√	√
	MM2	√	√	√	√	√	√	-	√	√	√	√
	MM3	√	√	√	√	√	√	√	√	√	√	√
	MM4	√	√	√	√	√	√	-	√	√	√	√
	MM5	√	√	..	√	..	-	-	..	√	√	..
G022.06+00.21...	MM1	√	√	√	√	√	√	√	√	√	√	√
	MM2	√	√	..	√	..	-	-	..	√	√	..
G023.28–00.12...	MM1	√	√	√	√	√	√	-	-	√	√	√
	MM2	√	√	..	√	..	-	-	..	√	√	..
G024.37–00.15...	MM1	√	√	..	√	..	-	-	..	√	√	..
	MM2	√	√	√	√	√	√	-	√	√	√	√
G024.61–00.33...	MM1	√	√	√	√	√	√	-	√	√	√	√
	MM2	√	√	..	√	..	-	-	..	√	√	..
G024.94–00.15...	MM1	√	√	√	√	√	√	-	√	√	√	√

Table C.1: continued.

HEC name		HCO^+ (1–0)	$H^{13}CO^+$ (1–0)	HCO^+ (4–3)	N_2H^+ (1–0)	N_2H^+ (3–2)	SiO (2–1)	CH_3CN (5–4)	H_2CO (4–3)	CO (2–1)	$C^{18}O$ (2–1)	CO (3–2)
	MM2	√	√	..	√	..	√	-	..	√	√	..
G025.79+00.81...	MM1	√	√	..	√	..	√	-	..	√	√	..
	MM2	√	√	..	√	..	-	-	..	√	√	..
G030.90+00.00A..	MM1	√	√	√	√	√	-	-	-	√	√	√
G030.90+00.00C..	MM2	√	√	√	√	√	-	-	-	√	√	√
G030.90+00.00B..	MM3	√	√	..	√	..	-	-	..	√	√	..
G034.71–00.63...	MM1	√	√	√	√	√	√	√	√	√	√	√
	MM2	√	√	√	√	√	√	-	-	√	√	√
	MM3	√	√	..	√	..	√	-	..	√	√	..
G034.77–00.81...	MM1	√	√	..	√	..	-	-	..	√	√	..
G034.85+00.43...	MM1	√	√	-	√	-	-	-	-	√	√	√
G035.49–00.30A..	MM1	√	√	..	√	..	-	-	..	√	√	..
G035.49–00.30B..	MM2	√	√	..	√	..	√	-	..	√	√	..
	MM3	√	√	..	√	..	√	-	..	√	√	..
G037.44+00.14A..	MM1	-	√	..	√	..	-	-	..	√	√	..
G037.44+00.14B..	MM2	√	√	..	√	..	-	-	..	√		..
G050.06+00.06...	MM1	√	√	..	√	..	-	-	..	√	√	..
	MM2	√	√	..	√	..	-	-	..	√	√	..
G053.81–00.00...	MM1	√	√	..	√	√	√	-	√	√	√	..

Table C.2: Infall and outflow study using HCO^+(1–0), ^{12}CO(2–1), HCO^+(4–3) and ^{12}CO(3–2)

HEC name		HCO^+(1–0)			^{12}CO(2–1)		HCO^+(4–3)		^{12}CO(3–2)	
		$\frac{T_{blue}}{T_{red}}$	δv (km s^{-1})	Profile	Profile	Wings/Range (km s^{-1})	Profile	δv (km s^{-1})	Profile	δv (km s^{-1})
G012.73–00.58...	MM1	..	0.19(0.01)	..	..	y/11	..	..	..	..
	MM2	0.43(0.04)	0.51(0.13)	R	..	y/13	..	..	..	..
G013.28–00.34...	MM1	1.58(0.34)	–0.59(0.13)	B	B	y/14	..	..	..	..
G013.91–00.51...	MM1	1.63(0.17)	–0.64(0.19)	B	R	y/27	B	–0.46(0.21)	..	..
G013.97–00.45...	MM1	1.24(0.17)	–0.73(0.13)	B	..	n	..	..	..	..
G014.39–00.75A..	MM1	..	–0.52(0.03)	B	B	y/18	..	..	..	..
	MM2	..	–0.45(0.03)	B	B	y/13	..	..	..	..
G014.39–00.75B..	MM3	..	–5.79(0.29)	B	..	y/15	..	..	..	..
G014.63–00.57...	MM1	1.05(0.09)	..	..	B	y/30	B	–0.59(0.21)	B	–2.06(0.21)
	MM2	0.45(0.13)	1.18(0.13)	R	B	y/23	B	–0.78(0.21)	..	..
	MM3	..	0.55(0.04)	R	B	y/16	..	..	..	..
	MM4	..	0.22(0.03)	..	..	y/12	..	..	..	..
G016.93+00.24...	MM1	..	–0.62(0.13)	B	..	n	..	..	..	..
G017.19+00.81...	MM1	0.35(0.04)	0.32(0.13)	R	R	y/29	R	0.37(0.21)	R	1.07(0.21)
	MM2	1.47(0.15)	–0.48(0.13)	B	R	y/43	R	0.55(0.21)	R	1.15(0.21)
	MM3	2.39(0.36)	–0.35(0.13)	B	B	y/35	..	..	..	..
	MM4	0.40(0.08)	0.27(0.16)	R	R	y/14	..	–0.06(0.23)	R	0.48(0.23)
G018.26–00.24...	MM1	..	–1.18(0.04)	B	B	y/20	R	0.42(0.22)	B	–1.45(0.22)
	MM2	..	–1.03(0.14)	B	B	y/12	..	–0.11(0.22)	B	–0.98(0.22)
	MM3	1.68(0.65)	–1.12(0.14)	B	B	y/25	..	0.00(0.22)	B	–1.18(0.22)
	MM4	0.89(0.35)	..	..	R	y/23	..	–0.04(0.23)	B	–1.14(0.23)
	MM5	..	0.49(0.16)	R	B	y/15	..	..	..	..
G022.06+00.21...	MM1	0.23(0.07)	0.79(0.14)	R	R	y/46	..	–0.11(0.22)	R	1.31(0.22)
	MM2	0.55(0.21)	0.76(0.15)	R	R	y/12	..	..	..	..
G023.28–00.12...	MM1	..	–0.47(0.14)	B	..	n	..	–0.23(0.22)	R	0.87(0.22)
	MM2	0.26(0.07)	0.33(0.22)	R	..	y/14	..	..	..	..
G024.37–00.15...	MM1	..	–0.59(0.22)	B	B	y/11	..	..	..	..
	MM2	..	–1.11(0.26)	B	R	y/17	..	–0.15(0.31)	B	–1.11(0.31)
G024.61–00.33...	MM1	..	–0.72(0.13)	B	B	y/27	R	0.26(0.22)	B	–1.75(0.21)

Table C.2: continued.

HEC name		HCO^+(1–0)			^{12}CO(2–1)		HCO^+(4–3)		^{12}CO(3–2)	
		$\frac{T_{\rm blue}}{T_{\rm red}}$	δv (km s^{-1})	Profile	Profile	Wings/Range (km s^{-1})	Profile	δv (km s^{-1})	Profile	δv (km s^{-1})
	MM2	..	–0.07(0.14)	..	B	y/40	..	..	..	..
G024.94–00.15...	MM1	2.03(0.24)	–0.80(0.14)	B	B	y/21	B	–0.43(0.28)	B	–0.99(0.22)
	MM2	2.24(0.30)	–0.66(0.16)	B	B	y/27	..	..	..	..
G025.79+00.81...	MM1	0.44(0.10)	1.08(0.14)	R	..	y/10	..	..	..	..
	MM2	..	0.25(0.06)	R	..	n	..	..	..	..
G030.90+00.00A..	MM1	..	0.66(0.03)	R	R	y/20	..	–0.04(0.16)	R	0.63(0.22)
G030.90+00.00B..	MM2	1.90(0.24)	–0.42(0.18)	B	B	y/13	..	–0.17(0.26)	..	–0.19(0.24)
G030.90+00.00C..	MM3	..	–0.27(0.02)	B	B	y/26	..	..	..	..
G034.71–00.63...	MM1	..	–0.11(0.01)	..	..	y/43	..	..	..	..
	MM2	..	–0.35(0.07)	B	R	y/25	B	–0.40(0.22)	R	0.35(0.22)
	MM3	..	1.09(0.04)	R	R	y/22	..	...	..	..
G034.77–00.81...	MM1	..	–0.76(0.07)	B	B	n	..	..	..	..
G034.85+00.43...	MM1	..	0.31(0.03)	R	B	..	..	..	..	..
G035.49–00.30A..	MM1	2.78(0.49)	–0.66(0.05)	B	B	y/16	..	..	..	..
G035.49–00.30B..	MM2	1.61(0.16)	–0.20(0.01)	..	B	y/11	..	..	..	..
	MM3	..	–0.18(0.01)	..	B	y/11	..	..	..	..
G037.44+00.14A..	MM1	..	..	..	..	n	..	..	..	..
G037.44+00.14B..	MM2	..	0.00(0.20)	..	..	..	..	..	..	..
G050.06+00.06...	MM1	0.97(0.12)	0.0(0.14)	..	..	y/14	..	..	..	..
	MM2	..	0.00(0.01)	..	..	y/17	..	..	..	..
G053.81–00.00...	MM1	3.02(0.33)	–0.34(0.13)	B	B	y/34	..	..	..	..

Table C.3: Molecular line survey results for HCO^+(1–0) and $H^{13}CO^+$(1–0); columns 7–11 are based on Gaussian fits

HEC name		HCO^+(1–0)						$H^{13}CO^+$(1–0)		
		$T_{\rm blue}$ (K)	$v_{\rm LSR,blue}$ (km s^{-1})	$T_{\rm red}$ (K)	$v_{\rm LSR,red}$ (km s^{-1})	T (K)	$v_{\rm LSR}$ (km s^{-1})	T (K)	$v_{\rm LSR}$ (km s^{-1})	ΔV (km s^{-1}
G012.73–00.58...	MM1					1.72(0.09)	6.82(0.01)	0.75(0.08)	6.69(0.02)	0.68(0.05)
	MM2	1.04(0.06)	5.16(0.25)	2.41(0.06)	6.87(0.25)			1.19(0.11)	6.50(0.02)	0.72(0.05)
G013.28–00.34...	MM1	1.20(0.10)	40.17(0.25)	0.76(0.10)	42.49(0.25)			0.55(0.06)	41.30(0.06)	1.91(0.15)
G013.91–00.51...	MM1	2.08(0.08)	22.08(0.25)	1.27(0.08)	24.05(0.25)			1.7(0.07)	22.97(0.02)	1.39(0.04)
G013.97–00.45...	MM1	1.43(0.09)	18.51(0.25)	1.15(0.09)	20.88(0.25)			0.82(0.06)	20.03(0.05)	2.08(0.11)
G014.39–00.75A..	MM1					2.39(0.12)	17.20(0.03)	1.02(0.08)	17.83(0.03)	1.22(0.07)
	MM2					0.86(0.12)	20.18(0.06)	0.79(0.06)	17.58(0.03)	1.3(0.08)
G014.39–00.75B..	MM3					0.39(0.07)	15.55(0.14)	0.87(0.06)	21.34(0.02)	1.00(0.05)
G014.63–00.57...	MM1	3.18(0.13)	16.19(0.25)	3.04(0.13)	20.30(0.25)			1.25(0.05)	18.55(0.03)	2.45(0.07)
	MM2	0.56(0.11)	17.14(0.25)	1.24(0.11)	20.28(0.25)			1.34(0.05)	18.44(0.02)	1.56(0.04)
	MM3					1.20(0.09)	18.24(0.06)	0.61(0.06)	17.41(0.05)	1.50(0.12)
	MM4					0.55(0.07)	19.42(0.09)	0.45(0.09)	19.24(0.04)	0.80(0.12)
G016.93+00.24...	MM1	2.55(0.11)	23.14(0.25)					1.13(0.05)	23.77(0.01)	1.01(0.04)
G017.19+00.81...	MM1	1.78(0.14)	23.68(0.25)	5.05(0.14)	25.48(0.25)			1.23(0.06)	25.00(0.02)	1.50(0.05)
	MM2	4.77(0.20)	21.93(0.25)	3.25(0.20)	24.82(0.25)			1.53(0.05)	22.79(0.02)	1.78(0.05)
	MM3	4.47(0.12)	22.18(0.25)	1.86(0.12)	24.44(0.25)			1.76(0.06)	22.73(0.02)	1.54(0.04)
	MM4	0.93(0.05)	19.89(0.25)	2.33(0.05)	22.69(0.25)			0.38(0.03)	22.1(0.05)	2.19(0.11)
G018.26–00.24...	MM1					1.51(0.1)	65.46(0.08)	0.78(0.04)	68.4(0.04)	2.49(0.09)
	MM2	1.36(0.12)	65.59(0.25)					1.00(0.05)	67.79(0.03)	2.14(0.08)
	MM3	1.16(0.17)	65.64(0.25)	0.69(0.17)	71.45(0.25)			0.89(0.04)	68.62(0.04)	2.67(0.09)
	MM4	0.84(0.17)	65.26(0.25)	0.94(0.17)	71.66(0.25)			0.72(0.04)	68.83(0.05)	2.95(0.11)
	MM5	0.71(0.25)	67.28(0.25)					0.75(0.04)	66.56(0.04)	2.43(0.11)
G022.06+00.21...	MM1	0.86(0.20)	46.54(0.25)	3.81(0.20)	52.95(0.25)			1.32(0.06)	51.35(0.03)	2.01(0.08)
	MM2	0.42(0.10)	49.35(0.25)	0.77(0.10)	53.16(0.25)			0.65(0.05)	51.82(0.05)	1.75(0.1)
G023.28–00.12...	MM1					3.25(0.12)	99.85(0.03)	0.77(0.05)	99.03(0.04)	2.03(0.09)
	MM2	0.42(0.09)	96.13(0.25)	1.63(0.09)	99.94(0.25)			0.32(0.06)	99.52(0.08)	1.31(0.18)
G024.37–00.15...	MM1	0.71(0.06)	57.77(0.25)					0.39(0.04)	59.24(0.08)	2.49(0.17)
	MM2					0.37(0.08)	53.7(0.24)	0.45(0.06)	56.23(0.08)	2.27(0.22)
G024.61–00.33...	MM1	1.08(0.14)	41.56(0.25)					1.44(0.06)	42.79(0.02)	1.72(0.05)
	MM2	1.23(0.09)	43.52(0.25)					0.70(0.06)	43.63(0.04)	1.41(0.09)

Table C.3: continued.

HEC name		HCO^+(1–0)						$H^{13}CO^+$(1–0)		
		$T_{\rm blue}$ (K)	$v_{\rm LSR,blue}$ (km s^{-1})	$T_{\rm red}$ (K)	$v_{\rm LSR,red}$ (km s^{-1})	T (K)	$v_{\rm LSR}$ (km s^{-1})	T (K)	$v_{\rm LSR}$ (km s^{-1})	ΔV (km s^{-1}
G024.94–00.15...	MM1	2.62(0.10)	45.77(0.25)	1.29(0.10)	49.28(0.25)			0.88(0.05)	47.37(0.04)	2.00(0.08)
	MM2	2.06(0.09)	46.93(0.25)	0.93(0.09)	49.91(0.25)			0.54(0.04)	48.17(0.05)	1.87(0.11)
G025.79+00.81...	MM1	0.49(0.08)	49.18(0.25)	1.11(0.08)	51.57(0.25)			0.62(0.05)	49.85(0.04)	1.60(0.09)
	MM2					0.25(0.04)	50.27(0.14)	0.26(0.08)	50.03(0.11)	0.97(0.24)
G030.90+00.00A..	MM1					2.61(0.14)	76.66(0.03)	0.99(0.06)	75.25(0.04)	2.14(0.09)
G030.90+00.00B..	MM2	2.43(0.11)	91.59(0.05)	1.28(0.11)	95.06(0.25)			0.79(0.05)	92.81(0.06)	2.94(0.13)
G030.90+00.00C..	MM3					0.74(0.03)	93.91(0.12)	0.52(0.05)	94.33(0.04)	1.58(0.12)
G034.71–00.63...	MM1					2.38(0.25)	44.52(0.07)	1.00(0.05)	44.76(0.03)	2.26(0.08)
	MM2	2.11(0.11)	45.23(0.25)					0.76(0.04)	45.83(0.03)	1.73(0.08)
	MM3	0.64(0.07)	48.41(0.25)					0.88(0.05)	46.49(0.03)	1.76(0.07)
G034.77–00.81...	MM1					0.59(0.07)	42(0.07)	0.23(0.03)	43.68(0.1)	2.21(0.21)
G034.85+00.43...	MM1					0.83(0.07)	56(0.04)	0.53(0.06)	55.72(0.03)	0.90(0.08)
G035.49–00.30A..	MM1	1.14(0.05)	54.06(0.25)	0.41(0.05)	57.7(0.25)			0.46(0.04)	55.61(0.07)	2.17(0.15)
G035.49–00.30B..	MM2	1.71(0.06)	44.14(0.25)	1.06(0.06)	46.24(0.25)			0.65(0.04)	45.39(0.03)	1.68(0.07)
	MM3	2.92(0.07)	45.02(0.25)					0.92(0.05)	45.85(0.04)	1.99(0.09)
G037.44+00.14A..	MM1							0.93(0.07)	18.26(0.02)	0.64(0.04)
G037.44+00.14B..	MM2					0.27(0.17)	40.46(0.08)	0.28(0.17)	40.46(0.08)	1.33(0.17)
G050.06+00.06...	MM1	0.98(0.06)	53.23(0.25)	1.01(0.06)	55.36(0.25)			0.62(0.04)	54.44(0.04)	1.89(0.09)
	MM2					2.96(0.06)	54.93(0.01)	0.60(0.05)	54.93(0.05)	1.73(0.11)
G053.81–00.00...	MM1	3.66(0.10)	23.69(0.25)	1.21(0.10)	25.74(0.25)			0.76(0.04)	24.13(0.02)	1.29(0.06)

Table C.4: Properties of N_2H^+(1–0) based on Gaussian fits

HEC name		$\int T_{\rm MB}\Delta v$ (K km s^{-1})	$v_{\rm LSR}$ (km s^{-1})	Δv (km s^{-1})	$\tau_{\rm tot}$	$T_{\rm ex}$ (K)	$N_{\rm N_2H^+}$ (10^{12} cm^{-2})
G012.73–00.58...	MM1	3.7(0.1)	6.68(0.01)	0.42(0.01)	4.11(1.18)	5.3(1.6)	5.3(2.2)
	MM2	6.7(0.2)	6.35(0.01)	0.83(0.04)	5.97(0.91)	4.6(0.8)	12.1(2.8)
G013.28–00.34..	MM1	9.3(0.4)	41.33(0.02)	1.68(0.07)	5.58(0.84)	4.3(0.8)	20.6(5.0)
G013.91–00.51...	MM1	12.9(0.4)	22.75(0.01)	1.19(0.03)	5.34(0.45)	5.7(0.6)	22.0(3.0)
G013.97–00.45...	MM1	8.5(0.3)	19.87(0.03)	2.07(0.09)	1.25(0.47)	7.8(3.0)	15.2(8.2)
G014.39–00.75A..	MM1	6.6(0.3)	17.64(0.02)	1.14(0.07)	-	-	-
	MM2	6.9(0.3)	17.12(0.02)	0.92(0.05)	-	-	-
G014.39–00.75B..	MM3	6.7(0.3)	21.15(0.01)	0.72(0.04)	8.99(1.55)	4.4(0.9)	14.8(4.0)
G014.63–00.57...	MM1	45.8(2.3)	18.45(0.01)	2.46(0.02)	2.35(0.13)	13.3(0.8)	89.0(7.4)
	MM2	17.9(0.7)	18.23(0.01)	1.27(0.03)	3.90(0.42)	7.6(0.9)	27.8(4.5)
	MM3	7.7(0.3)	17.44(0.03)	1.34(0.08)	3.71(0.93)	4.8(1.3)	13.0(4.8)
	MM4	2.8(0.2)	19.03(0.03)	0.63(0.06)	6.66(2.54)	3.7(1.6)	7.3(4.2)
G016.93+00.24...	MM1	8.7(0.3)	23.63(0.02)	0.84(0.05)	4.17(1.05)	5.9(1.6)	12.8(4.8)
G017.19+00.81...	MM1	21.3(0.6)	24.83(0.01)	1.54(0.04)	0.77(0.01)	36.7(0.9)	125.3(4.9)
	MM2	32.9(1.1)	22.65(0.01)	2.21(0.04)	1.0(0.17)	27.7(4.8)	135.0(32.7)
	MM3	25.1(0.7)	22.50(0.01)	1.74(0.02)	0.91(0.01)	30.3(0.3)	115.4(1.8)
	MM4	4.5(0.2)	22.00(0.03)	2.10(0.05)	0.45(0.12)	15.9(4.2)	20.1(7.5)
G018.26–00.24...	MM1	23.5(1.0)	68.45(0.02)	2.50(0.06)	2.10(0.32)	8.7(1.4)	37.4(8.3)
	MM2	26.0(1.0)	67.87(0.02)	2.16(0.01)	4.00(0.22)	7.1(0.4)	43.2(3.4)
	MM3	37.4(1.3)	68.65(0.01)	2.70(0.01)	-	-	-
	MM4	30.6(1.0)	68.72(0.01)	2.94(0.02)	-	-	-
	MM5	16.8(0.8)	66.24(0.02)	1.75(0.06)	3.47(0.45)	6.4(0.9)	25.5(5.0)
G022.06+00.21...	MM1	28.7(1.3)	51.25(0.01)	2.50(0.01)	1.17(0.01)	17.7(0.1)	76.6(0.5)
	MM2	8.3(0.4)	51.59(0.02)	1.74(0.08)	1.57(0.52)	7(2.4)	13.4(6.4)
G023.28–00.12...	MM1	17.9(0.6)	98.87(0.02)	2.11(0.06)	-	-	-
	MM2	4.07(0.2)	99.35(0.03)	0.95(0.09)	4.95(1.98)	3.9(1.8)	8.9(5.5)
G024.37–00.15...	MM1	13.5(0.8)	58.87(0.02)	2.53(0.05)	1.33(0.27)	8.6(1.8)	23.5(6.9)
	MM2	12.8(0.5)	56.18(0.02)	2.28(0.07)	1.55(0.32)	7.9(1.7)	21.4(6.4)
G024.61–00.33...	MM1	16.2(0.5)	42.82(0.01)	2.12(0.04)	-	-	
	MM2	10.6(0.4)	43.56(0.01)	1.66(0.04)	-	-	
G024.94–00.15...	MM1	20.0(0.8)	47.24(0.02)	2.48(0.05)	1.30(0.23)	12.1(2.2)	41.6(10.6)
	MM2	11.9(0.4)	48.22(0.01)	1.92(0.05)	0.36(0.01)	-	-
G025.79+00.81...	MM1	11.1(0.3)	49.78(0.01)	1.56(0.05)	1.35(0.34)	10.4(2.9)	20.7(8.2)
	MM2	3.0(0.2)	49.78(0.06)	1.90(0.24)	0.36(0.01)	-	-
G030.90+00.00A..	MM1	22.8(0.8)	75.21(0.01)	2.38(0.02)	0.26(0.02)	-	-
G030.90+00.00B..	MM2	25.2(0.3)	92.95(0.01)	3.15(0.02)	-	-	-
G030.90+00.00C..	MM3	13.6(0.6)	94.29(0.02)	1.50(0.06)	1.76(0.51)	9.6(2.9)	22.4(9.4)
G034.71–00.63...	MM1	11.7(0.7)	44.57(0.04)	2.31(0.10)	2.61(0.61)	5.3(1.4)	18.5(6.6)
	MM2	11.5(0.5)	45.54(0.02)	1.58(0.08)	4.90(0.91)	4.9(1.1)	20.9(6.2)
	MM3	8.9(0.3)	46.24(0.01)	1.59(0.05)	1.47(0.35)	8.1(2)	14.7(5.1)
G034.77–00.81...	MM1	1.6(0.1)	43.29(0.06)	1.60(0.19)	-	-	-
G034.85+00.43...	MM1	3.5(0.1)	55.68(0.02)	0.72(0.05)	8.20(2.04)	3.6(1.1)	9.8(3.9)
G035.49–00.30A..	MM1	8.3(0.3)	55.28(0.01)	2.14(0.04)	0.18(0.03)	-	-
G035.49–00.30B..	MM2	9.4(0.4)	45.40(0.01)	1.37(0.04)	5.52(0.64)	4.6(0.6)	18.4(3.3)
	MM3	14.8(0.5)	45.69(0.01)	1.86(0.04)	3.28(0.30)	6(0.6)	23.0(3.2)
G037.44+00.14A..	MM1	3.4(0.1)	18.14(0.01)	0.57(0.02)	4.19(0.90)	4.5(1)	5.6(1.7)
G037.44+00.14B..	MM2	1.0(0.1)	40.15(0.13)	1.07(0.35)	-	-	-
G050.06+00.06...	MM1	5.3(0.2)	54.23(0.02)	1.32(0.07)	3.83(0.82)	4.1(1)	10.3(3.4)
	MM2	4.3(0.2)	54.93(0.03)	1.32(0.08)	1.85(0.85)	5(2.4)	6.8(4.5)
G053.81–00.00...	MM1	9.0(0.3)	24.11(0.01)	1.64(0.03)	0.56(0.10)	4.1(1)	10.3(3.4)

Table C.5: Observed properties of N_2H^+(3–2) and HCO^+(4–3)

HEC name		N_2H^+(3–2)			HCO^+(4–3)						
		$\int T_{\rm MB}{\rm d}v$ (K km s^{-1})	$v_{\rm LSR}$ (km s^{-1})	Δv (km s^{-1})	$\int T_{\rm MB}{\rm d}v$ (K km s^{-1})	$v_{\rm LSR}$ (km s^{-1})	Δv (km s^{-1})	$T_{\rm blue}$ (K)	$v_{\rm LSR,blue}$ (km s^{-1})	$T_{\rm red}$ (km s^{-1})	$v_{\rm LSR,red}$
G013.91–00.51..	MM1	2.4(0.2)	22.77(0.08)	1.56(0.2)	4.2(0.4)	22.43(0.06)	1.38(0.16)	-	-	-	-
G014.39–00.75A.	MM1	1.9(0.3)	17.67(0.1)	1.32(0.26)	..	..	..	..	..	..	..
G014.63–00.57..	MM1	25.6(0.4)	18.63(0.04)	5.34(0.08)	27.9(0.4)	17.75(0.04)	5.05(0.1)	7.37(0.30)	17.1(0.2)	5.25(0.30)	20.4(0.2)
	MM2	8.2(0.4)	18.42(0.07)	3.31(0.2)	7.6(0.3)	18.29(0.08)	3.75(0.19)	2.34(0.26)	17.3(0.2)	2.22(0.26)	18.9(0.2)
G017.19+00.81..	MM1	9.8(0.4)	25.18(0.05)	2.88(0.14)	8.8(0.5)	25.05(0.06)	2.31(0.14)	-	-	4.00(0.45)	25.5(0.2)
	MM2	18.7(0.4)	22.82(0.04)	4.21(0.1)	25.5(0.7)	22.78(0.08)	5.99(0.19)	4.29(0.45)	21.4(0.2)	5.32(0.45)	23.8(0.2)
	MM4	1.7(0.3)	21.57(0.15)	1.88(0.37)	4.1(0.5)	21.97(0.15)	2.61(0.36)	1.37(0.44)	21.1(0.2)	1.92(0.44)	22.7(0.2)
G018.26–00.24..	MM1	8.6(0.3)	68.52(0.10)	5.05(0.21)	9.2(0.7)	68.67(0.21)	5.38(0.48)	1.31(0.46)	66.9(0.2)	2.21(0.46)	69.4(0.2)
	MM2	7.6(0.4)	67.95(0.10)	4.37(0.25)	3.6(0.3)	67.76(0.15)	3.15(0.28)	1.17(0.27)	67.3(0.2)	0.81(0.29)	68.9(0.2)
	MM3	12.9(0.3)	68.73(0.06)	4.33(0.14)	11.7(0.5)	68.52(0.09)	4.21(0.21)	2.93(0.35)	68.1(0.2)	-	-
	MM4	8.9(0.4)	68.90(0.09)	4.42(0.20)	7.2(0.5)	68.84(0.13)	4.26(0.32)	-	-	1.58(0.32)	69.4(0.2)
G022.06+00.21..	MM1	16.3(0.4)	51.24(0.06)	5.33(0.15)	27.0(0.9)	51.12(0.09)	5.31(0.22)	4.63(0.57)	50.5(0.2)	4.66(0.57)	52.2(0.2)
G023.28–00.12..	MM1	4.7(0.4)	98.96(0.14)	4.01(0.40)	5.1(0.6)	98.57(0.18)	3.03(0.46)	2.56(0.51)	97.8(0.2)	1.44(0.51)	99.1(0.2)
G024.37–00.15..	MM2	5.4(0.3)	56.21(0.11)	3.92(0.27)	6.1(0.7)	57.11(0.39)	5.48(0.86)	-	-	-	-
G024.61–00.33..	MM1	6.7(0.3)	42.86(0.07)	3.49(0.19)	9.8(0.6)	42.80(0.10)	3.10(0.24)	-	-	3.25(0.54)	43.5(0.2)
G024.94–00.15..	MM1	7.4(0.3)	47.13(0.09)	3.94(0.22)	8.7(0.6)	46.70(0.17)	4.67(0.35)	2.04(0.44)	45.9(0.2)	1.86(0.44)	47.9(0.2)
G030.90+00.00A.	MM1	7.7(0.3)	75.30(0.07)	3.73(0.17)	7.7(0.7)	75.17(0.13)	3.14(0.34)	-	-	-	-
G030.90+00.00B.	MM2	6.7(0.3)	92.96(0.11)	4.69(0.26)	5.2(0.6)	92.53(0.19)	3.54(0.54)	-	-	-	-
G034.71–00.63..	MM1	6.1(0.4)	44.76(0.12)	4.40(0.29)	16.6(0.9)	44.38(0.15)	6.16(0.41)	3.15(0.50)	43.8(0.2)	3.17(0.50)	45.8(0.2)
	MM2	2.7(0.4)	45.88(0.29)	4.09(0.62)	1.2(0.5)	45.14(0.13)	0.74(0.44)	-	-	-	-
G053.81–00.00	MM1	3.7(0.34)	24.44(0.11)	2.48(0.32)	..	..	..	..	..	..	..

Table C.6: Star formation tracers (ii): K levels of $CH_3CN(5–4)$

HEC name		K levels				$T_{\rm rot}$	N(CH_3CN)
		0	1	2	3	(K)	(10^{12}cm^{-2})
G014.63–00.57...	MM1	√	√	√	√	29(6)	5.9(2.6)
	MM2	√	√	√	√	59(46)	-
	MM4	√	-	-	-	-	-
G017.19+00.81...	MM1	√	√	-	√	86(64)	-
	MM2	√	√	√	-	39(21)	-
	MM3	√	√	-	-	45(29)	-
	MM4	√	√	√	-	33(18)	-
G018.26–00.24...	MM1	√	√	-	-	24(10)	-
	MM2	√	√	-	-	30(21)	-
	MM3	√	√	√	-	23(11)	-
	MM4	√	√	-	√	37(19)	-
G022.06+00.21...	MM1	√	√	√	√	34(5)	9.7(2.8)
G023.28–00.12...	MM1	√	√	-	-	54(31)	-
G024.37–00.15...	MM1	√	√	√	-	36(12)	3.2(2.2)
	MM2	√	√	√	-	63(34)	-
G024.61–00.33...	MM1	√	√	-	√	64(26)	5.3(4.1)
G024.94–00.15...	MM1	√	√	√	-	46(39)	-
	MM2	√	√	√	-	-	-
G025.79+00.81...	MM1	√	√	√	√	34(20)	0 0
G030.90+00.00A..	MM1	√	√	√	-	-	-
G030.90+00.00C..	MM3	√	√	-	-	-	-
G034.71–00.63...	MM1	√	√	√	√	28(7)	5.3(2.9)
	MM2	√	√	√	-	-	-
G035.49–00.30A..	MM1	√	-	-	-	-	-

Table C.7: Star formation tracers (i): SiO(2–1) and H_2CO(4–3) based on Gaussian fits

HEC name		SiO(2–1)			H_2CO(4–3)		
		T (K)	$v_{\rm LSR}$ (km s^{-1})	ΔV (km s^{-1})	T (K)	$v_{\rm LSR}$ (km s^{-1})	ΔV (km s^{-1})
G013.28–00.34...	MM1	0.11(0.03)	39.47(0.43)	4.74(0.88)	-	-	-
G013.91–00.51...	MM1	-	-	-	0.53(0.17)	22.94(0.13)	1.24(0.3)
G014.39–00.75A..	MM1	-	-	-	0.80(0.30)	17.64(0.14)	1.01(0.28)
G014.63–00.57...	MM1	0.45(0.04)	17.60(0.10)	5.17(0.34)	2.41(0.10)	17.23(0.05)	3.62(0.11)
	MM2	0.08(0.02)	18.73(0.53)	6.42(1.28)	0.85(0.15)	18.24(0.12)	2.71(0.37)
G017.19+00.81...	MM1	0.09(0.02)	24.68(0.50)	7.77(1.05	0.56(0.13)	24.96(0.17)	2.28(0.39)
	MM2	0.79(0.11)[a]	22.22(0.25)[a]	26.48(0.64)	1.39(0.10)	22.46(0.12)	5.92(0.34)
	MM3	0.76(0.11)[a]	21.95(0.25)[a]	19.42(0.60)	-	-	-
G018.26–00.24...	MM1	0.36(0.02)	66.88(0.16)	9.18(0.47)	0.69(0.12)	68.02(0.18)	3.69(0.49)
	MM2	0.09(0.02)	68.01(0.64)	11.14(2.35)	0.41(0.12)	67.74(0.29)	3.12(0.70)
	MM3	0.21(0.02)	68.50(0.27)	10.06(0.85)	0.46(0.14)	68.52(0.22)	3.06(0.75)
	MM4	0.25(0.02)	69.24(0.28)	13.02(0.83)	0.34(0.14)	69.91(0.43)	4.30(1.46)
G022.06+00.21...	MM1	0.24(0.02)	48.27(0.35)	16.26(0.89)	1.88(0.11)	51.04(0.08)	4.78(0.22)
G023.28–00.12...	MM1	0.13(0.02)	101.05(0.55)	12.37(1.39)	-	-	-
G024.37–00.15...	MM2	0.25(0.02)	54.53(0.30)	10.81(0.84)	0.69(0.11)	55.79(0.21)	5.13(0.64)
G024.61–00.33...	MM1	0.11(0.02)	40.44(0.49)	10.18(1.2)	0.54(0.10)	42.96(0.24)	3.63(0.50)
G024.94–00.15...	MM1	0.24(0.03)	47.14(0.19)	5.91(0.51)	0.69(0.12)	46.83(0.19)	3.87(0.50)
	MM2	0.18(0.02)	47.39(0.38)	11.61(1.08)	-	-	-
G025.79+00.81...	MM1	0.12(0.04)	49.20(0.56)	8.04(2.01)	-	-	-
G034.71–00.63...	MM1	0.15(0.02)	44.40(0.46)	14.14(1.19)	1.49(0.13)	44.12(0.08)	3.02(0.21)
	MM2	0.35(0.08)	45.47(0.23)	6.63(1.25)	0.27(0.09)	45.26(0.57)	5.03(1.31)
	MM3	0.17(0.04)	45.94(0.20)	3.37(0.62)	-	-	-
G035.49–00.30B..	MM2	0.14(0.03)	45.07(0.25)	3.88(0.67)	-	-	-
	MM3	0.18(0.05)	45.32(0.14)	1.57(0.32)	-	-	-
G053.81–00.00...	MM1	0.11(0.01)	23.14(0.24)	9.14(0.52)	0.47(0.11)	23.79(0.39)	4.81(0.79)

[a]Not based on Gaussian fit.

Table C.8: Observed properties of $C^{18}O(2–1)$ based on Gaussian fits

HEC name		$\int T_{\rm MB} {\rm d}v$ (K km s^{-1})	$v_{\rm LSR}$ (km s^{-1})	Δv (km s^{-1})
G012.73–00.58...	MM1	-	-	-
	MM2	2.1(0.7)	6.14(0.44)	1.84(0.7)
G013.28–00.34...	MM1	4.3(0.5)	41.09(0.12)	1.53(1.79)
G013.91–00.51...	MM1	9.7(0.5)	22.95(0.07)	2.81(0.19)
G013.97–00.45...	MM1	12.4(0.5)	19.66(0.05)	2.57(0.12)
G014.39–00.75A..	MM1	12.9(0.5)	17.67(0.04)	2.10(0.10)
	MM2	14.1(0.5)	17.6(0.04)	2.15(0.08)
G014.39–00.75B..	MM3	5.8(0.3)	21.06(0.04)	1.81(0.28)
G014.63–00.57...	MM1	18.8(0.2)	18.02(0.02)	3.14(0.05)
	MM2	17.1(0.3)	18.34(0.02)	2.77(0.05)
	MM3	11.0(0.2)	17.36(0.02)	2.24(0.04)
	MM4	6.2(0.2)	18.9(0.03)	1.96(0.14)
G016.93+00.24...	MM1	8.7(0.3)	23.55(0.04)	1.99(0.08)
G017.19+00.81...	MM1	9.9(0.2)	24.23(0.02)	2.85(0.06)
	MM2	9.6(0.2)	22.63(0.02)	2.41(0.05)
	MM3	9.0(0.1)	22.75(0.02)	2.51(0.05)
	MM4	12.5(0.1)	21.72(0.01)	2.66(0.04)
G018.26–00.24...	MM1	10.3(0.5)	67.82(0.09)	3.70(0.25)
	MM2	18.2(0.4)	67.44(0.03)	2.86(0.08)
	MM3	15.5(0.4)	68.51(0.05)	3.72(0.11)
	MM4	13.3(0.7)	68.4(0.1)	3.78(0.22)
	MM5	17.0(0.5)	66.48(0.04)	2.82(0.08)
G022.06+00.21...	MM1	19.0(0.3)	51.29(0.02)	3.08(0.05)
	MM2	9.6(0.4)	51.87(0.05)	2.69(0.12)
G023.28–00.12...	MM1	14.7(0.9)	99.15(0.08)	2.89(0.22)
	MM2	6.1(0.8)	99.54(0.15)	1.96(0.27)
G024.37–00.15...	MM1	14.6(0.4)	58.99(0.04)	2.93(0.1)
	MM2	4.6(0.5)	56.32(0.2)	3.67(0.44)
G024.61–00.33...	MM1	12.9(0.2)	42.43(0.02)	2.45(0.04)
	MM2	3.9(0.3)	43.43(0.09)	3.12(0.26)
G024.94–00.15...	MM1	5.5(0.3)	47.07(0.05)	2.48(0.16)
	MM2	4.7(0.3)	47.74(0.1)	3.26(0.2)
G025.79+00.81...	MM1	3.4(0.2)	49.8(0.06)	2.16(0.19)
	MM2	4.2(0.2)	49.04(0.05)	2.77(0.12)
G030.90+00.00A..	MM1	19.8(0.7)	75.11(0.05)	3.22(0.13)
G030.90+00.00B..	MM2	17.8(0.4)	92.64(0.04)	3.86(0.10)
G030.90+00.00C..	MM3	15.4(0.5)	94.35(0.08)	4.46(0.18)
G034.71–00.63...	MM1	7.9(0.2)	44.93(0.04)	3.31(0.12)
	MM2	5.7(0.2)	45.96(0.06)	2.82(0.14)
	MM3	6.3(0.2)	46.55(0.04)	2.66(0.09)
G034.77–00.81...	MM1	5.2(0.3)	43.72(0.08)	3.44(0.21)
G034.85+00.43...	MM1	2.8(0.2)	55.51(0.07)	2.11(0.14)
G035.49–00.30A..	MM1	11.8(0.2)	55.4(0.03)	2.77(0.06)
G035.49–00.30B..	MM2	4.1(0.2)	45.16(0.04)	2.04(0.13)
	MM3	5.7(0.2)	45.67(0.05)	2.46(0.11)
G037.44+00.14A..	MM1	1.0(0.1)	18.07(0.05)	1.37(1.5)
G037.44+00.14B..	MM2	8.0(0.2)	40.11(0.03)	1.87(0.05)
G050.06+00.06...	MM1	10.1(0.2)	54.19(0.02)	2.27(0.05)
	MM2	10.4(0.3)	54.82(0.03)	2.06(0.05)
G053.81–00.00...	MM1	3.8(0.1)	23.89(0.02)	2.30(0.07)

Table C.9: Derived abundance and depletion of $C^{18}O$(2–1)

HEC name		$T_{\rm rot}(NH_3)$ (K)	$N_{C^{18}O}$ (10^{15} cm^{-2})	N_{H_2} (10^{22} cm^{-2})	$\chi_{C^{18}O}$ (10^{-8})	η
G012.73–00.58...	MM1	9.3	-	4.5	..	..
	MM2	11.4	1.3(0.5)	..	..	..
G013.28–00.34...	MM1	14.9	2.4(0.3)	2.9	8.3	2.1
G013.91–00.51...	MM1	14.1	5.5(0.3)	7.7	7.1	2.4
G013.97–00.45...	MM1	16.6	6.9(0.3)	..	..	..
G014.39–00.75A..	MM1	17.4	7.2(0.3)	5.7	12.6	1.3
	MM2	20.0	7.9(0.3)	..	..	..
G014.39–00.75B..	MM3	11.8	3.5(0.2)	5.7	6.2	2.8
G014.63–00.57...	MM1	18.1	10.5(0.1)	26.3	4	4.3
	MM2	15.7	9.6(0.2)	15.4	6.2	2.7
	MM3	15.8	6.1(0.1)	5.2	11.8	1.4
	MM4	19.1	3.4(0.1)	3	11.5	1.5
G016.93+00.24...	MM1	14.0	4.9(0.2)	4.2	11.8	1.4
G017.19+00.81...	MM1	17.2	5.5(0.1)	4.9	11.3	1.5
	MM2	18.7	5.4(0.1)	17.4	3.1	5.5
	MM3	20.0	5.1(0.1)	5.3	9.6	1.8
	MM4	20.1	7.0(0.1)	2.9	24.3	0.7
G018.26–00.24...	MM1	18.2	5.7(0.3)	9.8	5.9	2.9
	MM2	17.4	10.1(0.2)	8.9	11.4	1.5
	MM3	15.7	8.7(0.2)	7.1	12.2	1.4
	MM4	16.6	7.4(0.4)	5.7	12.9	1.3
	MM5	16.8	9.5(0.2)	6	15.8	1.1
G022.06+00.21...	MM1	24.7	11.2(0.2)	25.4	4.4	3.8
	MM2	15.5	5.4(0.2)	7.9	6.8	2.5
G023.28–00.12...	MM1	18.1	8.2(0.5)	6.5	12.6	1.3
	MM2	10.0	3.4(0.6)	..	..	..
G024.37–00.15...	MM1	18.6	8.1(0.2)	4.9	16.6	1
	MM2	15.7	2.6(0.3)	4.4	5.8	2.9
G024.61–00.33...	MM1	17.5	7.2(0.1)	5.9	12.2	1.4
	MM2	15.5	2.2(0.1)	3.5	6.3	2.7
G024.94–00.15...	MM1	15.2	3.1(0.1)	6.5	4.7	3.6
	MM2	15.2	2.7(0.1)	5.5	4.8	3.5
G025.79+00.81...	MM1	13.1	1.9(0.1)	..	..	..
	MM2	15.0	2.4(0.1)	..	..	..
G030.90+00.00A..	MM1	18.6	11(0.4)	5.2	21.2	0.8
G030.90+00.00B..	MM2	15.0	10(0.2)	..	..	..
G030.90+00.00C..	MM3	16.4	8.6(0.3)	4.3	20	0.9
G034.71–00.63...	MM1	17.8	4.4(0.1)	5.8	7.6	2.2
	MM2	12.4	3.4(0.1)	5.2	6.5	2.6
	MM3	17.1	3.5(0.1)	2.5	14	1.2
G034.77–00.81...	MM1	15.0	2.9(0.1)	..	..	..
G034.85+00.43...	MM1	13.2	1.6(0.1)	..	..	..
G035.49–00.30A..	MM1	18.6	6.6(0.1)	6.6	10	1.7
G035.49–00.30B..	MM2	11.9	2.5(0.1)	5.3	4.6	3.7
	MM3	13.6	3.2(0.1)	4.2	7.7	2.2
G037.44+00.14A..	MM1	15.0	0.6(0.05)	..	..	..
G037.44+00.14B..	MM2	15.0	4.5(0.1)	..	..	..
G050.06+00.06...	MM1	14.9	5.6(0.1)	4.4	12.8	1.3
	MM2	14.1	5.9(0.1)	4.6	12.9	1.3
G053.81–00.00...	MM1	12.4	2.2(0.1)	6.9	3.2	5.3

APPENDIX D

Detailed parallax and proper motion results

Table D.1: Detailed results of parallax and proper motions measurements

Background source	$v_{\rm LSR}$ (km s^{-1})	Parallax (mas)	μ_α (mas yr^{-1})	μ_δ (mas yr^{-1})
		ON 1		
		Northern group		
J2003+3034	–0.4	0.521 ± 0.055	-3.33 ± 0.18	-5.26 ± 0.41
	0.0	0.401 ± 0.052	-3.72 ± 0.17	-5.26 ± 0.21
	0.4	0.361 ± 0.052	-3.82 ± 0.17	-5.28 ± 0.19
	0.7	0.526 ± 0.057	-3.36 ± 0.19	-5.19 ± 0.34
	Combined fit	0.299 ± 0.112[1]		
	Averaging data	0.391 ± 0.061		
J2009+3049	–0.4	0.380 ± 0.121	-2.87 ± 0.39	-4.88 ± 0.31
	0.0	0.459 ± 0.140	-2.68 ± 0.46	-4.80 ± 0.22
	0.4	0.483 ± 0.142	-2.59 ± 0.48	-4.79 ± 0.20
	0.7	0.415 ± 0.112	-2.81 ± 0.37	-4.78 ± 0.23
	Combined fit	0.482 ± 0.137[1]		
	Averaging data	0.368 ± 0.070		
		Southern group		
J2003+3034	14.4		-3.88 ± 0.12	-5.92 ± 0.14
	14.8		-3.75 ± 0.09	-6.03 ± 0.11
	15.1		-3.67 ± 0.21	-6.09 ± 0.19
J2009+3034	14.4		-3.00 ± 0.15	-5.49 ± 0.20
	14.8		-2.88 ± 0.21	-5.59 ± 0.26
	15.1		-2.77 ± 0.29	-5.65 ± 0.35
Both QSOs	Combined fit	0.390 ± 0.116[1]		
	Averaging data	$\mathbf{0.389 \pm 0.045}$		

[1]The error of the combined fit multiplied by $\sqrt{N}$, where N is the number of maser spots.

Table D.1: continued.

Background source	$v_{\rm LSR}$ (km s^{-1})	Parallax (mas)	μ_α (mas yr^{-1})	μ_δ (mas yr^{-1})
$<\mu>_{north}\,(\sigma)_{pm}$			$-3.15 \pm 0.89(0.44)$[2]	$-5.03 \pm 0.46(0.22)$[2]
$<\mu>_{south}\,(\sigma)_{pm}$			$-3.33 \pm 0.90(0.45)$[2]	$-5.80 \pm 0.46(0.23)$[2]
		L 1206		
J2223+6249	–13.3	1.163 ± 0.222	0.24 ± 0.85	-2.84 ± 0.40
	–12.9	1.116 ± 0.263	0.08 ± 0.92	-2.59 ± 0.48
	–10.9	1.083 ± 0.170	0.23 ± 0.90	-2.85 ± 0.23
	–10.5	1.485 ± 0.190	0.56 ± 0.31	-1.61 ± 1.42
	Combined fit	1.318 ± 0.282[1]		
	Averaging data	1.331 ± 0.180		
J2225+6411	–13.3	1.311 ± 0.408	0.22 ± 0.51	-0.28 ± 0.63
	–12.9	1.322 ± 0.386	0.41 ± 0.50	-0.65 ± 0.56
	–10.9	1.300 ± 0.416	0.35 ± 0.52	-0.50 ± 0.65
	–10.5	1.174 ± 0.237	0.05 ± 0.64	0.11 ± 0.27
	Combined fit	1.272 ± 0.384[1]		
	Averaging data	1.288 ± 0.241		
Both QSOs	Combined fit	1.331 ± 0.250[1]		
	Averaging data	$\mathbf{1.289 \pm 0.153}$		
$<\mu>\,(\sigma)_{pm}$			$0.27 \pm 0.23(0.16)$[2]	$-1.40 \pm 1.95(1.15)$[2]
		L 1287		
J0035+6130	–27.0	1.111 ± 0.074	-0.18 ± 0.10	-2.30 ± 0.25
	–23.9	0.928 ± 0.078	-1.02 ± 0.12	-2.28 ± 0.08
	–23.5	0.957 ± 0.093	-0.93 ± 0.11	-2.48 ± 0.12
	–23.2	1.002 ± 0.084	-0.88 ± 0.11	-2.39 ± 0.09
	–22.8	0.940 ± 0.083	-1.14 ± 0.11	-2.78 ± 0.10
	–22.5	0.917 ± 0.067	-1.17 ± 0.12	-3.28 ± 0.07
	Combined fit	0.984 ± 0.086[1]		
	Averaging data	1.016 ± 0.052		
J0037+6236	–27.0	1.306 ± 0.071	-0.14 ± 0.10	-1.71 ± 0.40
	–23.9	1.244 ± 0.044	-0.88 ± 0.04	-1.72 ± 0.27
	–23.5	1.225 ± 0.040	-0.81 ± 0.04	-1.77 ± 0.25
	–23.2	1.011 ± 0.101	-0.88 ± 0.14	-1.83 ± 0.12
	–22.8	0.945 ± 0.125	-1.17 ± 0.20	-2.20 ± 0.14
	–22.5	1.330 ± 0.043	-1.01 ± 0.04	-2.64 ± 0.37
	Combined fit	1.192 ± 0.107[1]		
	Averaging data	1.150 ± 0.052		
Both QSOs	Combined fit	1.079 ± 0.069[1]		
	Averaging data	$\mathbf{1.077 \pm 0.039}$		
$<\mu>\,(\sigma)_{pm}$			$-0.86 \pm 0.11(0.33)$[2]	$-2.29 \pm 0.56(0.46)$[2]
		NGC 281-W		
J0047+5657	–30.2	0.416 ± 0.054	-2.64 ± 0.15	-1.75 ± 0.10
	–29.9	0.380 ± 0.045	-2.54 ± 0.12	-1.72 ± 0.08

[2]We calculated an unweighted arithmetic mean of the individual proper motion results from all maser spots and background sources. The error bar on the mean is the standard error of the mean to which was added, in quadrature, the apparent movement between the two background sources of the respective coordinate. The uncertainty in the proper motion, which is introduced by the background source, is hereby taken into account. In parenthesis is given the standard deviation of the mean.

Table D.1: continued.

Background source	$v_{\rm LSR}$ (km s^{-1})	Parallax (mas)	μ_α (mas yr^{-1})	μ_δ (mas yr^{-1})
	–29.5	0.401 ± 0.041	-2.58 ± 0.19	-1.72 ± 0.07
	–29.2	0.404 ± 0.047	-2.69 ± 0.22	-1.75 ± 0.08
	–28.8	0.497 ± 0.026	-2.55 ± 0.04	-1.69 ± 0.13
	–28.1	0.529 ± 0.028	-2.68 ± 0.04	-1.52 ± 0.14
	Combined fit	0.400 ± 0.070[1]		
	Averaging data	0.398 ± 0.042		
J0052+5703	–30.2	0.459 ± 0.049	-2.79 ± 0.06	-1.87 ± 0.27
	–29.9	0.420 ± 0.048	-2.68 ± 0.05	-1.84 ± 0.25
	–29.5	0.388 ± 0.048	-2.75 ± 0.05	-1.84 ± 0.22
	–29.2	0.408 ± 0.054‘	-2.87 ± 0.07	-1.87 ± 0.20
	–28.8	0.602 ± 0.056	-2.65 ± 0.07	-1.82 ± 0.26
	–28.1	0.648 ± 0.055	-2.76 ± 0.07	-1.65 ± 0.34
	Combined fit	0.399 ± 0.054[1]		
	Averaging data	0.425 ± 0.024		
Both QSOs	Combined fit	0.412 ± 0.045[1]		
	Averaging data	$\mathbf{0.421 \pm 0.022}$		
$< \mu > (\sigma)_{pm}$			$-2.69 \pm 0.16(0.10)$[2]	$-1.77 \pm 0.11(0.10)$[2]
		S 255		
J0613+1708	4.6	$\mathbf{0.628 \pm 0.027}$	-0.14 ± 0.05	-0.84 ± 1.67
μ_{pm}			-0.14 ± 0.54[2]	-0.84 ± 1.76[2]

APPENDIX E

EVN background source images

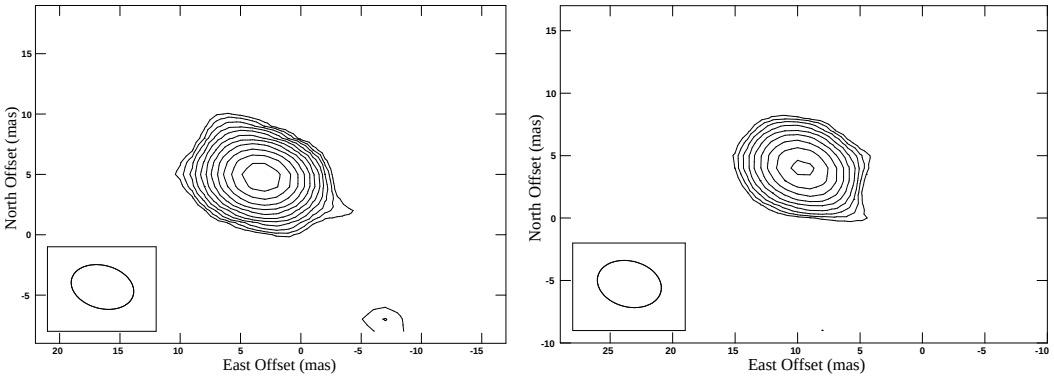

Figure E.1: Phase-referenced images for two background sources belonging to maser ON 1, J2003+3034 (*top*) and J2009+3049 (*bottom*) in the third epoch. Position offset (0,0) corresponds to the position listed in Table 5.2. The contour levels start at a 3σ level, 6.1, and 0.6 mJy beam^{-1}, respectively, and increase by factors of $\sqrt{2}$.

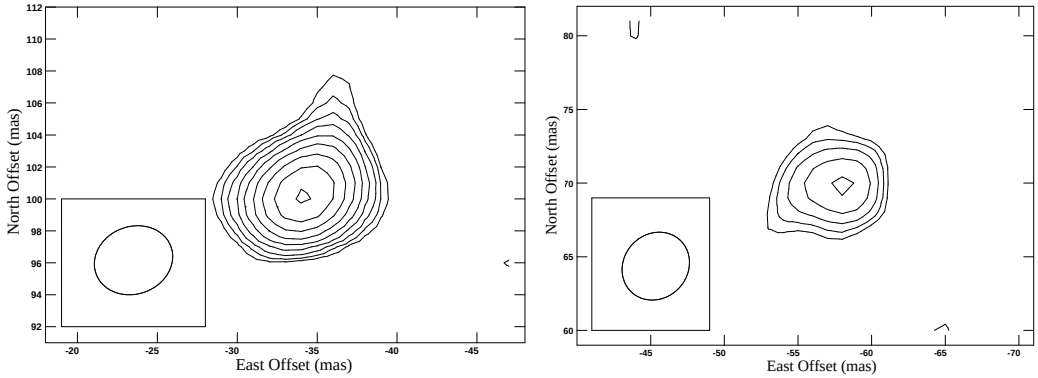

Figure E.2: Phase-referenced images for two background sources belonging to maser L 1206, J2223+6249 (*top*) and J2225+6411 (*bottom*) in the fifth epoch. Position offset (0,0) corresponds to the position listed in Table 5.2. Contour levels start at a 3σ level, 3.5, and 0.5 mJy beam^{-1} respectively, and increase by factors of $\sqrt{2}$.

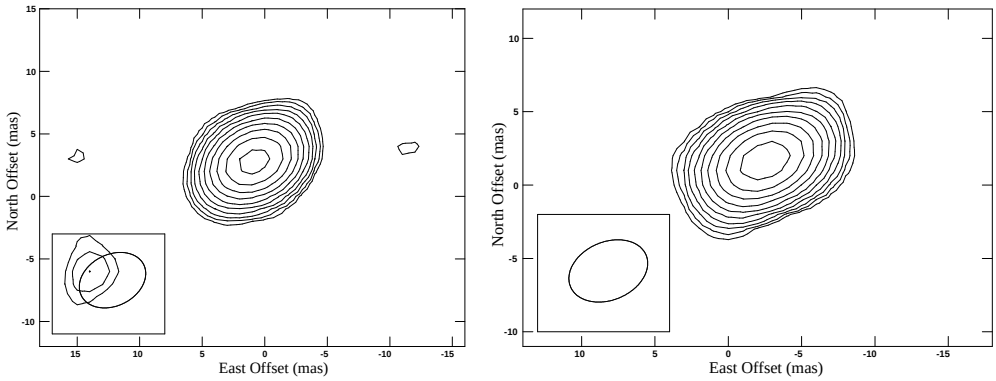

Figure E.3: Phase-referenced images for two background sources belonging to maser L 1287, J0035+6130 (*top*) and J0037+6236 (*bottom*) in epoch three. Position offset (0,0) corresponds to the position listed in Table 5.2. Contour levels start at a 3σ level, 3.6, and 2.4 mJy beam^{-1} respectively, and increase by factors of $\sqrt{2}$.

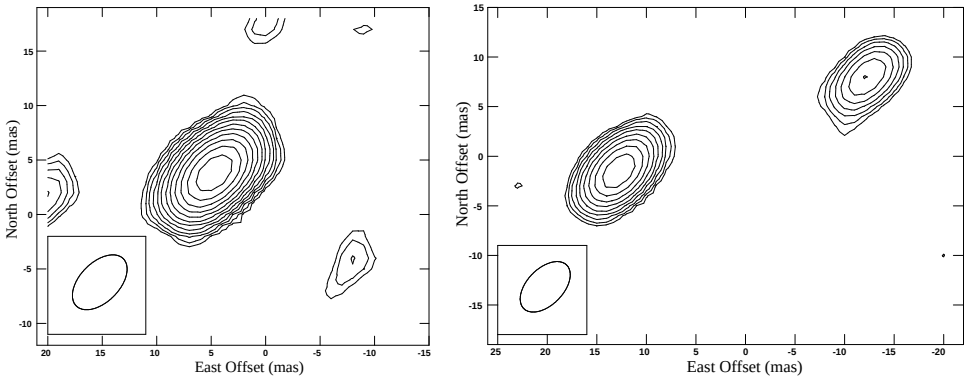

Figure E.4: Phase-referenced images for two background sources belonging to maser NGC 281-W, J0047+5657 (*top*) and J0052+5703 (*bottom*) in epoch five. Position offset (0,0) corresponds to the position listed in Table 5.2. Contour levels start at a 3σ level, 2.8, and 0.6 mJy beam^{-1} respectively, and increase by factors of $\sqrt{2}$. The bottom image shows also the additional component ~ 25 mas westward of J0052+5703.

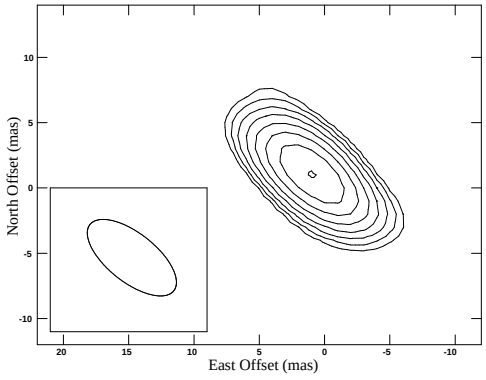

Figure E.5: Phase-referenced images for background source J0613+1708 belonging to maser S 255, in the third epoch. Position offset (0,0) corresponds to the position listed in Table 5.2. The contour levels start at a 3σ level, 3.0 mJy beam^{-1}, and increase by factors of $\sqrt{2}$.

Bibliography

Aikawa, Y., Ohashi, N., & Herbst, E. 2003, ApJ, 593, 906

Andre, P., Ward-Thompson, D., & Barsony, M. 2000, Protostars and Planets IV, 59

Araya, E., Hofner, P., Kurtz, S., Bronfman, L., & DeDeo, S. 2005, ApJS, 157, 279

Aumer, M. & Binney, J. J. 2009, MNRAS, 896

Baars, J. W. M., Genzel, R., Pauliny-Toth, I. I. K., & Witzel, A. 1977, A&A, 61, 99

Banerjee, R. & Pudritz, R. E. 2007, ApJ, 660, 479

Bartkiewicz, A., Brunthaler, A., Szymczak, M., van Langevelde, H. J., & Reid, M. J. 2008, A&A, 490, 787

Beasley, A. J., Gordon, D., Peck, A. B., et al. 2002, ApJS, 141, 13

Becker, R. H., White, R. L., Helfand, D. J., & Zoonematkermani, S. 1994, ApJS, 91, 347

Beltrán, M. T., Cesaroni, R., Codella, C., et al. 2006, Nature, 443, 427

Beltrán, M. T., Cesaroni, R., Moscadelli, L., et al. 2008, in Astronomical Society of the Pacific Conference Series, Vol. 387, Massive Star Formation: Observations Confront Theory, ed. H. Beuther, H. Linz, & T. Henning, 71–+

Benjamin, R. A., Churchwell, E., Babler, B. L., et al. 2003, PASP, 115, 953

Benson, P. J., Caselli, P., & Myers, P. C. 1998, ApJ, 506, 743

Bergin, E. A. & Langer, W. D. 1997, ApJ, 486, 316

Bertoldi, F. & McKee, C. F. 1992, ApJ, 395, 140

Beuther, H., Leurini, S., Schilke, P., et al. 2007, A&A, 466, 1065

Beuther, H., Schilke, P., Menten, K. M., et al. 2002a, ApJ, 566, 945

Beuther, H., Schilke, P., Sridharan, T. K., et al. 2002b, A&A, 383, 892

Beuther, H. & Sridharan, T. K. 2007, ApJ, 668, 348

Blitz, L., Fich, M., & Stark, A. A. 1982, ApJS, 49, 183

Bohlin, R. C., Savage, B. D., & Drake, J. F. 1978, ApJ, 224, 132

Bonnell, I. A. & Bate, M. R. 2002, MNRAS, 336, 659

Bonnell, I. A. & Bate, M. R. 2006, MNRAS, 370, 488

Bonnell, I. A., Bate, M. R., Clarke, C. J., & Pringle, J. E. 2001, MNRAS, 323, 785

Brand, J. & Blitz, L. 1993, A&A, 275, 67

Brogan, C. L., Gelfand, J. D., Gaensler, B. M., Kassim, N. E., & Lazio, T. J. W. 2006, ApJ, 639, L25

Brunthaler, A., Reid, M. J., & Falcke, H. 2005, in Astronomical Society of the Pacific Conference Series, Vol. 340, Future Directions in High Resolution Astronomy, ed. J. Romney & M. . Reid, 455

Brunthaler, A., Reid, M. J., Falcke, H., Henkel, C., & Menten, K. M. 2007, A&A, 462, 101

Carey, S. J., Clark, F. O., Egan, M. P., et al. 1998, ApJ, 508, 721

Carey, S. J., Feldman, P. A., Redman, R. O., et al. 2000, ApJ, 543, L157

Caselli, P., Myers, P. C., & Thaddeus, P. 1995, ApJ, 455, L77+

Cesaroni, R., Churchwell, E., Hofner, P., Walmsley, C. M., & Kurtz, S. 1994, A&A, 288, 903

Cesaroni, R., Walmsley, C. M., & Churchwell, E. 1992, A&A, 256, 618

Chambers, E. T., Jackson, J. M., Rathborne, J. M., & Simon, R. 2009, ApJS, 181, 360

Chapman, N. L., Mundy, L. G., Lai, S.-P., & Evans, N. J. 2009, ApJ, 690, 496

Chen, X., Shen, Z., Li, J., Xu, Y., & He, J. 2009, ArXiv e-prints

Churchwell, E., Walmsley, C. M., & Cesaroni, R. 1990, A&AS, 83, 119

Churchwell, E., Walmsley, C. M., & Wood, D. O. S. 1992, A&A, 253, 541

Clark, P. C., Klessen, R. S., Bonnell, I. A., & Smith, R. J. 2008, in Astronomical Society of the Pacific Conference Series, Vol. 387, Massive Star Formation: Observations Confront Theory, ed. H. Beuther, H. Linz, & T. Henning, 208–+

Clemens, D. P. 1985, ApJ, 295, 422

Condon, J. J., Cotton, W. D., Greisen, E. W., et al. 1998, AJ, 115, 1693

Crapsi, A., Caselli, P., Walmsley, C. M., et al. 2005, ApJ, 619, 379

Cruz-González, C., Recillas-Cruz, E., Costero, R., Peimbert, M., & Torres-Peimbert, S. 1974, Revista Mexicana de Astronomia y Astrofisica, 1, 211

Cyganowski, C. J., Whitney, B. A., Holden, E., et al. 2008, AJ, 136, 2391

Dame, T. M., Elmegreen, B. G., Cohen, R. S., & Thaddeus, P. 1986, ApJ, 305, 892

Dame, T. M., Ungerechts, H., Cohen, R. S., et al. 1987, ApJ, 322, 706

Danby, G., Flower, D. R., Valiron, P., Schilke, P., & Walmsley, C. M. 1988, MNRAS, 235, 229

Deharveng, L., Zavagno, A., & Caplan, J. 2005, A&A, 433, 565

Deharveng, L., Zavagno, A., Schuller, F., et al. 2009, A&A, 496, 177

Dehnen, W. & Binney, J. J. 1998, MNRAS, 298, 387

Draine, B. T. 2003, ARA&A, 41, 241

Egan, M. P., Shipman, R. F., Price, S. D., et al. 1998, ApJ, 494, L199+

Ellingsen, S. P. 2006, ApJ, 638, 241

Estalella, R., Mauersberger, R., Torrelles, J. M., et al. 1993, ApJ, 419, 698

Evans, II, N. 2003, in SFChem 2002: Chemistry as a Diagnostic of Star Formation, ed. C. L. Curry & M. Fich, 157–+

Evans, II, N. J. 1999, ARA&A, 37, 311

Fazio, G. G., Hora, J. L., Allen, L. E., et al. 2004, ApJS, 154, 10

Fich, M., Blitz, L., & Stark, A. A. 1989, ApJ, 342, 272

Fish, V. L. & Reid, M. J. 2007, ApJ, 670, 1159

Flaherty, K. M., Pipher, J. L., Megeath, S. T., et al. 2007, ApJ, 663, 1069

Fomalont, E. B., Petrov, L., MacMillan, D. S., Gordon, D., & Ma, C. 2003, AJ, 126, 2562

Fontani, F., Cesaroni, R., Caselli, P., & Olmi, L. 2002, A&A, 389, 603

Frerking, M. A., Langer, W. D., & Wilson, R. W. 1982, ApJ, 262, 590

Froebrich, D. & del Burgo, C. 2006, MNRAS, 369, 1901

Fuller, G. A., Williams, S. J., & Sridharan, T. K. 2005, A&A, 442, 949

Garzon, F., Lopez-Corredoira, M., Hammersley, P., et al. 1997, ApJ, 491, L31+

Green, J. A., Caswell, J. L., Fuller, G. A., et al. 2009, MNRAS, 392, 783

Guetter, H. H. & Turner, D. G. 1997, AJ, 113, 2116

Hachisuka, K., Brunthaler, A., Menten, K. M., et al. 2006, ApJ, 645, 337

Hachisuka, K., Brunthaler, A., Menten, K. M., et al. 2009, ApJ, 696, 1981

Haynes, R. F., Caswell, J. L., & Simons, L. W. J. 1979, Australian Journal of Physics Astrophysical Supplement, 48, 1

Helfand, D. J., Becker, R. H., White, R. L., Fallon, A., & Tuttle, S. 2006, AJ, 131, 2525

Helou, G. & Walker, D. W., eds. 1988, Infrared astronomical satellite (IRAS) catalogs and atlases. Volume 7: The small scale structure catalog, Vol. 7

Henning, T., Martin, K., Reimann, H.-G., et al. 1994, A&A, 288, 282

Hildebrand, R. H. 1983, QJRAS, 24, 267

Hill, T., Thompson, M. A., Burton, M. G., et al. 2006, MNRAS, 368, 1223

Hillenbrand, L. A., Massey, P., Strom, S. E., & Merrill, K. M. 1993, AJ, 106, 1906

Hirota, T., Bushimata, T., Choi, Y. K., et al. 2007, PASJ, 59, 897

Ho, P. T. P. & Townes, C. H. 1983, ARA&A, 21, 239

Honma, M., Bushimata, T., Choi, Y. K., et al. 2007, PASJ, 59, 889

Indebetouw, R., Mathis, J. S., Babler, B. L., et al. 2005, ApJ, 619, 931

Jackson, J. M., Finn, S. C., Rathborne, J. M., Chambers, E. T., & Simon, R. 2008, ApJ, 680, 349

Jackson, J. M., Rathborne, J. M., Shah, R. Y., et al. 2006, ApJS, 163, 145

Jaffe, D. T., Guesten, R., & Downes, D. 1981, ApJ, 250, 621

Jiménez-Serra, I., Martín-Pintado, J., Rodríguez-Franco, A., & Martín, S. 2005, ApJ, 627, L121

Joshi, Y. C. 2007, MNRAS, 378, 768

Kim, M. K., Hirota, T., Honma, M., et al. 2008, PASJ, 60, 991

Kirby, L. 2009, ApJ, 694, 1056

Kirk, J. M., Ward-Thompson, D., & André, P. 2005, MNRAS, 360, 1506

Klessen, R. S., Burkert, A., & Bate, M. R. 1998, ApJ, 501, L205+

Knödlseder, J. 2000, A&A, 360, 539

Kovalev, Y. Y., Petrov, L., Fomalont, E. B., & Gordon, D. 2007, AJ, 133, 1236

Krumholz, M. R., Klein, R. I., McKee, C. F., Offner, S. S. R., & Cunningham, A. J. 2009, Science, 323, 754

Krumholz, M. R. & McKee, C. F. 2008, Nature, 451, 1082

Krumholz, M. R., McKee, C. F., & Klein, R. I. 2005, Nature, 438, 332

Kurtz, S., Cesaroni, R., Churchwell, E., Hofner, P., & Walmsley, C. M. 2000, Protostars and Planets IV, 299

Lada, C. J. & Lada, E. A. 2003, ARA&A, 41, 57

Lada, C. J., Lada, E. A., Clemens, D. P., & Bally, J. 1994, ApJ, 429, 694

Larson, R. B. 1981, MNRAS, 194, 809

Lee, Y. & Jung, J.-H. 2003, New Astronomy, 8, 191

Leung, C. M. & Brown, R. L. 1977, ApJ, 214, L73

Li, D., Goldsmith, P. F., & Menten, K. 2003, ApJ, 587, 262

Lindegren, L. 2009, American Astronomical Society, IAU Symposium #261. Relativity in Fundamental Astronomy: Dynamics, Reference Frames, and Data Analysis 27 April - 1 May 2009 Virginia Beach, VA, USA, #16.01; Bulletin of the American Astronomical Society, Vol. 41, p.890, 261, 1601

Ma, C., Arias, E. F., Eubanks, T. M., et al. 1998, AJ, 116, 516

MacLaren, I., Richardson, K. M., & Wolfendale, A. W. 1988, ApJ, 333, 821

MacLeod, G. C., Scalise, E. J., Saedt, S., Galt, J. A., & Gaylard, M. J. 1998, AJ, 116, 1897

Mangum, J. G. & Wootten, A. 1993, ApJS, 89, 123

Mangum, J. G., Wootten, A., & Mundy, L. G. 1992, ApJ, 388, 467

Mardones, D., Myers, P. C., Tafalla, M., et al. 1997, ApJ, 489, 719

McCutcheon, W. H., Sato, T., Dewdney, P. E., & Purton, C. R. 1991, AJ, 101, 1435

McKee, C. F. & Tan, J. C. 2003, ApJ, 585, 850

McMillan, P. J. & Binney, J. J. 2009, [ArXiv:0907.4685]

Megeath, S. T., Biller, B., Dame, T. M., et al. 2003, in Revista Mexicana de Astronomia y Astrofisica Conference Series, Vol. 15, Winds, Bubbles, and Explosions: a conference to honor John Dyson, ed. J. Arthur & W. J. Henney, 151–153

Menten, K. M. 1991, ApJ, 380, L75

Menten, K. M. 1996, in IAU Symposium, Vol. 178, Molecules in Astrophysics: Probes & Processes, ed. E. F. van Dishoeck, 163

Menten, K. M., Reid, M. J., Forbrich, J., & Brunthaler, A. 2007, A&A, 474, 515

Minier, V., Peretto, N., Longmore, S. N., et al. 2007, in IAU Symposium, Vol. 237, IAU Symposium, ed. B. G. Elmegreen & J. Palous, 160–164

Moellenbrock, G. A., Claussen, M. J., & Goss, W. M. 2009, ApJ, 694, 192

Moffat, A. F. J., Jackson, P. D., & Fitzgerald, M. P. 1979, A&AS, 38, 197

Molinari, S., Brand, J., Cesaroni, R., & Palla, F. 1996, A&A, 308, 573

Moore, T. J. T., Lumsden, S. L., Ridge, N. A., & Puxley, P. J. 2005, MNRAS, 359, 589

Moscadelli, L., Reid, M. J., Menten, K. M., et al. 2009, ApJ, 693, 406

Motte, F., Bontemps, S., Schilke, P., et al. 2007, A&A, 476, 1243

Myers, P. C. 1983, ApJ, 270, 105

Myers, P. C., Mardones, D., Tafalla, M., Williams, J. P., & Wilner, D. J. 1996, ApJ, 465, L133+

Nammahachak, S., Asanok, K., Hutawarakorn Kramer, B., et al. 2006, MNRAS, 371, 619

Nishiyama, S., Tamura, M., Hatano, H., et al. 2009, ApJ, 696, 1407

Olmi, L., Cesaroni, R., Neri, R., & Walmsley, C. M. 1996, A&A, 315, 565

Ormel, C. W., Shipman, R. F., Ossenkopf, V., & Helmich, F. P. 2005, A&A, 439, 613

Ossenkopf, V. & Henning, T. 1994, A&A, 291, 943

Ott, M., Witzel, A., Quirrenbach, A., et al. 1994, A&A, 284, 331

Pagani, L., Pardo, J., Apponi, A. J., Bacmann, A., & Cabrit, S. 2005, A&A, 429, 181

Palla, F. & Stahler, S. W. 1993, ApJ, 418, 414

Parker, Q. A., Phillipps, S., Pierce, M. J., et al. 2005, MNRAS, 362, 689

Perault, M., Omont, A., Simon, G., et al. 1996, A&A, 315, L165

Peretto, N., André, P., & Belloche, A. 2006, A&A, 445, 979

Perryman, M. A. C., Lindegren, L., Kovalevsky, J., et al. 1995, A&A, 304, 69

Pestalozzi, M. R., Chrysostomou, A., Collett, J. L., et al. 2007, A&A, 463, 1009

Pestalozzi, M. R., Minier, V., & Booth, R. S. 2005, A&A, 432, 737

Petrov, L., Kovalev, Y. Y., Fomalont, E., & Gordon, D. 2005, AJ, 129, 1163

Petrov, L., Kovalev, Y. Y., Fomalont, E. B., & Gordon, D. 2006, AJ, 131, 1872

Pety, J. 2005, in SF2A-2005: Semaine de l'Astrophysique Francaise, ed. F. Casoli, T. Contini, J. M. Hameury, & L. Pagani, 721–+

Pillai, T., Wyrowski, F., Carey, S. J., & Menten, K. M. 2006, A&A, 450, 569

Pillai, T., Wyrowski, F., Hatchell, J., Gibb, A. G., & Thompson, M. A. 2007, A&A, 467, 207

Pineau des Forets, G., Roueff, E., Schilke, P., & Flower, D. R. 1993, MNRAS, 262, 915

Pirogov, L., Zinchenko, I., Caselli, P., & Johansson, L. E. B. 2007, A&A, 461, 523

Purcell, C. R., Balasubramanyam, R., Burton, M. G., et al. 2006, MNRAS, 367, 553

Purcell, C. R., Minier, V., Longmore, S. N., et al. 2009, A&A, 504, 139

Ragan, S. E., Bergin, E. A., Plume, R., et al. 2006, ApJS, 166, 567

Rathborne, J. M., Jackson, J. M., & Simon, R. 2006, ApJ, 641, 389

Rathborne, J. M., Jackson, J. M., Zhang, Q., & Simon, R. 2008, ApJ, 689, 1141

Rathborne, J. M., Simon, R., & Jackson, J. M. 2007, ApJ, 662, 1082

Reach, W. T., Megeath, S. T., Cohen, M., et al. 2005, PASP, 117, 978

Reid, M. J. & Brunthaler, A. 2004, ApJ, 616, 872

Reid, M. J., Menten, K. M., Brunthaler, A., et al. 2009a, ApJ, 693, 397

Reid, M. J., Menten, K. M., Zheng, X. W., et al. 2009b, ApJ, 700, 137

Rohlfs, K. & Wilson, T. L. 2004, Tools of radio astronomy, ed. K. Rohlfs & T. L. Wilson

Ros, E., Marcaide, J. M., Guirado, J. C., Sardón, E., & Shapiro, I. I. 2000, A&A, 356, 357

Rosolowsky, E., Dunham, M. K., Ginsburg, A., et al. 2009, ArXiv e-prints

Rygl, K. L. J., Brunthaler, A., Menten, K. M., Reid, M. J., & van Langevelde, H. J. 2008, in The role of VLBI in the Golden Age for Radio Astronomy, ArXiv e-print 0812.0905

Rygl, K. L. J., Brunthaler, A., Reid, M. J., et al. 2010a, A&A, 511, A2

Rygl, K. L. J., Wyrowski, F., Schuller, F., & Menten, K. M. 2010b, ArXiv e-print 1003.5102

Sandstrom, K. M., Peek, J. E. G., Bower, G. C., Bolatto, A. D., & Plambeck, R. L. 2007, ApJ, 667, 1161

Sato, M., Hirota, T., Honma, M., et al. 2007, PASJ, 59, 743

Sato, M., Hirota, T., Honma, M., et al. 2008, PASJ, 60, 975

Schilke, P., Walmsley, C. M., Pineau des Forets, G., & Flower, D. R. 1997, A&A, 321, 293

Schneider, N., Bontemps, S., Simon, R., et al. 2006, A&A, 458, 855

Schneider, N., Csengeri, T., Bontemps, S., et al. 2010, ArXiv e-prints

Schöier, F. L., van der Tak, F. F. S., van Dishoeck, E. F., & Black, J. H. 2005, A&A, 432, 369

Schuller, F., Menten, K. M., Contreras, Y., et al. 2009, A&A, 504, 415

Sharpless, S. 1954, ApJ, 119, 334

Shinnaga, H., Ohashi, N., Lee, S., & Moriarty-Schieven, G. H. 2004, ApJ, 601, 962

Shu, F. H., Najita, J. R., Shang, H., & Li, Z. 2000, Protostars and Planets IV, 789

Simon, R., Jackson, J. M., Rathborne, J. M., & Chambers, E. T. 2006a, ApJ, 639, 227

Simon, R., Rathborne, J. M., Shah, R. Y., Jackson, J. M., & Chambers, E. T. 2006b, ApJ, 653, 1325

Snow, T. P. & McCall, B. J. 2006, ARA&A, 44, 367

Sobolev, A. M., Cragg, D. M., Ellingsen, S. P., et al. 2007, in IAU Symposium, Vol. 242, IAU Symposium, ed. J. M. Chapman & W. A. Baan, 81–88

Solomon, P. M., Jefferts, K. B., Penzias, A. A., & Wilson, R. W. 1971, ApJ, 168, L107+

Sridharan, T. K., Beuther, H., Schilke, P., Menten, K. M., & Wyrowski, F. 2002, ApJ, 566, 931

Stead, J. J. & Hoare, M. G. 2009, MNRAS, 400, 731

Su, Y.-N., Liu, S.-Y., & Lim, J. 2009, ApJ, 698, 1981

Sutton, E. C., Blake, G. A., Masson, C. R., & Phillips, T. G. 1985, ApJS, 58, 341

Swift, J. J. 2009, ApJ, 705, 1456

Szymczak, M., Hrynek, G., & Kus, A. J. 2000, A&AS, 143, 269

Tafalla, M., Myers, P. C., Caselli, P., Walmsley, C. M., & Comito, C. 2002, ApJ, 569, 815

Tafalla, M. & Santiago, J. 2004, A&A, 414, L53

Thompson, A. R., Moran, J. M., & Swenson, G. W. 1991, Interferometry and synthesis in radio astronomy, ed. A. R. Thompson, J. M. Moran, & G. W. Swenson

Vallée, J. P. 2008, AJ, 135, 1301

Val'tts, I. E. 1998, Astronomy Letters, 24, 788

van der Tak, F. F. S., Black, J. H., Schöier, F. L., Jansen, D. J., & van Dishoeck, E. F. 2007, A&A, 468, 627

van der Walt, J. 2005, MNRAS, 360, 153

Walmsley, C. M. & Ungerechts, H. 1983, A&A, 122, 164

Walsh, A. J., Burton, M. G., Hyland, A. R., & Robinson, G. 1998, MNRAS, 301, 640

Weingartner, J. C. & Draine, B. T. 2001, ApJ, 548, 296

Whitney, B. A., Kenyon, S. J., & Gomez, M. 1997, ApJ, 485, 703

Wilking, B. A., Blackwell, J. H., Mundy, L. G., & Howe, J. E. 1989, ApJ, 345, 257

Wilson, T. L. & Rood, R. 1994, ARA&A, 32, 191

Wood, D. O. S. & Churchwell, E. 1989, ApJ, 340, 265

Wouterloot, J. G. A. & Brand, J. 1989, A&AS, 80, 149

Wu, Y., Zhu, M., Wei, Y., et al. 2005, ApJ, 628, L57

Wyrowski, F., Heyminck, S., Güsten, R., & Menten, K. M. 2006, A&A, 454, L95

Wyrowski, F., Schilke, P., Walmsley, C. M., & Menten, K. M. 1999, ApJ, 514, L43

Xu, Y., Reid, M. J., Zheng, X. W., & Menten, K. M. 2006, Science, 311, 54

Yang, J., Umemoto, T., Iwata, T., & Fukui, Y. 1991, ApJ, 373, 137

Zasowski, G., Majewski, S. R., Indebetouw, R., et al. 2009, ApJ, 707, 510

Zavagno, A., Deharveng, L., Brand, J., et al. 2005, in IAU Symposium, Vol. 227, Massive Star Birth: A Crossroads of Astrophysics, ed. R. Cesaroni, M. Felli, E. Churchwell, & M. Walmsley, 346–351

Zavagno, A., Deharveng, L., Comerón, F., et al. 2006, A&A, 446, 171

Zhang, Q., Wang, Y., Pillai, T., & Rathborne, J. 2009, ApJ, 696, 268

Zheng, X. W., Ho, P. T. P., Reid, M. J., & Schneps, M. H. 1985, ApJ, 293, 522

Zhou, S., Evans, II, N. J., Koempe, C., & Walmsley, C. M. 1993, ApJ, 404, 232

Zinchenko, I., Henkel, C., & Mao, R. Q. 2000, A&A, 361, 1079

Acknowledgements

To Prof. Karl Menten and Prof. Pavel Kroupa I am grateful for their support and their comments that significantly improved this PhD thesis. I worked closely together with Dr. Andreas Brunthaler and Dr. Friedrich Wyrowski, without them this work would have been impossible. Both introduced me to their field of expertise and allowed me to gather my own experience. They were always available for discussions and questions, which, together with their advice, I value deeply. I thank Prof. Ian Brock from the Physikalisches Institut and Prof. Gerhard von der Emde from the Institut für Zoologie for being part of the examination board.

I thank Prof. Karl Menten, director of the submm group of MPIfR, and Prof. Anton Zensus, director of the International Max-Planck Research School for Astronomy and Astrophysics at the universities of Bonn and Cologne (IMPRS), for giving me the possibility of doing my PhD in radioastronomy. During three years of my PhD I was financially supported by the IMPRS, for which I am very grateful. I acknowledge travel support from both the IMPRS and Prof. Menten, which gave the possibility to visit summer/winter schools and conferences. During all my time in Bonn I was a member of the IMPRS, which, amongst many things, gave me the possibility to be in touch with PhD students from different astronomical fields and widen knowledge through the Monday seminars and the retreats. The IMPRS coordinators, Eduardo Ros and Emmanouil Angelakis and their assistants Gabi Breuer and Simone Pott, helped me a lot over all these years and without their enthousiastic support this PhD would have been a much bigger mountain to climb.

I thank all the members of the submm and VLBI group at the MPIfR, for the friendly atmosphere, the nice chats, but also for always being there to help me with any small problems that I ran into. I also want to thank my co-authors during my PhD, for their reviews of my drafts and useful comments. This work made an intensive use of observational data, observed by myself or other observers. The assistance of the staff of the Effelsberg telescope, the IRAM 30m telescope, the APEX telescope, the European VLBI Network, in particlar the staff of JIVE, were crucial. Additionally, this work made use of many databases such as ADS[1], SIMBAD[2], GLIMPSE and MIPSGAL surveys available at the NASA/IPAC infrared Science Archive[3] , Galactic Ring Survey data[4], JPL molecular database[5], and the LAMBDA molecular database[6].

I had a lot of fun during the PhD, and for this I have to thank my roommates, Peng, Lies,

[1] http://adswww.harvard.edu/
[2] http://simbad.u-strasbg.fr/simbad/
[3] http://irsa.ipac.caltech.edu/index.html
[4] http://www.bu.edu/galacticring/
[5] http://spec.jpl.nasa.gov/
[6] http://www.strw.leidenuniv.nl/ moldata/

Esteban, and Yiping, as well as Miguel, Kosmas, Maca, Manolis, Frank, Giannis, Lilia and Lars for the good times - mostly downtown in a pub :). The biggest fulfillment during my time on Bonn, was my time I spent with you, Nicola, as I hope we will spend much more together. I am very grateful to you for always cheering me up and making me laugh, even in the hardest of moods wings and times of stress.

My friends from the WG (Venusbergweg 50, yeah!) and from Amsterdam + surroundings I want to thank for keeping me sane by taking my mind off astronomy completely. The kitchen discussions, visits to Bonn, phone-calls, house parties, and WG dinners and BBQs were some of the highlights of my stay in Germany. Finally, but not last in my mind, I want to thank my family for always having tried to be interested in the utterly not understandable field of science which I chose to pursue.